UNIVERSITAT POLITÈCNICA
DE CATALUNYA
BARCELONATECH

Simulation and design of all-optical logic gates based on photonic crystals

Oraman Yoosefi

UNIVERSITAT POLITÈCNICA DE CATALUNYA
BARCELONATECH
Departament d'Enginyeria Electrònica

Simulation and Design of All-Optical Logic Gates Based on Photonic Crystals

Department of Electronic Engineering
University Polytechnic of Catalonia

Autor:Oraman Yoosefi

Director of the thesis:Angel Rodriguez Martines

March 30, 2021

Dissemination of Work

Accepted

1-Yoosefi, O., Rodríguez, A., 2020 . Design and Analysis of A Complete Full Adder Based On Metal-Insulator-Metal (MIM) Waveguide-Based Plasmonic Waves. *Research Square*.

2-Yoosefi, O., Rodríguez, A., 2019 , Improved design of all-optica half subtractor based 2-dimensional photonic crystal, *international Journal of Advance Engineering and Research Development*. 6(3) .

3- Yoosefi, O., Yahyapour, M.J., Segura, D., Vega, D., Dios, F.,and. Rodriguez, A., 2017 . Development of gas sensors based in photonic crystal slabs,2017 *Spanish Conference on Electron Devices (CDE).*

ABSTRACT

The photonic crystal is an artificially designed optical material in which dielectric constant changes periodically. There are some wavelengths that can't propagate through the structure and form the photonic band gap (PBG). By engineering the photonic band gap, the flow of light can be controlled.

Due to their unique properties, the photonic crystal-based logic gates have numerous advantages over the conventional logic gates such as compactness, simple structure, high speed, and high confinement. The size of the optical logic gate based on the photonic crystal is in the order of wavelength. By engineering the photonic band gap, the flow of light can be controlled. These logic structures are the key components of optical network and optical communication systems. Because of various advantages, it is propitious for use of future optical signal processors and optical computers. Therefore, in this thesis, the design of photonic crystal logic gates have been focused. The simulation of proposed designs is carried out by the finite difference time domain (FDTD) method.

In this thesis, a complete and appropriate analysis of photonic crystal logic gates is presented. Also, several structures of the photonic crystal-based logic gates are designed and simulated. Initially simple structures of NOT, OR and AND gates are presented. Then the NOR and NAND gates were designed by combining these logic gates without using any external devices. Simulation results show that the proposed logic gates have high contrast ratio and low power consumption. Another logic gate based on the self-collimated beam is proposed that has low unwanted backward light propagation in input ports. Finally, an AND logic gate based on Kerr nonlinear switching with high contrast ratio is designed and simulated.

Therefore, a proper design for XOR can be effective in improving the performance of the compressor (4:2) and can improve the efficiency of the whole multiplier system. In this thesis, the design of the compressor (4:2) based on the proposed XOR gate is presented with carbon nanotube transistors (CNTT) and the results are simulated in 32-nanometer carbon nanotube field-effect transistor (CNTFET) technology. Comparing the results of this implementation with the best accessible designs shows that the design of the provided compressor, while reducing the number of circuit transistors, can improve the delay by 4.31%, the power consumption by 45.99% and the power multiplication delay by 47.72% as compared to previously-designed compressors.

In this complete full adder, by combining resonant waves in the first and second modes, a high transmission coefficient is obtained. Undeniably, the obtained complete full adder operates through designing 4-input AND, XOR, OR, and NOT logic gates, instead of conventional 2-input AND and OR gates or even 2- or 3-input AND and XOR gates. Therefore, a complete full adder with four 4-input gates in this research is able to decrease manufacturing complications and costs.

In this thesis, two-dimensional (2D) PC-based 8 channel demultiplexers are proposed and designed and the functional characteristics of demultiplexer specifically resonant wavelength, transmission efficiency, quality factor, spectral width, channel spacing, and crosstalk are

investigated. For wavelength selection, 6 circular-shaped ring resonators were used and as for the selection of the 7 different wavelengths, in order to acquire our wavelength division demultiplexer, a structure built based on 3 different values of dielectric constants was utilized. This structure has a better performance with an average transmitted power of 90.5%

Using the 2D Finite Difference Time Domain (2D FDTD) method, properties of the demultiplexer such as resonant wavelength and Q factor have been theoretically investigated. The Photonic Band Gap (PBG) of the designed structure is calculated by the Plane Wave Expansion (PWE) method.

Keywords: Photonic crystal, Self-collimating effect, Interference, Plane wave expansion, Photonic band gap, Photonic crystal logic gates, Finite difference time domain method, Full adder, OR gate, Plasmonic waves, Resonance wavelength, MIM Waveguide, Photonic band gap, Ring resonator, Demultiplexer

TABLE OF CONTENTS

LIST OF FIGURES

LIST OF TABLES

Chapter 1
Introduction

1-1- INTRODUCTION

Optics is the science of light, which has a history that dates back to the dawn of mankind. In the modern world of Information and Communications Technology (ICT), optics and photonics are utilized in optical telecommunication applications such as sender lasers and optical fiber transmission media.

In the past, high costs were barriers to the use of optical elements in computers and processors. However, with the maturity of optical technology, the prices have dropped, and the required miniaturization has been materialized. The computer industry re-assesses the situation and brings optical alternatives into computer systems. Meanwhile, the use of all types of optical equipment in communication networks and computers increases the speed of progress in the telecommunication industry.

Nowadays, the most common application of optical technology in fiber-optic telecommunication networks is for high-speed connections such as server racks, terminal connections, WANs, and so on.

Photonic crystals are effective structures for making new artificial materials with controlled light characteristics for special functions. It is necessary to mention that, before the development of photonic crystals, the control of light in dielectric environments was impossible, and the only way to use the properties of light was in a reflected state against different materials.

For instance, the production and control of positive or negative dispersion characteristics of light had been impossible, nowadays thanks to photonic crystals, it is possible. By using photonic crystals, the velocity of light could be controlled, even stop and store it, amplifying and removing special light modes, etc.. This new structure can be used in different fields like Electro-optics equipment, lasers, light emitted diodes and optical components, different kind of sensors (biological, chemical, mechanical and physical), processing light signals, and optic integrated devices Bouamami and Naoum (2013) [1].

Photonic crystals could be used in photonics instruments for different applications like controlling, producing, amplifying, conducting, combining, separating, measuring and detecting the light in micro and nano scales. For each application, the structure has to be designed
To fabricate these structures for nano optics in the photonic field, the same techniques used in the ULSI (ultra-large-scale integration) fabrication process in microelectronics can be applied.

A waveguide can be made with a photonic crystal. Its function depends on the length of the wave. For making photonic crystal waveguide, linearity defect (two-dimension wave guider) and plate (three-dimension wave guide) can be used.

1-2- Electromagnetic waves

Before describing the techniques used for communications, in particular the wavelength-division multiplexing (WDM) method, and before describing the kinds of material structures and light-matter configurations we have addressed in this thesis work, let us remember the notion and properties of the electromagnetic waves in free space, in dielectrics and in conductors, with a description of the equations to which they obey.

1-2-1- Electromagnetic waves in free space

In free space (i.e., in the absence of any charges or currents) Maxwell's equations have a trivial solution in which all the fields vanish. However, there are also non-trivial solutions with considerable practical importance. In general, it is difficult to solve Maxwell's equations because two of theequations involve both the electric and magnetic fields. However, by taking additional derivatives, it ispossible to write equations for the fields that involve only either the electric or the magnetic field. Thismakes it easier to write down solutions Taflove and Hagness (1998) [2]. However, the drawback is that instead of first-order differentialequations, the new equations are second-order in the derivatives. There is no guarantee that a solution to the second-order equations will also satisfy the first-order equations, and it is necessary to impose additional constraints to ensure that the first-order equations are satisfied. Fortunately, it turns out that this is not difficult to do, and taking additional derivatives is a useful technique for simplifying the analytical solution of Maxwell's equations in simple cases.

1-2-1-1- Wave equation for the electric field

In free space, Maxwell's Equations for the electric field $\vec{E}$ and the magnetic field $\vec{B}$ take the form:

$$\nabla \cdot \vec{E} = 0, \qquad (1.1)$$

$$\nabla \cdot \vec{B} = 0, \qquad (1.2)$$

$$\nabla \times \vec{B} = \frac{1}{c^2}\frac{\partial \vec{E}}{\partial t}, \qquad (1.3)$$

$$\nabla \times \vec{E} = -\frac{\partial \vec{B}}{\partial t}, \qquad (1.4)$$

Where

$$\frac{1}{c^2} = \mu_0 \varepsilon_0 \quad , \qquad (1.5)$$

μ_0 and ε_0 being the magnetic permeability and electrical permittivity of vacuum, respectively, and *c* the speed of light in vacuum. The goal is to find a form of the equation in which the fields $\vec{E}$ and $\vec{B}$, appear separately, not together in the same equation. As the first step, the curl of both sides of **Equation 1-4** would be taken, and interchange the order of differentiation on the right-hand side (which we are allowed to do since the space and time coordinates are independent). The equation below is obtained:

$$\nabla \times \nabla \times \vec{E} = -\frac{\partial}{\partial t}\nabla \times \vec{B}\,. \qquad (1.6)$$

Substituting for $\nabla \times \vec{B}$ from **Equation 1-3** , this becomes:

$$\nabla \times \nabla \times \vec{E} = -\frac{1}{c^2}\frac{\partial^2 \vec{E}}{\partial t^2}. \qquad (1.7)$$

This second-order differential equation involves only the electric field $\vec{E}$ so the aim of decoupling the field equations has been achieved. However, it is possible to make a further simplification using a mathematical identity. For any differentiable vector field $\vec{a}$,

$$\nabla \times \nabla \times \vec{a} \equiv \nabla(\nabla \cdot \vec{a}) - \nabla^2 \vec{a}. \qquad (1.8)$$

Equation below is finally obtained:

$$\nabla^2 \vec{E} - \frac{1}{c^2} \frac{\partial^2 \vec{E}}{\partial t^2} = 0. \qquad (1.9)$$

Equation 1-9 is the wave equation in three spatial dimensions. Note that each component of the electricfield independently satisfies the wave equation. The solution, representing a plane wave propagating in the direction of the vector $\vec{k}$, may be written in the form:

$$\vec{E} = \vec{E}_0 \cos(\vec{k} \cdot \vec{r} - \omega t + \varphi_0), \qquad (1.10)$$

Where $\vec{E}_0$ is a constant vector, φ_0 is a constant phase, ω and $\vec{k}$ are constants related to the frequency ν and wavelength λ of the wave by:

$$\omega = 2\pi\nu \ , \qquad (1.11)$$

$$\lambda = \frac{2\pi}{|\vec{k}|} . \qquad (1.12)$$

If **Equation 1-10** substitutes into the wave **Equation 1-9,** it could be found that it provides a valid solution as long as the angular frequency ω and wave vector $\vec{k}$ satisfy the dispersion relation:

$$\frac{\omega}{|\vec{k}|} = c. \qquad (1.13)$$

Inspecting **Equation 1-10**, it could be seen that a particle travelling in the direction of $\vec{k}$ has to move at a speed $\omega/|\vec{k}|$ in order to remain at the same phase in the wave. Thus the quantity c is the phase velocity ofthe wave. This quantity c is, of course, the speed of light in vacuum and the identification of light with an electromagnetic wave (with the phase velocity related to the electric permittivity and magneticpermeability by **Equation 1-5**) was one of the great achievements of 19th century physics.

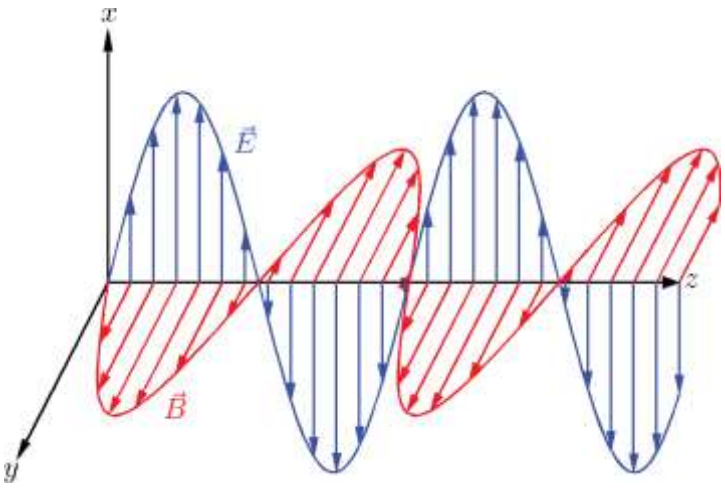

Figure 1-1: Electric and magnetic fields in a plane electromagnetic wave in free space. The wave vector $\vec{k}$ is in the direction of the +z axis[2].

1-2-1-2- Wave equation for the magnetic field

So far, just the electric field has been considered. But Maxwell's equation tells us that an electric field that varies with time must have a magnetic field associated with it. Therefore, a(non-trivial) solution for the magnetic field in free space should be looked for. Starting with **Equation 1-3**, and following the same procedure as above, it could be found that the magnetic field also satisfies the wave equation:

$$\nabla^2\vec{B} - \frac{1}{c^2}\frac{\partial^2\vec{B}}{\partial t^2} = 0\,, \qquad (1.14)$$

with a similar solution:

$$\vec{B} = \vec{B}_0 \cos\left(\vec{k}\cdot\vec{r} - \omega t + \varphi_0\right). \qquad (1.15)$$

Here, the same constants "ω", $\vec{k}$, and φ_0 have been written as used for the electric field, though we do not so far know they have to be the same. In the following section the fact that these constants do indeed need to be the same for both the electric field and the magnetic field would be shown.

1-2-1-3- Relations between electric and magnetic fields in a plane wave in free space

As commented above, although taking additional derivatives of Maxwell's equations allows us to decouple the equations for the electric and magnetic fields, additional constraints should be imposed on the solutions to ensure that the first-order equations are satisfied. In particular, substituting the expressionsfor the fields (1-10) and (1-15) into **Equation 1-1 and 1-2** respectively, and noting that the latter equations must be satisfied at all points in space and at all times, it is obtained:

$$\vec{k}\cdot\vec{E}_0 = 0, \qquad (1.16)$$

$$\vec{k}\cdot\vec{B}_0 = 0. \qquad (1.17)$$

Since $\vec{k}$ represents the direction of propagation of the wave, it can be seen that the electric and magnetic fields must at all times and all places be perpendicular to the direction in which the wave is travelling. This is a feature that does not appear if only the second-order equations is considered.

Finally, substituting the expressions for the fields (1-10) and (1-15) into **Equation 1-4 and 1-3**, respectively, and again noting that the latter equations must be satisfied at all points in space and at all times, first it can be seen that the quantities ω, $\vec{k}$, and φ_0 appearing in (1-10) and (1-15) must be the same in each case. Also there are relations between the magnitudes and directions of the fields as shown bellow:

$$\vec{k} \times \vec{E}_0 = \omega \vec{B}_0, \qquad (1.18)$$

$$\vec{k} \times \vec{B}_0 = -\omega \vec{E}_0. \qquad (1.19)$$

If a coordinate system is chosen, so that $\vec{E}_0$ is parallel to the x axis and $\vec{B}_0$ is parallel to the y axis, then $\vec{k}$ must be parallel to the z axis. Note that the vector product $\vec{E} \times \vec{B}$ is in the same direction as the direction of propagation of the wave see **Figure 1-1**. The magnitudes of the electric and magnetic fields are related by:

$$\frac{|\vec{E}|}{|\vec{B}|} = c. \qquad (1.20)$$

Note that the wave vector $\vec{k}$ can be chosen arbitrarily. There are infinitely many 'modes' in which an electromagnetic wave propagating in free space may appear and the most general solution will be a sum over all modes. When the mode is specified (by giving the components of $\vec{k}$), the frequency is determined from the dispersion **Equation 1-13**. However, the amplitude and phase are not determined (although the electric and magnetic fields must have the same phase, and their amplitudes must be related by **Equation 1-20**).

1-2-1-4- Complex notation for electromagnetic waves

This section would be finished by introducing the complex notation for free waves. Note that the electric field given by **Equation 1-10** can also be written as:

$$\vec{E} = \mathrm{Re}\vec{E}_0 e^{i\varphi 0}\, e^{i(\vec{k}\cdot\vec{r}-\omega t)}. \qquad (1.21)$$

To avoid continually writing a constant phase factor when dealing with solutions to the wave equation, the real (constant) vector $\vec{E}_0$ would be replaced by the complex (constant) vector $\vec{E}'_0 = \vec{E}_0 e^{i\varphi 0}$. Since all the equations describing the fields are linear, and that any two solutions can be linearly superposed to construct a third solution, the complex vectors below are noted:

$$\vec{E}' = \vec{E}'_0\, e^{i(\vec{k}\cdot\vec{r}-\omega t)}, \qquad (1.22)$$

$$\vec{B}' = \vec{B}'_0\, e^{i(\vec{k}\cdot\vec{r}-\omega t)} \qquad (1.23)$$

Provide mathematically valid solutions to Maxwell's equations in free space, with the same relationships between the various quantities (frequency, wave vector, amplitudes, phase) as the

solutions given in **Equation 1-10 and 1-15**. Therefore, as long as linear equations are dealt with, all the algebraic manipulation using complex field vectors could be carried out, where it is implicit that the physical quantities are obtained by taking the real parts of the complex vectors. However, when using the complex notation, particular care is needed when taking the product of two complex vectors. To be safe, one should always take the real part before multiplying two complex quantities, the real parts of which represent physical quantities. Products of the electromagnetic field vectors occur in expressions for the energy density and energy fluxin an electromagnetic field.

Finally, note that all the results derived in this section are strictly true only for electromagnetic fields in a vacuum. The generalization to fields in uniform, homogenous, linear (i.e., constant permeability μ and permittivity ε) nonconducting media (i.e., dielectric media) is straightforward, with the use of the frequency-dependent refractive index to characterize the response of the medium to the electromagnetic wave. In such conditions, the wavevector and the wavenumber for an electromagnetic wave of frequency ω propagating inside a medium with refractive index $n(\omega)$ (which in general can be complex) increase by a factor $n(\omega)$ with respect to the wavevector and wavenumber of the wave in vacuum.

However, new features appear for waves in conductors, which are summarized below (in Subsection 1-2-2). Also, the concepts of phase and group velocities, as well as the boundary conditions at the surface of materials, are reviewed below (Subsections 1-2-3 and 1-2-4, respectively). On the other hand, the special case of nonlinear media will be considered in Chapter 2.

1-2-2- Electromagnetic waves in conductors

Electromagnetic waves in free space are characterized by an amplitude that remains constant in space and time. This is also true for waves traveling through any isotropic, homogeneous, linear, non-conducting medium, which could be referred to as an 'ideal' dielectric. The fact that real materials contain electric charges that can respond to electromagnetic fields means that the vacuum is really the only 'ideal' dielectric. Some real materials (for example, many gases, and materials such as glass) have properties that approximate those of an ideal dielectric, at least over certain frequency ranges. Many of these materials are transparent for a certain range of frequencies. However, it is known that conductors are not transparent: even a thin sheet of a good conductor such as aluminum or copper, for example, can provide an effective barrier for electromagnetic radiation over a wide range of frequencies.

To understand the shielding effect of good conductors is relatively straightforward. Essentially, the same procedure is followed to derive the wave equations for the electromagnetic fields as it was done for the case of a vacuum, but additional terms are included to represent the conductivity of the medium. These additional terms have the consequence that the amplitude of the wave decays as the wave propagates through the medium. The rate of decay of the wave is characterized by the skin depth, which depends (amongst other things) on the conductivity of the medium.

Let us consider an ohmic conductor. An ohmic conductor is defined by the relationship between the current density $\vec{J}$ at a point in the conductor, and the electric field $\vec{E}$ existing at the same point in the conductor:

$$\vec{J} = \sigma\vec{E} \qquad (1.24)$$

Where σ is a constant, the conductivity of the material.

In an uncharged ohmic conductor, Maxwell's equations take the form:

$$\nabla \cdot \vec{E} = 0, \qquad (1.25)$$

$$\nabla \cdot \vec{B} = 0, \qquad (1.26)$$

$$\nabla \times \vec{B} = \mu\sigma\vec{E} + \mu\varepsilon\frac{\partial\vec{E}}{\partial t}, \qquad (1.27)$$

$$\nabla \times \vec{E} = -\frac{\partial\vec{B}}{\partial t}, \qquad (1.28)$$

Where μ is the (absolute) permeability of the medium, and ε is the (absolute) permittivity. Notice the appearance of the additional term on the right-hand side of **Equation 1-27**, compared to **Equation 1-3**.

Following the same procedure as led to **Equation 1-9**, the following equation is derived for the electricfield in a conducting medium:

$$\nabla^2\vec{E} - \mu\sigma\frac{\partial\vec{E}}{\partial t} - \mu\varepsilon\frac{\partial^2\vec{E}}{\partial t^2} = 0. \qquad (1.29)$$

This is again a wave equation, but with a term that includes a first-order time derivative. In the equationfor a simple harmonic oscillator, such a term would represent a frictional force that leads to dissipationof the energy in the oscillator. There is a similar effect here. To see this, let us try a solution of the sameform as for a wave in free space. The results needed can be obtained more directly if thecomplex notation is used:

$$\vec{E} = \vec{E}_0\, e^{i(\vec{k}\cdot\vec{r}-\omega t)}. \qquad (1.30)$$

Substituting into the wave **Equation 1-29**, the dispersion relation is obtained:

$$-\vec{k}^2 + i\mu\sigma\omega + \mu\varepsilon\omega^2 = 0. \qquad (1.31)$$

Let us assume that the frequency ω is a real number. Then, to find a solution to **Equation 1-31**, the wave vector $\vec{k}$ is allowed to be complex. Let us write the real and imaginary parts as $\vec{\alpha}$ and $\vec{\beta}$ respectively:

$$\vec{k} = \vec{\alpha} + i\vec{\beta}\,. \qquad (1.32)$$

Substituting **Equation 1-32** into **Equation 1-31** and equating real and imaginary parts, it is found (after some algebra) that:

$$|\vec{\alpha}| = \omega\sqrt{\mu\varepsilon}\left(\frac{1}{2}+\frac{1}{2}\sqrt{1+\frac{\sigma^2}{\omega^2\,\varepsilon^2}}\right)^{\frac{1}{2}}, \qquad (1.33)$$

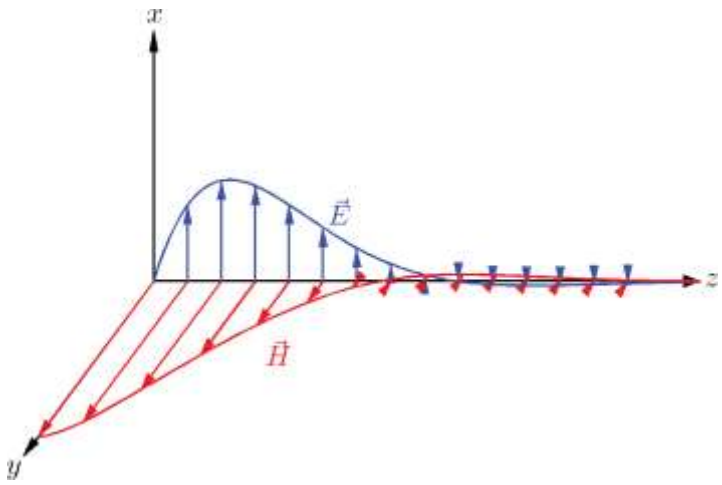

Figure 1-2: Electric and magnetic fields in a plane electromagnetic wave in a conductor. The wave vector is in the direction of the +z axis[2].

$$|\vec{\beta}| = \frac{\omega\mu\sigma}{2|\vec{\alpha}|}. \qquad (1.34)$$

To understand the physical significance of $\vec{\alpha}$ and $\vec{\beta}$, the **Equation 1-33** is written to the wave equation as:

$$\vec{E} = \vec{E}_0 e^{-\vec{\beta}.\vec{r}}\, e^{i(\vec{\alpha}\cdot\vec{r}-\omega t)}. \qquad (1.35)$$

It can be seen that there is still a wave-like oscillation of the electric field, but there is now also an exponentialdecay of the amplitude. The wavelength is determined by the real part of the wave vector:

$$\lambda = \frac{2\pi}{|\vec{\alpha}|}. \qquad (1.36)$$

The imaginary part of the wave vector gives the distance δ over which the amplitude of the wave falls bya factor 1/e, known as the skin depth:

$$\delta = \frac{1}{|\vec{\beta}|}. \qquad (1.37)$$

Accompanying the electric field, there must be a magnetic field:

$$\vec{B} = \vec{B}_0 \, e^{i(\vec{k}\cdot\vec{r}-\omega t)}. \qquad (1.38)$$

From Maxwell's equation, the amplitudes of the electric and magnetic fields must be related by:

$$\vec{k} \times \vec{E}_0 = \omega\vec{\beta}_0 \, . \qquad (1.39)$$

The electric and magnetic fields are perpendicular to each other and to the wave vector: this is the same situation as occurred for a plane wave in free space. However, since $\vec{k}$ is complex for a wave in a conductor, there is a phase difference between the electric and magnetic fields, given by the complex phase of $\vec{k}$. The fields in a plane wave in a conductor are illustrated in **Figure 1-2**.

The dispersion **Equation 1-31** gives a rather complicated algebraic relationship between the frequency and the wave vector, in which the electromagnetic properties of the medium (permittivity, permeability, and conductivity) all appear. However, in many cases, it is possible to write much simpler expressions that provide good approximations. First, there is the poor conductor regime:

$$\text{if } \sigma \ll \omega\varepsilon, \text{then} |\vec{\alpha}| \approx \omega\sqrt{\mu\varepsilon}\,, \quad |\vec{\beta}| \approx \frac{\sigma}{2}\sqrt{\frac{\mu}{\varepsilon}} \, . \qquad (1.40)$$

The wavelength is related to the frequency in a way that a dielectric would be expected .Next there is the good conductor regime:

$$\text{if } \sigma \gg \omega\varepsilon, \text{then} |\vec{\alpha}| \approx \omega\sqrt{\frac{\omega\sigma\mu}{2}}\,, \quad |\vec{\beta}| \approx |\vec{\alpha}| \, . \qquad (1.41)$$

Here the situation is very different. The wavelength depends directly on the conductivity: for a good conductor, the wavelength is very much shorter than it would be for a wave at the same frequency in freespace. The real and imaginary parts of the wave vector are approximately equal. This means that there is a significant reduction in the amplitude of the wave even over one wavelength. Also, the electric andmagnetic fields are approximately $\pi/4$ out of phase.

The reduction in amplitude of a wave as it travels through a conductor is not difficult to understand. The electric charges in the conductor move in response to the electric field in the wave. The motion of the charges constitutes an electric current in the conductor, which results in ohmic losses: ultimately, the energy in the wave is dissipated as heat in the conductor. Note that whether a given material can or cannot bedescribed as a good conductor depends on the frequency of the wave (and permittivity of the material). At a high enough frequency, any material will become a poor conductor.

1-2-3- Phase velocity and group velocity.

In 2013 Brillouin and Massey [3] mentioned that the distinction between the phase velocity and the group velocity of a wave is a concept of general significance for many different waves in physics: electromagnetic waves, particle waves, elastic waves and so on.

Considering a general one-dimensional wave:

$$A(x,t) = A_0 e^{i(kx-\omega(k)t)} \quad , \quad (1.42)$$

Where A_0 is the amplitude, k the wave number, ω(k) the angular frequency, and the time. The important thing to note is that ω depends on the wave number k or the wavelength λ =2π/k. This phenomenon is called dispersion, and it might be familiar from optics, where the speed of light in a material (or the index of refraction) depends on the wavelength. Starting from the dispersion ω(k), the phase velocity as would be defined:

$$v_p = \frac{\omega}{k} \ , \quad (1.43)$$

Where ω is the wave's angular frequency (usually expressed in radians per second), and k is the angular wavenumber (usually expressed in radians per meter).

And the group velocity:

$$v_g = \frac{\partial \omega}{\partial k} \ , \quad (1.44)$$

Obviously, these two are the same for a linear dispersion with $\omega(k) = ak$.

We are familiar with different kinds of dispersion relations, and these are illustrated in **Figure 1-3.** For light in a vacuum, there is :

$$\omega(k) = kc, \quad (1.45)$$

Where c is the (vacuum) speed of light. This dispersion is shown in **Figure 1-3(a).** In general matter, n(ω) is greater than 1 and also depends on ω. This leads to a reduced and energy-dependent speed of light in matter:

$$\omega(k) = \frac{kc}{n(\omega)} \ , \quad (1.46)$$

With $n(\omega)$ being the index of refraction.

For a free, non-relativistic quantum mechanical particle of mass m, there is:

$$E(k) = \hbar\omega(k) = \frac{\hbar^2 k^2}{2m} \quad , \quad (1.47)$$

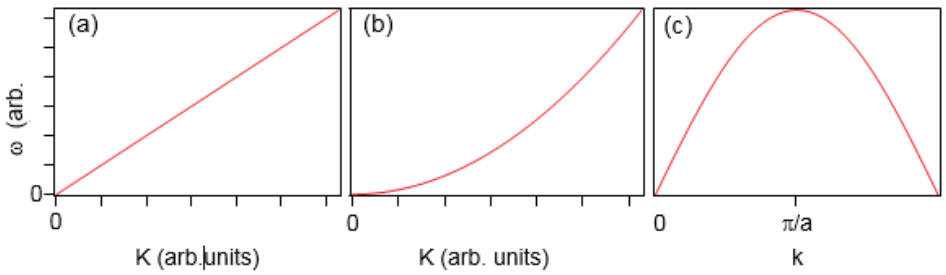

Figure 1-3: Dispersion relations $\omega(k)$ for different physical situations: (a) light in vacuum (equation 1-45), (b) a free, non-relativistic quantum mechanical particle (equation 1.47), (c) the acoustic branch of vibrations in a crystal (equation 1-49). a is the one-dimensional lattice constant[3].

So that:

$$\omega(k) = \frac{\hbar k^2}{2m} \ , \qquad (1.48)$$

And for the mechanical wave representing the vibrations in a one-dimensional chain, there is:

$$\omega(k) = 2\sqrt{\frac{\gamma}{M}} \left|\sin\frac{ka}{2}\right| . \qquad (1.49)$$

These cases are illustrated in **Figures 1-3(b)** and **(c)**, respectively.

In the following, the difference of group velocity and phase velocity for a few situations associated with these different dispersions would be noted. In each case, the propagation of waves with different values of k (and thus of ω) would be studied. Then a package of such waves centered around the k-point of interest would be formed. Such a package can be interpreted as a "particle" localized in space. For the three cases shown in **Figure1-3**, these "particles" could be photons, electrons and phonons, respectively. It can be seen that the "particle" is not particularly well localized. Indeed, it is not expected to be because only a small range Δk is used to form the wave package, and according to Heisenberg's uncertainty principle, this implies a large extension Δx in space.

For a linear dispersion, e. g., for light in a vacuum, a package of partial waves with the different k values would be formed, indicated by the dots in **Figure 1-4(a).** The propagations of the partial wave at the center of the package (blue dot) and of all partial waves are given in **Figure 1-4(b) and (c)**, respectively. All partial waves propagate with the same phase velocity v_p = ω/k = c. can be seen**. Figure 1-4(d)** shows the propagation of the package formed by these partial waves. The package is strongly peaked around one position, and this peak corresponds to our "photon". It can be seen that the "photon" propagates with the same velocity as the partial waves. The velocity of the wave package propagation is the group velocity v_g = ∂ω/∂k(= c). In this particular case, it is of course the same as the phase velocity. Also, it can be seen that the moving wave package does not change its shape. This is also a consequence of the linear dispersion that makes all partial waves travel with the same velocity.

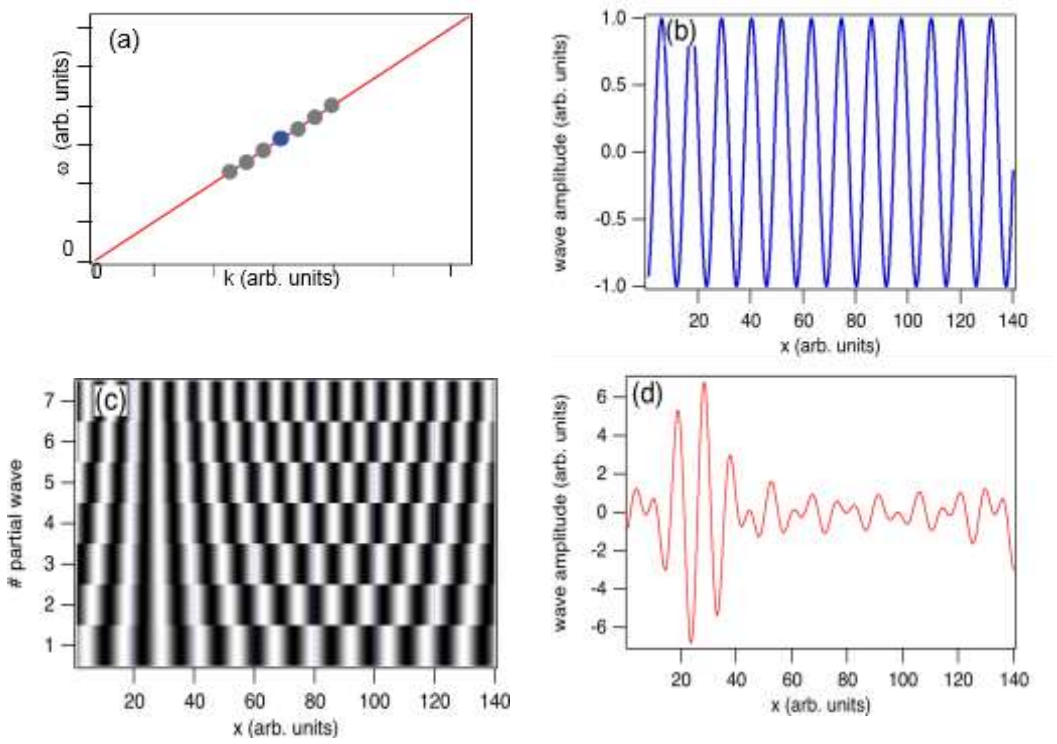

Figure 1-4: Propagation of partial waves and wave package for a linear dispersion. (a) Dispersion with markers corresponding to the k values chosen for forming a wave package. (b) Propagation of the partial wave in the center of the package (the one with the blue dot). (c) Propagation of all seven partial waves. (d) Propagation of the package formed from all partial waves[3].

Now the same analysis would be applied to the quantum mechanical particle described by **Equation 1-47.** The result is shown in **Figure 1-5.** Now the partial wave does not all move with the same velocity because of the quadratic dispersion. A very important consequence of this is that the initial wave package broadens out with time because the partial waves forming it gradually move out of phase with each other. So even if we start with a fairly localized "particle", it will soon lose this localization. The group velocity for this dispersion could be calculated as:

$$v_g = \frac{\partial \omega(k)}{\partial k} = \frac{\hbar k}{m}, \qquad (1.50)$$

And this is perfectly consistent with the movement of a semi classical particle for which the momentum is $p = \hbar k$ and the group velocity thus p/m = vg.

Now the dispersion of the lattice vibrations would be studied in **Equation 1-49** and **Figure 1-3(c).** Here, there is three interesting situations. For the first, a wave package around a small k value could be chosen where the dispersion is linear.

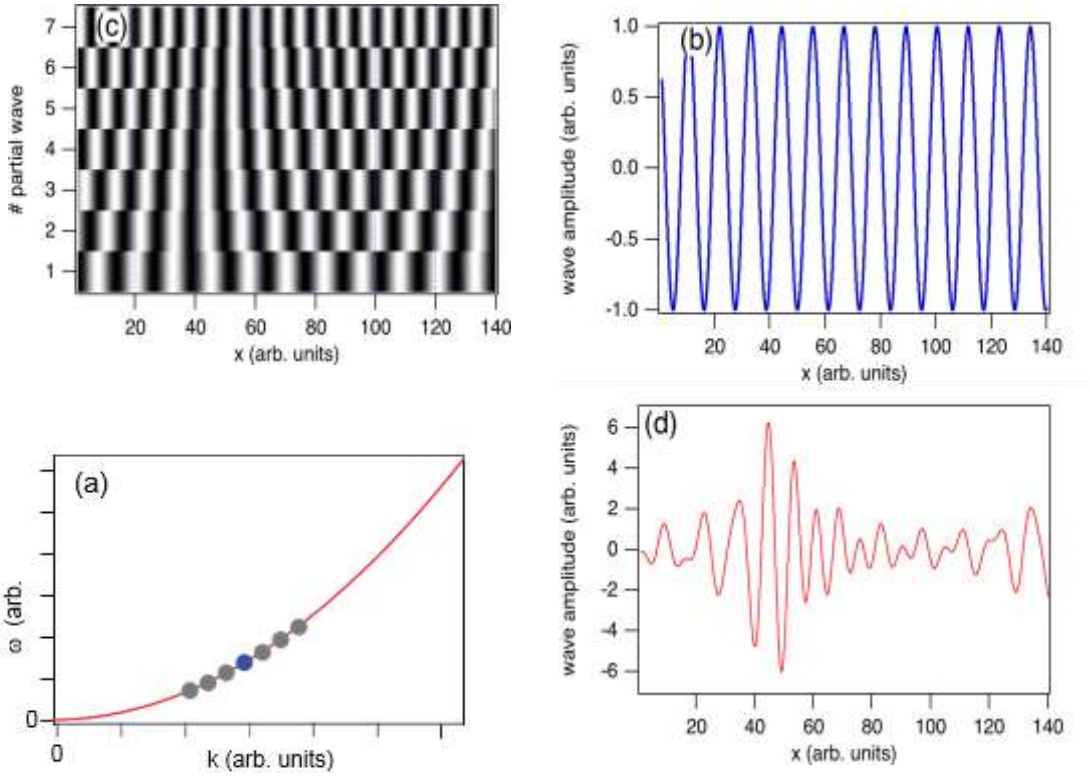

Figure 1-5: Propagation of partial waves and wave package for a quadratic dispersion. (a) Dispersion with markers corresponding to the *k* values chosen for forming a wave package. (b) Propagation of the partial wave in the center of the package (the one with the blue dot). (c) Propagation of all seven partial waves. (d) Propagation of the package formed from all partial waves[3].

This is the regime corresponding to acoustic waves (sound waves) in the solid. It can be seen that the situation is exactly the same as for the linear dispersion in **Figure 1-4,** there is no need to treat it here again. The only important difference is that the waves do not propagate with the speed of light but with the speed of sound.

The second interesting case is a wave package formed from partial waves around the maximum of the dispersion curve at $k = \pi/a$, that is, at the Brillouin zone boundary. This is illustrated in **Figure 1-6.** The group velocity $v_g = \partial\omega/\partial k$ would be expected to be zero If we are sufficiently close to the maximum of the dispersion, that is, we would expect a standing wave. To conclude, while all partial waves still have a positive phase velocity, the localized "phonon" does not move at all. When inspecting **Figure 1-6(c)**, it can be seen why this is so, the phase velocity of all partial waves is different, but it is always so that the faster ones "catch up" with the slower ones in the middle of the image.

A particularly good illustration of how different the group and phase velocity of a particle can be arises for the dispersion of acoustic waves as we go past the maximum, near the next Brillouin zone center at $2\pi/a$. This situation is shown in **Figure 1-7.** Now the group velocity is obviously negative (but linear), and the wave packet does indeed move in the negative direction, even though all partial waves move in the positive direction.

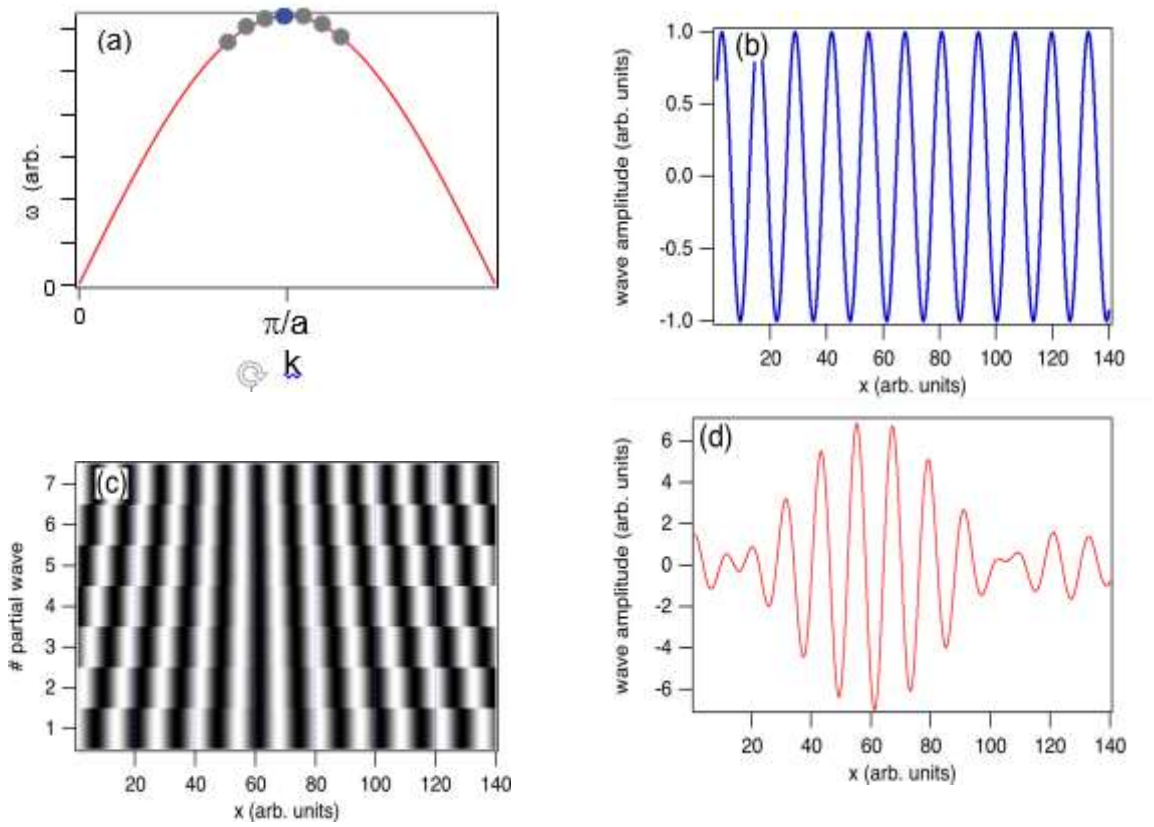

Figure 1-6: Propagation of partial waves and wave package for an acoustic phonon dispersion. The wave package is formed from partial waves around the Brillouin zone boundary at $k = \pi/a$. (a) Dispersion with markers corresponding to the k values chosen for forming a wave package. (b) Propagation of the partial wave in the center of the package (the one with the blue dot). (c) Propagation of all seven partial waves.(d) Propagation of the package formed from all partial waves[3].

Move in the positive direction. Note that a different point of view could be adopted and state that the same vibration for a wave packet would be gotten with a wave vector moved by one reciprocal lattice vector, as illustrated in **Figure 1-8.** Then the negative group velocity would not be so surprising.

Returning to the case of a quantum mechanical particle **(Equation 1-47 and Figure 1-5),** it could be asked that if there is any possibility to prevent the wave function from spreading out. For this, a linear dispersion is needed. One way this can be done becomes apparent when the relativistic dispersion relation for a semi- classical particle is considered:

$$\omega(k) = \frac{1}{\hbar}\sqrt{(mc^2)^2 + (\hbar kc)^2}\,. \qquad (1.54)$$

From this, a linear dispersion in two ways can be achieved. Either a particle with rest mass zero or such a high k could be chosen in a way that the rest mass contribution to the energy becomes negligible against the kinetic energy. Both ways do not appear very practical in a solid. It is not easy to see how the mass of the electrons should vanish, and it is certainly not possible to go to a kinetic energy that is high compared to the rest mass energy(511 keV for a free electron).

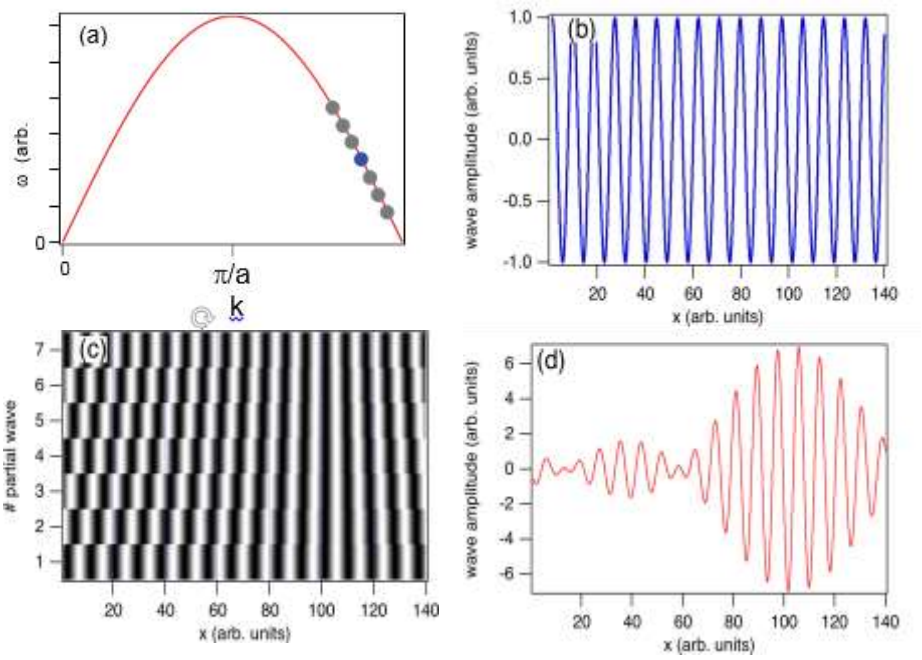

Figure 1-7: Propagation of partial waves and wave package for an acoustic phonon dispersion. The wave package is formed from partial waves close to the next Brillouin zone centre at $k = 2\pi/a$. (a) Dispersion with markers corresponding to the k values chosen for forming a wave package. (b) Propagation of the partial wave in the center of the package (the one with the blue dot). (c) Propagation of all seven partial waves. (d) Propagation of the package formed from all partial waves[3].

However, the band structure of the solid allows a way to a situation that corresponds to a vanishing rest mass and a dispersion similar to that of light (**Equation 1-45**). This is illustrated in **Figure 1-8,** which shows a simple band in a one-dimensional solid. As the band disperses only over a limited energy range, the curvature has to change from positive to negative and thus, it becomes nearly zero for a small range of k values. There the dispersion is, in fact, locally linear and light-like. The group velocity is, of course, not the speed of light, but it is given by the degree of dispersion and the lattice constant. Such a situation is especially important when the linear dispersion is situated at the Fermi energy. The most important example for this appears in the electronic band structure of graphene, a single layer of carbon atoms.

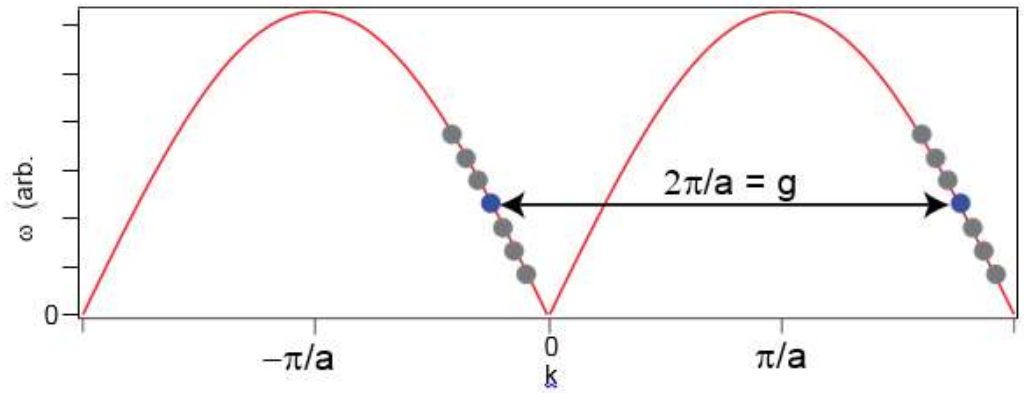

Figure 1-8: The lattice vibrations corresponding to the situation in Figure 1-7 could also be represented by a wave package that has been translated by one reciprocal lattice vector. In this case, the wave package still has a negative group velocity but so have all the partial waves[3].

1-2-4- Boundary conditions.

When, as in some of the devices that will be studied in this work, the electromagnetic wave crosses the boundary between two different media, discontinuities in the electric or magnetic field of the wave can appear. The "boundary conditions" for two media, "1" and "2" can be expressed in this way [2]:

$$\hat{n} \times \left(\vec{E}_1 - \vec{E}_2\right) = 0 \quad , \qquad \hat{n} \cdot \left(\vec{D}_1 - \vec{D}_2\right) = \sigma'$$

$$\hat{n} \times \left(\vec{H}_1 - \vec{H}_2\right) = \vec{K} \quad , \qquad \hat{n} \cdot \left(\vec{B}_1 - \vec{B}_2\right) = 0$$

where σ' and $\vec{K}$ are the surface charge and current densities; $\hat{n}$ is a unit vector perpendicular to the boundary surface, pointing in direction from medium 2 to medium 1, and $\vec{D}_i$ and $\vec{H}_i$ represent the electric field displacement and magnetic field strength, respectively.

From these boundary conditions, the reflection and transmission coefficients of the electromagnetic wave can be determined. They are given by the well-known Fresnel's equations Taflove and Hagness (1998) [2].

1-3- Familiarity with the WDM method

Since the early 1980s, the WDM method has been considered and used as the main method for the transmission of information in optical telecommunication systems. In addition, nowadays, many efforts are being made for the optimal use of this method in different applications. CWDM (Coarse Wavelength Division Multiplexing) and DWDM (Dense Wavelength Division Multiplexing) are two main methods used in fiber-optic telecommunication networks. In this chapter, the concepts of optical networks would be explained, then the WDM method and the characteristics of CWDM and DWDM methods would be evaluated, and to conclude, they would be compared.

If the current problems of telecommunication industry is considered, especially in the field of providing services to the users, the importance of WDM would be clear. The first challenge that the telecommunication industry faces is the ever-increasing demand for higher speeds. Thus, the demand for bandwidth is huge, to the extent that some scientists believe that the network capacity should be doubled every six months. The second fundamental challenge is that different technologies, used in different types of networks, such as IP (Internet Protocol), ATM (Asynchronous Transfer Mode), and SONET (Synchronous Optical Network), each of them having its own advantages, require some equipment in order to interact with others Ballart and Ching (1989)[4].

Using optical networks and the WDM method, these problems can be resolved to a large extent. By using this method, a bandwidth of up to 1,600 gigabits per second could be achieved, and using such a bandwidth, transferring more than 30 million phone calls by using just one optical fiber would be possible. Besides, the problem of different technologies can be solved easily. Using the WDM method, information is sent on an optical fiber on different wavelengths, which act independently of each other. Thus, different types of data can easily be used in this regard, and the users can be provided with different services such as audio, video, information, and multimedia.

The solution of choice in order to increase the capacity of the network, should be economical, and easy to use, to persuade the user to use it. The first option that comes to mind is to use more optical fibers to access higher bandwidth. Unfortunately, this is not a good economical option since it is completely a hardware solution. Hardware solutions are time and money consuming. Besides, using more optical fibers does not necessarily enable ISP(internet service provider)to provide new services. The second solution for increasing the speed is the use of time-division multiplexing (TDM), which makes sending more information on the optical fiber possible through time division. This method is usually used on the current telecommunication networks, but it is not possible to arbitrarily increase the speed through this method. Based on the defined standard, the next step is to achieve the speed of 40 Gbps, which will not be possible by merely using the TDM method, not even in the near future, and requires technological advances in the manufacture of electronic components. The TDM method is now used in the transmission networks based on SONET, which is a standard for North America, and SDH (defined the transport of 1.5/2/6/34/45/140 Mbps within a transmission rate of 155.52 Mbps and is being developed to carry other types of traffic, such as asynchronous transfer mode (ATM) and Internet protocol (IP), within rates that are integer multiples of 155.52 Mbps).,

which is an international standard. It is worth mentioning that SONET and SDH are standards that are defined for digital signals and that standardizes the speed of communications, the structure of packages, and the optical interfaces.

There is also a third solution to ISPs; that is, using the WDM method. In this method, a certain wavelength and/or frequency is assigned to each of the input optical signals, and then all the signals will be sent on one optical fiber. Since each of these wavelengths are independent and has no effects on others, this allows ISPs to optimally utilize the existing network facilities and allows them to make use of different technologies. In fact, WDM combines several optical signals, amplifies them and sends them in the form of a group of signals, which will increase the capacity. Each of these signals can have different speeds and can be in different formats.

But what has made WDM so valuable and useful are the amplifiers that amplify the optical signal without converting it into an electrical signal. These amplifiers have a certain bandwidth in which they can amplify up to 100 wavelengths. The EDFA (Erbium-Doped Fiber amplifier) and DBFA (The double-bandwidth fiber) amplifiers are among these amplifiers, which are used in the 1530-1560 and 1528-1610 nm wavelength bands, respectively.
Generally, the advantages of the WDM method can be listed as follows: providing higher speeds on one optical fiber, and higher reliability and security.

The next step to increase the capacity is the simultaneous use of the two methods; WDM and TDM. In the TDM method, increasing the capacity and the speed are both done on one communication line, whereas in the WDM method, this task is done using different wavelengths by increasing the number of communication lines. Therefore, by combining these two methods, a higher capacity on optical fiber can be achieved, and with technological advances in the manufacture of electronic components, it can always be possible to use it effectively to increase the speed of optical networks.

The transmission medium in optical networks is an optical fiber. In addition, the wavelength band, which can be used to send information, is between 1,260 and 1,625 nm, that is, the second and third optical telecommunication windows. It should be noted that the first optical telecommunication window is at a wavelength of 850 nm, and the second and third windows are at wavelengths of 1,300 nm with minimal dispersion and 1,550 nm with minimal losses, respectively. This wavelength band, which is used to transfer information on the optical fiber, is divided into 5 bands shown in **Table 1-1**, which are employed in different WDM methods.

Table 1-1: The wavelength band used to transfer information on the optical fiber.

Name of the band	**The wavelength range in nm**
O-Band	1260-1360
E-Band	1360-1460
S-Band	1460-1530
C-Band	1530-1565
L-Band	1565-1625

To make maximum use of the optical fiber capacity in the WDM method, the distance between the wavelengths used to transfer information should be reduced so that more information can be sent on an optical fiber. Therefore, the DWDM method was introduced in the early 1990s to take advantage of the optical fiber for the transmission of information over long distances and in wide area networks. In the DWDM method, the distance between the channels used to send information is 0.4 nm, and each channel provides a bandwidth up to 10 gigabits per second for the users. This method is used in C-band and L-band, and between 32 and 160 channels are created. With this number of channels, a bandwidth of 100-1600 Gbps can be achieved. But it should be noted that this method is only suitable for sending information over long distances because the ancillary equipment employed to implement this method, such as optical fibers, sender lasers, repeaters, etc., have properties that drastically increase the costs. So the economic cost for each channel will only be justified for sending information over long distances and WAN networks. Aiming to employ this method in urban or metropolitan area networks (MAN) and local area (LAN) networks, the economical cost for each user would be excessively high, and consequently the demand for its use would decrease. This was a problem that many service provider companies were facing in the late 1990s and 2000. At that time, the CWDM method, which had been introduced at the beginning of the 1980s, again gained attention. The basic difference between CWDM and DWDM is in the distance between their channels. In the CWDM method, the distance between the channels is 20 nm, and this method is employed in O-, E-, S-, C-, and L-bands. This range provides a wavelength with 8 to 16 channels, each of which has a bandwidth up to 2.5 Gbps; and a bandwidth up to 40 Gbps on a single-mode optical fiber can be achieved. Ahmed et al (2013) [5]

The reason why CWDM has gained such a huge attention nowadays is, the lower cost of CWDM compared to DWDM. The CWDM method, which is widely used in launching FTTH (Fiber to the home) and FTTC(Fiber to the curb/cabinet) networks, does not need any repeaters to send information to a distance of up to 70 km with appropriate quality.

1-3-1- Transmission modes

In this section, the concepts related to WDM would be discussed. First, the concepts and methods of sending information would be clarified, and in the next step, the reasons for choosing DWDM would be explained.

There are three transmission modes in data transmission channels that include:

1- Simple, simplex, or unidirectional transmission, also called SX: This method is specific for sending data in one direction, in which one side is always a transmitter, and the other is a receiver.

2- Half duplex, also called HDX: In this method, data can be sent and received on the channel, but not simultaneously (communication is only in one direction at a time, but the direction of transmission can be changed) such as two-way radios.

3- Full duplex, also called FDX: In this method, data can be simultaneously sent and received on the channel such as telephones.

1-3-2- Multiplexing

The capacity or bandwidth of a data transmission medium is usually higher than the bandwidth required for a transmitter and has to be shared among different users. The multiplexing

(division) technique makes it possible to simultaneously (or quasi-simultaneously) transmit several different signals over one line and to make optimal use of the capacity of the medium. The act of putting several signals on a line at the origin is done by a device called the multiplexer, and the act of separating them at the destination is done by a device called the de-multiplexer Cameron and Yu (2007)[6].

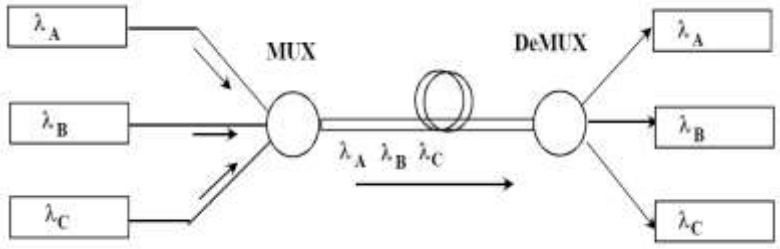

Figure 1-9: The introduction of several signals simultaneously into a line at the origin is done by a device called multiplexer. The reverse act of separating them at the destination is made by a de-multiplexer.

Different types of multiplexing methods can be categorized as follows:

1. FDM: Frequency Division Multiplexing

2. TDM: Time Division Multiplexing

(Synchronous TDM and Asynchronous TDM or Smart TDM, which are also called Statistical Multiplexing.)

3. WDM: Wave–Length Division Multiplexing

4. Code Division Multiplexing Access (CDM or CDMA)

1-3-3- The WDM method

Transmission of multiple signals with different wavelengths is applied in special cases.

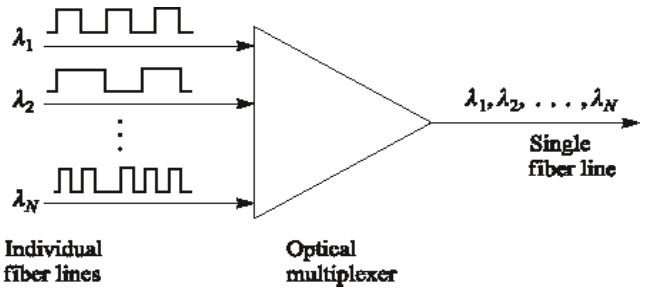

Figure 1-10: Transmission of multiple signals with different wavelengths.

One of the reasons for using WDM in certain cases is that each time the signals have to be regenerated, they must already have been separated in the repeaters and sent into the optical fiber again for retransmission with suitable wavelengths. As a result, there are currently only a few systems, which use one technique to increase their transmission capacity.

In this method, used in optical fibers, several optical waves with different wavelengths are simultaneously propagated in an optical fiber. It is obvious that, for example, the separation of two optical signals with blue and red wavelengths will easily be possible at the destination.

1-3-4- DENSE – WDM

In the modern world of telecommunications, increasing demands for bandwidth have far exceeded the limits of expectations. For this reason, fundamental changes have occurred in the requirements of future network structures. When it is time to develop existing connections, simple and affordable solutions will be needed not to disrupt the working systems. Obviously, the greater the flexibility in the design and construction of a communication system, the fewer the problems that we will face during the development of the existing structures. The major challenges that we are faced with in the world of telecommunications and customer access areas are as follows: the quick setup for new customers, the development of services in the existing networks, and increasing their capacities. Due to increasing demands for data communications because of the fast development of cellphones market, cable TV, video and audio multimedia and other demands such as banking communication from home as well as the Internet and other networks, further development and implementation of optical fiber lines is crucial. One of the methods for solving this problem is the addition of new optical fibers in the existing networks. Due to the high costs of laying cables, this procedure is very time-consuming and costly. On the other hand, development towards higher BIT speeds (10 Gbits/s TDM) is not possible in any of the? Fiber types. If the data speed is up to 2.5 Gbits/s, and the fiber-optic routes are short enough, the physical properties of the fiber can more or less be ignored, but at higher data speeds and at longer routes, the issue of chromatic dispersion will be a limiting factor. For example, if the BIT speed quadruples, it will be required to reduce the route length 16 times due to the development of unwanted pulses. It can easily be understood that if the speed of data transmitted through a fixed-length optical channel increases, its technology will become more complex. In recent years, optical fibers have been developed to work at higher BIT speeds. Carbonneau and Wisely (1998)[7]

Wavelengths of 1,310 and 1,550 nm are used in telecommunication applications based on the second and third optical windows. To put it in simple terms, a DWDM system is similar to a group of parallel optical channels, whose small difference in wavelength will cause their simultaneous transmission in a single optical fiber.

Since the suitable range of wavelengths for amplification is currently limited, all the carrier wavelengths used in DWDM systems are between 1,530 and 1,656 nm in the third optical window. On the other hand, optical light-generation channels are usually amplified at wavelengths outside this range and are located at 1480, 1510 and/or 1625 nm. One of the standards in the frequency network, which has been used as an optical information carrier in dense WDM (DWDM) systems, has been defined by the International Telecommunication

Union (Recommendation G.692 ITU-T), where optical frequencies have been defined with identical distances (spacing of 100 GHz), and with a reference of 193.10 THz.as shown in **Figure 1-11** Ahmed et al 2014 [8].

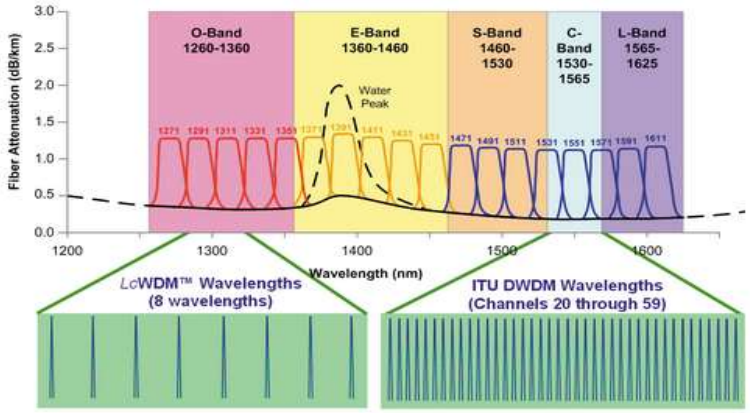

Figure 1-11: Union (Recommendation G.692 ITU-T), with a reference of 193.10 THz.

1-3-5- The standards defined for DWDM

To design and implement DWDM systems and components flexibly and prospectively, a basic standard is needed. Making sure that parts and circuits from different manufacturers match the parameters defined for the media and can interact with each other adequately is possible by this means only.

Since the existing standards are limited to 4 to 8-channel systems (until 2014), various combinations can be assumed for the wavelengths being used in the systems. Therefore, each manufacturer must agree on certain central wavelengths to ensure the interaction of various elements of a system without any problems. It is common that the wavelength range between 1,530 and 1,565 nm is divided into two bands. Subsequently, the band under 1,545 nm is also divided into two bands. The band under 1,545 nm is known as a shortwave band, and the band over 1,545 nm is known as a longwave band Rostami et al (2010) [9].

Topics related to optical WDM were discussed overall in this chapter. Functional and affordable full optical elements are essential in future telecommunication networks.

Chapter 2

History and Principles of Performance in Photonic Crystal Gates and Review of Previous Research

2-1- Introduction

The realization of ultra-fast processing in all-optical information and computation, based on micro-nanometer scale integrated optical devices, is one goal of integrated optical technology development. The need for new materials to control photon flow has been the main idea for designing the photonic crystals. Traditional mechanisms utilized to control photon flux are generally based in internal reflection or absorption phenomena, but photonic crystals use a quite different mechanism to control light emission. As a counterpart to semiconductor materials (Solid-state structures), photonic crystals, with unique optical band structures, include transient bands and defect modes that control photon's behavior. Photonic crystals comprise of one, two, or three-dimensional regular structures with spatial periods of the order of several hundred nanometers, i.e., several times smaller than the wavelength of the light propagating through the structure. For each of these alternating structures, band gaps (i.e., "forbidden" ranges of frequencies) are defined. The propagation of light in these structures is strongly influenced by the photonic band gaps (PBG), as light propagation in a photonic band gap is impossible.

Manufacturing and implementation of nanoscale integrated optical devices are some of the main applications of photonic crystals. In recent years, along with the great achievements in the manufacture of high-quality photonic crystal samples, various integrated optical devices have been implemented, including the design and manufacture of logic gates based on photonic crystals.

Logic devices are one of the essential components of optical computing systems and ultra-fast information processing. Logic gates can be built on the effects of the photonic band gap, waveguides, and severe light limitations in photonic crystal microcavities. Important parameters in the design of the photonic crystal gates are the lattice constant of structure (a), the material type used for the dielectric rods and the base (and the value of the corresponding refractive index), the type of modes and band gap of the structure according to the dimensions and shape of the design, the geometry and dimensions of the defects, radius of dielectric rods and so on.

2-2- History of photonic crystals

To investigate photonic crystal logic gates, the history of photonic crystals should be examined. Although light crystals are thought to have been the focus of attention only in recent decades, early assumptions about the possibility of light propagation using alternating structures date back to 1887. That year, Lord Rayleigh became the initiator of optical crystals' study by introducing a forbidden optical band in alternating one-dimensional structures [11]. Afterward, in 1928, Felix Bloch studied on the propagation of waves in three-dimensional alternating environments [12]. According to Bloch's theory, The field in periodic media can be replaced by a plane wave whose coefficient is alternating. This theory is used to describe optical band structures.In 1972, Vladimir Bykov theoretically studied a one-dimensional structure in his book: "Reversible Crystal Plasticity" to investigate the possibility of using alternating structures and photonic band gap effects on spontaneous emissions of atoms and molecules

[13]**.** Vladimir Bykov also conducted studies on using these structures in two and three dimensions. Afterward, Ohtaka (1979) introduced the general concept of three-dimensional photonic crystals [14]. However, the initial researches considered as the starting point for major developments in photonic crystals are the works of Eli Yablonovitch [15] and John. S, [16] in 1987. In that year, two studies were conducted simultaneously by Yablonovitch and John. Yablonovitch investigated the inhibited spontaneous emission in solid-state physics and electronics, and John, in his study, examined the settling power of photons in photonic crystals. Following these articles' publication, in 1990, a joint paper on the computational theory of photonic crystal structures was published by Ho and Soukoulis [17]**.** One year later, Gruning.(1995), studied the computational theory of photonic crystal structures experimentally. In 1995, large-scale photonic crystals [18], and in 1998, small-scale photonic crystals Gruning.(1998) [19] emerged. In 1999, the first optical devices based on photonic crystals were produced.

2-3- Introduction and review of the properties of photonic crystals

Photonic crystals are a new set of optical environments whose refractive index changes periodically in space, enabling the control of the direction of light. The structure of natural crystals inspires photonic crystals. With the development of instruments for observing and measuring small structures, especially all kinds of electron microscopes, it was found that natural photonic crystals are available in the structure of many natural materials. Among these natural materials, butterfly wings, many mineral rocks, especially a particular group called opal, mussels, and many marine creatures could be mentioned. **Figure 2-1** shows an example of natural crystals in which the periodic structure is clearly recognizable.

The basis of photonic crystals is the same as any other crystal in Bragg diffraction. Bragg diffraction is a decentralized effect, in which the incoming wave is scattered by each of the constituent elements of a crystal, and these diffractions in some directions and wavelengths amplify each other in a constructive fashion, whereas in other directions and wavelengths, they attenuate each other by destructive interference.

Figure 2-2 shows the destructive and constructive interference of the reflected wave from an array of wave reflectors. These wave reflectors represent, inside the photonic crystal, the regions filled with a material with a given value of the refractive index. Each of these periodically ordered plates acts as a semi-transparent mirror (reflecting a part of the wave according to Snell's law and passing through a part of it) Ohtaka (1979) [20].

Figure 2-3 shows the oblique collision of a plane wave with an array of reflecting surfaces.

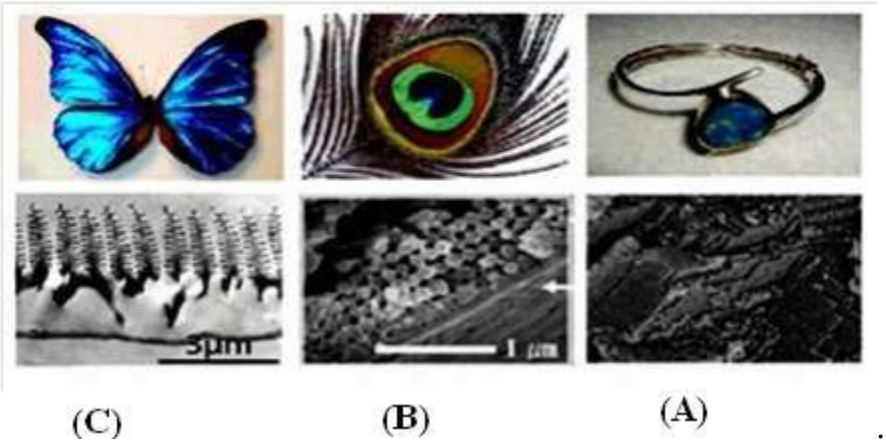

Figure 2-1: An example of natural crystals: a) opal stone, b) peacock feather, and c) butterfly wing [20].

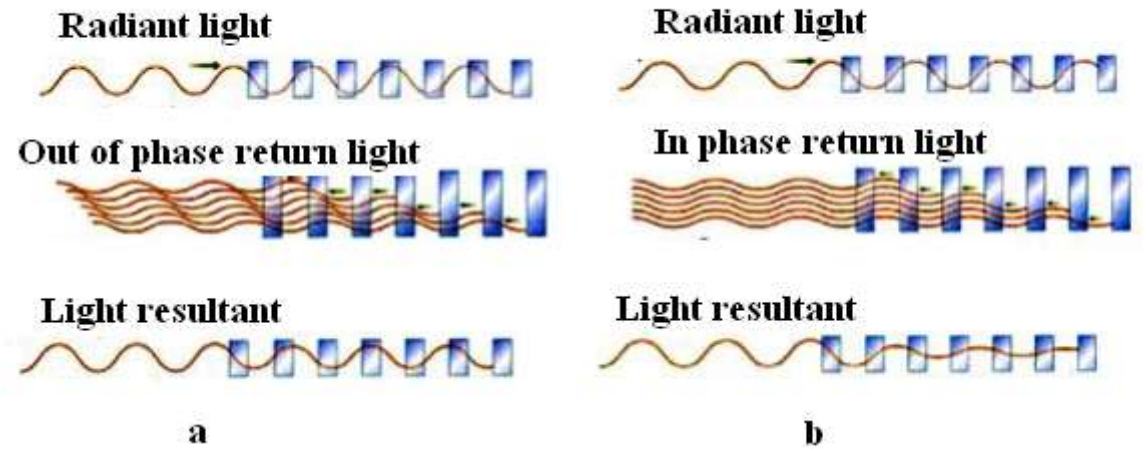

Figure 2-2: Interference a) constructive and b) destructive for waves reflected from a regular array of wave diffractions [20].

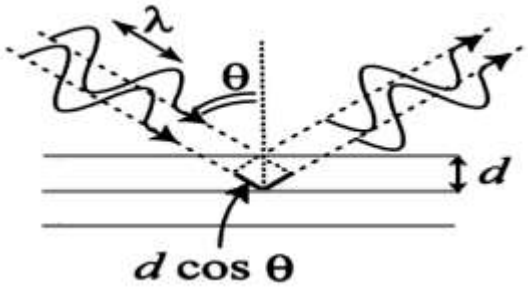

Figure 2-3: Bragg reflection of a plane wave that collides obliquely with the plates of a crystal or of a photonic crystal. When the reflection of consecutive plates is constructive, 2dcosθ is an integral multiple of the wavelength of the incident light in the medium [20].

For in-phase amplification, the path difference shown in the **Figures 2-1, 2-2** and **2-3** must be an integer multiple of the wavelength λ of the light beam in the medium. It can be expressed as:

$$n\lambda = 2d\sin\theta \qquad (2.1)$$

Where θ is the incidence angle of the incoming light and *n is an integer number*. This is Bragg's reflection conditions. Therefore, the wavelengths that fulfill condition (2.1) return with a reflection angle, and the rest pass through the crystal, so it has a non-uniform reflectance spectrum, unlike full metals. If this non-uniformity is in the area of the visible portion, it will make the photonic crystal look like a butterfly's wing.

2-4- Photonic band gap

The most important feature that clarifies the practical importance of photonic crystals is the presence of a photonic band gap (PBG). Like semiconductors that have an energy band gap for electrons, there are a series of unauthorized modes for photons in the photonic crystals called the banned light band. In fact, the banned optical band is a continuous and bounded limit in the frequency domain that waves cannot be propagated in this frequency range. When the light whose frequency is in the PBG range illumination on the photonic crystals, this beam is fully reflected by photonic crystals. The light cannot propagate inside the photonic crystal.

The propagation of light in the structure of optical crystals depends on their wavelength. The wavelengths of light that are allowed to propagate are called modes. TE (Transverse Electric) band TM (Transverse Magnetic) modes are two important modes in optical crystals. TE mode is the transverse mode of the electric field. The electric field is perpendicular to the incidence plane, and the magnetic field is parallel to the plane. While the TM mode is the transverse mode of the magnetic field where the electric field is parallel to the incidence plane and the magnetic field is perpendicular to the plane. It is shown in **Figure 2-4**.

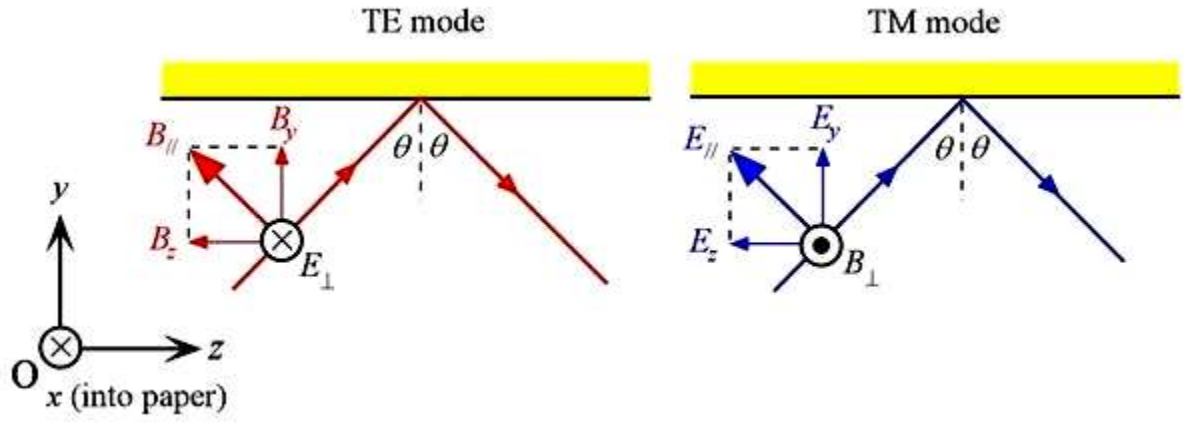

Figure 2-4: TE and TM mode on the XYZ plane [21]**.**

The band diagram is different for modes with various polarizations; therefore, the band gap may be only for a specific polarization for a particular structure. Structures in the form of dielectric rods in the air are an example of discrete structures, shown in **Figure 2-5**. In these structures, the band gap is often observed for TM polarization. The structures in the form of cavities in the surface of a material (Figure 2-5 again) are an example of continuous structures, and in these structures, the band gap of TE polarization is visible. An example of the photonic band gap for discrete and continuous structures is shown in **Figure 2-6.**

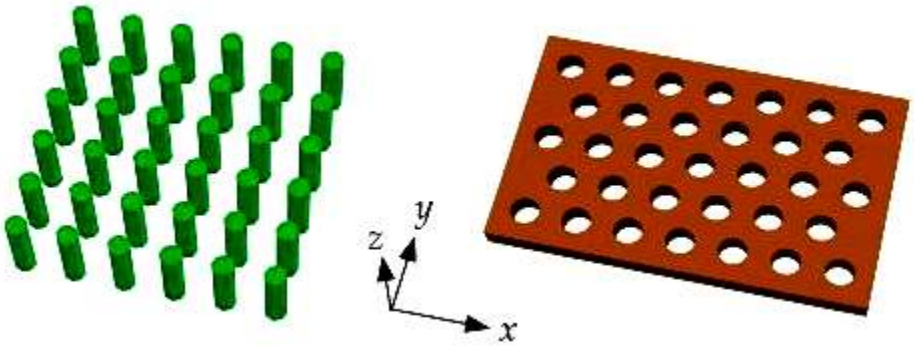

Figure 2-5: **Discrete structure (left) and continuous structure (right) of two-dimensional photonic crystal [21].**

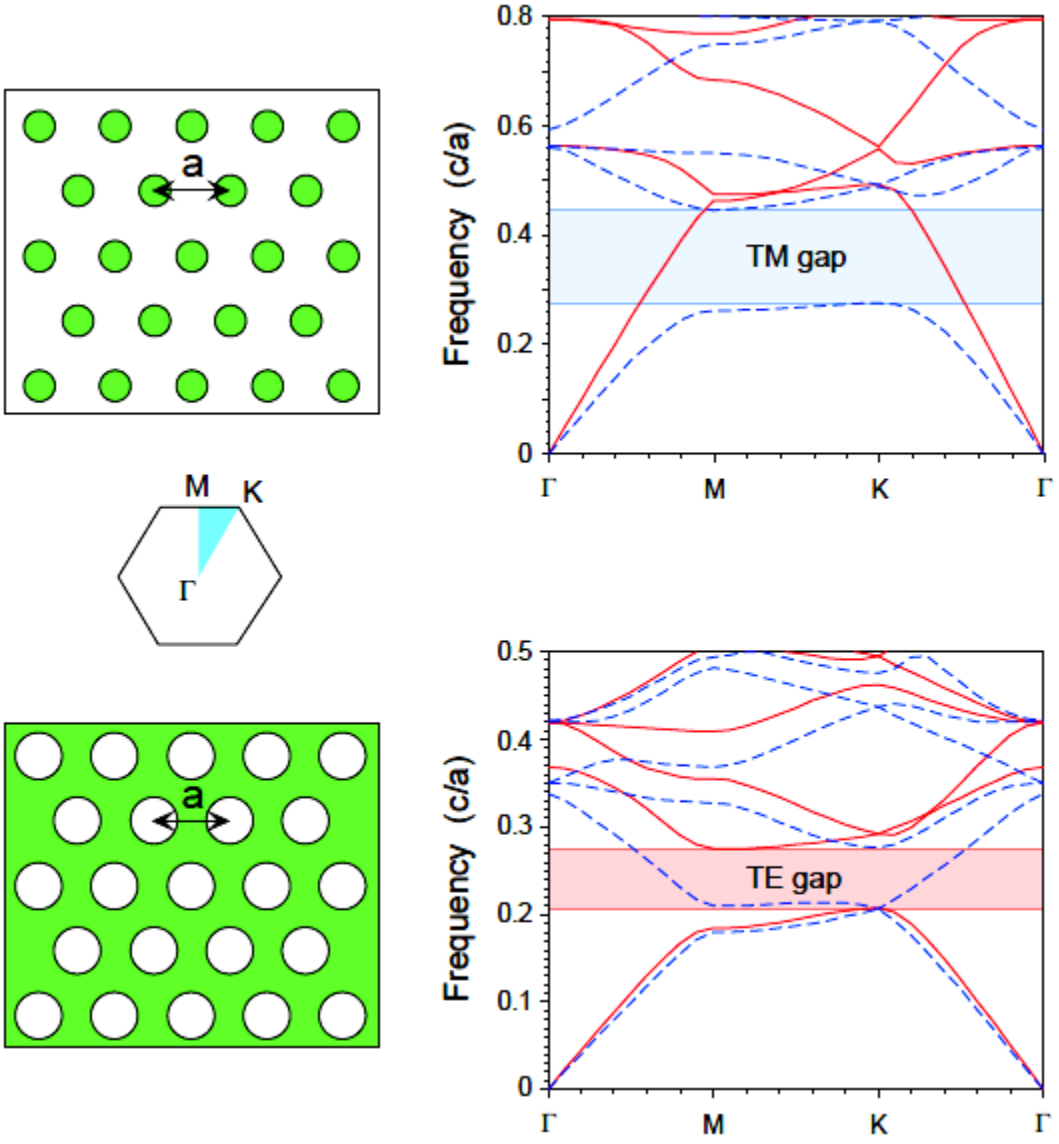

Figure 2-6: Band gap for two polarizations of TE and TM [28].

Obtaining a suitable band gap is very important in the design of optical crystal-based devices, and in a two-dimensional optical crystal, the band gap depends on the refractive index of the materials, the shape of the rods, the crystal structure, the radius of the rods, and the lattice constant.

Here it is pointed out that a usual way to describe the response of a photonic crystal to a monochromatic wave of frequency ω (in particular the appearance of the photonic band gaps, PBGs) is using the "dispersion curves", which represent the frequency ω as a function of the component of the wavevector $\vec{k}$ along several directions in space. The PBGs can be seen very clearly there (as in Figure 2-6, for instance).

At the frequencies ω inside the photonic band gap, the transmittance and reflectance of electromagnetic waves would be close to zero and one, correspondingly, everywhere except the resonant frequency ω related to an extra vorte , Foteinopoulou (2003) [23].

Employing a finite-difference time-domain (FDTD) technique, the time and space evolution of the emitted EM (Electromagnetic) waves would be followed as they reach the PC's surface and they propagate eventually within the PC. If monitoring the field configuration is our interest, a monochromatic source becomes appropriate. The introduction of a monochromatic source involves turning the fields on abruptly from a zero value. This causes field fluctuations that carry on the entire computational time. Therefore, it is imperative to assign a profile that ensures that ensures the source field turns on smoothly Agio et al (2000) [24].

Moreover, there are cases where we are interested in the Fourier transformed amplitudes of the fields inside the structure, excited by a monochromatic signal. The fields are smoothly turned on from zero to a maximum value and subsequently turned off again from this value to zero. This pulse train corresponds to a small width around the central value in the frequency domain.

Here I will describe how a photonic crystal can modify the diffraction of a light beam inside the structure. For that, I included some particular cases of a 2D photonic crystal and the iso-frequency lines in the wavevector space. The curvature of the iso-frequency line determines the amount of diffraction that will exist in each case. Concave curvature entails positive diffraction, convex curvature entails negative diffraction (focusing), and inflexion points entail zero diffraction (self-collimation) Kosaka et al (1999) [*25*].

There are analogies between conventional crystals and photonic crystals. Normal crystals have a periodic structure at the atomic level, which creates periodic potentials for electrons with the same modulation. Photonic crystals can mold and control the flow of light, as semiconductor crystals control electrons' flow. Photonic crystals are characterized by frequency regions where no electromagnetic (EM) wave propagation is allowed for any incidence angle. These regions are known as complete photonic band gaps or stop bands. For other frequency regions, propagation is allowed in some or all directions.

For instance, the negative refraction and self-collimation of light or the transport properties of electrons are directly linked with the iso-frequency or energy contour in photonic crystals or solids, respectively Kosaka et al (1999) [25]. Therefore, to understand the properties of either photonic crystals or solids, the determination of iso-frequency contour is crucial. Experimentally, the iso-energy contours can be measured with angle-resolved photoemission spectroscopy for solids. However, experimentally direct observation of iso-frequency contours in photonic crystals is difficult, as it has been discussed before, shi et al (2010) [26]. In the present work, monochromatic light of different frequencies is used to irradiate the practical structure.

However, traditional band-structures are limited to analyzing the effects of the direction of the group velocity, such as negative refraction, because they only show the modes along high symmetry directions in the Brillouin zone. Instead of traditional band structures, iso-frequency contours would help analyze how light propagates in photonic crystals, By Xin et al (2012)

[27]. Like band-structure, the iso-frequency contour can also describe the dispersion of waves propagating in periodic structures. In momentum k space, iso-frequency contour or iso-energy contour consists of all the terminals of wave vectors corresponding to the same frequency or the same energy. Almost all the properties of waves propagating in the periodic structure can be deduced from the iso-frequency contours. Therefore, the determination of iso-frequency contour is crucial to understanding the properties of either photonic crystals or solids.

2-5- Defects in photonic crystals

The study of propagation properties inside PCs' defect structures, such as coupled cavities, waveguides, and bends, is considerable. Successful coupling of an input source into a waveguide and mode conversion in bends are issues that plague these devices' performance. A careful study of the propagation properties inside these defect structures may shed light in this direction.

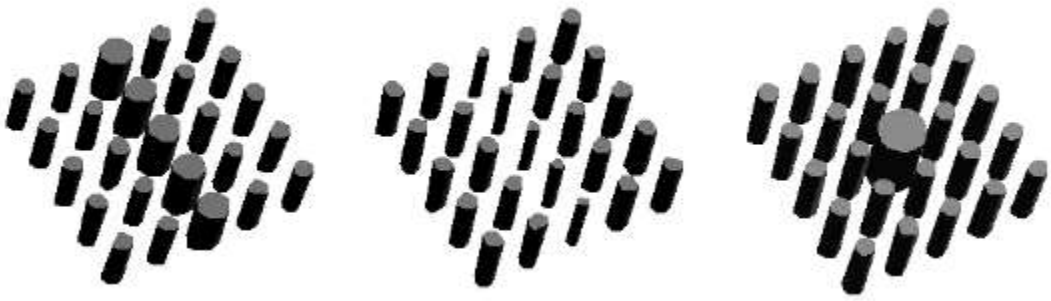

Figure 2-7: Defects in the photonic crystal structure [21]: two linear defects and one point defect.

Any irregularities in the crystal structure are called defects. Two classes of defects, point and linear defects in two-dimensional photonic crystals, can be mentioned among the photonic crystal defects. Generally, point defects in a photonic crystal structure can be caused by removing one or more rods and holes, changing the radius, or making changes in rods' refractive index. Linear defects can be created by removing or changing the radius or changing the refractive index of one or more rows of rods (or holes) in photonic crystals. Resonant cavities and waveguides are formed by creating point and linear defects in photonic crystals' structures, respectively. An example of point and linear defects in the photonic crystal structure is given in **Figure 2-7.**

Making defects in the structure of photonic crystals, as adding impurities into the semiconductor in electronics, result in the creation of energy levels in the photonic band gap. These defects in photonic crystals allow the propagation through the structure of a wave with a certain frequency (resonance frequency, or single mode) within the frequency band gap shown in **Figure 2-8**. This is similar to the propagation of electrons in a semiconductor with

an impurity defect, for certain values of the electron's energy belonging to the energy band gap.

.

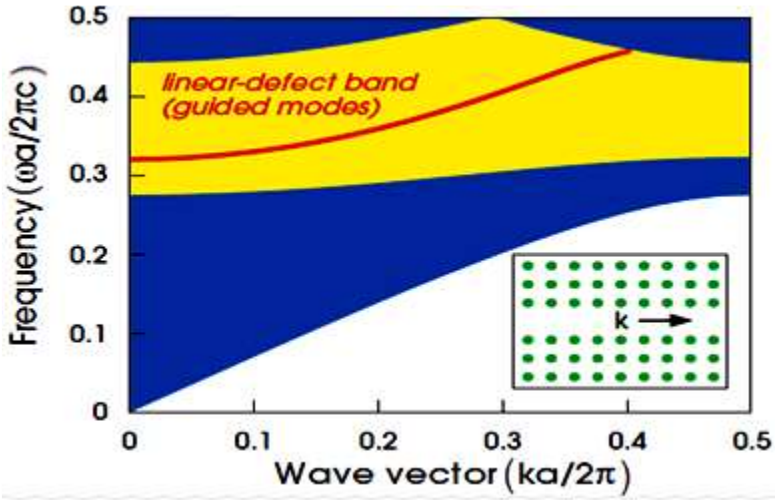

Figure 2-8: The influence of defect on photonic crystal structure on photonic band gap [21].

The observability of the iso-frequency contour due to defects is essential. It could be used to study the dispersion of periodic structures and understand light propagation properties in the periodic photonic structures. In summary, the iso-frequency contour of the photonic crystals is directly observed in real space. It is found that the inevitable defects forming in the self-assembly process allow for the iso-frequency observation. Above all, to understand the physical picture of direct observation of iso-frequency contour in real space clearly, the light scattering of a HPPC (High-performance-thermoplastic-composite) structure is considered in the presence of randomly distributed defects, shi et al (2010) [26].

If there is a decrease in the radius of the point defect, the corresponding resonance frequency approaches the upper limit of the band gap. And, inversely, the resonance frequency approaches the lower limit of the band gap as the defect radius increases, as shown in **Figure 2-9**.

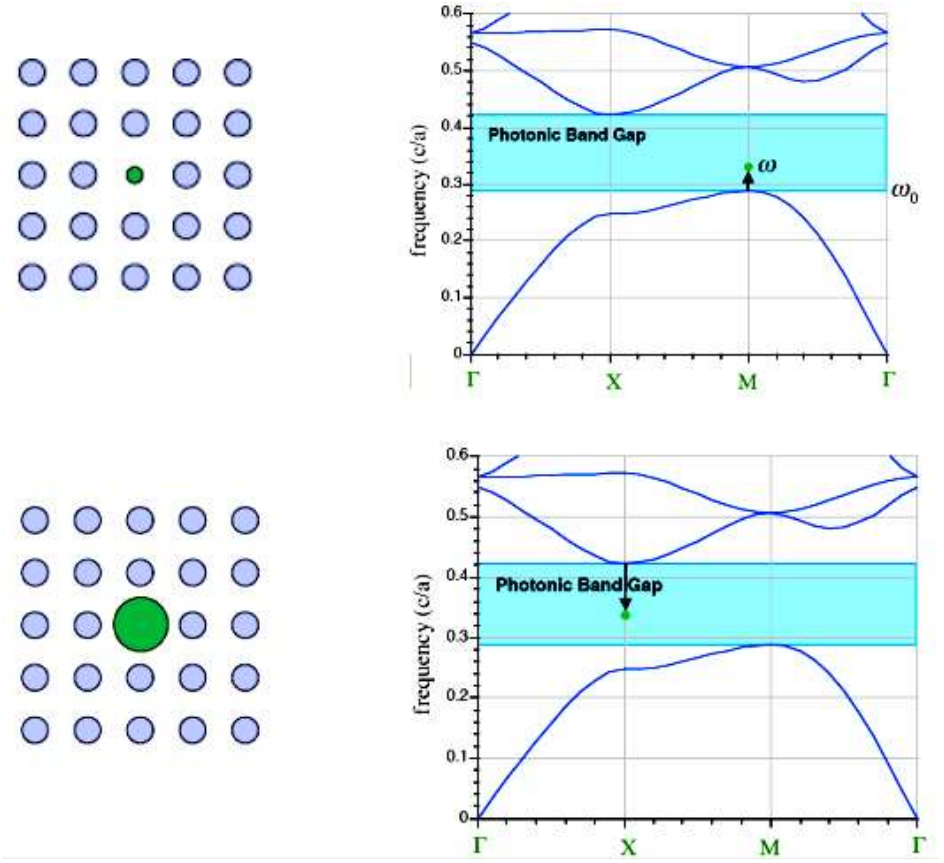

Figure 2-9: Effect of defect dimension change on the frequency of the single-mode in the band gap of two-dimensional photonic crystals [28].

2-6- History of photonic Crystal based Logic Gates

With the photonic crystals' development since the late 90's, many scientists studied these structures mostly for optical processing because of their unique properties such as dimensions of light wavelength, low power consumption, and ease of integration.

The first optical switch using nonlinear effects of optical crystals was introduced by Schloz and Hess (1998) [29]. They presented a one-dimensional type design and utilized a powerful control signal. After presenting this structure, in 2000, Centeno and Felbacq proposed a design for the implementation of optical switches by examining nonlinear photonic crystal waveguides coupled to cavities [30]. In 2002, three studies on optical processing were conducted simultaneously. In one study, Soljacic et al [31] proposed an optical switch using nonlinear photonic crystals. In another work, Fan (2002) [32] introduced another optical switch using a waveguide coupled to the cavity in nonlinear photonic crystals. In 2002, optical limiters using nonlinear elements in photonic crystal waveguides were obtained by Mingaleev and Kivshar [33]. In two separate studies, in 2004, Locatelli & Cuesta-soto et al, introduced directional couplers based optical switches in photonic crystals [34],[35]. In 2006, the AND gate of photonic Crystal was implemented by Zhu et al [36]. In their published structure, several rods with nonlinear Kerr effect have been used to detect the function of AND gate. In 2007, Zhang et al, introduced OR and XOR logic gates based on the property of self-parallel photonic

crystals [37] while moving to the logic elements of the photonic crystal. Shinya, in 2008 implemented optical memory on the photonic crystal chip [38].

In the same year, the half adder structure of photonic crystal suggested by Liu et al (2008) [39] for XOR logic gate based on the fuzzy interference of incoming beams was published by Lee et al (2008) [40]. In 2009, the AND logic gate scheme and the NOR gate using circular resonator structure in nonlinear photonic crystals was published by Andalib (2009) [41]. The performance of the relevant circular structures was in a way that, they behaved differently at high intensity powers due to the nonlinear Kerr effect. That same year, another design was proposed by Jung et al (2009), in which logic gates were obtained using nonlinear photonic crystal cavities [42]. In addition to coding, the structure of a 2 × 4 coder was also proposed by Lee et al (2009) [43]. In the last decade, various designs have been proposed for the implementation of photonic crystal-based gates. These structures have been proposed to improve the characteristics of photonic crystal-based logic gates, including reducing power consumption, increasing bandwidth, and raising the contrast ratio. They also use different materials and semiconductors to implement and improve the properties of photonic crystal-based logic gates. Some of these structures implement two gates simultaneously. During this decade, other designs were introduced that utilized the multi-mode interference feature to realize photonic crystal-based logic gates. These schemes include the one proposed by Ishizaka et al (2010) [44] to implement the AND and XOR gates based on multi-mode interference.

2-7- Principles and concepts of photonic crystals (PhCs) based logic gates

Studies on photonic crystal-based logic gates are divided into the major categories of interference-based logic gates of photonic crystals, resonator-based logic gates of photonic crystals, and self-collimation logic gates of photonic crystals Salmanpour et al (2014) [45].

2-7-1- Interference-based photonic crystal logic gates

The first studies on photonic crystal logic gates were published in 2006 based on multi-mode interference waveguides Mitsugi et al (2003) [46].

According to **Figure 2-10**, the constructive interference occurs when the phase difference and the path difference are 2 nπ and nλ respectively, and the destructive interference occurs when the phase difference and the path difference are equal to (2n + 1) π and (2n + 1) $\lambda/2$ respectively.

To get stable interferences in photonic-crystal structures, two (or more) waves of the same frequency should be introduced with stable and controllable relative phase. These two (or more) waves must be guided inside the structure to superpose in some regions of the structure, giving rise to interferences there. Because of these interferences, and depending on the relative initial phase between the two (or more) input fields, the interferences can make the wave superposition constructive in one or another output channels and destructive in other output channels.

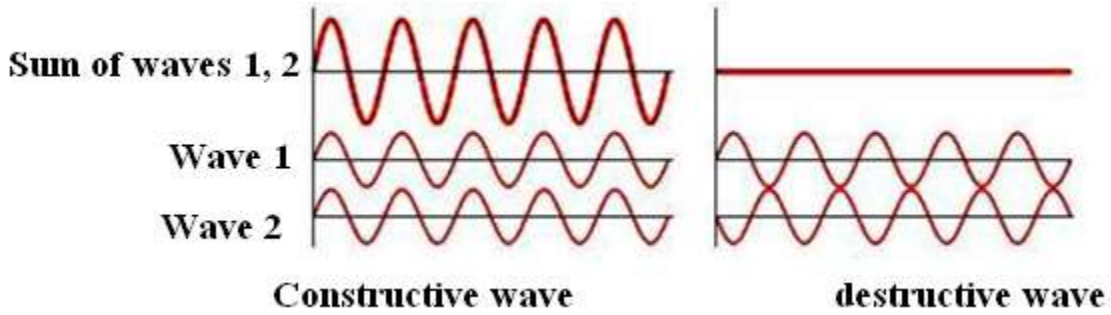

Figure 2-10: Destructive and constructive interference between waves.

2-7-2- Resonance-based photonic crystal logic gates

A point defect in the photonic crystal creates a small cavity for the oscillation of the waves. One way to create logic gates is to use resonant tunneling filters Notomi et al (2004)-Shinya et al (2005) [47]-[48]. These filters are composed of cavities and linear defect-based waveguides with low consumption and high-speed powers Passaro (2009)-Youcef Mahmoud et al (2012) [49]-[50].

Circular resonators are useful tools, and because of the narrow linewidth created by the resonators, they are used for the design of optical devices such as optical filters Djavid et al (2008) [51] and optical switches Ahmadi Tameh et al (2011) [52]. The structure of waveguides, photonic crystals and cavities play an important role in the design of resonator-based gates.

The ring resonator's quality factor, which indicates the limitation of light in the resonator, is an important factor in determining the switching of optical gates. When using cyclic resonators in the manufacture of optical gates, a compromise must be made between increasing the quality factor (Q factor) and reducing the coupling.

The Photonic Crystal Ring Resonator (PCRR) is a simple optical device consisting of a resonant ring and two parallel waveguides, which are called "bus" and "drop" waveguides shown in **Figure 2-11**. At a specific wavelength (called resonance wavelength), the optical waves of the bus waveguide are transmitted by the circular resonator to the drop waveguide, so the PCRR, performs the filtering function, as well as the resonance wavelength of the PCRR depends on the structural parameters of the ring core Mehdizadeh et al (2013) [53]. The output PCRR spectrum is shown in **Figure 2-12.**

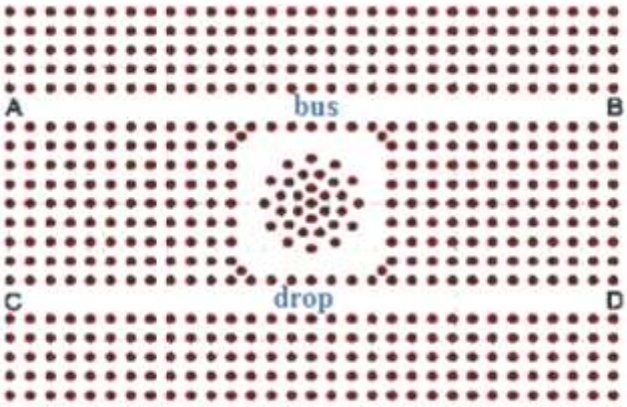

Figure 2-11: Photonic Crystal Ring Resonator [53].

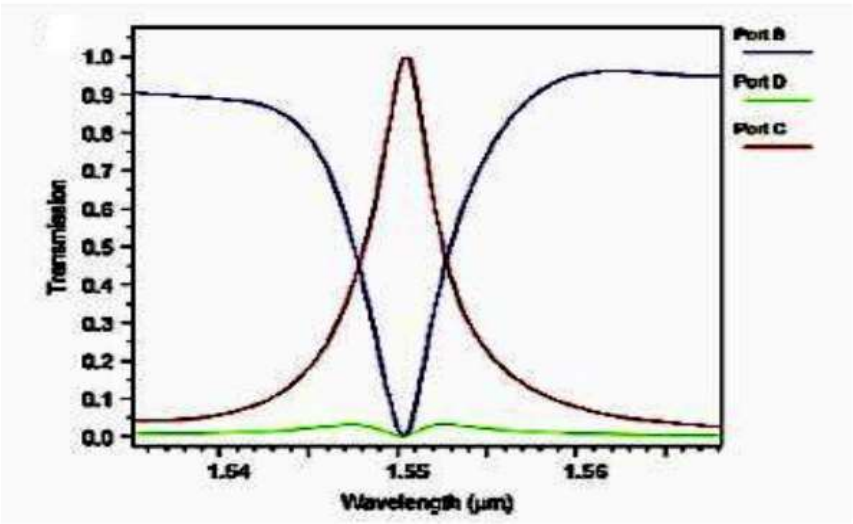

Figure 2-12: Output PCRR spectrum [53].

2-7-3- Self-collimation based photonic crystal logic gates

Self-collimation is a phenomenon that allows the diverging input beam to be emitted and paralleled without the use of a nonlinear effect Kosaka et al (1999) [25]. Many of the works published in Nonlinear Optics have fundamental limitations such as power consumption and narrow frequency range. In contrast, the phenomenon of self-collimation is independent of the incoming radiation intensity and does not require the full-optical band gap compared to crystal photonic waveguides Witzens et al (2002) [54]. Compared to conventional dielectric waveguides and photonic crystal waveguides, which operate with the photonic band gap, the phenomenon of self-collimation does not require the lateral range to prevent divergence and refraction of the beams. Therefore, self-collimation-based devices have a high potential for optical integrated circuits.

One way to parallel the emission beams in the photonic crystal structure is to reduce the rods' radius instead of eliminating them to create a linear defect. This reduction eliminates the overall

reflection, and subsequently, partial reflection of the tunneling wave remains. It is expected that there will be a phase difference between the reflection beam and the tunneling beam. Therefore, if another self-collimation beam is introduced with the appropriate initial phase, the transmitted or reflected beams may create constructive or destructive interference and switching and logic performance.

An integrated light circuit is a promising application of PCs. For this realization, it is necessary to precisely control the profile of the propagation light. Beam-like propagation without divergence is especially required to achieve simple interconnects. In reference Kosaka et al (1999) [25] self-collimating phenomena were reported showing collimated light propagation insensitive to the incident beam's divergence, without applying a nonlinear effect (for example, a Kerr effect that causes self- focusing phenomena or soliton propagation). With the self-collimating phenomena, the propagation is independent from the light intensity (contrary to what occurs with the nonlinear effects), and a waveguide structure, as used in the PCW, is not needed to prevent either the beam divergence or diffraction broadening. In addition, lens-like divergent propagation is demonstrated by using the same PC. These demonstrations will enable flexible design of light path in photonic crystal integrated optics as well as in conventional optics.

To describe how self-collimations works, let us describe part of the work done in reference Kosaka et al (1999) [25]. The light beam propagation in a PC is governed by its dispersion surfaces, which correspond to the index ellipsoid in conventional crystalline optics. A typical branch of a dispersion surface in reciprocal space for a PC is schematically shown as a thick curve in **Figure 2-13** Kosaka et al (1999) [25]. The curvature of the dispersion surface turns from downward to upward, and incident light comes from the top of the figure. The direction of propagation light in the PC is normal to the dispersion surface at the tie points (A1, A2, and B) because the energy velocityintegrated over a unit cell is identical with the group velocity, which is given by:

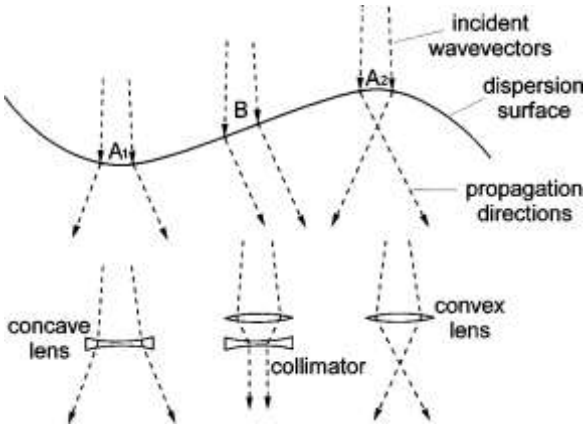

Figure 2-13: A schematic illustration of the self-collimating phenomena (*B*) together with the divergence (A_1) and convergence (A_2) case. Each case corresponds to, respectively, the collimator (*B*), concave lens (A_1), and convex lens (A_2) in conventional optics. Arrows above the dispersion sur- face indicate incident wave vectors in

reciprocal space. Arrows below the dispersion surface indicate the energy flow in real space [25].

$$v_g = \nabla_k \omega(\mathrm{k}), \qquad (2.2)$$

Where ω is the optical frequency at the wave vector *k*, note that the direction in reciprocal space exactly corresponds to that in real space because of the symmetry.

Thus, the light propagation could be categorized in a PC into the following three cases: (1) At the tie point of downward curvature (point A_1), the light in the PC shows divergent propagation as in a concave lens. (2) At the tie point of upward curvature (point A_2), the light shows divergent propagation after convergence as in a convex lens. (3) At the approximately linear area around the inflection point from downward to upward curvature (point *B*), the light shows almost collimated propagation. As this phenomenon is analogous to a collimator, which is made with a combination of concave and convex lenses as shown in the figure, here this is called the ''*collimator case*''. In contrast, as cases (1) and (2) and generally appear simultaneously, these two are referred together as the ''*lens case*''.

In ref. Kosaka et al (1999) [25], the PC was fabricated by depositing alternate layers of amorphous Si and SiO_2 on a Si substrate with a SiO_2 buffer that had a hexagonal array of holes. As a result of the replication of the buffer surface pattern, the three-dimensional (3D) structure consisted of alternately stacked triangular lateral lattices of Si or SiO_2 disks that were self-organized. The fabricated total thickness of 6.4 μm (20 pairs with 0.32 μm pitch) provided sufficient vertical guiding and beam coupling. The lateral lattice constant of 0.33 μm was designed to show a particular anisotropy in the incident light's dispersion relation with a wavelength of 0.956μm. The incident edge is normal to the Γ-*M* direction.

For analysis of the experimental results, in reference Kosaka et al (1999) [25] the photonic-band structure was showing the energy-dispersion relation as a function of a wave vector, using the plane-wave expansion method. 1258 plane waves were taken to ensure accuracy within 1%. **Figure 2-15** (right side) shows the constant-energy contours, the dispersion surfaces, of the photonic band in TM polarization at particular incident energy Kosaka et al (1999) [25]. The wave vector k was normalized by the lateral lattice constant a as ka/2π. Propagation waves in the circled area in **Figure 2-15** were selectively excited under a momentum conservation condition. The distribution of the incident wave vector Δk due to the beam focusing determines the propagation wave vector's distribution. In the wave-vector region denoted by A in **Figure 2-15**, the dispersion surfaces correspond to the concave case (upper branch) and convex case (lower branch), which in turn correspond to A_1 and A_2 respectively, in **Figure 2-13**. Thus, the propagation directions in case A vary in the single-hatched fan-like area in **Figure 2-15**, which corresponds to the fan-like beam path of case A in **Figure 2-14**, the other hand, in the wave-vector region denoted by B, there is only one dispersion surface, and the curvature is approximately linear within the range of the wave-vector divergence. Thus, the corresponding propagation directions are almost unique, as shown in **Figure 2-15**. This means that the sharpness of the beam waist is maintained throughout the light propagation, as shown in the single-hatched rectangular area, which corresponds to case B's narrow beam path in **Figure 2-14**.

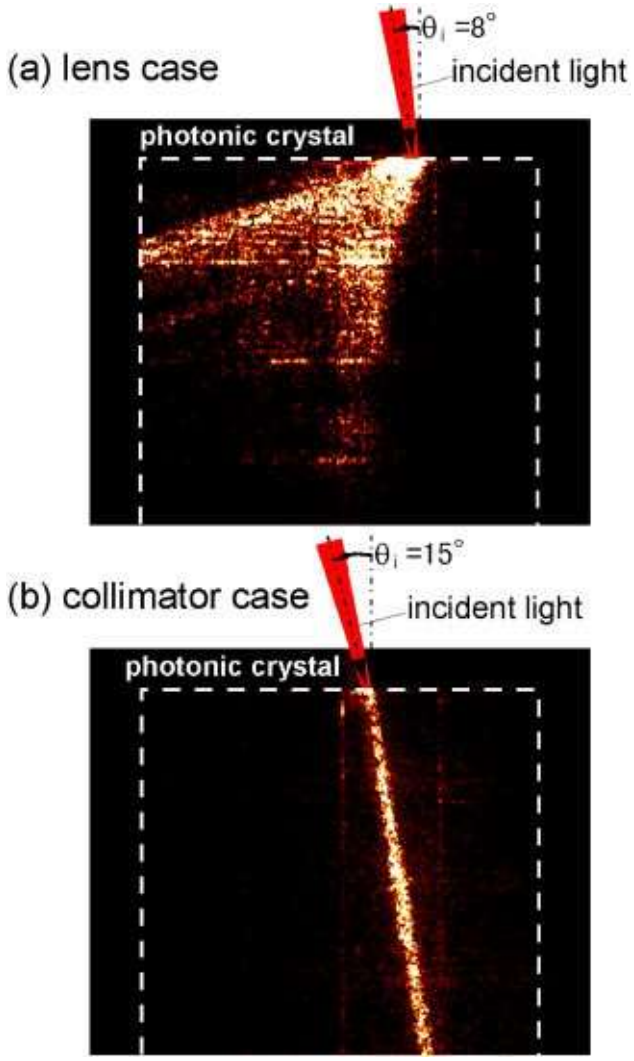

Figure 2-14: Photographs showing the beam paths inside the PCs in (a) the lens case and (b) the collimator case at the respective incident angles of 8° and 15°. TM-polarized light with a divergence of 6° was focused onto the incident edge of the PC. Case (a) shows fan-like expansion that consists of the overlapping of the lens-like propagation in cases A_1 and A_2 in Figure 2-18. In contrast, case (b) shows almost fully collimated propagation with a nearly constant beam waist in case *B* [25].

To confirm the exact correspondence described above, the divergence angle was numerically calculated from the dispersion curve shown in **Figure 2-15** as a function of the incidentangle **Figure 2-16**. The solid curve and the broken curve, respectively, correspond to the upper and lower branches in **Figure 2-15** at the incident angle of 15°, corresponding to case *B*, the divergence angle becomes nearly zero. In contrast, the divergence angles for both branches reach a maximum of about 70° at around 8°, corresponding to case A. This behavior agrees well with the observed beam divergence shown in **Figure 2-14.**

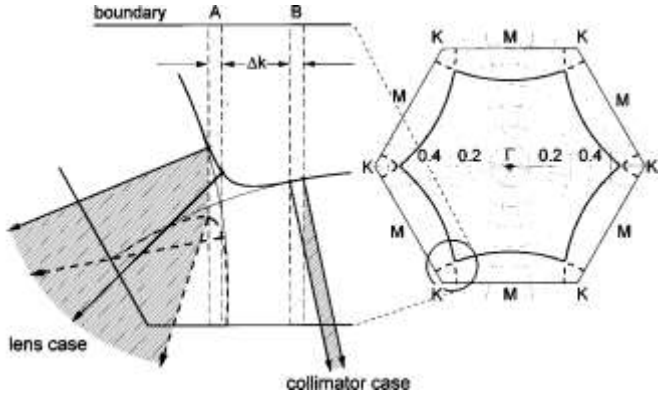

Figure 2-15: Numerically calculated dispersion surfaces in reciprocal space at a particular frequency of the incident light. Only the TM mode is shown. The left side shows the magnified dispersion in the resonant region marked by the circle. The solid and broken curves show two different branches. Cross- hatching denotes the distributions of the incident wave vector for cases *A* and case *B*, corresponding to those in Figure 2-14. Single-hatching denotes the resulting distributions of the propagation direction, which corresponds to the energy flow in real space [25].

In conventional Gaussian optics, the beam width (2 w) develops from the beam waist (2 w_0), due to natural diffraction, as:

$$w^2(x) = w_0^2\left[1 + \left(\frac{\lambda x}{\pi w_0^2}\right)^2\right], \qquad (2.3)$$

Where λ is the wavelength and x is the propagation distance from the beam waist. If this equation was applicable to the experiment shown in **Figure 2-14**, the beam width at the output edge (28 μm) would be more than twice that of the waist at the incident edge (13 μm), even when the effective refractive index ($\approx$2) was taken into consideration. However, this was contrary to the observations of ref. Kosaka et al (1999) [25].

In conclusion, in reference Kosaka et al (1999) [25] self-collimated light propagation and lens-like propagation in PCs were demonstrated. Phenomena similar to the lens-like case had been previously reported for planar waveguide gratings and x-ray diffraction, but that was the first report for the collimator case. That self- collimating phenomenon originates from the much stronger coupling strength that is, for instance, five orders of magnitude greater than that in the x-ray case. In that experiment, an almost fully collimated light beam was visually observed in a 3D-PC, and this beam was independent of the incident-light intensity. The divergent angle was numerically analyzed using the dispersion surfaces derived from the photonic-band calculation. The fundamental importance of this phenomenon is that the light propagation is not affected by the incident beam divergence or diffraction broadening under a designated condition as a result of the coherent scattering in the PC.

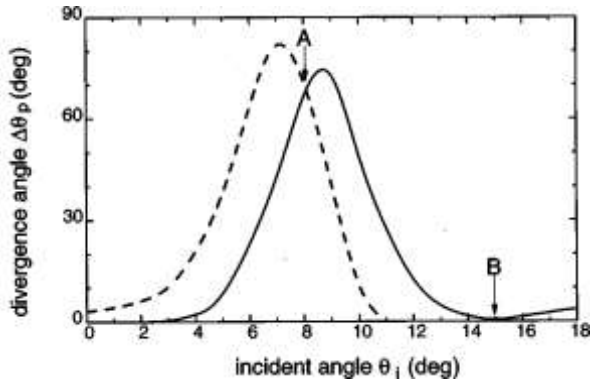

Figure 2-16: Numerically calculated divergence angle of the propagation direction in the PC as a function of the incident angle. The solid and the broken curves, respectively, correspond to the upper and lower branch in Figure 2-15 [25].

This property should also be a technical advantage in terms of the required space and alignment tolerance compared to a conventional collimator, in which the propagation depends critically on the position of a light source or a pin-hole. The other technical significance of that self-collimating phenomenon can be summarized as follows: (1) The effect requires neither a complete PBG nor intentionally formed linear defects to act as a waveguide, in contrast to PCWs. (2) Light-beam coupling of a PC with an optical fiber or a conventional laser is much more efficient than that of a PCW.

The phenomenon is independent of the incident-light intensity and free from absorption loss in contrast to the self-focusing phenomena. This demonstration should open the way toward realizing photonic crystal-integrated light circuits as small as the electronic circuits on an LSI chip with state of the art fabrication technologies. It could also represent a first step towards developing photonic crystal optics.

As it will be shown later, we have used the self-collimation phenomenon in some of our designs and calculations.

2-7-4- Nonlinear Kerr effect

In this section, the physical phenomenon of the “nonlinear Kerr effect” described as it has also been used in the thesis to design some of the structures.

2-7-4-1-Third-order nonlinear processes.

The most general third-order nonlinear process involves the interaction of waves at four different frequencies, linked by: ω1 + ω2 + ω3 = ω4. Fortunately, in all common cases, some of the frequencies are the same, and some may be also zero, or the negatives of the others. The contribution to the polarization at ω4 brought about by the other three waves is given by Moreno (2018) [55]:

$$\widehat{P}_i(\omega_4) = \frac{1}{2}\varepsilon_0 \sum_p \sum_{jkl} \chi^{(3)}_{ijkl}(\omega_4; \omega_1, \omega_2, \omega_3)\, \widehat{E}_J(\omega_1)\, \hat{E}_k(\omega_2) \widehat{E}_l(\omega_3) \quad (2.4)$$

Where ijkl can be x, y or z, and $\sum_p$ indicates the right-hand side is to be summed over all distinct permutations of ω1, ω2 and ω3. This means that the form of the polarization depends on the frequency arranged and it is specific of the kind of process. So, for the DC Kerr effect we have (ω = 0 + 0 + ω)

$$\widehat{P}_i(\omega) = 3\varepsilon_0 \sum_{jkl} \chi^{k}_{ijkl}(\omega; 0,0,\omega) \widehat{E}_J(0) \hat{E}_k(0) \widehat{E}_l(\omega), \quad (2.5)$$

This concerns refractive index changes caused by an applied DC field.

In the optical or AC Kerr effect, an intense beam of light in a medium can itself provide the modulating electric field, without the need for an external field to be applied. For the optical Kerr effect we have ($\omega_1 = \omega_2 - \omega_2 + \omega_1$):

$$\widehat{P}_i(\omega_1) = \frac{2}{3}\varepsilon_0 \sum_{jkl} \chi^{OK}_{ijkl}(\omega_1; \omega_2, -\omega_2, \omega_1) \widehat{E}_J(\omega_2) \hat{E}^*_k(\omega_2) \widehat{E}_l(\omega_1). \quad (2.6)$$

In this case, the refractive index of an optical wave at ω_1 is modified in the presence of a wave at ω_2 (cross-phase modulation). It should be also noted that in cases where two (or more) optical waves are involved, these need not necessarily travel in the same direction. There is, for example, no reason in principle why the two waves in **Equation 2-6** need to be collinear, and in this case their frequencies could even be the same. This, in particular, means that the optical Kerr effect can occur even with a unique light beam (self-phase modulation).

2-7-4-1- -Tensor nature of the third order susceptibility

Let us see how to determine the tensor nature of the third-order susceptibility for the case of an isotropic material such as a glass, a liquid, or a vapor. We begin by considering the general case in which the applied frequencies are arbitrary, and the susceptibility would be represented as $\chi_{ijkl} \equiv \chi^{(3)}_{ijkl}(\omega_4 = \omega_1 + \omega_2 + \omega_3)$. In a lossless crystal of the most general triclinic symmetry, there are $3^4 = 81$ independent nonlinear coefficients; for other symmetry classes, number is lower, and a list of independent coefficients in each class can be found in reference Moreno (2018) [55]. In an isotropic media, in which all directions are equivalent, the orientation of the *xyz* axes can be chosen to make calculations as simple as possible. In this case, only 21 of the 81 coefficients are non-zero, and these are of four types: type 1 (three members) in which all indices are identical ($X1 \equiv \chi_{iiii}$), and types 2, 3 and 4(six members each) in which two pairs of indices are the same, namely $X_2 = \chi_{jjkk}$, $X_3 = \chi_{jkjk}$ *and* $X_4 = \chi_{jkkj}$ $(j \neq k)$

Before describing **Equation 2-11,** introduction relations should be defined as follows:

For a nonlinear material, the electric polarization field

P will depend on the electric field E:

$$P = \varepsilon_0 x^{(1)} E + \varepsilon_0 x^{(2)} EE + \varepsilon_0 x^{(3)} EEE + \cdots, \qquad (2.7)$$

where ε_0 is the vacuum permittivity and $\chi^{(n)}$ is the n-th order component of the electric susceptibility of the medium. We can write that relationship for the i-th component for the vector P, expressed as:

$$P_i = \varepsilon_0 \sum_{j=1}^{3} X_{ij}^{(1)} E_j + \varepsilon_0 \sum_{j=1}^{3}\sum_{k=1}^{3} X_{ijk}^{(2)} E_j E_k + \varepsilon_0 \sum_{j=1}^{3}\sum_{k=1}^{3}\sum_{t=1}^{3} X_{ijkl}^{(3)} E_j E_k E_l + \cdots \quad (2.8)$$

it is worth pointing out that the different numerical pre-factors in **Equation 2-9** result from the permutation operation in **Equation 2-8**

$$P^{TOT}(\omega) = \varepsilon_0 x^{(1)} E(\omega) + 2\varepsilon_0 x^{(2)} E(\omega) E(0) + 3\varepsilon_0 x^{(3)} |E(\omega)|^2 E(\omega) + \cdots \quad (2.9)$$

If we consider the two first terms of **Equation 2-9**, this approximation is known as the linear electro-optic Pockelseffect, which leads to an electric field induced change in the refractive index. On the other side, the part of thenonlinear polarization that influences the propagation ofa beam of frequency ω is just given by the third term of **Equation 2-9**, which leads us to the study of the Kerr effect. In this case, we can express the polarization as

$$P(\omega) \cong \varepsilon_0 x^{(1)} E(\omega) + 3\varepsilon_0 x^{(3)} |E(\omega)|^2 E(\omega) = \varepsilon_0 x_{eff} E(\omega), \qquad (2.10)$$

Where we have introduced the effective susceptibility,

$$x_{eff} = x^1 + 3\varepsilon_0 x^{(3)} |E(\omega)|^2$$

The numbering scheme ensures that indices **Equation 2-7** and **Equation 2-8** are the same inX_2 indices **Equation 2-7** and **Equation 2-9** in X_3 , and **Equation 2-7** and **Equation 2-10** in X_4. Within each type, all members are equal and, as it is shown below, the symmetry of a structurally isotropic medium imposes the further constraint that

$$x_1 = x_2 + x_3 + x_3 \qquad (2.11)$$

In terms of indices, the non-zero coefficients can be listed as follows:

1: xxxx = yyyy = zzzz

2: xxyy = yyzz = zzxx = yyxx = zzyy = xxzz

3: xyxy = yzyz = zxzx = yxyx = zyzy = xzxz

4: xyyx = yzzy = zxxz = yxxy = zyyz = xzzx (2.12)

The key conclusion is that a structurally isotropic medium has just three independent third-order coefficients. For collinear beams, it makes sense to set the *z* axis along the direction of propagation, in which case all coefficients involving z in **Equation 2-12** can be ignored; this reduces the number of relevant non-zero coefficients. Moreover, if all beams are plane polarized in the same direction, the *x* axis can be chosen as the directionof polarization; in this case, the only relevant coefficient is $X_{xxxx} = X_1$.

2-7-4-2- Electro-optical Kerr effect

In the Electro-optical or DC Kerr effect, a strong DC field changes the refractive index of a medium. If the DC field is y-polarized, **Equation 2-5** indicates that the respective polarizations in the *x* and *y* directions are Moreno (2018) [55]:

$$\hat{P}_x(\omega) = 3\epsilon_0\, \chi^k_{xyyx}\,(\omega; 0,0,\omega) E_y^2\,(0)\hat{E}_x(\omega) = 3\epsilon_0\, X_4^k E_y^2\,(0)\hat{E}_x(\omega)$$

$$\hat{P}_x(\omega) = 3\epsilon_0\, \chi^k_{yyyy}\,(\omega; 0,0,\omega) E_y^2\,(0)\hat{E}_y(\omega) = 3\epsilon_0\, X_1^k E_y^2\,(0)\hat{E}_y(\omega) \quad (2.13)$$

The DC field creates a refractive index difference between the two polarizations given by:

$$n \parallel - n \perp \cong \frac{3\left(X_1^k - X_4^k\right)E_y^2\,(0)}{2n} = \frac{3X_2^k\, E_y^2\,(0)}{n}, \quad (2.14)$$

Where $n \parallel$ and $n \perp$ are the respective indices for light polarized parallel and perpendicular to the DC field, and *n* is the zero field refractive index. From **Equation 2-11**, and because X_2^k and X_3^k are indistinguishable from **Equation 2-5** the Kerr constant K of the medium is defined by the equation:

$$\Delta n \equiv n \parallel - n \perp = \lambda_0 K E^2(0), \quad (2.15)$$

Where λ_0 is the wavelength in a vacuum and K = $3X_2^k/\lambda_0 n$. This difference in index of refraction causes the material to act like a quarter waveplate when light is incident on it in a direction perpendicular to the electric field. If the material is placed between two perpendicular linear polarizers, no light will be transmitted when the electric field is turned off, while nearly all of the light will be transmitted for some optimum value of the electric field.

2-7-4-3- Optical Kerr effect

In the optical Kerr effect, a strong wave at frequencyω_2 and intensity $I(\omega_2)$ changes the refractive index of a weak probe wave at ω_1, a process known as cross-phase modulation. If the two waves have the same polarization, the operative term in the polarization is Moreno (2018) [55]:

$$\hat{P}_x(\omega_1) = \frac{3}{2}\varepsilon_0\, \chi^{OK}_{xxxx}\,(\omega_1;\omega_2-\omega_2,\omega_1)\left|\hat{E}_x(\omega_2)\right|^2\hat{E}_x(\omega_1), \quad (2.16)$$

Which implies that the refractive index of the weak waveis changed by:

$$\Delta n_x \cong \frac{3\chi^{OK}_{xxxx}\, I(\omega_2)}{2n(\omega_1)n(\omega_2)c\varepsilon_0} \qquad (2.17)$$

If, on the other hand, the weak and strong waves are,respectively, x and y-polarized, **Equation 2-16** becomes:

$$\hat{P}_x(\omega_1) = \frac{3}{2}\varepsilon_0\, \chi^{OK}_{xyyx}\,(\omega_1;\omega_2-\omega_2,\omega_1)\left|\hat{E}_y(\omega_2)\right|^2\hat{E}_x(\omega_1), \quad (2.18)$$

This is the same as **Equation 2-16** apart from the fact that it contains a type 4 coefficient, and so the index changeis weaker.

An important special case of the optical Kerr effect occurs when a single beam at $\omega = \omega_1 = \omega_2$ modifiesits own refractive index. This is known as self-phase modulation. For the case of plane polarizedlight, **Equation 2-6** can be written in the simple form:

$$\hat{P}_x(\omega) = \frac{3}{4}\varepsilon_0\, \chi^{OK}_{1}\,(\omega;\omega-\omega,\omega)\left|\hat{E}_x(\omega_2)\right|^2\hat{E}_x(\omega), \qquad (2.19)$$

This implies that the refractive index is changed to:

$$n = n_0 + \left(\frac{3\chi_1^{OK}}{4n_0^2 c\varepsilon_0}\right) I = n_0 + n_2 I, \qquad (2.20)$$

Where I is the intensity, n_0 is the low-intensity index, and the equation defines n_2 as the nonlinear refractive index. It is no surprise that the refractive index change implied by **Equation 2-20** is essentially the same as that of **Equation 2-17**. the extra factor of 2 in the denominator of n_2 arises from the different pre-factors in **Equation 2-6**.

A full justification of **Equations 2-16, 2-19** is given in New, G (2011) [56] and Mills (1999) [57] .Again, it is worth pointing out that the different numerical pre-factors in **Equations 2-16, 2-19** result from the permutation operation in **Equation 2-4**.

2-7-4-5 Applications of the Kerr effect

The optical Kerr effect plays a significant role in nonlinear optics using high-power pulsed lasers. It is one of the mechanisms contributing to self-focusing in liquids and solids and has also been used as a fast optical shutter for picosecond optical pulses. Some of the areas of application of the Kerr effect includes spectroscopy of liquids, including the study of liquid mixtures and the behavior of liquids in nanoconfinement, the development of waveguides (devices constructed out of a birefringent material, for which the index of refraction is different for different orientations of light passing through it) and photonic and electro-optic devices. **Figure 2-17** shows an induced birefringence of graphene oxide liquid crystals with an extremely large Kerr coefficient allowed to fabricate electro-optic devices with macroscopic electrodes, as well as well-aligned, defect-free graphene oxide over wide areas.

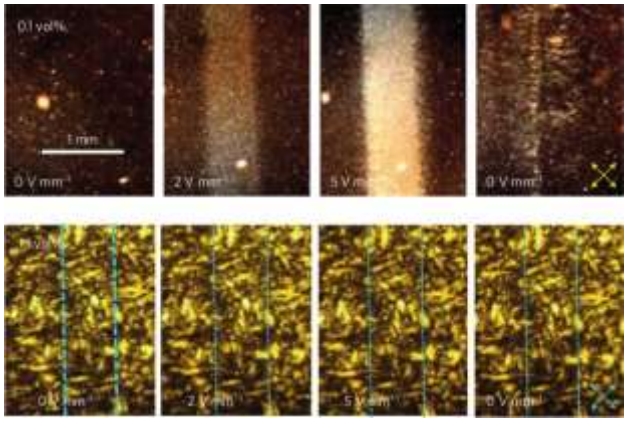

Figure 2-17: Electric-field-induced birefringence. Top row: Field-induced birefringence was generated by applying electric fields (10 kHz) to an aqueous 0.1 vol % graphene oxide dispersion. When the field was switched off, the field-induced birefringence almost disappeared, with only slight nematic aggregation remaining.

Bottom row: In the same cell structure with a 1.1 vol % GO LC, no change was detected up to 20 V mm^{-1} [55].

2-8- All-optical logic gates based on photonic crystals. Review of literature

All-optical logic gates, such as NOT, OR, AND, etc., are essential components for building different computing units. Photonic crystal waveguides and microcavities are often used to make logic gates.

2-8-1- "AND" Gate

The AND gate is used to identify the address and to confirm the integrity of the information and is capable of performing the following logic operations:

0 AND 0 = 0

1 AND 0 = 0

0 AND 1 = 0

1 AND 1 = 1

The all-optical AND Gate of photonic crystal optics can be accomplished using nonlinear frequency conversion of non-linear tunable microcavity in the optical waveguide and other similar methods. The nonlinear optical Kerr effect can be applied to the implementation of all-optical logic gates. As indicated in section 2-7-4, the optical Kerr effect is one of the effects in the nonlinear equation of order 3 and depends on the light intensity.

Equation 2-19 tells us that, in the optical Kerr effect, when an electromagnetic wave of intensity "I" crosses the material, the refractive index grows in the form Zhu et al (2006) [36]:

$$n = n_0 + n_2 I \qquad (2.21)$$

Where n_0 is the linear refractive index, *"I"* is the optical field intensity, and n_2 is the nonlinear Kerr refraction coefficient. Considering the nonlinear effects of polarization, the set of linear and nonlinear polarizations can be represented and defined below Zhu et al (2006) [36]:

$$P=P_L+P_{NL}=\varepsilon_0[X^{(1)} \quad E+ \quad X^{(2)} \quad E^2+X^{(3)} \quad E^3) \qquad (2.22)$$

Consequently, the wave equation in nonlinear environment according to Maxwell's equations is obtained as follows:

$$\nabla^2 E - \mu_0 \varepsilon_0 {n_0}^2 \frac{\partial^2 E}{\partial t^2} = \frac{\partial^2 P_{NL}}{\partial t^2} \qquad (2.23)$$

Where the term of $\frac{\partial^2 p_{NL}}{\partial t^2}$ is a nonlinear expression. According to the new refraction coefficient, the permittivity coefficient is obtained from the following equation Zhu et al (2006) [36]:

$$\varepsilon = n^2 = (n_0 + n_2 E^2)^2 \qquad (2.24)$$

Zhou et al, developed a plan to achieve a high-contrast AND gate based on the optical waveguide of nonlinear two-dimensional photonic crystal. The two-dimensional photonic crystal of this gate consists of a square lattice of dielectric rods in the air background. As shown in **Figure 2-18**, the optical structure is a combination of two waveguides A, B, an output waveguide F and an interference waveguide. Three dielectric rods with strong third-order nonlinear properties are placed at the end of the interference waveguide. In this structure, the lattice constant (a) is 528 nm, and the rod radius is 0.18 a.

When the signal comes from waveguide A or B, the interference of input light and reflective light causes a static wave in the interference area. As a result, no signal will be able to reach the output waveguide F, and the output signal is approximately zero. This action corresponds to the logic action 1 AND 0 = 0. When the input signal exists in the waveguides A and B, the intensity of light in the three nonlinear rods in the curved area can be increased to change the refractive index of the three dielectric rods effectively. However, complete reflection in the curved area can no longer be established, and light can be transmitted through the interference waveguide in this area. Therefore, a strong signal is at the output, and this corresponds to the logic operation of 1 AND 1 = 1 Zhu et al (2006) [36].

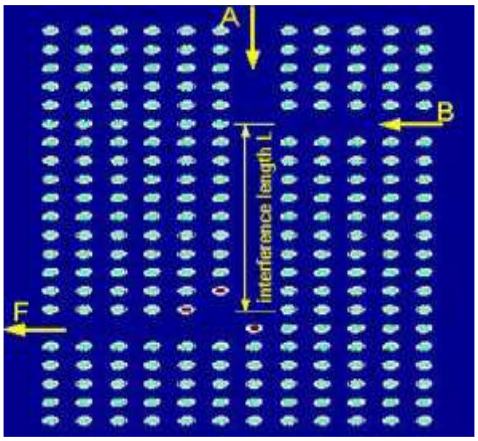

Figure 2-18: Gate AND based on interference and Kerr effect [36].

In 2009, Andalib and Granpayeh [41] presented the AND logic gate based on the fact that silicon nanocrystals have a strong nonlinear effect in the third telecommunication window. This material has been used in the creation of a ring resonator. As shown in **Figure 2-19**, the resonators are between three parallel waveguides. This network only has a TM photonic band gap, so the logic gate provided is designed for TM modes. This structure's lattice constant (a = 455nm, r = 0.2) is selected to operate in the third communication window and suitable coupling.

To analyze the proposed structure's performance, part of the gate mentioned above consisting of a resonator and two passing channels is shown in **Figure 2-19**.

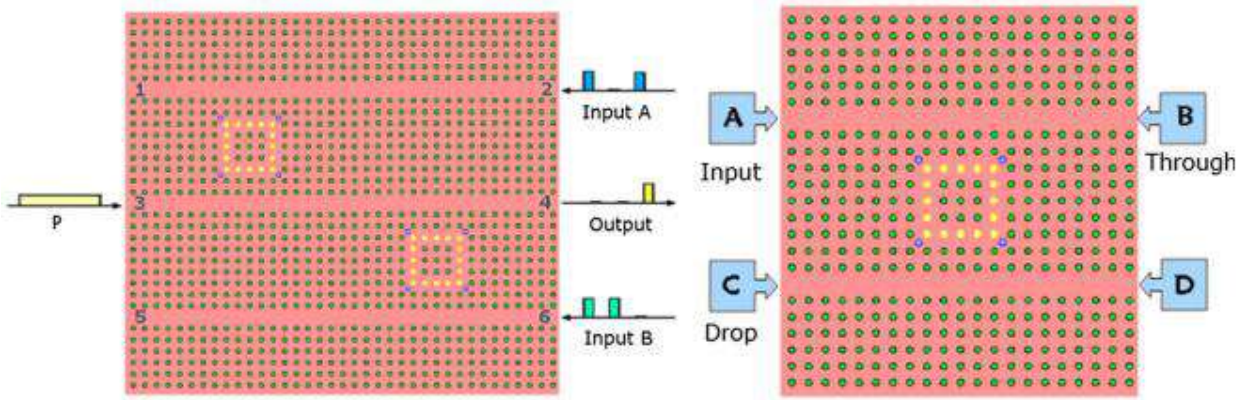

Figure 2-19: Ring resonator based AND gate [41].

The linear performance would be encountered for powers lower than 33W/μm, and resonance occurs at 1594.2 nm. Nonlinear conditions at powers above 33W/μm with the resonance wavelength of 1550.2nm. This phenomenon is used in the design of the provided AND logic gates.

The silicon rods' nonlinear property causes the resonance wavelength to be changed relative to the linear mode. In this structure, when the low-power continuous-wave signal enters the gate through input 2, since the signal's frequency is equal to the frequency of ring resonance, this signal enters the circular resonators and transmits to the outputs 1 and 5 from there. Therefore, the output will be logic zero. But if both high-power A and B signals enter the waveguide, they can change the resonance frequency of the resonant rings. as a result, the signal does not enter each of the resonant rings and will exit output 4, so the output will be equivalent to logic 1.

Ishazaka et al (2011) [46] presented AND logic gates with low power consumption without the use of nonlinear effects based on photonic crystal waveguide, including multi-mode interference such as **Figure 2-20**. Multi-modal interference-based structures (MMI) are simple, small, and low power dissipation structures with a large width. MMI-based structures act based on the self-imaging effect Ishazaka et al (2011) [46].

The self-imaging is a property of multi-mode waveguides by which the input field is propagated in a single image or multiple images at alternating distances towards propagation. In other words, when a signal enters the structure, the conductive modes of the MMI segment are stimulated and consequently interacted with each other. Alipour-Banaei et al (2016) [58], researchers have used the genetic algorithm and optimized the r_s to align the rods with the appropriate radius in the bent and multi-modal areas for better transmission.

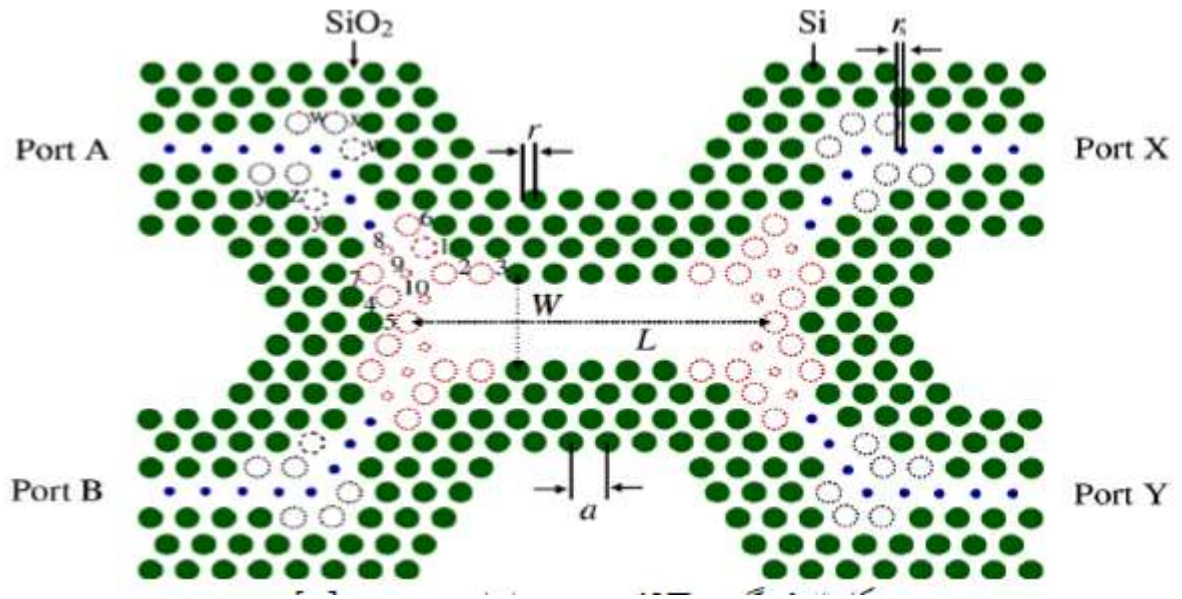

Figure 2-20: Gate AND based on multi-mode interference [46].

Due to the change of radius and optimization, the transmission in the whole "band c" in bends is over 99%. A and B are input ports, and X and Y are output ports, and MMI is a center with length L and width W. The platform substrate of sio_2 and the rod material is silicon.

In 2011, the AND gate was introduced with a transition time of less than 1ps using a two-dimensional photonic crystal network with holes in the GaAs substrate. The radius of the holes in the structure 0.3 μm and the dielectric constant for wavelength 1.55 μm is 13. There is a photonic band gap for TE. One of the best ways to create a strong switching mechanism in optical crystals is to create nonlinear optical crystal cavities coupled with waveguides. Reducing the radius, cavities in the structure, and making the defect cause the modes of the cavity Danaie and Kaatuzian (2011) [59].

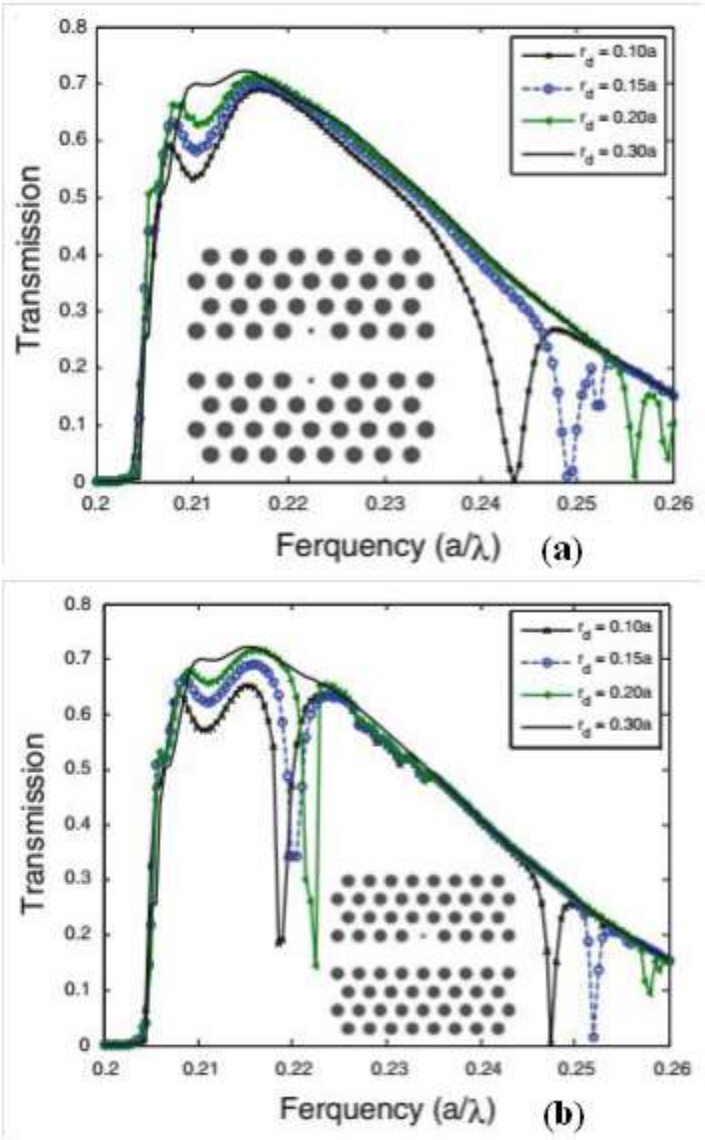

Figure 2-21: Creating a defect in the row adjacent to W1 waveguide. a Transmission curve for different values of defect radius. b Normalized transmission with regard to the W1 waveguide [59].

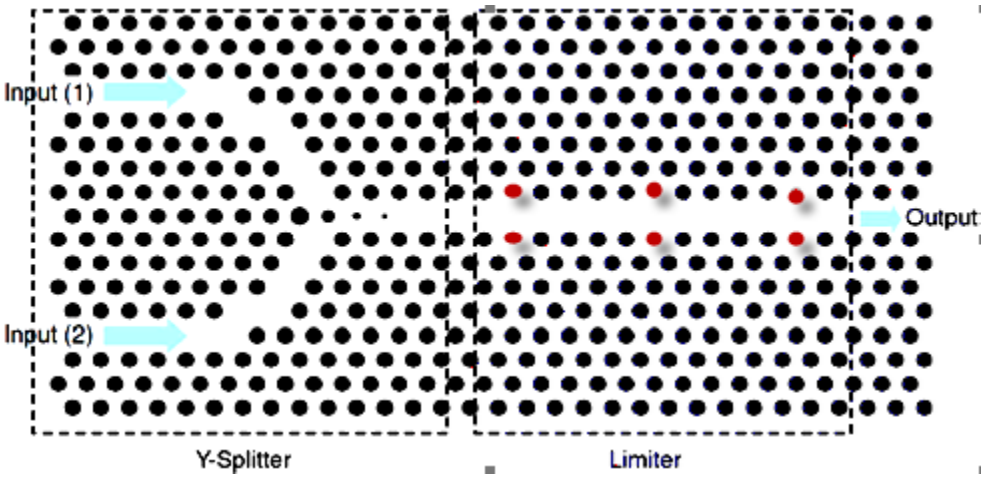

Figure 2-22: AND gate based on Y defect and resonant cavity [59].

According to **Figure 2-21**, two symmetric defects have been added to the coupled waveguide to improve the AND gate's performance and to obtain further separation of the modes. The frequency shift in this mode is increased. In addition, at the central gap's frequency, the normalized transmission curve reaches zero, which means less leakage and a higher contrast ratio. The cavities have an optimal defect radius of r_d=0.25a and a Kerr effect of $n_2=2.7\times10^{-19}$.

As shown in **Figure 2-22**, in the limiter section's design to prevent the loading effect of cavities on each other, three nonlinear rods with a radius less than 5a were placed above and below the adjacent rows of the waveguide. The proposed scheme has a delay time of less than 0.4 ps and an area of less than 100 μm^2.

Yang et al (2013) [60] proposed a two-dimensional crystalline triangular lattice-based gate AND design with a dielectric constant of 11.56 and a radius of 0.35a (μm)**.** As shown in **Figure 2-23**, the proposed structure comprises the photonic crystal hexagonal ring resonator (PCHRR) and the Y-effect, in which the directional coupling arms are the Y-defect inputs. It has rarely been reported that optical gates operate at more than one wavelength.

However, providing structures with multiple functional wavelengths is more flexible in applications such as optical processing. The directional coupler divides the input light beam into two beams, such as a power beam divider. One of the beams is rotated clockwise at 60 degrees, and the other is rotated counterclockwise at 120 degrees. The presented structure, due to the general TIR reflection phenomenon and interference with the ring resonator, can act with wavelengths of 1.55 μm, 1.51 μm, 1.49 μm, 1.42 μm, 1.2 μm. Logic levels of 0 and 1 are considered less than 25% and more than 95%, respectively Yang et al (2013) [60].

2-8-2- "OR" Gate

The logic functions in OR gate are defined as follows:

0 OR 0 = 0

1 OR 0 = 1

1 OR 0 = 1

1 OR 1 = 1

Fu et al (2013) [61] have theoretically designed five gates, including the OR gate. The structure of these gates is based on optical beam interference. **Figure 2-24** shows the outline of the proposed structure.

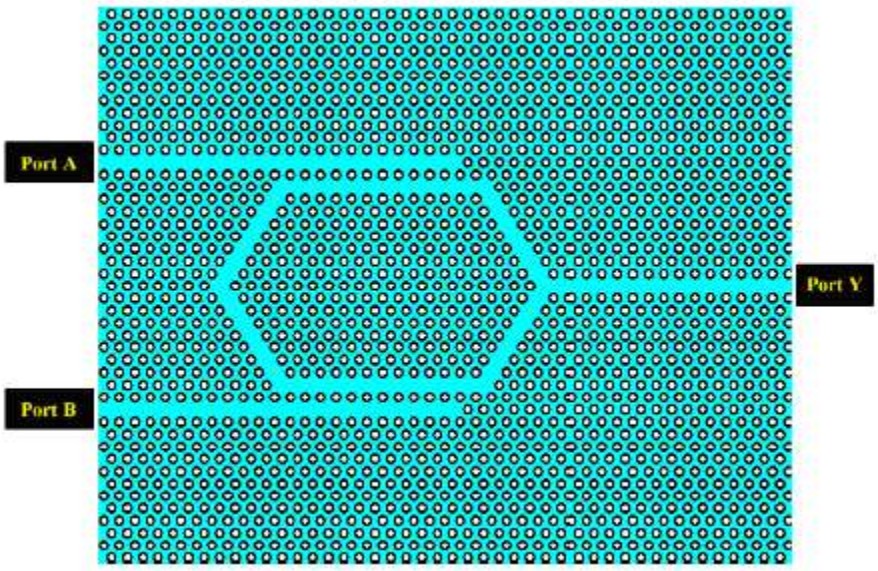

Figure 2-23: Resonator and coupling-based gate AND [60].

The photonic crystal structure is composed of a triangular network of silicon cylindrical rods with an air background. By removing two rows of rods, two symmetric optical waveguides are formed. In this ingenious design, it is possible to control the optical path difference to realize different gates. Since the gates do not require high power for their logic performance and have a maximum contrast ratio of 20DB, this is a simple and effective way to realize integrated all-optical logic devices Yang et al (2013) [60].

Zhang (2007) [62] simulated two gates, including the OR gate, using self-collimation beams. A square lattice of silicon rods is intended in the air. Linear defect, by reducing the radius of the rods to 0.274a in the ΓX direction, shown by the red area in **Figure 2-25**.

Figure 2-24: OR gate base on Interference [61].

Due to the dispersive relations, the structure of self-collimation phenomenon in 0.194 a/λ occurs along the ΓX. The linear defect causes the PC structure to become a 2dB power divider of the self-collimation beams. This means that the amplitude of the reflected and transmitted waves will be the amplitude of the reflected wave and the amplitude of the transient wave.

$(t=r=\frac{1}{\sqrt{2}})$, $(\frac{e^{i(\varphi+\frac{\pi}{2})}}{\sqrt{2}})$ and $(\frac{e^{i\varphi}}{\sqrt{2}})$ respectively.

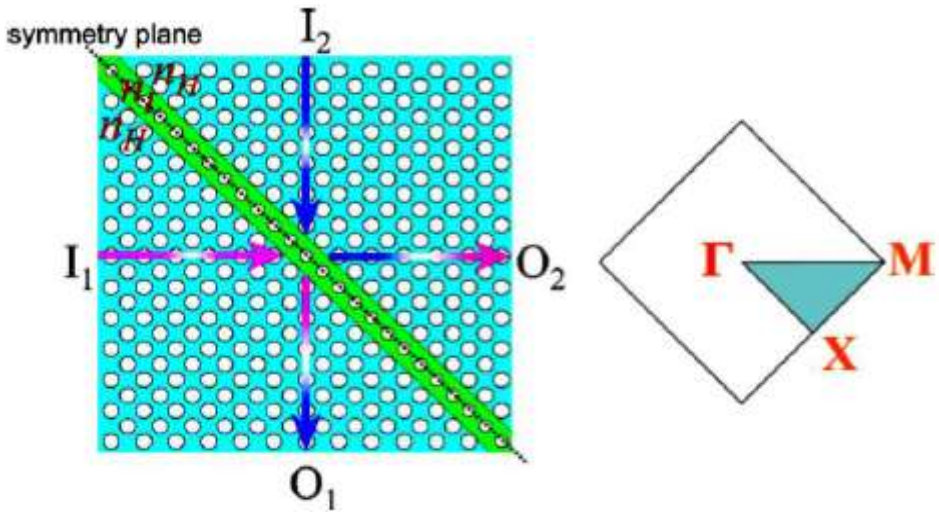

Figure 2-25: OR gate based on self-collimation phenomenon [62].

Assuming that the light beam $E_1=uE^{-j\varphi 1}$ is entered in the part I_2 and the light beam $E_2=uE^{-j\varphi 2}$ in the inlet part I_2, E represents a flat wave, and "u" is a similar periodic operator of the PC structure. It is observed that there is only one phase difference between the beams. As a result, the reflected and transmitted rays are expressed as follows:

$$T_{I_1}=E_1 te^{i\varphi}=\frac{uEe^{-i(\varphi_1-\varphi)}}{\sqrt{2}} \quad (2.25)$$

$$T_{I_2}=E_2 te^{i(\varphi+\frac{\pi}{2})}=\frac{uEe^{-i(\varphi_1-\varphi\frac{\pi}{2})}}{\sqrt{2}} \quad (2.26)$$

The output is written based on the linear relationship between the transmitted and reflected beams.

$$O_1=T_{I_2}+R_{I_2}=\frac{uEe^{-i(\varphi_1-\varphi)}}{\sqrt{2}}+\frac{uEe^{-i(\varphi_1-\varphi\frac{\pi}{2})}}{\sqrt{2}}=\sqrt{2}uE\cos(-\frac{\varphi_1-\varphi_2}{2}+\frac{\pi}{2})e^{-i(\frac{\varphi_1-\varphi_2}{2}-\varphi-\frac{\pi}{4})} \quad (2.27)$$

$$O_1 = T_{I_2} + R_{I_2} = \frac{uEe^{-i(\varphi_1 - \varphi\frac{\pi}{2})}}{\sqrt{2}} + \frac{uEe^{-i(\varphi_1 - \varphi)}}{\sqrt{2}} = \sqrt{2}uE\cos(-\frac{\varphi_1 - \varphi_2}{2} + \frac{\pi}{2})e^{-i(\frac{\varphi_1 - \varphi_2}{2} - \varphi - \frac{\pi}{4})} \quad (2.28)$$

So I_{0_1} and I_{0_2} can be written as follows:

$$I_{0_2} = \left|0_2\right|^2 = \sqrt{2}\left|uE\right|^2 \cos^2(-\frac{\varphi_1 - \varphi_2}{2} + \frac{\pi}{4}) = \left|uE\right|^2 (1 + \mathrm{Sin}(\varphi_1 - \varphi_2) \quad (2.29)$$

According to the formulas above, by applying a 90-degree phase difference between the input beams, one can simulate the OR's logic performance in the O_1 output. The reported contrast ratio for this structure is 20 db, and the proposed structure is suitable for photonic integrated circuits.

In 2016, a plan was made to implement logic gates, including the OR gate, Goudarzi et al [63]. According to **Figure 2-26**, point and linear logic gates are created in a square lattice of silicon rods with a radius of 0.25a in the air. When the phase difference between the two light beams is $\pm\pi/2$, then the light beams interfere destructively or constructively. According to **Equation 2-30**, a rod with the same radius and different refractive oblique is used to create this phase difference between the incoming light beams at input port A.

$$\Delta\varphi = 2\pi/\lambda_0 \times 2r \quad (2.30)$$

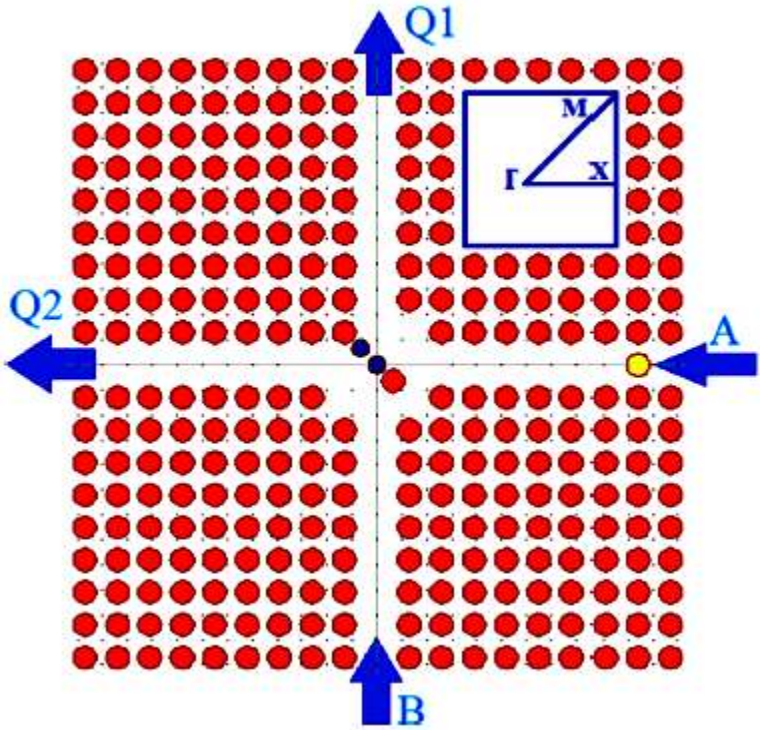

Figure 2-26: OR gate based on linear and point defects. The yellow bar is used to create a 63 ° phase difference between the incoming beams [63].

The simulation results show that the device can act as an XOR and an OR logic gate. It is applicable in the frequency range of 0-0.45 (a/λ). However, for low dispersion conditions, it would be set at (a/λ =) 0.419; correspondingly, the lambda is equal to 1.55 um. The maximum delay time to respond to the input signals is about 0.4 ps; hence the device's speed is about 2.5 THz. Also, 6.767 dB is the maximum contrast ratio of the device., Goudarzi et al (2016) [63].

The structure is simple, so it is suitable for digital optical integrated circuits. Younis et al (2014) [64] presented an OR gate structure based on linear defect and cyclic cavity, as illustrated in **Figure 2-27**. The proposed scheme consists of two linear defects, two ring resonators, and one Y-waveguide.

The ring resonator causes the signal to reach from the input port to the output port. Geometric parameters of the structure are optimized for achieving maximum transfer in the output. For this purpose, half of the original structure is used. The amount of transmitted power can be improved by adding a bend and creating a distance of ξ. **Figure 2-28** shows the computational transmitted power in structures A, C, and D (in the range of ξ) in the values of 3a, 5a, and 6a, respectively. As it can be seen, to reach the maximum transmitted power, ξ is three times the considered lattice constant.

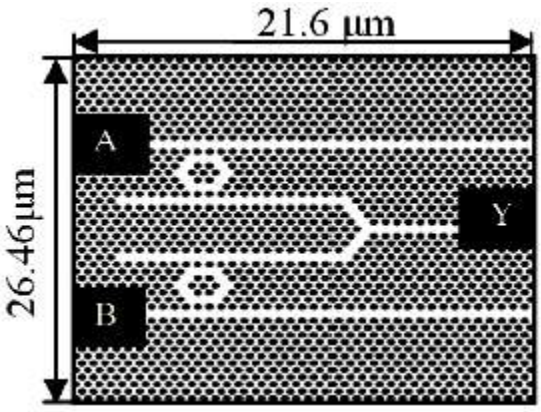

Figure 2-27: OR gate based on linear defect and ring resonator [64].

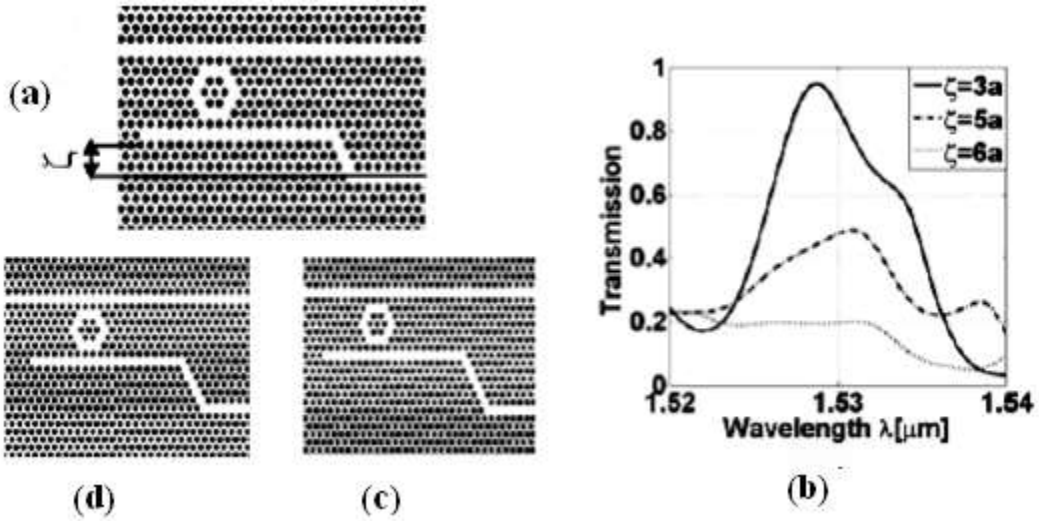

Figure 2-28: Computational transmitted power versus changes of ξ [64].

The bit rate of the design provided is $0.5^{Tbit/s}$, and the structural error tolerance is $\pm 10\%$ for the radius of the center rod Younis et al (2014) [64].

2-8-3- "NOT" Gate

The NOT gate acts as a switch and its logic function is as follows:

NOT 1 = 0

NOT 0 = 1

In Jiang et al (2011) [65] a NOT gate was provided using PCRR without the use of any nonlinear material. The design includes a square lattice of silicon and air, in which the radius of rods is 0.1a, and the lattice constant of the structure is 910 nm. The wavelength of the input and probe signals is the same, and by PCRR optimization, the efficiency is about 90%, and the factor quality obtained at 1550 nm is 840.

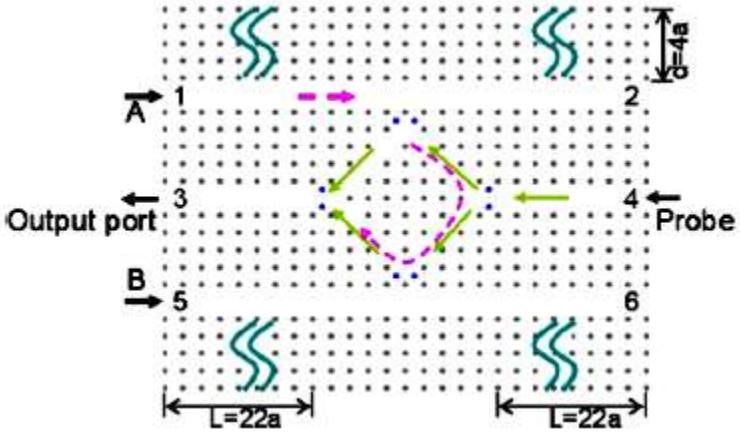

Figure 2.29: Ring resonator-based gate [65].

Based on **Figure 2-29**, this structure's performance is based on the fact that when the probe signal is applied to the structure, light exits ports 1, 3, and 5 and the probe signal interferes with the other signals and is transmitted to the output improved this structure based on the perturbation theory and the interference rule of signals. They chose the radius of 0.185a for the silicon rods Jiang et al (2011) [65].

In 2012 Noshad et al [66] a plan was presented to implement three logic gates, including the NOT gate based on photonic crystal cross waveguides, resonant cavity, and nonlinear Kerr effect. **Figure 2-30** shows a schematic of the proposed structure consisting of a square lattice. The material used to make nonlinear rods is AlGaAs. The logic performance is based on the resonant frequency shift caused by the nonlinear Kerr effect. **Figure 2.31** shows the NOT gate frequency shift.

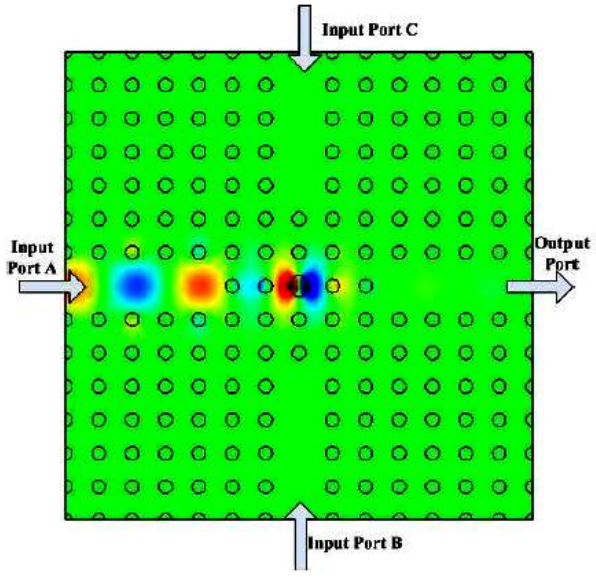

Figure 2-30: NOT Gate based on resonant cavities and nonlinear Kerr effect [66].

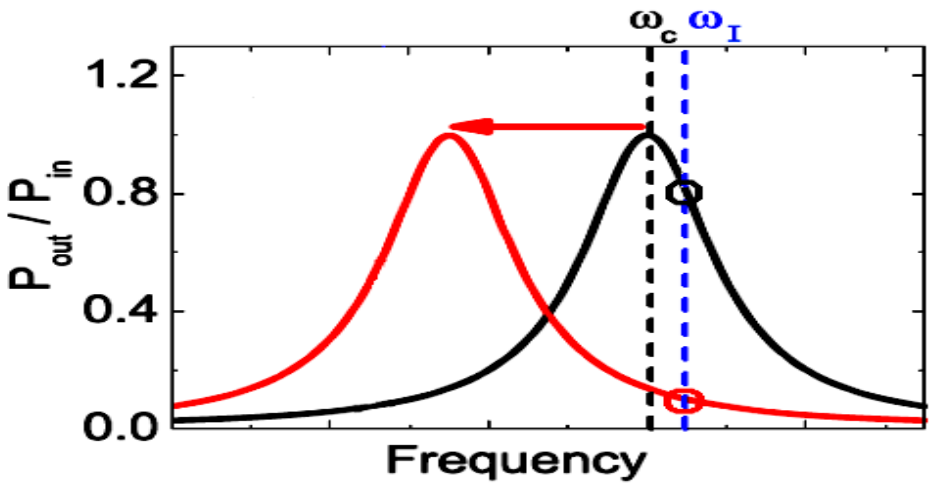

Figure 2-31: Frequency shift of a cavity due to non-linear Kerr phenomena [66].

The highlighted characteristics of these gates, as compared to the other designs, are their rapid changeover status as well as the simple and dense structure of these gates Noshad et al (2012) [66].

2-8-4- "XOR" Gate

XOR gate performs the comparison of data patterns for address recognition as well as switching, encryption, and decryption of packets. The XOR gate is capable of performing the following logic operations:

0 XOR 0 = 0

0 XOR 1 = 1

1 XOR 0 = 1

1 XOR 1 = 0

Lee et al (2008) [67] Introduced an XOR logic gate with a frequency range of 3/4445-3/0051(a/λ) based on a two-dimensional cylindrical photonic crystal triangular lattice which consisted of silicon rods in the air. This gate is given in **Figure2-32**. The structure comprises an asymmetric Y-waveguide where the light beams affect each other after being injected into the interference region of length L and width W. The dielectric constant and radius of silicon rods are 0.25a and 11.56, respectively. The Y-shaped asymmetric linear defect waveguide is used to shift the phase between the two inputs and allow the logic operations of constructive and destructive interference.

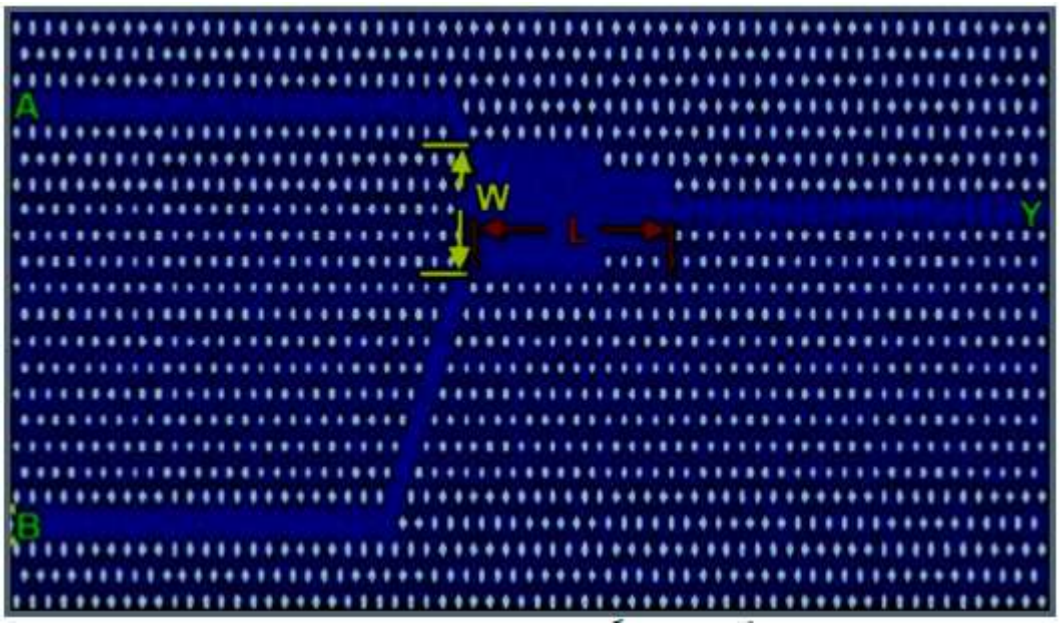

Figure 2-32: Interference-Based XOR Gate [67].

By examining the power curve transmitted to the output according to the interference region's length and width,, to transfer the optimum power to the output, the interference length (L) of 13a and the waveguide width (W) of 5a are selected. A contrast ratio of 7 dB has been reported.

Tang et al (2014) [68] presented a multi-modal interference-based design to simulate the XOR gate. The proposed structure consists of silicon rods in the silica substrate. The refraction coefficients of Si and SiO_2 are 2.4 and 1.45, respectively, and the radius of dielectric rods is 0.2a, shown in **Figure. 2-33**.

As mentioned earlier, multimodal interference-based schemes use directional mode interference in the MMI segment. In this scheme, waveguides of different lengths are used to create the phase difference between the incoming beams. **Figures 2-34** and **2-35** show the photonic crystal triangular lattice dispersion diagram after removing one and three rows of rods, respectively. According to **Figure 2-34,** the waveguide supports the normalized frequency of 0.275. Using **Equation (2-19),** in which the normalized frequency as (β) and MA as the path difference of the two input waveguides and the lattice constant of the structure are defined, MA = 2A is selected to create a 270^0 phase difference between the input beams.

$$\beta ma = \frac{(2n+1)}{2}\pi \qquad (2.31)$$

The MMI area's interference length is defined according to **Equation 2-32**, where the β_0 and β_1 are propagation constants of the base mode and the first order mode, respectively. Using the above equation and the normalized frequency of 0.257, the MMI area's length is chosen 2a.

$$L_X = \frac{\mu}{\beta_0 - \beta_1} \qquad (2.32)$$

to have the best contrast ratio of the radiuses, the r_1 has been optimized relative to the reported contrast ratio of 21db. Multi-modal interference-based gates not only have a simple structure and small size but also have low power consumption to avoid non-linear effects Tang et al (2014) [68].

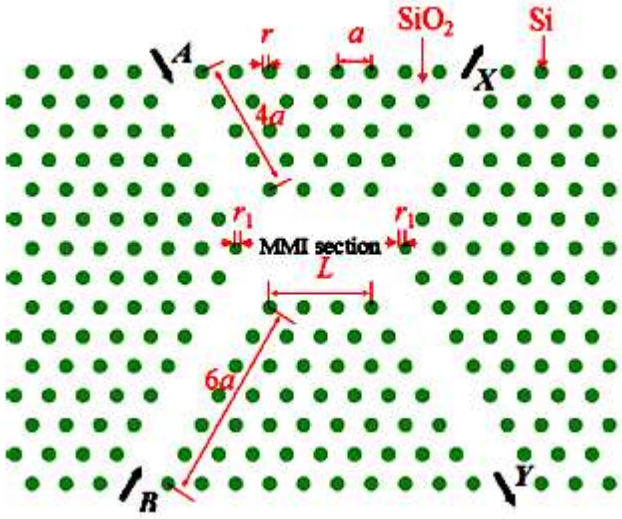

Figure 2-33: Interference-based XOR gate [68].

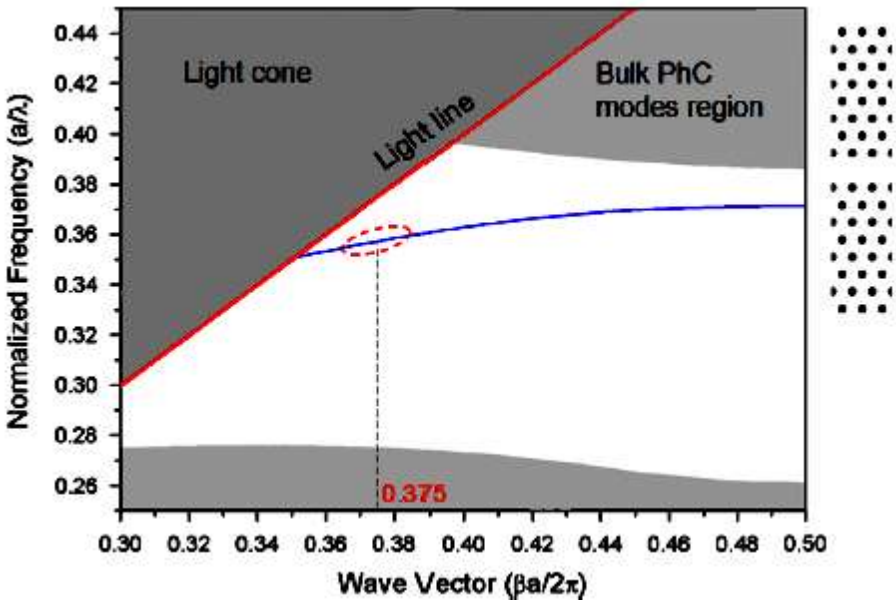

Figure 2-34: Lattice dispersion after removing a row of rods [68].

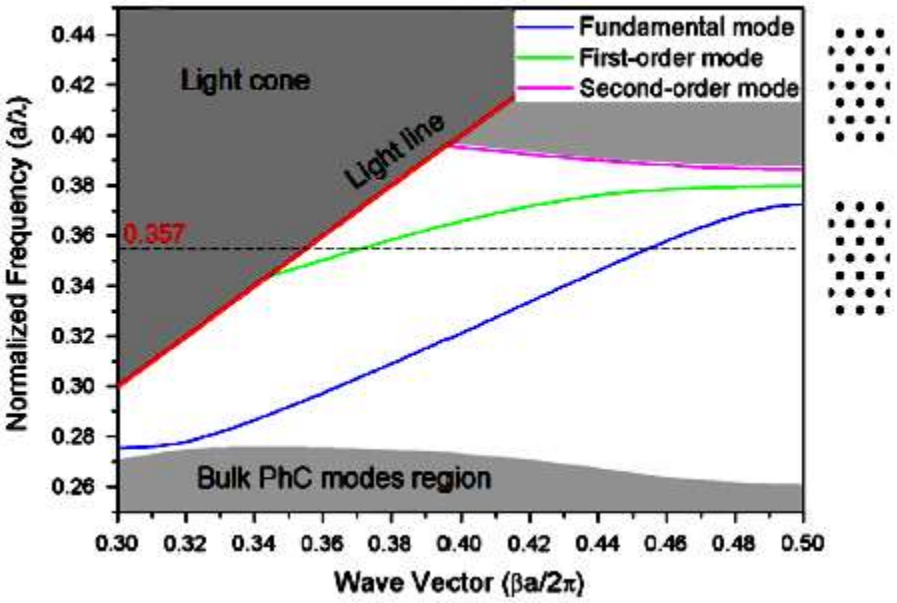

Figure 2-35: Lattice dispersion after removing three rows of rods [68].

2-8-5- "NAND" Gate

Kabillan et al (2009) [69] presented a plan to realize the NAND gate. The structure consists of silicon rods in the air substrate. The rods' radius and dielectric constant are 0.25 a (lattice constant of structure) and 12, respectively. A linear defect was created by reducing the radius of 25 rods in the direction ΓX of 0.274α) to use the self-collimation phenomenon. The self-collimation phenomenon occurs for optical waves with TE polarization.

According to **Figure 2-36**, to create the NAND performance, I_1I_2 from the left of I_3, which is considered the reference signal, is applied to the structure from. The results show that when $\varphi_1-\varphi_3=\frac{\pi}{2},\frac{I_1}{2}=\frac{I_2}{2}=I_3$ then the structure can act as a NAND gate.

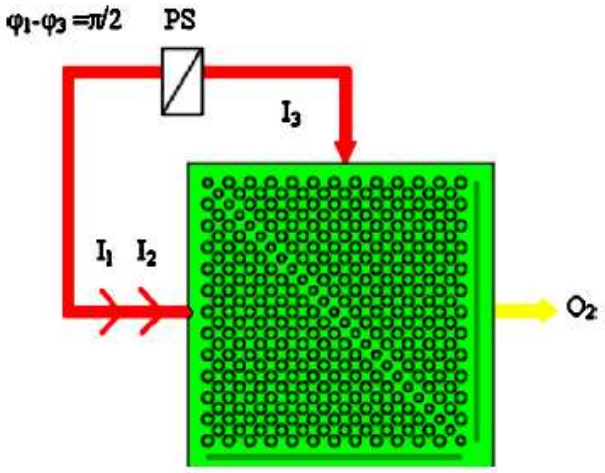

Figure 2-36: NAND gate based on self-collimation phenomena [69].

Bao et al (2014) [70] Developed a NAND gate using a square lattice of air rods in the silica substrate. As shown in **Figure 2-37**, the proposed structure is composed of ring resonators and cross waveguides without the use of nonlinear effects. Because of the coupling effect, existing light in two vertical waveguides interferes with the BUS waveguide (CD waveguide). To achieve the best coupling, the distance between the vertical waveguide and the bus as well as the vertical waveguide length H is optimized. Compared to nonlinear structures, the proposed design has less power consumption. This structure can be used in optical logic integrated circuits and large-scale integrated circuits.

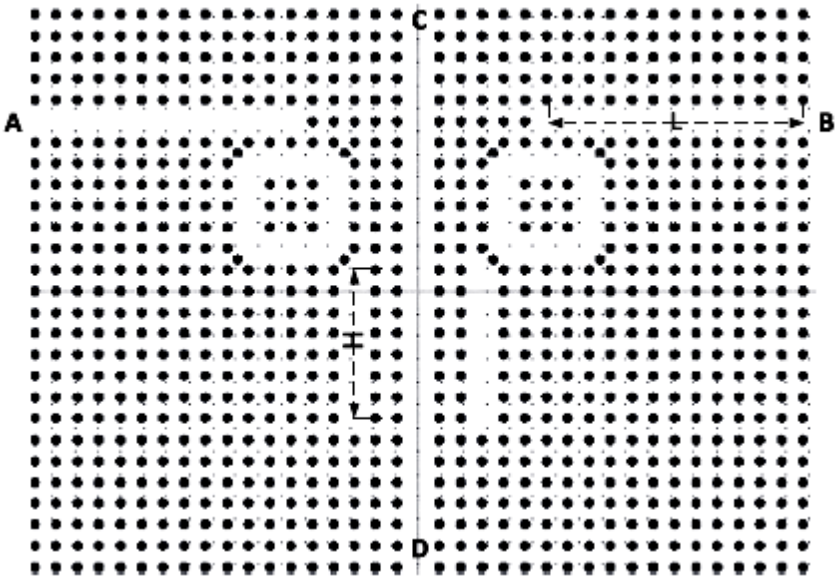

Figure 2-37: NAND gate based on coupling and ring resonators [70].

2-8-6- "NOR" Gate

Alipour-Banaei et al (2014) [71], 21×21 Square lattice of glass rods in the air were considered for the design of NOR and NAND gates using PCRR. The rods' radius, the lattice constant of structure, and the refractive oblique of rods are 0.215a, 620 nm, and 2.1, respectively. The provided lattice supports the TM modes with a frequency of $0.3 < (a/\lambda) < 0.42$. The rods' nonlinear coefficients and the PCRR resonance wavelength are $n_2=9*10^{-17}$ m^2/w and $\lambda = 1.55\mu m$, respectively. PCRR behavior can be controlled by injecting a high-power input light beam into the structure and utilizing the nonlinear Kerr effect. The optical behavior of PCRR is shown in **Figure 2-38** for different input power intensities. As a result, the injective threshold power for creating the Kerr effect is $2kW/\mu m^2$.

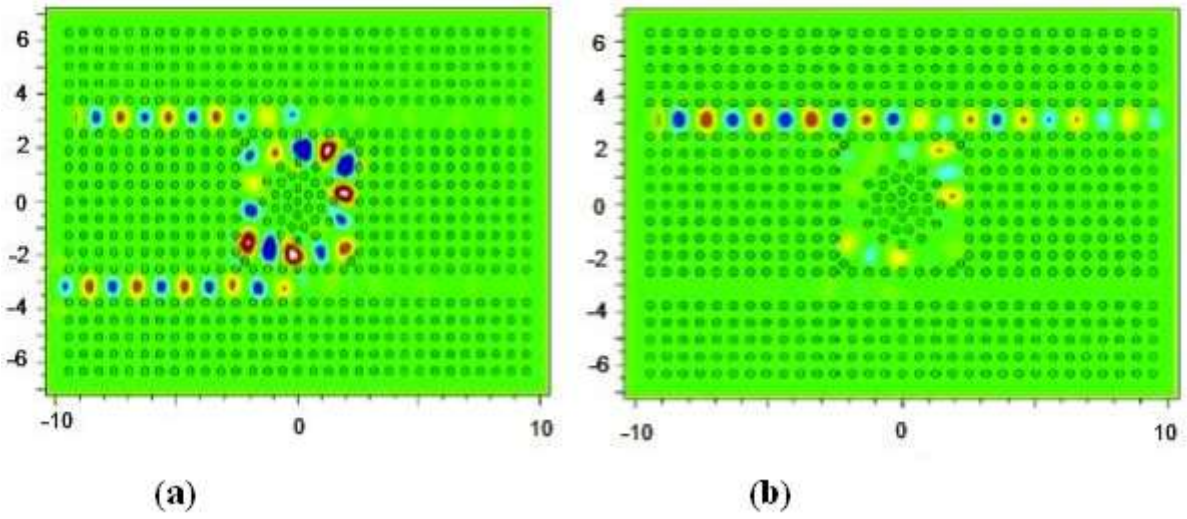

Figure 2-38: PCRR field distribution: a) input radiation intensity 1 kw/mm^2 and b) input radiation intensity 2kW/mm^2 [71].

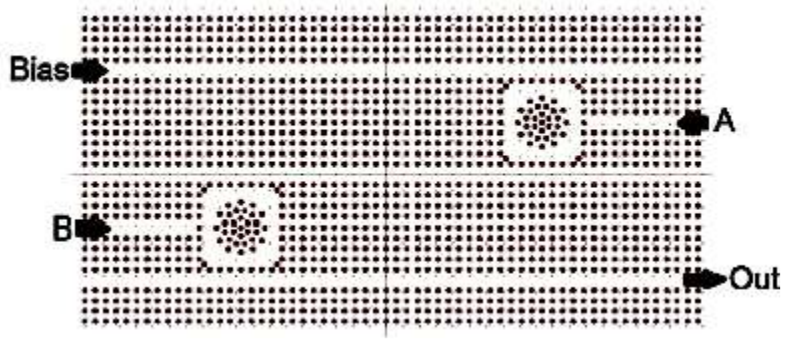

Figure 2-39: Resonator-based NOR gate [71].

The NOR gate's proposed structure is shown in **Figure 2-39** according to the above explanations and using PCRR. In this structure, the resonance rings are designed so that the resonance wavelength at low input power intensities is 1550 nm Alipour-Banaei et al (2014) [71].

2-8-7- "XNOR" gate

Xavier et al (2012) [72] all-optical logic gates, including the XNOR gate, were introduced with the size of $10\mu m \times 10\mu m$ and contrast ratio of 6db.

In this design, a self-collimation phenomenon occurs in the direction of ΓX with a frequency of 0. 194(a/λ) for the light polarized. Silicon rods with a radius of 105nm have been used, and the lattice constant of the structure is 202nm. According to **Figure 2-40**, two linear defects have been created by reducing the radius of 15 rods in the direction of ΓX up to 83 nm to use the self- collimation beams in the design of logic gates. I_1 and I_2 are Gaussian input signals with TM and I polarization of the reference optical signal. The wavelength of the input and reference signals is also 1550 nm. The reported results show that the power of transmitted and reflected beams is identical, and the phase difference is π/2. The simulations performed by the

FDTD method show that the structure acting as the XNOR gate has a contrast ratio of 5.2db Xavier et al (2012) [72].

As pointed in the study of structures, the photonic crystal-based gates have been designed and simulated using various methods. Each of these methods has particular advantages and disadvantages. The study of these structures shows that some problems should be eliminated in the design of photonic crystal-based logic gates. One problem is the unwanted emission of the backlight. When only one of the inputs is applied to the structure, the equal frequency for the different input signals simplifies the integration process. Structures with different input frequencies can usually be used as the switch. Some of the structures are strongly dependent on the input phase difference.

One of the interesting confinement mechanisms of the light guiding in the photonic crystals is the self-collimation effect. It exploits the spatial dispersion properties of Bloch waves in PhCs to achieve the electromagnetic wave without diffraction and retaining spatial width confinement without line defect waveguide or nonlinearities. The shape of the PhC dispersion surface is the essential feature for determining the self-collimation and can be optimized and manipulated. For instance, by lattice symmetry, material parameters and the constituents' geometry shape logic gates based on the self-collimation phenomenon are independent of the incoming radiation intensity. In fact, in these designs, the self-collimation phenomenon provides the wide frequency range and does not depend on the radiation beams' divergence. Despite these benefits, some structures require a particular volume scale to implement gates based on this effect, and these cause limitations in reducing the size. Also, the wavelength difference in some structures can affect the use of these structures for optical integrated circuits Xavier et al (2013) [73].

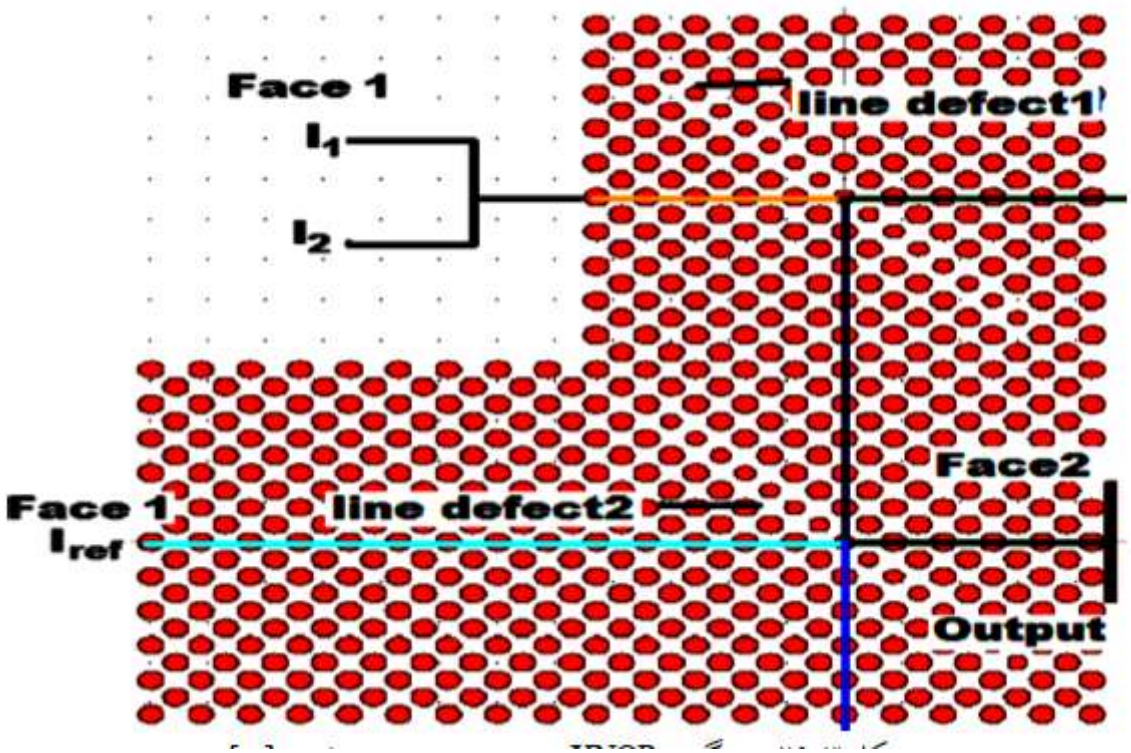

Figure 2-40: Self-collimation phenomenon-based gate [72].

2-9- Photonic crystal fiber-based gas sensors

Photonic crystal fibers are new structures of optical waveguides that contain an array of air cavities along the fiber length. A small defect in these structures provides an optical path in which the optical spectrum can be propagated at a specific frequency. As a result, it forms a photonic crystal fiber that contains an array of air cavities along the length of the fiber (which also acted as the shell) and a defect in the periodic structure (which plays as the fiber core shown in **Figure 2-41**, Ramamoorthy et al (2003)- Bridge et al (1979) [74]-[75].

These fibers have a new capability to enhance the interaction of light and gas or liquid within the cavities through the damping field. These fibers are used in a variety of applications, including sensor design Healey et al (1997) [76]. In photonic crystal fiber-based gas sensors, the use of parameters such as cavity diameter and lattice constant give rise to significant properties, including single-mode, loss, and relative sensitivity. In fact, these design parameters can provide more flexibility in improving sensor properties such as loss and relative sensitivity Hoo et al (2003) [77].

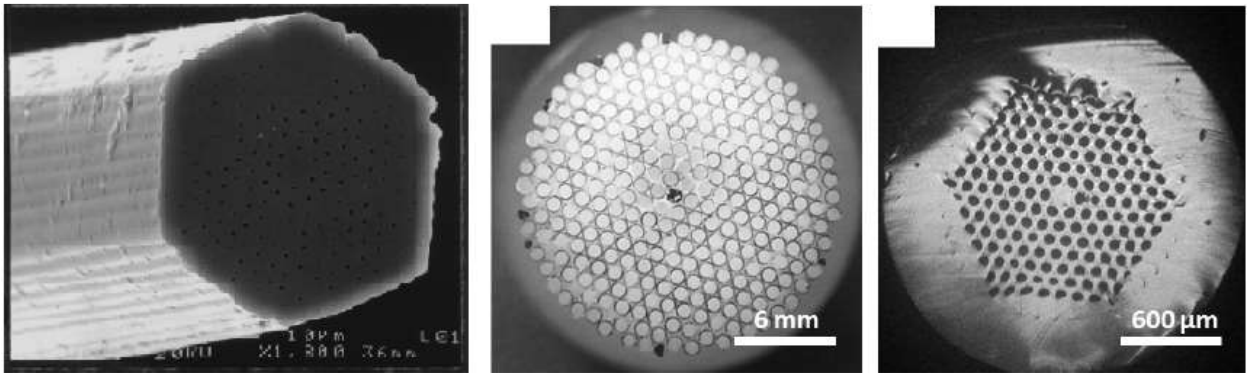

Figure 2-41: Some examples of the tested structures of photonic crystal fibers [74].

2-10- Photonic crystal waveguide-based gas sensor

Photonic crystal waveguide-based gas sensor acts based on the interactions between light and gas Hoo et al (2003) [77], especially when the refractive index in the photonic crystal changes due to a change in gas. The photonic crystal's defect allows the light to be controlled and directed, resulting in creating a waveguide or cavity.

The characteristic of these structures is their periodic change of refractive index. Suppose this alternation is in one-dimensional photonic crystals. In that case, the crystals formed are called one-dimensional photonic crystals; if the alternation is in two- and three-dimensional structures, it will produce two- and three-dimensional photonic crystals. For the first time, in 1987, two- and three-dimensional structures were employed by Yablonovitch [15]. But due to the lack of technology and proper manufacturing methods, mass production of photonic

crystals was delayed up until 1997. After that, the design and modeling of gas sensors were began based on photonic crystals.

According to Hoo et al (2003) [77], the photonic crystal waveguide-based gas sensor is suggested. Gas sensing is introduced based on the interaction between the states of light and gas. The photonic crystal waveguide change increases due to the gas changes, and the slow light in the photonic crystal waveguide is also affected by its wavelength changes. **Figure 2-42** shows a schematic diagram of the photonic crystal waveguide-based sensor, in which "a" becomes the lattice constant and "r" is the radius of the holes.

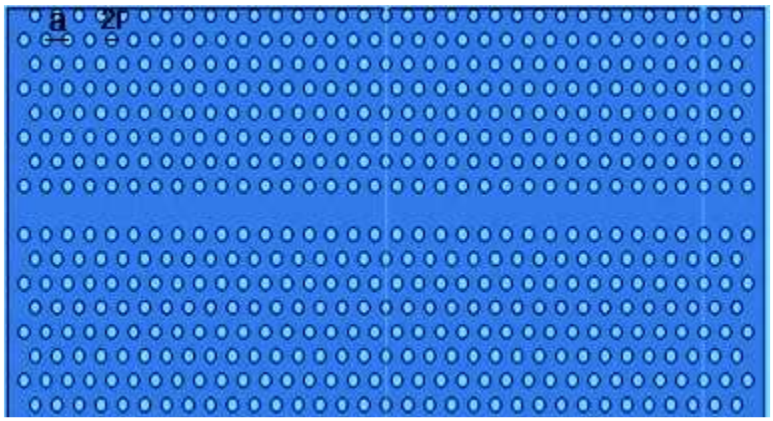

Figure 2-42: A schematic diagram of the photonic crystal waveguide-based gas sensor [77].

Figure 2-43 shows a comparison of the outline for the photonic crystal waveguide-based helium gas sensor (refractive index (n) = 1.000035) or air (refractive index (n) = 1.000292) as the reference gas. As presented in the figure, the sensor reacts with helium gas and its wavelength changes relative to air (0.6nm). The central wavelength variation of the spectrum is the basis of sensing in gas sensors.

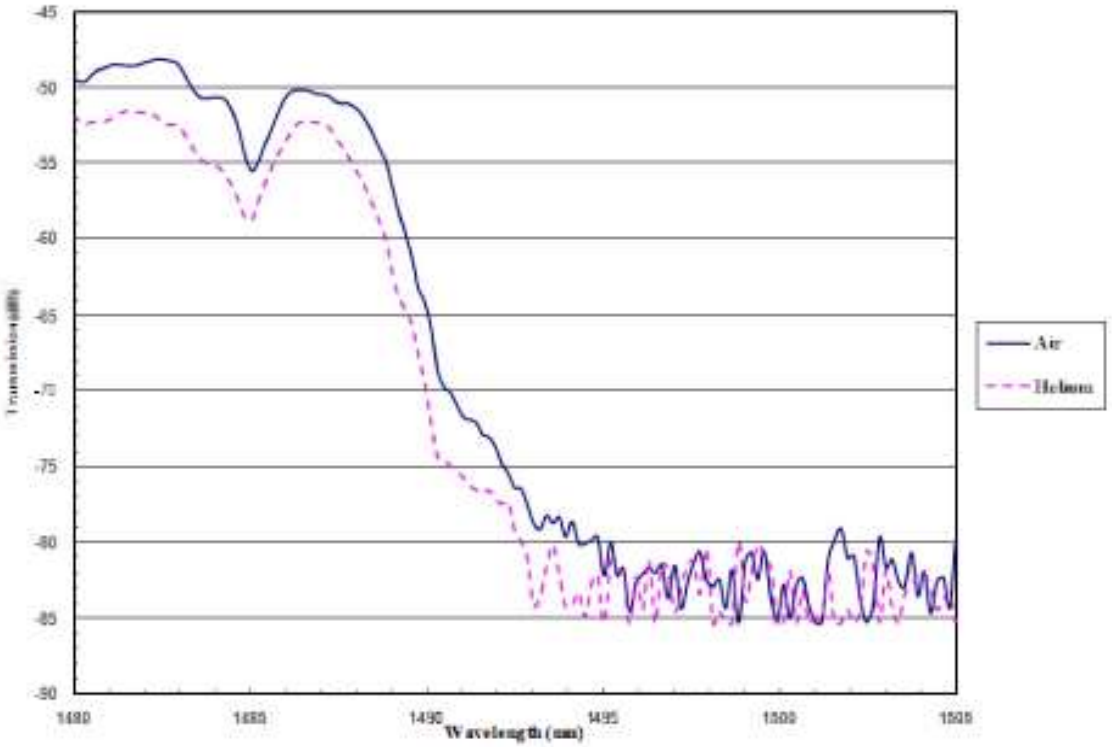

Figure 2-43: Transmission spectrum versus wavelength for helium and air with a = 441nm and r = 0.33a [77].

Figure 2-44 is a comparison between the transition spectrum of argon gas (refractive index (n) = 1.000282) and air (refractive index (n) = 1.000282). According to this graph, the wavelength change between air and argon is about 0.05 nm.

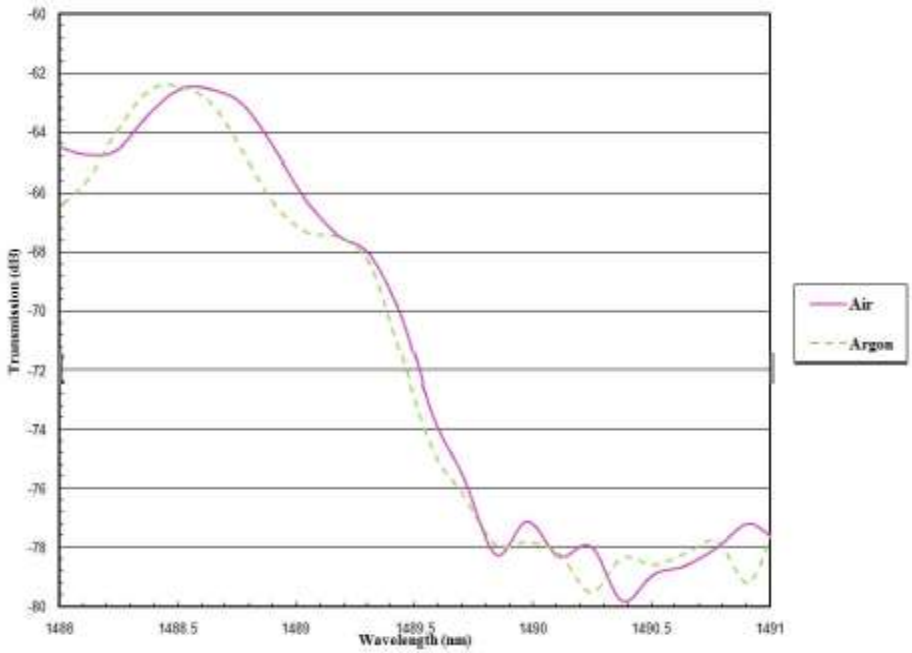

Figure 2-44: Transmission spectrum versus wavelength for argon and air with a = 441nm and r = 0.33a [77].

As noted in the reference Haxha et al (2008) [78], the gas sensor is based on a gap in the photonic crystal waveguide that its substrate uses (silicon-on-insulator) SOI. Using this technology, it will be possible to fabricate photonic crystal blades in the form of air cavities as well as dielectric rods inside the background material.

Figure 2-45 shows the sensor's structure based on the gap in the photonic crystal waveguide. In this figure, by removing a row of air cavities and replacing a narrow gap, the test gas can penetrate the holes through that gap. In this sensor, the location of the first and second rows of air cavities is changed to improve the light properties of the photonic crystal waveguide. In this structure, "a" is lattice constant, r is the radius of the holes, w is the gap width, and h is the gap thickness.

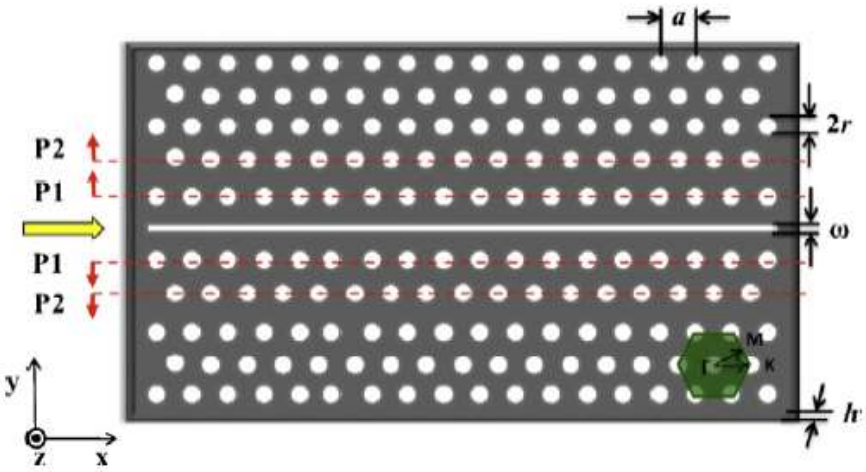

Figure 2-45: the structure of the sensor based on the gap in the photonic crystal waveguide [78].

In the gas sensor structure based on the gap in photonic crystal waveguides, there are parameters such as the diameter of the holes in the structure, waveguide diameter, inlet and outlet width of the waveguide, etc. Using these parameters optimize the structure [78]. **Figure 2-46** shows the optimized sensor structure along with the transmission spectrum. The sensitivity of the sensor (a = 413. 9nm, r = 0 .5a, s = 2. 9a, w = 4. 9a) can be increased 1260 times as the light speed decreases in the gap of the photonic crystal waveguide.

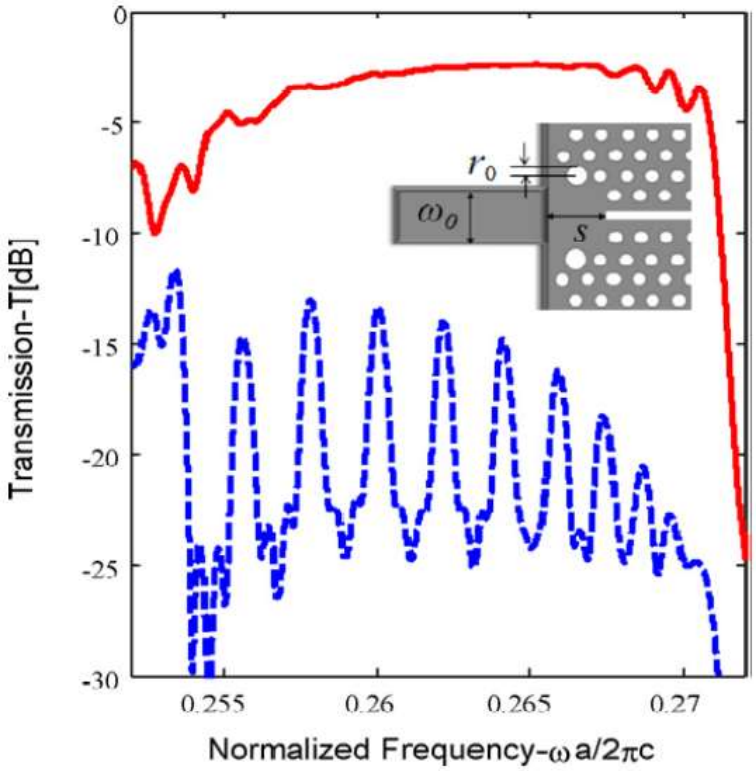

Figure 2-46: optimized sensor structure along with the transmission spectrum [78].

2-11- Photonic crystal fibers-based gas sensor

Photonic crystal fibers were used practically as low-loss waveguides in early 1996. Their initial manufacturing took four years due to the lack of technology needed. Nowadays, with the increasing development of manufacturing techniques, it is possible to produce these micro-structures with high-precision from air glass precisely. This development enables the control of optical properties in the alternating structure of the photonic crystal fiber coating Wu et al (2017) [79].
In 1997, D-shaped fiber' efforts were aimed at detecting gas through the attenuating field, but very low sensitivity of about 0.1% to 0.2%. Afterward, Mönor et al (1999) performed experiments to detect gas from photonic crystal fiber. They predicted that sensitivity could be obtained without significant optical fiber properties loss by changing the photonic crystal fiber parameters [80].

In 2003, gas detection was carried out through a damping field with silica-air micro-structure fiber, which its detection sensitivity was 5.5% Knight (2003) [81]. The design and modeling of a photonic crystal fiber-based gas sensor were developed to improve the relative sensitivity and loss-of-confinement. In this design, air cavities of different sizes and different lattice constants were used simultaneously to obtain high sensitivity and low confinement loss.

The photonic crystal fiber sensitivity is a function of the wavelength, which has a relative sensitivity of 12.6% for acetylene gas and 14.9% for methane gas, which is 50 times the sensitivity of D-shaped optical fiber Zhi-guo et al (2008) [82].

Since then, extensive researches have been done to improve the relative sensitivity and confinement loss. One of the works done to improve the relative sensitivity and confinement loss is to reduce the network constant for increasing the relative sensitivity. Also, different air cavities and lattice constants can be used to obtain high sensitivity and low limitation loss simultaneously Olyaee and Naraghi (2013), Olyaee et al (2014), Park et al (2011) [83-85].

For increasing the relative sensitivity, the lattice constant can be reduced. Because as the lattice constant increases, the air filling fraction in the crust increases, which means that the total power fraction inside the holes increases. Also, with increasing the wavelength, the relative sensitivity increases because the power of light penetrating the crust cavities increases. On the other hand, the smaller the central cavity's diameter, the lower the confinement losses because the core index is more different from the crust index, and the greater light power is limited in the core region Olyaee and Naraghi (2013), Olyaee et al (2014), Park et al (2011) [83-85].

Additionally, by increasing the outer cavities' diameter, the confinement loss decreases because when the mode is released into the core, leakage of the modes from the core to the outer air cavity area is inevitable due to the limited air layers. Therefore, to prevent this leakage, the outer ring cavities diameter would be increased Olyaee and Naraghi (2013), Olyaee et al (2014), Park et al (2011) [83-85].

Other methods of achieving high relative sensitivity and low confinement loss are to insert a ring of germanium oxide around the nucleus. In fact, high sensitivity and low confinement loss can be achieved by changing the ring of germanium oxide around the nucleus Ranka et al (2000) [86].

In the reference [82] Zhi-guo et al (2008), a photonic crystal fiber-based gas sensor has been proposed, and in this method, the gas sensing using PCF with air-core finite element method (FEM) is investigated, and by optimizing the central cavity diameter, the diameter of coverage cavity and lattice constant can increase relative sensitivity above 50%. **Figure 2-47** shows a quarter of the structure of photonic crystal fiber-based gas sensor with the variables of lattice constant Λ, the diameter of the crust holes d, the center hole diameter d_1, and the refractive index of the context n_1 and air cavities n_2.

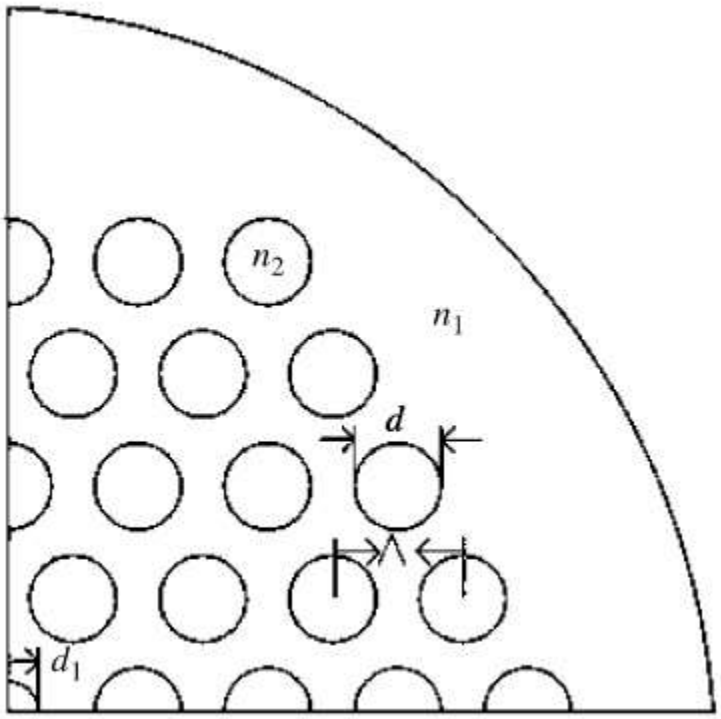

Figure 2-47: Cross-section of photonic crystal fiber with air core [82].

Here, relative sensitivity is measured by the effective refractive index of n_1.

In this study, first the relationship between the gas sensing sensitivity of the index-guided PCF with air-core and fiber parameters would be analyzed numerically, as well as the operating wavelength. The results are shown in **Figures 2-48(a)** and **2-48(b)** by the relationship curves. In **Figure 2-48(a)**, the curves present the relationship between the relative sensitivity f and wavelength l while the diameter of the air-core d1 equals 0.6, 0.8, 1.0 and 1.2 mm, respectively, with d ¼ 1.4 mm, L 2.3 mm, and n1 1.5 mm. And **Figure 2-48(b)**, the curves present the relationship between the relative sensitivity f and the refractive index n1 while the diameter of the air-core d1 equals 0.6, 0.8, 1.0 and 1.2 mm, respectively, with d ¼ 1.4 mm, L ¼ 2.3 mm and l ¼ 1.6 mm Zhi-guo et al (2008) [82].

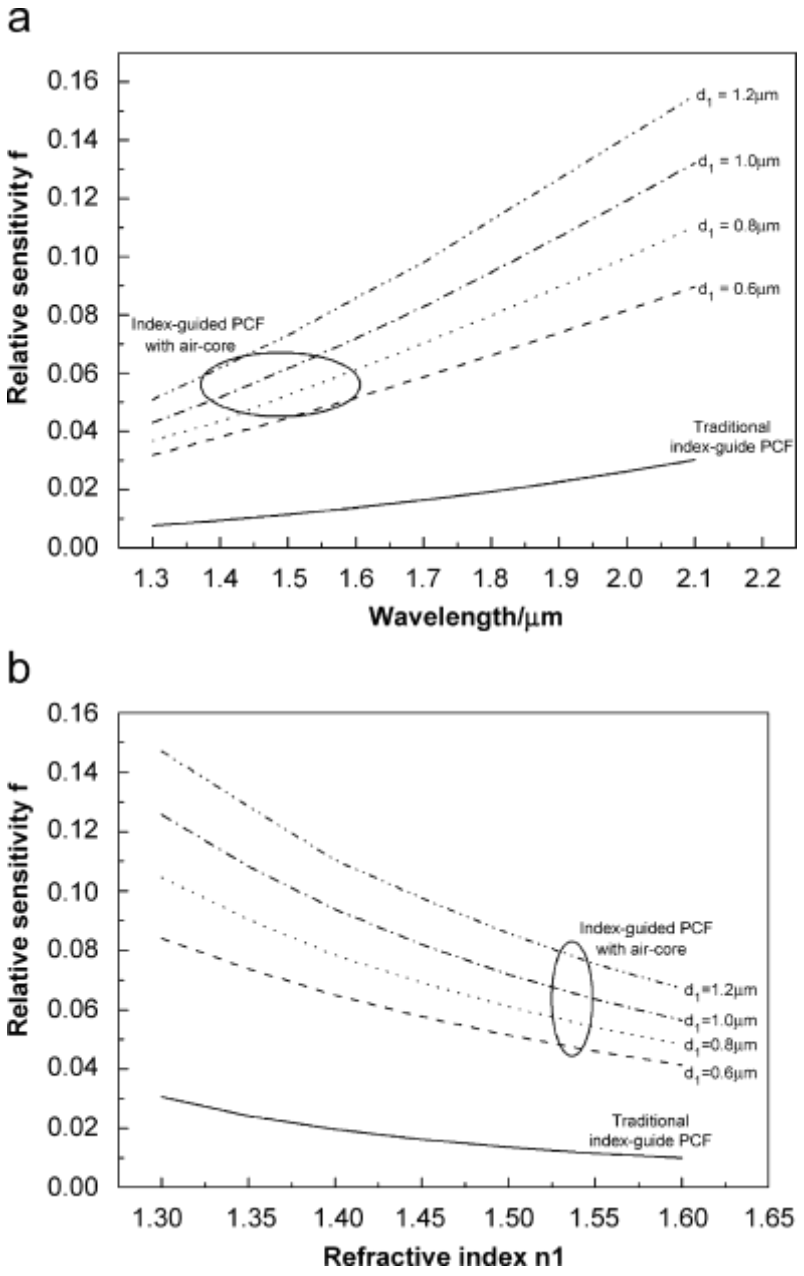

Figure 2-48: (a) Relative sensitivity f versus wavelength l. Here, L ¼ 2.3 mm, d ¼ 1.4 mm and n1 ¼ 1.5; (b) relative sensitivity f versus refractive index n1. Here, L ¼ 2.3 mm, d ¼ 1.4 mm and l ¼ 1.6 mm [82].

As shown in **Figure 2-49 (a)**. In this case, PCFs (Photonic Crystal Fyber), the larger central hole diameter dc, showed the higher evanescent field fraction; nevertheless, it should be less than cladding hole diameter d, to satisfy the effective index guiding criterion. Despite the improved evanescent interaction, the prior PCFs with a larger dc, suffered from an excessive confinement loss, which raised a critical trade-off between the sensitivity and the confinement loss in PCF design for sensing applications. In order to cope with ever increasing demands for chemical- and bio-sensing PCF devices, there exist compelling needs to develop a novel waveguide structure to overcome this critical trade-off in prior PCFs Park et al (2011) [85].

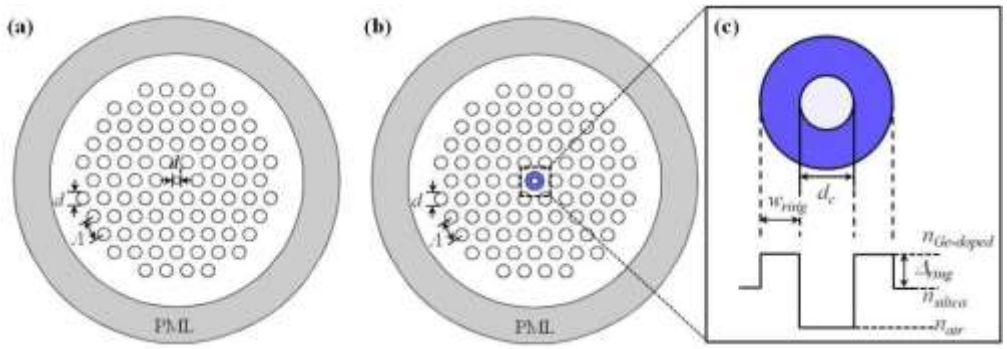

Figure 2-49: (a) prior PCF with a central air-hole defect with the diameter *dc*, (b) proposed PCF with a hollow high index ring defect, and (c) its enlarged view with structural parameters: central hole diameter *dc*, ring width *wring,* and the relative index difference of the ring $\Delta ring$. PML is perfect matched layer used in numerical analysis. The cladding air holes are characterized by their diameter, *d*, and pitch, Λ. 5 layers of air holes are assumed here [85].

In this study, a new index-guided PCF for chemical sensing applications would be proposed with a hollow GeO_2-doped high index ring defect to simultaneously achieve a higher evanescent wave interaction efficiency, a lower confinement loss, and a lower splicing loss than prior PCFs, for the first time to the best knowledge of the authors. The schematic structure of the proposed PCF is shown in **Figure 2-49**(b), where the hollow high index ring defect at the center is depicted along with its structural parameters in **Figure 2-49(c).** In addition to the central hole diameter d_c, the proposed defect provides two additional waveguide parameters as indicated in **Figure 2-49**(c): the thickness W_{ring} and relative index difference Δ_{ring}, of doped ring, which can endow a new degree of freedom in waveguide design. The defect is adopted from the hollow optical fiber, which has a high index GeO_2 doped silica ring core and has been successfully implemented in index guiding PCFs for dispersion and polarization control.

In the proposed PCF, Δring was varied from 0.4 to 2.0%, and its effects over the confinement loss and relative sensitivity were analyzed in **Figure 2-50(a)** and **(b)**, respectively. Here we fixed other parameters; Λ = 2.3μm, d = 1.4μm for the cladding, and dc = 1.2μm, and wring = 0.6 μm for the hollow ring defect. Higher Δring could reduce the confinement loss by orders of magnitude to achieve a low confinement loss less than 8.1dB/m in the whole operating wavelength range for Δring = 2.0%. At the wavelength of λ = 1.5μm, the confinement loss of the proposed PCF was 0.023dB/m, while that of the prior PCF was as large as 32dB/m Park et al (2011) [85].

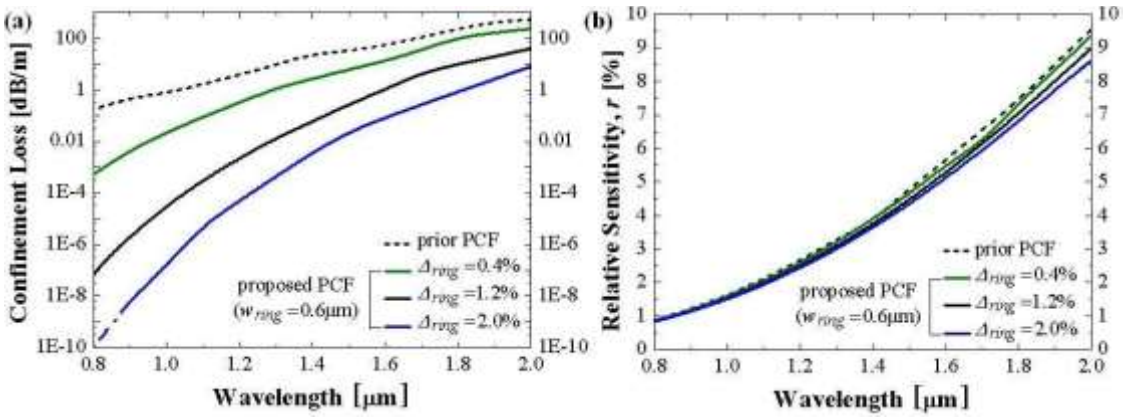

Figure 2-50: Comparison of optical properties (a) confinement loss and (b) relative sensitivity of the proposed PCF (solid lines) with those of the prior PCF (dotted line). Here, we varied the relative index differences *Δring* of the proposed PCF with the fixed *wring* = 0.6μm and set the central hole size *dc* = 1.2μm along with Λ = 2.3μm, *d* = 1.4μm, and *ns* = 1 [85].

According to Olyaee and Naraghi (2013) [83], a photonic crystal fiber-based gas sensor has been which has been able to achieve high relative sensitivity and low limitation losses by increasing the outer ring holes. **Figure 2-51** illustrates with the lattice constant "a", central cavity diameter "d_c", the outer cavity diameter d_2, and the diameter of other cavities "d_1". In this reference, all analyzes are considered with a context refractive index (up to 1.5) and a refractive index of the air cavity (up to 1). Furthermore, for the lattice constants of a= 2, 2.2, 2.3 μm the dimensions of the outer two-ring ring cavities equal to d_2 = 1.8 μm, for a = 1.8 μm equal to d_2 = 1.74 μm and for a = 1.6 μm equal to d_2 = 1.56 μm**. Figure 2-52** shows that the relative sensitivity will change with the change of lattice constant from 1.6 μm to 2-3 μm. As we can see in the figure, the relative sensitivity will be 62% in the lattice constant of 1.6 μm and wavelength of 1.2 μm. One reason is that as the lattice constant decreases, the air filling fraction in the crust increases, which means an increase in the total power fraction inside the cavities. Moreover, the increase of wavelength can raise relative sensitivity.

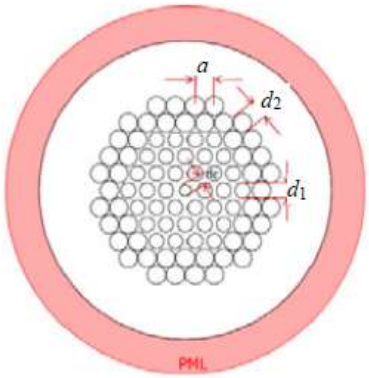

Figure 2-51: The cross-sectional of the photonic crystal fiber by increasing the outer two-ring cavities [83].

Figure 2-52 shows the confinement loss relative to wavelength by changing the central hole's dimensions in the PCF. As shown, the smaller the central hole's diameter, the lower the confinement loss because the core index has more difference with the crust index, and most of the light power is confined to the core region.

Also, by increasing the diameter of outer ring cavities, the confinement loss reduces because when the mode is released, due to the limited air layers, the modes leakage from the core to the area of the outer air cavities is inevitable; thus, the diameter of the outer ring cavities would be increased for preventing this leakage.

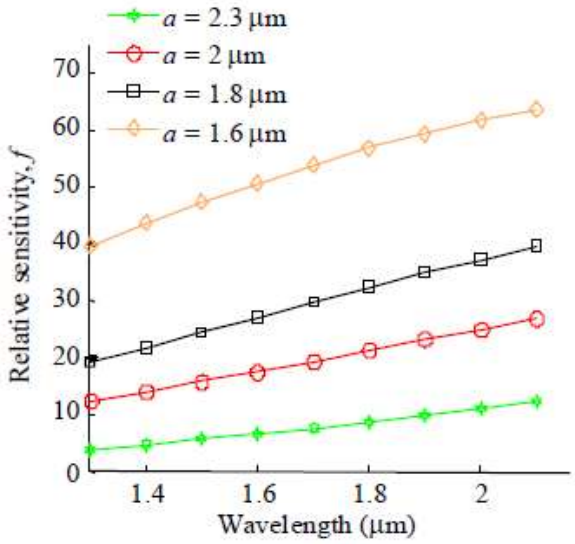

Figure 2-52: Relative Sensitivity in various Wavelengths with (d1 = 1.56 µm, d2 = 1.4 µm, dc = 1µm) [83].

In reference Olyaee and Naraghi (2013) [83], a photonic crystalline fiber-based gas sensor has been proposed, in which the high relative sensitivity and low confinement loss has been achieved by modifying the diameter of cavities and doping part of the core with germanium oxide.

Figure 2-53 shows the suggested structures in this study. As shown in the figure, by varying the doped ring's cavities, the relative sensitivity and different confinement losses can be achieved. In this design, both circular and hexagonal structures are used around the doped ring, and the sensitivity is compared with the two structures. Furthermore, the scheme also calculates the variation of the confinement loss relative to "w" (ring outer diameter).

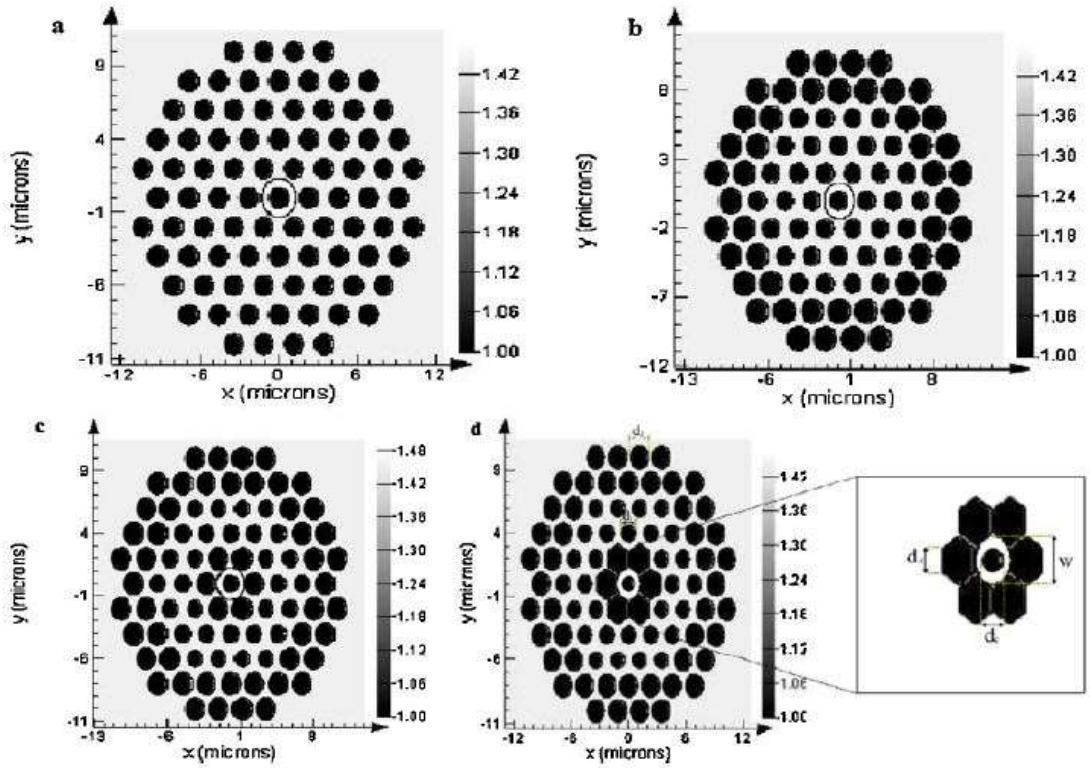

Figure 2-53: The layout sketch of (a) prior photonic crystal fiber (PCF1) with a hollow high index ring defect, and improved PCFs (b) PCF2, (c) PCF3, and (d) PCF4 along its enlarged view with structural parameters: central hole diameter dc, ring outer diameter W; the cladding air holes are characterized by their diameter, d1 : diameter of holes in rings 2 and 3, d2: diameter of holes in rings 4 and 5, d2: diameter of holes in ring 1 (innermost ring), and pitch, 2. Here we assumed 5 layers of air holes [84].

As shown in **Figure 2-54**, the relative sensitivity increases when we use hexagonal cavities around the ring doped with germanium oxide. This is due to an increase in the air filling fraction that can heighten the total power fraction inside the cavities Olyaee et al (2014) [84].

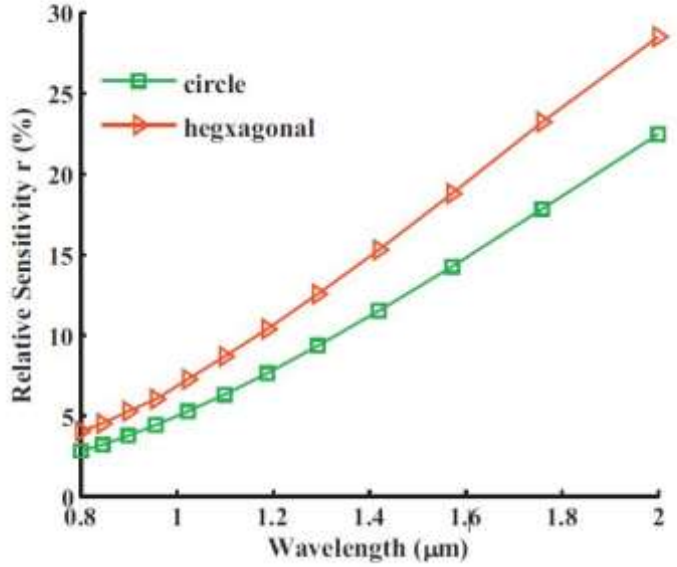

Figure 2-54: Relative sensitivity relative to wavelength for both (circular and hexagonal) (d1 = 1.4 µm, A = 2.3 µm, dc = 1.2µm), for circular type (d3 = 2 µm) and for hexagonal type (d2 =1.8 µm, d4 = 1.2 µm, w =0.6 µm) [84].

Figure 2-55 shows the confinement loss relative to w (ring outer diameter). We can see that increasing "w" causes less confinement loss because the core index is more different from the crust index. The greater the light powers in the core area, the lower the confinement loss.

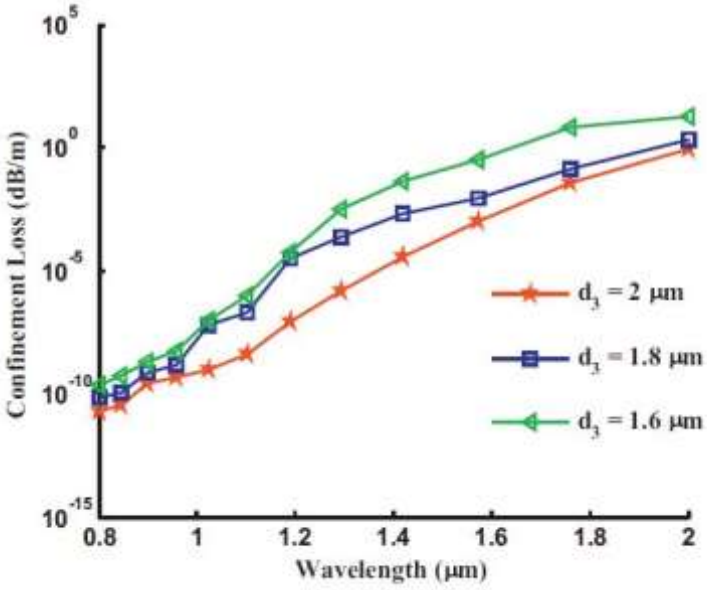

Figure 2-55: confinement loss relative to wavelength (d1 = 1.4 µm, A = 2.3 µm, dc = 1.2µm, d2 = d3 = 1.8 µm) [84].

To compare the properties of the optical crystal fiber-based gas sensor, **Table 2-1** presents the results of the relative sensitivity and confinement loss obtained by simulating in some investigations during the wavelength of 1.5 μm and the average values in the wavelength range of 1.3 to 1.2 μm. The comparison results show that the highest relative sensitivity and the lowest confinement loss during the wavelength of 1.5 μm are related to the reference [83] Olyaee and Naraghi (2013) with a relative sensitivity of 48% and the confinement loss 1.255×10^{-8} db/m, indicating the superiority of this design quality over the existing designs.

Table 2-1: The results of the relative sensitivity and confinement loss using simulation in some investigations.

Confinement loss (dB/m)	Relative sensitivity (%)	Wavelength λ (μm)	Reference
-	35	1.5	[83]
0.753	41.22	Average	
	5	1.5	[85]
75.14	6.98	Average	
9×10^{-9}	17	5.1	[84]
0.2112	21.72	Average	[83]
2.33×10^{-4}	52.44		

2-12- Method of making photonic crystal gas-based sensor

The construction of photonic crystals is of paramount importance. The theory of photonic crystals has been debated for many years. Many concepts have been predicted for photonic crystals in the regions with visible and near-infrared wavelength, but these structures are not feasible and cause problems. The construction of 2D photonic crystals is straightforward and flexible due to the manufacturing method's sharing in the standard semiconductor technology. Also, this thesis emphasizes two-dimensional photonic crystals. Therefore, the only reference is on the fabrication of a two-dimensional photonic crystals .The technology we study for the fabrication of photonic crystal devices is (silicon-on-insulator) SOI, because one of the considered appropriate choices is silicon-on-insulator material. It also has excellent features in the wavelength related to telecommunications systems. CMOS (Complementary Metal Oxide Semiconductor) is with the manufacturing processes and uses this technology to make photonic crystal blades in the form of air cavities. A silicon layer (SOI) is a thin silicon layer on a coating layer made of oxide, which is itself embedded on a silicon wafer. Silicon on the insulator material is a very suitable structure for making optical waveguides. Due to the refractive index

of silicon core n = 4.53 and its oxide coating layer n = 1.45, the value difference of refractive index in this regard is high Ranka et al (2000) [86].

The fabrication of this crystal starts with the production of the SOI wafer process shown in **Figure 2-56** and then coating its surface with a photoresist and then with an anti-reflective material. As a result of ultraviolet radiation, parts of the photoresist are illuminated and heated for a while to stabilize the rest of the photoresist. The light's illuminated segments are then dissolved in the solvent, and the remainder is used as a mask to remove silicon and then oxide Birks et al (1997) [87].

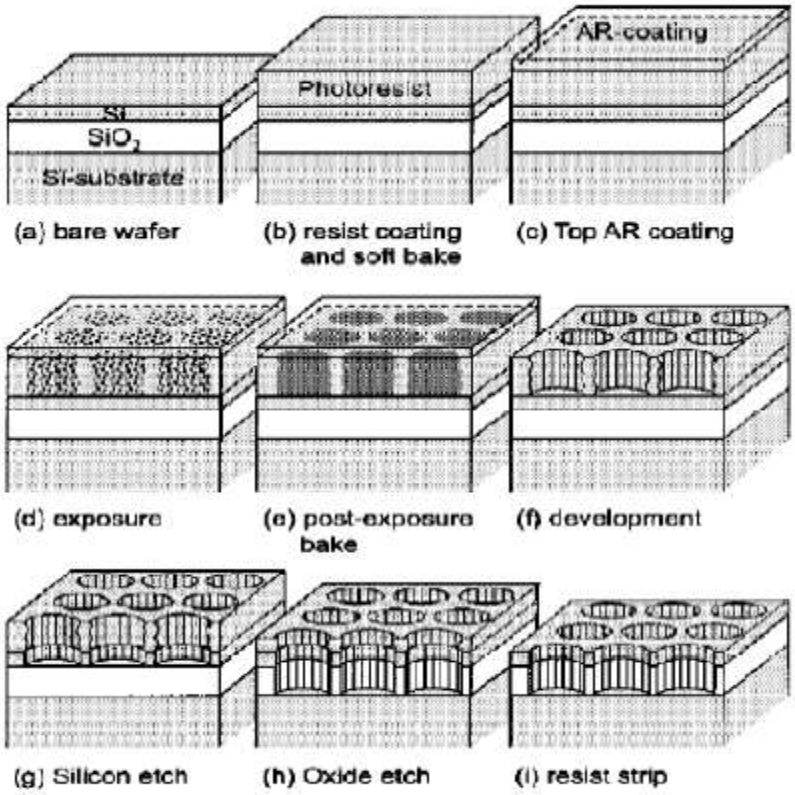

Figure 2-56: The steps of making photonic crystals on SOI wafers [87].

2-13- Method of manufacturing photonic crystal fiber-based gas sensor

After the invention of PCFs, the first challenge was the method of their construction. There were no practical, useful examples, and no one had ever tried to make such a fiber. After several failed attempts, it was discovered the silica strips could be stacked together and then drew to form the PCF to the desired pattern. This method, known as stack and draw, is fast, inexpensive, and flexible. This method is one of the most widely used methods of making photonic crystal fibers Peyrilloux et al (2003) [88]. This method's first step is pre-fabrication (a macroscopic model from the pattern and the microscopic structure of PCF) Quimby et al (2006) [89]. This method starts by constructing the strikes of specific size and the ratio of inner diameter and outer diameter (ID/OD) based on the ratio of the diameter of each air cavity in the fiber to the

lattice constant (d/Λ). The constructed strikes are then assembled in triangular lattices using special tools. Afterwards, using the toolstation bitumen paint, a pre-fabrication of produced PCF by precisely adjusting the clock and furnace temperature converts the fiber to the desired dimensions. The strikes of main elements of the PCF pre- fabrication clock are in the stacking method. The quality of the strikes is important and must be taken into account to ensure the integrity of the pre-fabricated PCF structure and reduce the fragility and debilitation. The strikes are made of not-doped and special silica tubes with an external diameter of 1-2 mm. If the diameter of the strike is less than 1 mm, it will be difficult to maintain in its proprietary lattice position during the stacking phase and will reduce the rings in the strikes with a larger diameter. Proper stacking is also important for forming alternate PCF coatings. At this point, the strikes are made, cleaned, and divided into 30 cm pieces. It is essential to clean the strikes before stacking. Because of their contamination, they increase the scattering losses and reduce the strikes' mechanical strength and shorten them, making it easier to operate and prevent irregularities in the lattice.

Hexagonal metal tools are used as patterns in stacking strikes in triangular lattice arrangements. The stacked strikes are first grouped into hexagons and then fitted into a suitable tubular veneer, and the voids around the hexagons are filled with rods of various sizes. To create the PCF core the central strike is replaced by a beam of equal diameter.

After stacking the strikes and inserting them into the veneer tube, the pre-fabrication produced to convert to the desired dimensions are placed in a towing tower. The temperature of the furnace is adjusted in the range of 1900^0C-2000^0C. Temperatures above 2000^0C can damage cavities, and temperatures below 1900^0C may cause cracking Peyrilloux et al (2003) [88]. Proper adjustment of pressure and vacuum during tensile operation allows for limited control over the final structural parameters such as d/Λ value Quimby et al (2006) [89].

Control of light using light is the most fundamental topic in all-optical integrated circuits, which have many applications in all-optical telecommunication networks Fang et al (2015)-Zhang et al (2012) [90]-[91]. Extensive research has been conducted on optical computing structures since the 1980s Dixit et al (2013) [92]. However, the intensity of the research activities decreased due to some limitations of materials used in the manufacture of optical chips that prevented small and inexpensive optical chips for laboratory research. The main reason for this is the problem of optical diffraction in optical devices that could be overcome using plasmonic waves Wang et al (2016)- Gramotnev et al (2010) [93]-[94]. With the advent of plasmonic structures and the approach of technology towards the integrity of optoelectronic circuits, manufacturing problems and phenomena that helped prevent further compression of the structure led to the study and use of plasmonic structures and plasmonic waves. In petitesizes lower than the wavelengths, surface plasmons provide a suitable basis for the realization and manufacture of all-optical devices due to the increased intensity of concentrated optical fields. MIM waveguides are fundamental structures in plasmonic devices due to guiding surface plasmons in the cross-section of metal-dielectric structure Song et al (2019)-Yan et al (2019)-Yu et al (2019)-Kour et al (2020) [95]-[96]-[97]-[98]. Because these waveguides support the propagation of modes with very small wavelengths and high group velocities and show their ability to guide the wave in relatively long distances. The combination of these

waveguides with nano-resonators in various shapes, which are side-coupled to them, creates various new structures, which have many applications in all-optical devices [90]. The transmission medium in optical networks is the optical fiber, and the wavelength band, which can be used to transmit information, is 1550 nm with minimal losses in the third optical telecommunication window. Therefore, the full adder for a wavelength of 1550 nm (C-Band: 1530-1565nm) has been designed by Madsen et al (2019)- Sung et al (2010)- Olyaee et al (2019) [99]-[100]-[101].

One of the major problems in the expansion of optical networks is the limitation of diffraction in the limited size of optical devices due to the wavelength of light transmitted by the network, which increases the sizes of optical devices relative to those of electronic devices. The diffraction limit can be broken using plasmonics Zhang et al (2012) [91].

Diffraction is a phenomenon that occurs when a wave encounters an obstacle, It is defined as the bending of (electromagnetic) waves around the corners of an obstacle or aperture and their propagation into the region of obstacle's geometrical shadow.

Using optical devices, like silicon photonic devices, causes other problems, such as cases where the Pockels constant equals zero. Although effects such as the thermo-optic effect and dispersion effect of free carriers have been dynamically employed to control silicon's optical properties, these technologies have adverse effects on velocity, losses, and so on. It is challenging to integrate high-speed optical devices using silicon technology Yan et al (2019) [97]. Using plasmonic waveguides offers a new opportunity to integrate electro-optic polymers in high-speed optical technology Lu et al (2014) [102].

The term plasmonic has been explained based on the process of interactions between electromagnetic waves and conduction electrons in metals with nanoscale dimensions. Many plasmonic waveguides and optical equipment, based on the propagation of surface plasmons, have been presented in recent studies Olyaee et al (2019) [101]. All-optical logic gates with plasmonic waveguide structures have been introduced and simulated in Lu et al (2014) [102] using a waveguide Y-branch splitter. In an all-optical integrated circuit, it is necessary to have several logic gates working in series. And if each gate causes a lot of loss, the practical application will not be possible. In an all-optical integrated circuit, it is necessary to have several logic gates working in series. If each gate causes a lot of loss, and practical application will not be possible. In a recent work by Bozhevolnyi et al (2008) [103], a photonic crystal waveguide and the nonlinear properties of optical materials have been used to design all-optical logic gates. Although photonic crystal structures and nonlinear light have important applications, compared to plasmonic structures, they have major disadvantages, such as the enlarged size of pieces and high-power losses for logic gates. Kaboli and Akhlaghi (2016) [104] have benefited from full absorption in periodic plasmonic nanoparticles and the operation of pumping optical power to these nanoparticles to modify the output and to create an AND logic gate. Although their gate is a new design, it has a very high manufacturing complexity for a simple logic gate. The piece's size is large, and the power consumption is high due to the permanent pumping of optical power. In reference [105] Fu et al (2012), the uses of plasmonic waveguides and slot cavity resonators have been proposed for basic logic gates and have used

transmission coefficients for the amplitude of waves in waveguides.

Multipliers, as key elements in various circuits, are as important especially in the calculation unit of microprocessors and the implementation of digital signal processing (DSP) algorithms. Therefore, the multipliers' velocity is an essential factor in determining the microprocessors' efficiency Rouholamini et al (2007) [106]. Each multiplier consists of three basic parts: the partial product generator (PPG), the partial product reduction (PPR), and the carry propagate adders (CPAs). In the meantime, the PPR part has the largest occupied area and the highest consumption capacity [106].

On the other hand, among the various methods for performing multiplication, the compressors' use to reduce latency, power, and area is the most common. But what's important is the presence of XOR-XNOR gates in the compressor design. Therefore, designing high-speed and low-power XORs improves the efficiency of compressor circuits; As a result, increasing the compressor speed and reducing their power consumption leads to the production of more efficient multipliers Aliparast et al (2013) [107].

Furthermore, the use of appropriate technology to design the XOR gate, followed by the compressor design, significantly improves large-scale multiplier circuits' efficiency. Therefore, due to the limitations of MOSFET, the use of emerging technologies such as carbon nanotubes (CNT) can play an effective role in circuit design Cho et al (2009) [109]. Therefore, in this study, due to the extraordinary features in CNTs described below, the design of XOR gates and proposed compressor circuits at the transistor level and based on the technology of *carbon nanotube* field-effect transistor (CNTFET) has been conducted.

In recent years, the use of light waves has gained importance, since it can provide a higher speed in optical communication networks and can transfer large amount of data with faster speed in longer distances in optical fiber. In wide cities with millions of users, it is important to associate an optical fiber for each user, which results in a massive quantity of cables to cover all customers in a specific area, which will be very costly. One of the solutions for this complication is to provide one single fiber for many customers since it is possible to transfer many wavelengths together inside the optical fiber with wavelength-division multiplexing (WDM) technique Theis et al (2017) [108].

Nowadays, the design of high performance with miniaturized optical devices is one of the most important technological challenges of information processing systems in optical communication. Photonic crystal (PC) is one of the right candidates for wavelength division multiplexing (WDM) systems as it offers high wavelength sensitivity, terahertz speed and miniaturized size without degrading the performance of the device. Recently, WDM Hoanca (2002) [112] systems receive keen attention in the research community as it supports many channels with narrow channel spacing in a single fiber. It is classified by coarse wavelength division multiplexing (CWDM) and dense wavelength division multiplexing (DWDM). The CWDM system (ITU-T Recommendation G.694.2) supports a smaller number of channels over the wavelength range between 1260 and 1675 nm with 20 nm channel spacing. Alternatively, the DWDM system (ITU-T Recommendation G.694.1) facilitates a bigger number of channels

from 1535 to 1565 nm with narrow channel spacing (1.6 nm/0.8 nm/0.4 nm). Hence, the DWDM system will be employed for point-to-point high-capacity networks; however, CWDM will be used for access networks and regional networks. In this work, the DWDM system is considered for demultiplexer design.

Typically, PC-based optical devices are realized either in a cubic lattice or in a hexagonal lattice. The cubic is referred to as a square lattice, and hexagonal is referred to as a triangular lattice. In the cubic lattice, the photonic band gap (PBG) size is narrow Wu et al (2012) [113], there is low dispersion, high power transmission Sakoda (2004) [114], and easy fabrication facility compared to the hexagonal lattice. Hence, the proposed device is designed using a two-dimensional photonic crystal (2DPC) in a cubic lattice. The cubic lattice is composed of a periodic array of dielectric rods embedded in an air medium. The 2DPC has PBG as the PC comprises periodic dielectric constant variations in two different directions. The PBG design Joannopoulos et al (1995) [115] in PC plays an active role in identifying the desired operating range. It is used to control and manipulate the light waves propagating through the PC.

The number of output channels, transmission efficiency, quality factor, crosstalk, and channel spacing are the most crucial characteristics of PhC-based demultiplexers. Savarimuthu and Rangaswamy (2011) [116] Recently, many attempts have been focused on improving the aforementioned characteristics. For instance, a five-channel demultiplexer has been proposed by horizontally cascading five single-channel drop filters with different lattice constants; in this structure, the channel spacing was around 8 nm Djavid et al (2008) [117].

The lattice constant a, radius of dielectric rod r and refractive index difference Δ are the important PC parameters to generate and control PBG. The device can be realized by various defects that are introduced in PC. The defects are classified as line defects and point defects. Once defects are introduced in the periodic structure, the PBG is entirely broken, making the modes propagate inside the defect-based structure. The defects are used to trap or localize the light. By having the aforementioned principle, many PC based optical devices are realized, such as a cavity, ring resonator (RR), waveguide, etc., which are actively used to design optical filter Youcef Mahmoud et al (2012) [118], switches Rao et al (2010) [119], sensors Liu et al (2012) [120], polarizers Cui et al (2008) [121], mirrors Yang et al (2012) [122], splitters Park (2004) [123], multiplexers Manzacca et al (2007) [124], and demultiplexers Rawal et (2009) [125], etc.

In the literature survey, the PC-based demultiplexers are designed by introducing point defects and line defects alone or combining point and line defects. Generally, the combination of point and line defects is used to develop ring resonator-based PC devices. The demultiplexers are designed using different shapes using either line or point defects alone, such as Y shape Zhang et al (2012) [126], T shape Alipour at al (2013) [127], cascaded T shape Sakoda (2004) [128], tree shape Alipour et al (2015) [129] which offer better transmission efficiency, high quality factor, narrow channel spacing, and small size. However, it is challenging to reduce crosstalk. Alternatively, the eight shaped ring resonator [121]-[129], elliptical type ring resonator Zhang et al (2012) [126], ring resonator-based square ring resonator Alipour-Banaei et al (2013) [127],

circle type ring resonator Sakoda (2004) [128] and square ring resonator-based octagon-shaped resonator Alipour-Banaei et al (2015) [129] are incorporated to design the demultiplexer.

Manufacturing and realizing a nanoscale integrated optical device is one of the most important applications of photonic crystals. In recent years various integrated optical devices have been implemented alongside major changes to high-quality photonic crystal samples, including the design and fabrication of logic gates based on photonic crystals.

Logic devices are the essential components of optical computing systems and ultra-fast information processing. Logic gates can be developed based on the effects of optical band gaps and waveguides as well as severe light confinement in photonic crystal microcavities. Important parameters in the design of photonic crystal gates are the lattice constant of the structure, the power of material used for the dielectric rods and the background dielectric constant, the type of material and the band gap of the structure according to the dimensions and shape of the design, the geometry and dimensions of the defects, radius of dielectric rods and so on.

With the development of photonic crystals since the late '90s, many scientists studied these structures mostly for optical processing because of their unique properties such as dimensions of light wavelength, low power consumption and easiness of integration.

Many of the works published in Nonlinear Optics have fundamental limitations such as high-power consumption and narrow frequency range. In contrast, the phenomenon of self-collimation is independent of the incoming radiation intensity and does not require the all-optical band gap compared to photonic crystal waveguides Scholz et al (1998) [130]. Hussein et al.(2018) introduced new designs of all-optical logic gates as AND, OR, NOT, NOR, XOR and used the combination of OR and XOR gates to realize a NAND gate. Each of these gates exhibited a reasonable contrast ratio between logic ‘1’ and logic ‘0’, varying between 5.036 dB for the NAND gate to 12.155 dB for the XOR gate.[131]. Alipour-Banaei et al (2017) suggested an AND and NOT gates using square lattice PhC of chalcogenide glass rods embedded in air. The device is designed using a nonlinear ring resonator connected to waveguides for the inputs and the output. The resonator has a drop resonance wavelength of 1550 nm shifted for the threshold power value higher than 1 KW = $1\mu m^2$ [132].
The resonant wavelength of PhCRRs depends on the ring core's structural parameters such as lattice constant, radius, and refractive index of dielectric rods. We know that the resonant wavelength of the photonic crystal ring resonator is very sensitive upon the refractive index of dielectric rods. On the other hand, the refractive index of dielectric materials depends on the optical power intensity.
The refractive index of most dielectric materials has a term (or contribution) which is proportional to the incident light intensity. This is known as the optical Kerr effect. The resonant wavelength of PhCRRs depends on the ring core's structural parameters such as lattice constant, radius and refractive index of dielectric rods. .The optical behavior of the photonic crystal ring resonators (PhCRR) structure can be controlled via input intensity Ahmadi et al (2011) [133]. Therefore, the analysis of the performance of the proposed PhCRR can be used as a function of the Kerr effect. Logic gates’ operation is realized using nonlinear Kerr

materials. Hence, by increasing or decreasing the signal’s intensity values, the structure's properties, such as the ranges of operating wavelengths, are changed. In this context, Pashamehr et al (2016) proposed the OR, AND, and NOT gates based on nonlinear Kerr materials in photonic crystal ring resonator structure [134]. Moreover, Alipour-Banaei et al (2017) suggested the AND and NOT gates using square lattice PhC of chalcogenide glass rods embedded in air. The device is designed using a nonlinear ring resonator connected to waveguides for the inputs and the output [132].

2-14- Conclusion

This chapter, first, describes the history of photonic crystals. Then, the properties and characteristics of photonic crystals, the optical band gap, and types of defects in photonic crystals were investigated.

Afterwards, the history of optical logic gates and a structure of photonic crystal-based gas sensing were presented. The concepts and principles of optical logic gates based on photonic crystals were discussed. As mentioned, photonic crystal gates have unique properties whose main factor is controlling the defects created as cavity and waveguide in photonic crystals and their band gap. By changing the dimensions and geometry of dielectric rods and the type of optical crystal lattice, optimum results can be obtained to improve photonic crystal-based optical logic gates' properties. In the structure of photonic crystal-based gas sensors, their types and their structural changes were investigated to improve their quality. As mentioned, the relative sensitivity can be increased by decreasing the lattice constants, and also the confinement loss can be decreased by increasing the diameter of the outer ring cavities. Finally, a summary of some of the basic designs of photonic crystal logic gates and the structure of photonic crystal gas sensors was investigated.

Chapter 3

Proposed Work

3-1- Introduction

In this chapter, I introduce the mathematical expression of the electromagnetic waves that are going to be discussed; also their parameters will be defined.

3-1-1- Theoretical equations of plasmonic structures

To implement logic gates in this study, a metal-insulator-metal (MIM) waveguide will be used. In it, a nanoscale insulator is placed between two metal structures. When the distance between the two metals is very short, surface Plasmons can be stimulated, and the plasmonic waves, which propagate between the two metal surfaces, can be used as messengers. In this study, the insulator is assumed to be air, the metal to be Drude Model silver, and in which the relative dielectric function for metals is expressed by **Equation 3-1** Alwayn (2004) [163] :

$$\varepsilon_m(\omega) = \varepsilon_\infty - \frac{\omega_p^2}{\omega(\omega + j\gamma)} \qquad (3.1)$$

Where, ε_∞ is the dielectric constant of the material at the infinite frequency, ω_p shows the plasma frequency, and γ denotes the angular frequency of damping. As for silver, these values are as follows: $\varepsilon_\infty = 3.7,\ \omega_p = 9.1\ eV\ and\ \gamma = .018\ eV$. The width of the waveguides is assumed to be 100 nm so that only the first and second modes (TM0, TM1) are stimulated and depending on the application of equipment; the first or second mode is used. By solving the Maxwell equations, the dispersion equation shown in **Equation 3-2** could be reached**:**

$$\tanh\left(\frac{k_d}{2}w\right) = -\frac{\varepsilon_d\, k_m}{\varepsilon_m k_d} \qquad (3.2)$$

Where ε_∞ the dielectric coefficient of the material with infinite frequency, ωp represents the plasma frequency, and γ denotes the damping angular frequency. The value of these parameters for silver are: ωp=9.1 $e.$,=.018 $e.v$, and ε_∞ =3.7. The width of waveguides is taken as 100 nm in order to stimulate only the first and second modes (TM0, TM1). Also, either the first mode or second mode can be used given the device application. By solving Maxwell relationships, one can obtain dispersion relation in **Equation 3-2.**

Where, ε_d is the insulator-dielectric coefficient (i.e., the air that is unity), ε_m represents the metal-dielectric coefficient (silver) kd and km are the wave numbers related to the dielectric and metal, respectively.

If the complex emission constant in the plasmonic waveguide is β, **Equation 3-3** and **3-4** could be simply obtained by embedding electrical and magnetic fields within the dielectric and metal using boundary conditions Alwayn (2004) [163]:

$$k_d = \sqrt{(\beta^2 - \varepsilon_d k_0^2)} \qquad (3.3)$$

$$k_m = \sqrt{(\beta^2 - \varepsilon_d k_0^2)} \qquad (3.4)$$

By solving **Equation 3-2 and 3-4** simultaneously, the emission constant in the waveguide (β) can be obtained.

The basic illustration of these studies, consisting of a MIM waveguide and a rectangular cavity with a length of Ls. Once the MIM waveguide is excited and resonance conditions are established in a rectangular cavity, plasmonic waves will be stationary with consecutive frequency sweeps. The resonance occurs when a phase shift, developed by consecutive sweeps in the cavity (along with phase differences which are developed at the ends of the cavity), is an integer proportion of π that is $\Delta\varphi = \beta_m L_s + \varphi_r = m\pi$. Where it can be neglected considering the negligibility of φ_r.

$\Delta\varphi$ is the phase difference between reflection and transmission beams, which is determined by the reflector radius, and ΔL is the optical path difference of two partial reflectors.

If the refractive index in plasmonic waveguides and resonance cavity is n_{eff} where $k_0 = \frac{2\pi}{\lambda}$ the wavenumber in a vacuum is, then $n_{eff} = \frac{\beta}{k_0}$ is obtained as follows:

$$\beta_m L_s = m\pi \Longrightarrow n_{eff}.\frac{2\pi}{\lambda_m}.L_s = m\pi \Longrightarrow \lambda_m = \frac{2L_s.n_{eff}}{m} \qquad (3.5)$$

(3.5)

If the input port is excited by an electromagnetic wave at optical frequencies, electrical and magnetic fields in stationary resonance in the rectangular cavity can be obtained by solving Maxwell equations. The intensity of magnetic fields in the resonator nanogap for MTH mode is obtained using **Equation 3-6.**

$$H_m(x.t) = \frac{2H_0\cos(\beta_m x - \frac{\beta_m.L_s}{2})}{\sigma}\left[e^{j\left(\frac{3}{2}\beta_m.L_m - \beta_m.\Delta L\right)} + e^{j\left(\beta_m.\Delta L - \frac{1}{2}\beta_m.L_m\right)}\right] \qquad (3.6)$$

Where ΔL is the distance from the input port to the middle of the rectangular Nano-slot, and since waveguides usually reach the edge of the Nano-slot, $\Delta L = \frac{L_S}{2}$ is usually true (of course, it can be less than this value too, and will not cause any problems). Given that we assumed the waveguides' width to be very small, only the first and second modes are stimulated in the Nano-slot. For instance, the magnetic field intensity equation for the first mode is as shown in **Equation 3-7**.

$$m = 1 \Longrightarrow H_m(x,t) = \frac{2H_0.\sin(\beta_1.x)}{\sigma}\left[-\sin(\beta_1.\Delta L)e^{-j(\omega_1.t)}\right] \qquad (3.7)$$

From **Equation 3-7**, we derived the necessary idea to design the AND, OR, and XOR gates, which are necessary bases for the adder because if we assume two input waveguides, whose distances to the middle of the Nano-resonator are asymmetric to each other. That is, for one of them, the distance is ΔL_1, and for the other $\Delta L_2 = -\Delta L_1$, then the two resonated magnetic fields

in the rectangular slot will neutralize each other, and the field inside the rectangular slot will become zero. Also, by increasing the number of waveguides and adjusting their distances to each other, the desired output parameters can be obtained Alwayn (2004) [163].

3-2- Numerical analysis

Several numerical methods are reported to obtain PBG and normalized output spectra of the periodic and non-periodic PC structure. They are plane wave expansion (PWE) method Johnson and Joannopoulos (2001) [135], transfer matrix method (TMM) Pendry and MacKinnon (1992) [136], finite-difference time-domain method (FDTD) Taflove and Hagness (1998) [2], and finite element method (FEM) Pelosi et al (1997) [137], etc. The PWE and FDTD methods are predicting the accurate behavior of 2DPC. Hence, the PWE is applied in the frequency domain to analyze the PBG and estimate the PC structures' electromagnetic modes. The band diagram calculations of the electric field are carried out by solving Maxwell's equation Kane (1966) [138], which is;

$$\nabla \times E + \frac{\partial B}{\partial t} = 0 . \qquad (3.8)$$

$$\nabla . B = 0 . \qquad (3.9)$$

$$\nabla \times H - \frac{\partial D}{\partial t} = J . \qquad (3.10)$$

$$\nabla . D = \rho \qquad (3.11)$$

The magnetic field $H(r)$ equation is:

$$\nabla \times \left[\frac{1}{\varepsilon(r)} \nabla \times H(r) \right] = \left(\frac{\omega}{c} \right)^2 H(r) \qquad (3.12)$$

The Maxwell electromagnetism appears as an eigenvalue problem for the harmonic modes of the magnetic field $H(r)$, and the solution of the electric field is:

$$\nabla \times \nabla \times E(r) = \left(\frac{\omega}{c} \right)^2 \varepsilon(r) E(r) \qquad (3.13)$$

It manipulates PBG at high speed but, it cannot extract backward reflections and light wave propagation in the 2DPC structure. Hence, Maxwell's equation is employed in the time domain called FDTD method to analyze the field distribution of PC based optical devices. FDTD method is employed to analyze the performance of transmission spectra of PC-based optical devices. It simulates the electromagnetic devices for all ranges of frequencies, from the

microwave to the optical regime. It is one of the most important computational techniques for analyzing the electromagnetic waves propagating through PC devices and extracting backward reflections. It is a simple, attractive, accurate, and efficient way to discretize Maxwell's equations. In this proposed structure, the normalized transmission spectra are obtained by taking fast Fourier transform (FFT) of the fields that are calculated by 2D FDTD method. Generally, 1D FDTD method offers fast simulation with less accuracy, and 3D FDTD method requires more simulation time, large memory size, and provides accurate behavior of PCs. Even though 3D FDTD method affords accurate results, the same results can be obtained using 2D FDTD with less time and less memory space. Hence, 2D FDTD method is considered in the present work. In 2DPC, electromagnetic fields are propagated in the form of transversely two polarized modes (**Equation 3-14 and 3-15**) TE and TM. The time-stepping equation Kane (1966) [130] for FDTD is given as follows:

$$E_x\Big|_{i,j}^{n+1} = E_x\Big|_{i,j}^{n} + \frac{c\Delta t}{\varepsilon_0}\frac{H_z\Big|_{i,j+1/2}^{n+1/2} - H_z\Big|_{i,j-1/2}^{n+1/2}}{\Delta y} \tag{3.14}$$

$$E_y\Big|_{i,j}^{n+1} = E_y\Big|_{i,j}^{n} + \frac{c\Delta t}{\varepsilon_0}\frac{H_z\Big|_{i,j+1/2}^{n+1/2} - H_z\Big|_{i,j-1/2,j}^{n+1/2}}{\Delta x} \tag{3.15}$$

$$H_Z\Big|_{i,j}^{n+1/2} = E_Z\Big|_{i,j}^{n-1/2} + \frac{c\Big|\Delta t}{\varepsilon_0}\left[\frac{E_x\Big|_{i,j+1/2}^{n} - E_x\Big|_{i,j-1/2}^{n}}{\Delta y} - \frac{E_y\Big|_{i+1/2,j}^{n} - E_y\Big|_{i-1/2,j}^{n}}{\Delta x}\right] \tag{3.16}$$

Where the indices *i* and *j* denote the discretized lattice point in the *XY* plane, and index *n* denotes the discrete time step.

3-3- CNT transistors

According to Moore's Law, decreasing the size of transistors built into integrated circuits in CMOS technology and increasing their number on the chip has been about four decades. In 1965, Gordon Moore predicted that the number of transistors on a chip's surface would double every two years. Thus, chip manufacturers have been steadily reducing the size of chips for achieving greater speed. This size reduction, both in the longitudinal direction (reducing the distance between the pin and the drain) and in the thickness direction (reducing the oxide layer of the gate), leads to problems in the design of stable circuits such as exponentially increasing leakage currents, power consumption increase, manufacturing cost increase and the chip cooling in CMOS technology. Thus, according to ITRS forecasts, the construction of silicon circuits in 2020 will be limited, forcing the semiconductor industry to choose an alternative to CMOS Cho et al (2009) [109].

Restrictions on the process of making transistors smaller in the microelectronics industry have led to the emergence of a new research field at 100 nanometers in the field of nanotechnology. Quantum cellular automata technology (QCA), the field effect transistors (FET) that use wire-Nano as a transistor channel, single-electron transistors (SET), Fin-FETs described by Intel,

multidimensional technologies such as graphene or MOS_2-based transistors, spin-FETs, and CNTFET introduced by IBM Cho et al (2009)-Ghasemzadeh (2016) [109]-[110] can be mentioned as examples. CNTFET, meanwhile, is a promising alternative to silicon MOSFETs in both the academic and industrial sectors. This advantage is because of its excellent features such as good charge carrier mobility, quasi-ballistic current transmission, good thermal conductivity and, most importantly, having a structure similar to COMS technology Raychowdhury et al (2006)- Bachtold et al (2001) [111]-[139].

Nanotube-based transistors are constructed by placing nanotubes as channels in MOSFET transistors, as shown in **Figure 3-1** Rodriguez et al (2015) [140].

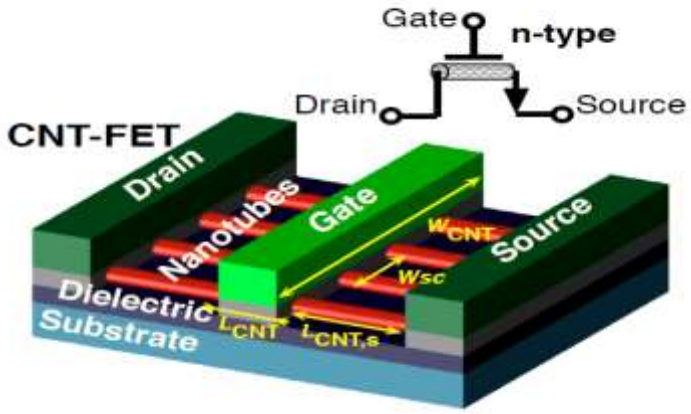

Figure 3-1: Overview of the CNTFET structure [140].

Each nanotube-based transistor can consist of one or more nanotubes built by rolling a graphene sheet around the chiral vector ($Ch = ma_1 + na_2$), where (m, n) are integers and (a_1, a_2) are the base vectors. If n is equal to zero, m is an integer, and the angle between the two vectors (a_1, a_2) is equal to zero. The nanotube will have a semiconductor property and is suitable to make a transistor Rodriguez et al (2015) [140].

Another important feature of CNTFET is the easy switching of the threshold voltage (Vth) that is possible by changing the diameter of the nanotube, making CNTFET flexible in designing high-speed digital circuits. The nanotube's diameters can be obtained from **Equation 3-17** Ali Usmani and Hasan (2010) [141].

$$D_{CNT} = \frac{a}{\pi}\sqrt{m^2 + n^2 + m.n} \qquad (3.17)$$

(m, n) are the integers of the Chiral Vector and "a" is the distance between the two carbon atoms, which is about 2.49 angstroms. Also, the threshold voltage at a nanotube or the intrinsic CNT channel is calculated as **Equation 3-18** Park and Bao (2013) [142].

$$V_{th} \approx \frac{a.V_\pi}{e.D_{CNT}} \approx \frac{0/43}{D_{CNT}(nm)} \qquad (3.18)$$

In **Equation 3-17,** D_{CNT} is the diameter of a nanotube, a is the distance between the two carbon atoms, V_{th} is the threshold voltage (Vth) of the intrinsic CNT channel, V_π is the energy of a carbon bonding, and e is the charge of an electron Bachtold et al (2001)- Rodriguez et al (2015) [139]-[140].

3-4- Two-input XORs

Exclusive OR (XOR) and exclusive NOR (XNOR) gates are key components in many digital systems that are widely used in parity checker systems, comparators, computing circuits, cryptographic algorithms, especially the AES algorithm, error detection and correction circuits, FPGAs and compressors are used [143] Moaiyeri et al (2010). In many of these systems, XOR gates are part of a critical path that significantly affects overall circuit delay. Therefore, improving the performance of the XOR gate will improve the overall system performance Moaiyeri et al (2010) [143]. A review of two input XORs commonly used in the design of different circuits, and the proposed models would be presented as follows.

3-5- Existent XORs

The XOR gate implementation function is A⊕B = A'B + AB'. In general, a conventional two-input XOR (C-XOR) composed of the twelve transistors shown in **Figure 3-2**.

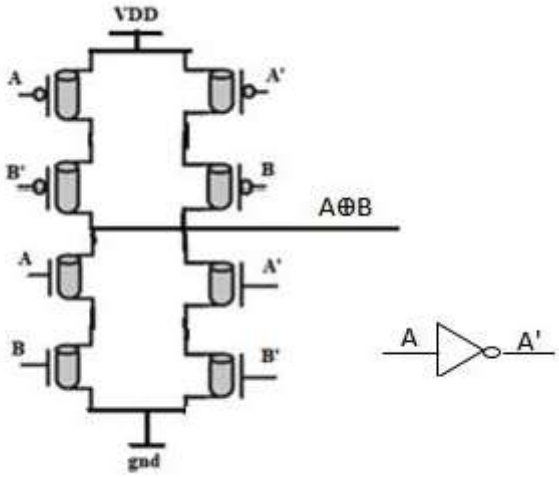

Figure 3-2: Conventional two-input XOR (C-XOR).

On the other hand, the use of the C-XOR model with this volume of transistors in large-scale systems, increases the area of the circuit, and also greatly increases the power of the system. Therefore, according to different applications, different implementations of it have been expressed in articles Moaiyeri et al (2010) [143]. Thus, some of the most popular two-entry XOR gates are considered as benchmarks to compare with the proposed models.

One of the newest designs for the XOR is the six-transistor model described in reference Saraswat and Sharma (2018) [169]. The XOR gate provided in this paper consists of an Inverter

gate and a transistor gate in the CNTFET technology. In reference Shanka et al (2010) [144], the XOR gate is introduced in CMOS technology; for an accurate comparison, the proposed design in the form of CNTFET is presented in this study. This model is based on the Double Pass-transistor Logic (DPL), whose main disadvantage is the large size of the gate, which is composed of a transistor.

Another model is proposed in the reference Lee and Sobelman (1997) [145], which is presented in the form of a CNTFET proposal in this study for a detailed comparison. In [145], the XOR gate consists of six transistors consisting of three inverters in a row (Inverter-based XOR). The main problem with this circuit is that it has multiple connections, which increases the circuit delay and the power consumption, especially in circuits with low voltage levels.

3-6- Recommended XOR model

The XOR gates proposed in this paper are presented in two designs, Model-1 and Model-2, and in the technology of CNTFET, which are shown in **Figures 3-3 (a)** and **3-3 (b)**, respectively.

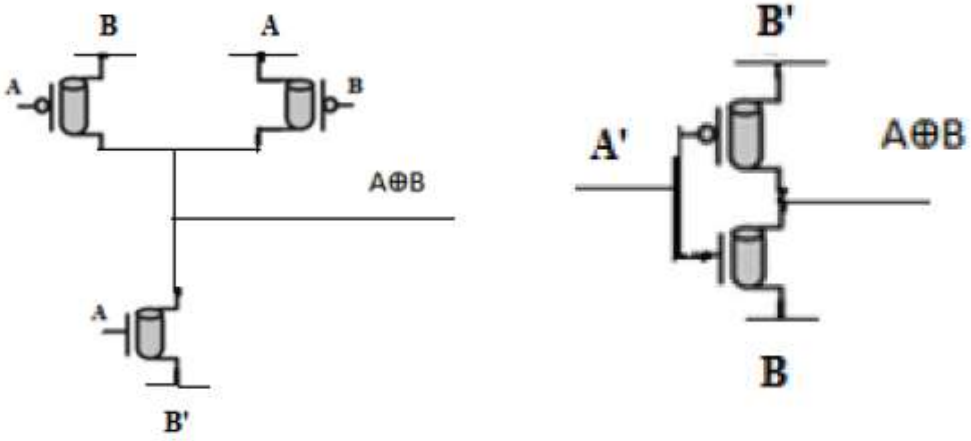

(a) (b)

Figure 3-3: Suggested XORs (a) Model -1 and (b) Model -2.

The proposed Model-1 gate consists of five transistors, in which the pull-up part is a Semi-XOR, and the pull-down part is a pass transistor. In this model, when AB = 01/10, the logic is "one", and when AB = 11, the logic "zero" gets to output. Only when AB = 00, a weak zero passes through the lift section by changing the nanotube diameter, and threshold voltage size, based on the **Equation (3.17) and (3.18)**, this voltage weakness reaches its minimum value.

This model, in addition to reducing the number of transistors by less than half compared to the conventional XOR gate, also eliminates the weaknesses in the proposed models Sharma et al (2010)- Singh et al (2012) [146]-[147], weaknesses such as the existence of two levels of logic for one mode or several levels of poor logic.

The Model-2 is designed with two inverter gates, including six transistors. This model consumes more power than model 1 because of the way the transistors are connected, and the input is inverted; nevertheless, at voltages above 0.9 V, it has less power leakage than model-1. Also, Model-2 has a lower voltage weakness than the proposed model in reference Atefinasab (2016) [148] due to the reverse input. Therefore, Model-2 can perform better in applications where the voltage drop reduction is very important.

3-7- Compressor (4:2)

Compressor (4:2) is one of the widely used bit compression elements for applications such as multiplier and multitasking hardware, which would be used for compressing four partial products into two. The compressor has five inputs and three outputs, Sum, Carry, and Cout, as shown in **Figure 3-4** Kumar Nath, (2017) [149].

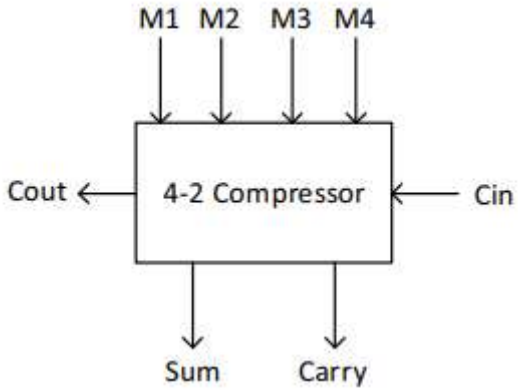

Figure 3-4: Diagram of the compressor (4:2).

In compressor (4:2), the Cin input is one output from the previous compressor, and the Cout output is one input for the next compressor.

A compressor (4:2) is normally implemented as two series adders, as shown in **Figure 3-5**, whose mathematical function is given in **Equation (3.19)** Koren (2002) [150].

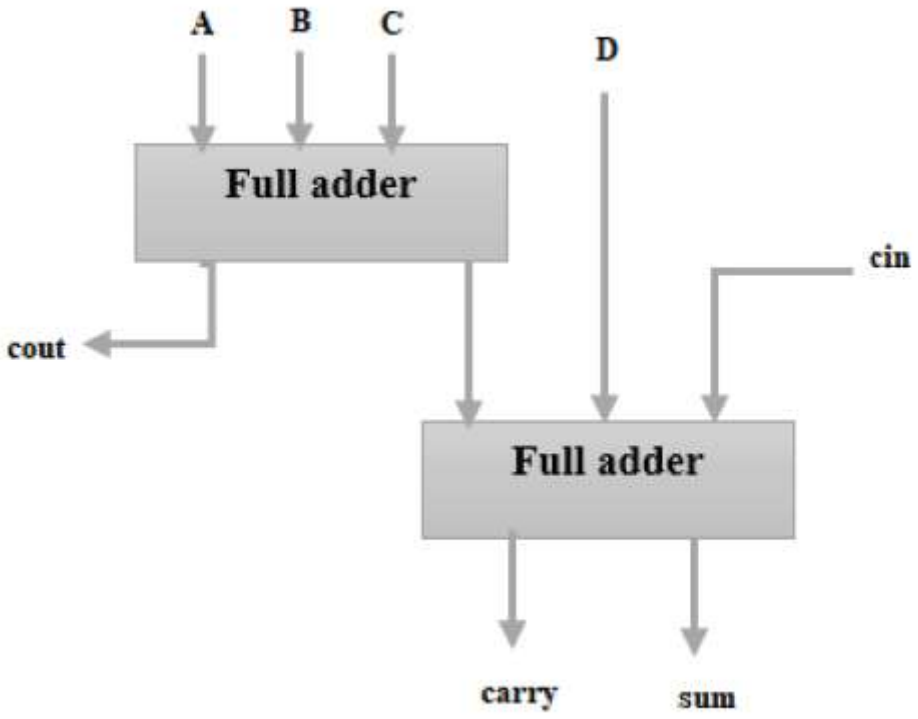

Figure 3-5: Implementation of a compressor (4:2) in normal mode.

$$A + B + C + D + cin = sum + 2 \times (carry + cout) \qquad (3.19)$$

This implementation of the compressor has the longest delay, which is considered as a delay of two collectors (2ΔFA) or a delay of four gates (4ΔXOR) XOR at the gate level.

Therefore, given that the compressor is used in larger circuits such as multipliers, this delay is significant. By decomposing **Figure 3-5** into different structures, the delay rate in a compressor (4:2) is at least 25% lower than normal (4ΔXOR) and reduced to the delay of $3\Delta XOR$ Koren (2002) [150].

Therefore, there are several designs for compressors (4:2), which are described below.

3-7-1- The check of the available (4:2) compressors

One of the proposed designs for the compressor (4:2) is related to reference Chang et al (2004) [151], the delay of which is 3ΔXOR, and one of its proposed XORs for designing compressor (4:2) is the model provided in reference Kumar Nath, (2017) [149]. According to the proposed XOR, there are eight transistors and multiplexers Nehru et al (2017) [152], which reduce the compressor's total area to almost half the normal state.

There is another structure in reference Dadashi et al (2016) [153], which uses two and three-input XORs and reduces the output delay to less than 3ΔXOR. The next design is related to reference [154] Pishvaie et al (2013), in which the XOR and Multiplexer gates in the critical path are analyzed to the AND/NOR gate to reduce circuit delay, but due to the use of logical

gate structure in the conventional state, the area and the circuit delay is increased greatly. Another model to compare is the design in reference [155] Rahnamaei et al (2019), in which the structure is studied aiming to optimize the compressor's trust table and use of the Multiplexer in **Figure 3-7**.

3-7-2- Proposed (4:2) compressor

One of the most common structures for decomposing two series adders is shown in **Figure 3-6**, which is given in the reference [151] Chang et al (2004).

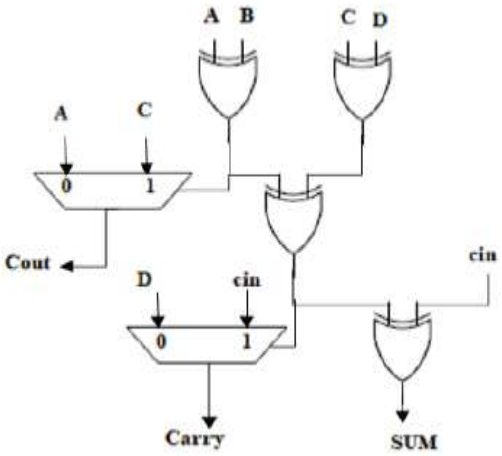

Figure 3-6: (4:2) compressor circuit.

The three outputs in compressor (4:2) are obtained using **Equation (3.20)**:

$$\begin{aligned} \mathrm{Cout} &= (\mathrm{A} \oplus \mathrm{B}).\mathrm{C} + \mathrm{AB} = (\mathrm{A} \oplus \mathrm{B}).\mathrm{C} + \overline{(\mathrm{A} \oplus \mathrm{B})}.\mathrm{A} \\ Sum &= \mathrm{A} \oplus \mathrm{B} \oplus \mathrm{C} \oplus \mathrm{D} \oplus \mathrm{Cin} \\ \mathrm{Carry} &= (\mathrm{A} \oplus \mathrm{B} \oplus \mathrm{C} \oplus \mathrm{D}).\mathrm{Cin} + \overline{(\mathrm{A} \oplus \mathrm{B} \oplus \mathrm{C} \oplus \mathrm{D})}.\mathrm{D} \end{aligned} \qquad (3.20)$$

Although the critical path's delay for this design is calculated as a delay of three XOR gates, due to the use of the best XOR proposed in this study (Model-1), the compressor's delay and power are reduced significantly compared to other designs. On the other hand, the proposed XOR in this article consists of five transistors that reduce the total number of transistors in the compressor by less than half.

Besides, the design shown in **Figure 3-7** has been selected to use in the compressor, among the existing designs for implementing multiplexers, which would be used in low-consumption applications most of the times Dadashi et al (2016) [153].

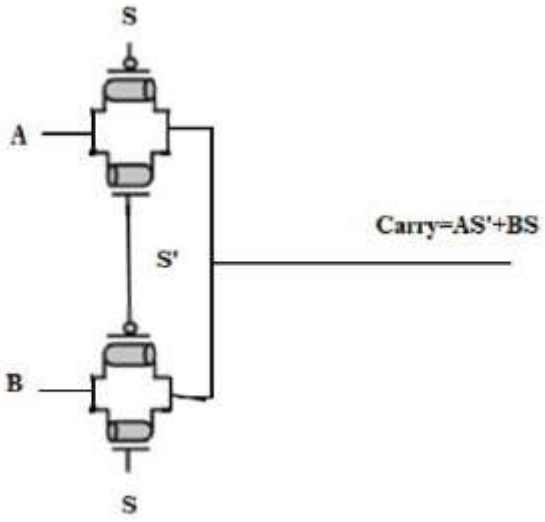

Figure 3-7: Multiplexer used in compressor (4:2).

3-8- Optical crystal gates based on point and linear defects

In this section, the structures that have high contrast ratio and low losses would be described. The proposed designs are based on the interference of waves. Also, the radius of point defects causes a resonance mode in the output.

Different numerical methods have been used to analyze optical crystal structures. The plane wave expansion method (PWE) and finite-difference time-domain method (FDTD) are more famous than other methods. In the PWE method, by the Fourier expansion of the electric field or the magnetic field, the electric permeability coefficient, and their placement in Maxwell's equations along with intermittent boundary conditions, a special value problem is solved. The FDTD method is a new method that provides a dynamic study for PBG structures. Based on Maxwell's equations' discretization, this method is a replacement of partial derivatives with a finite difference.

The material used in the proposed designs of this dissertation is silicon. As we know, silicon can provide different refractive indices based on its quasi-crystalline, crystalline, and amorphous structures. The reason why the silicon is used is the abundance of this material and the possibility of its high-quality artificial growth. Another reason for using this material is the developing of lithographic technology related to silicon structures that their precision has achieved in a nanoscale limit. Also, nowadays, optical properties and the technology of manufacturing optical devices in silicon-based complex circuits are well-known. The desired functional wavelength is also considered equal to the central wavelength of the telecommunication C-band (1550 nm). The proposed gate structure is a two-dimensional optical crystal with a square lattice of silicon rods in the air.

Optional band gaps are used for calculating the radius of the rods and the lattice constant, as shown in **Figure 3-8**. For designing the proposed gates, we have used a two-dimensional

optical crystal structure with a 15 × 15 square lattice of dielectric rods in the air (**Figure 3-8a**). The dielectric rods are made of silicon. In optical gates' design using two-dimensional optical crystals, the optical band gap of the structure must first be calculated and extracted. The best way to extract an optical band gap is to use numerical methods. One of the numerical methods is the plane wave expansion (PWE) method, which usually calculates the special frequencies of intermittent structures in the frequency domain by numerically solving the Maxwell equations. An optical band gap of the structure is obtained in a two-dimensional graph in lattice vectors by drawing these special frequencies.

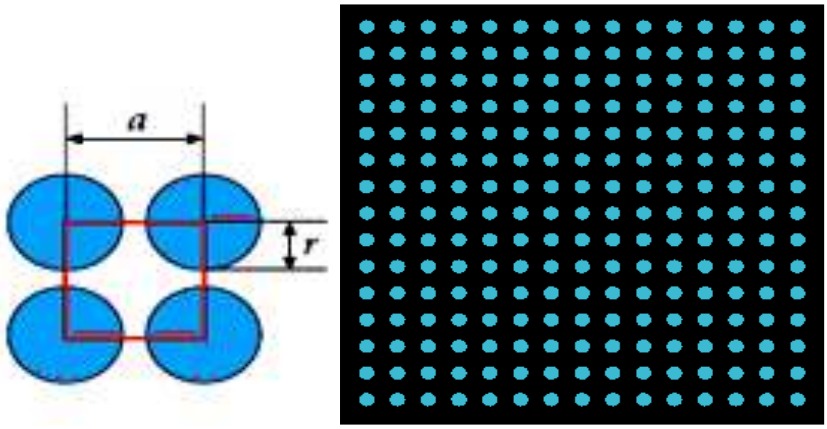

(a)

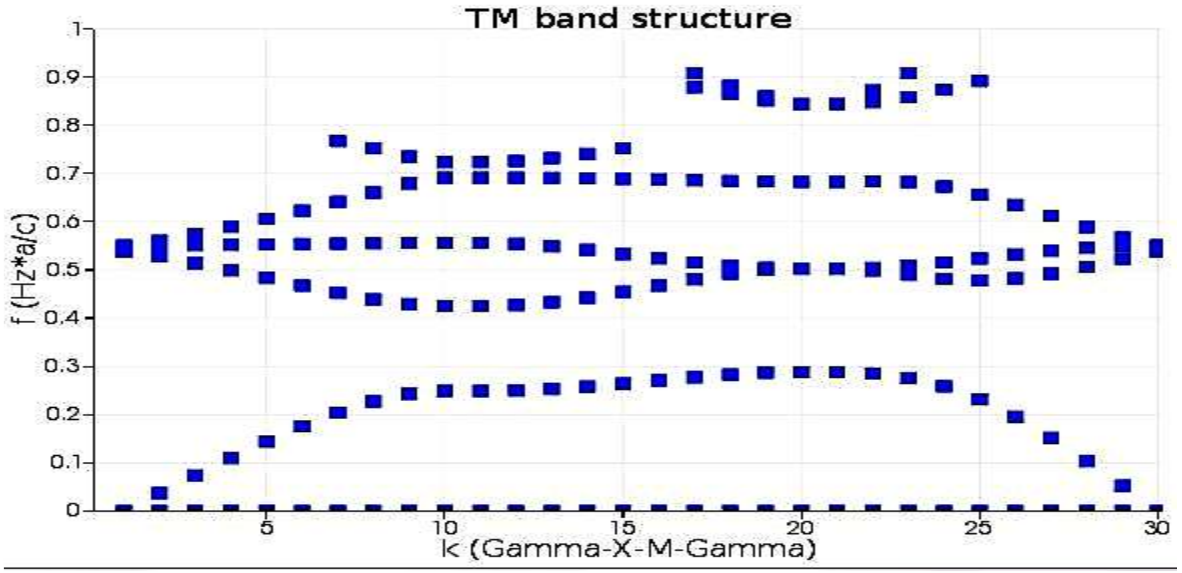

(b)

Figure 3-8: (a) Lattice structure (a and r are lattice constant and radius of rods, respectively) and (b) optical band gap of the proposed structure based on point and linear defects.

In **Figure 3-8 (a)** the rods' radius (r) is 0.2a, and the lattice constant (a) is 477 nm. These numbers are obtained based on the band gap analysis of the structure. As the band diagram

shows, for the radius mentioned, the band gap has been obtained in the frequency range of 0.28153 – 0.425395 for TM mode. First, the structure and operation process for the three base gates NOT, OR, AND would be discussed.

3-9- Photonic crystal AND gate based on self-collimated beams

Self-collimation (SC) allows self-guiding propagation in photonic crystals. As previously mentioned, a series of optical gates are designed using the self-collimating phenomenon. The self-collimating phenomenon is an interesting light guidance mechanism that, as described in detail in Section 2-7-3, allows divergent input beams to propagate parallel without using nonlinear effects Feitelson (1988) [162], Kosaka et al (1999) [25]. By this phenomenon, an electromagnetic wave with a certain frequency moves in the direction of propagation.

The self-sustaining phenomenon is independent of the incident radiation intensity and does not require a complete optical band gap in comparison with photonic crystal waveguides. Also, according to the comparison between the conventional dielectric waveguides and PBG-based crystal waveguides, there is no need for limitations with side effects to prevent divergence and refraction of the beams. Therefore, self-collimating devices have a high potential for optical complex circuits.

In the discussion of a logical AND gate, the proposed structure is independent of the input power intensity. Additionally, in this structure's design, linear materials have been used that greatly reduce energy consumption. To design the proposed structure, a square lattice of silicon rods is used. The radius of the rods and the coefficient of electrical permittivity are 0.35a and 12, respectively.

One way to parallelize the diffusion beams in photonic crystal (PhC) structures and create a self-collimating phenomenon is to reduce the rods radius instead of eliminating them to create a linear defect. This way leads to the overall reflection and leaves the partial reflection of the tunneling wave. Then, it is expected to see a phase difference between the reflecting beam and tunneling beam (transmission beam). Therefore, if another self-collimating beam is introduced with a suitable initial phase, the transmission or reflection beams may create a destructive or constructive interference and set logic and switching functions.

An important point in studying of this phenomenon is choosing an appropriate frequency with the requirements for the beams to be parallelized. **Figure 3-9** shows the dispersion diagram, and **Figure 3-10** shows the scattering diagram of the crystal lattice with the above characteristics.

This structure has been obtained by the plane wave expansion method for the polarized waves of TM. In **Figure 3-10**, the iso-frequency curve corresponding to a frequency around $0.194a/\lambda$ (λ, free space wavelength) is a square with rounded corners has an approximately flat region (no curvature) when propagating in the direction of the diagonal (i.e., in direction $\Gamma - M$). This means that, as the wavefront of the beam propagates perpendicularly to the iso-frequency curve (as discussed in Section 2-7-3), the beam will propagate without diffraction (self-collimation). Furthermore, in this propagation direction, the direction of the group velocity [which is defined

by **Equation (2.2)**] coincides with such direction. This means that the light beam will propagate forward. On the other hand, the value of the group velocity can be estimated from **Figure 3-9**, as it is given by the slope of the curve $\omega(k)$. Such slope must be calculated at the point where the red horizontal line (which corresponds to a frequency of 0.194a/λ) intersects the curve corresponding to the direction $\Gamma - M$.

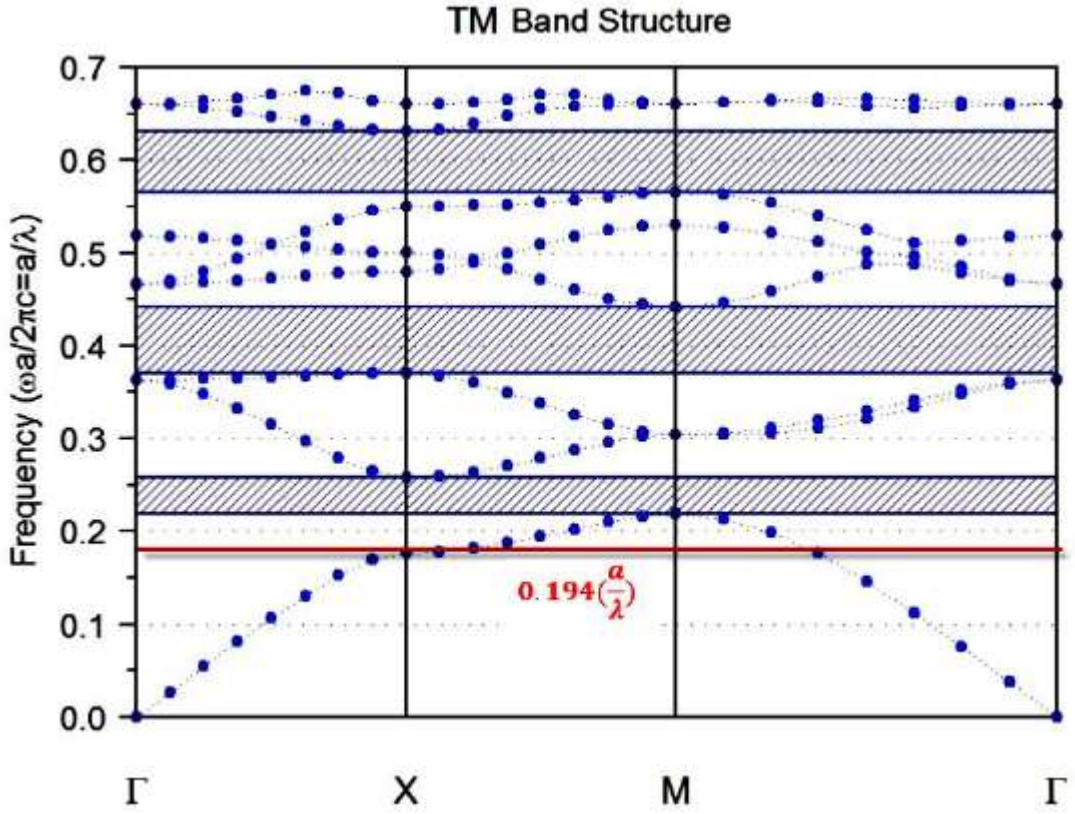

Figure 3-9: Dispersion diagram of the considered photonic crystal structure (frequency as a function of the wavevector, in different directions in the reciprocal space).

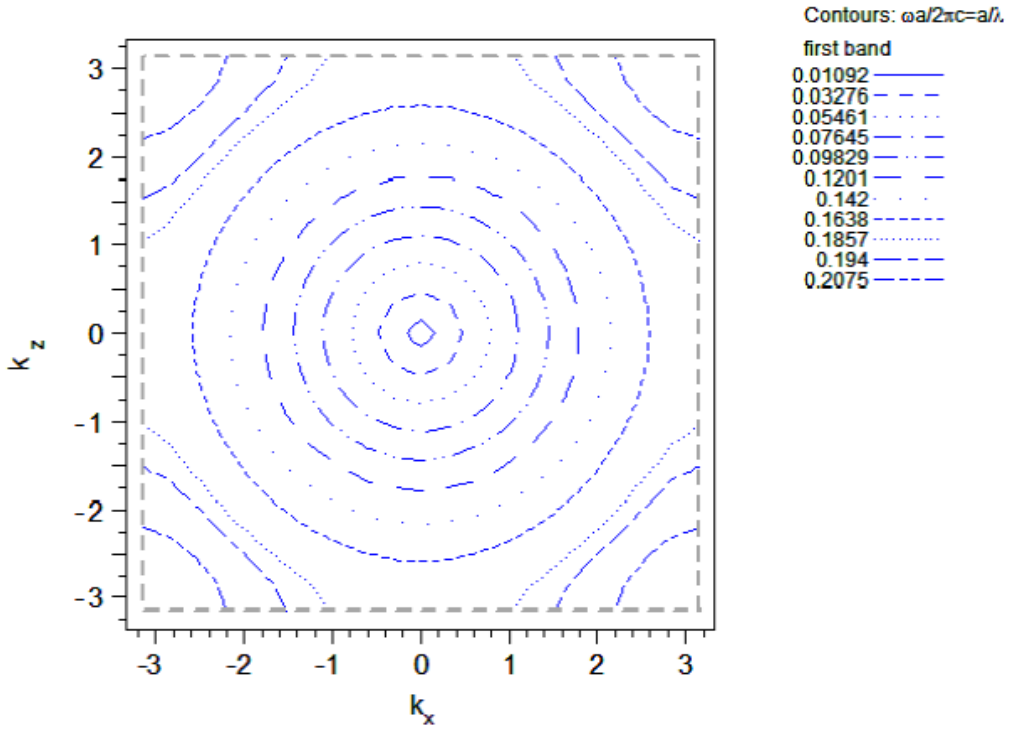

Figure 3-10: Equifrequency contours in the reciprocal (wavevector) space, for the same structure as in the previous figure.

In designing this structure, the TM polarized wave at a frequency of 0.194 (a/λ) is used for a presented logical gate. The provided logic gate in this structure also requires direct power divider devices. An optical power divider is a row of rods, which is arranged with a radius of r_d in the direction of ΓM. The power divider structure is depicted in **Figure 3-11(a)**. A Gaussian beam is applied to the structure at a frequency of 0.194 (a/λ) from the left. The values of Reflection (R) and Transmission (T) obtained from the radius of the rods are shown in **Figure 3-11(b)**.

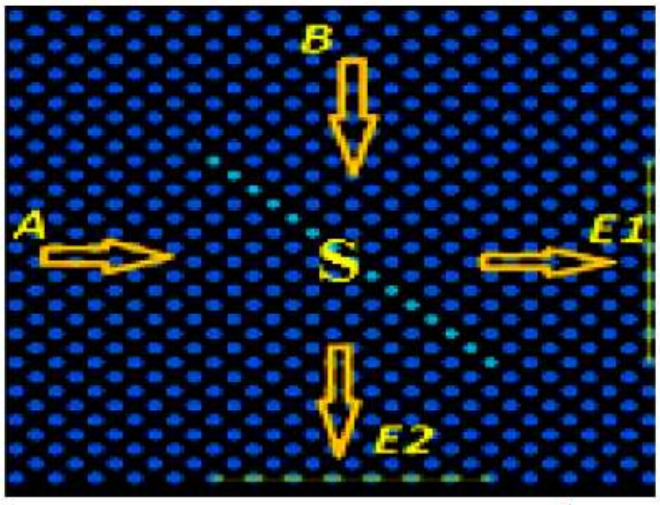

Figure 3-11(a): Optical divider using photonic crystals.

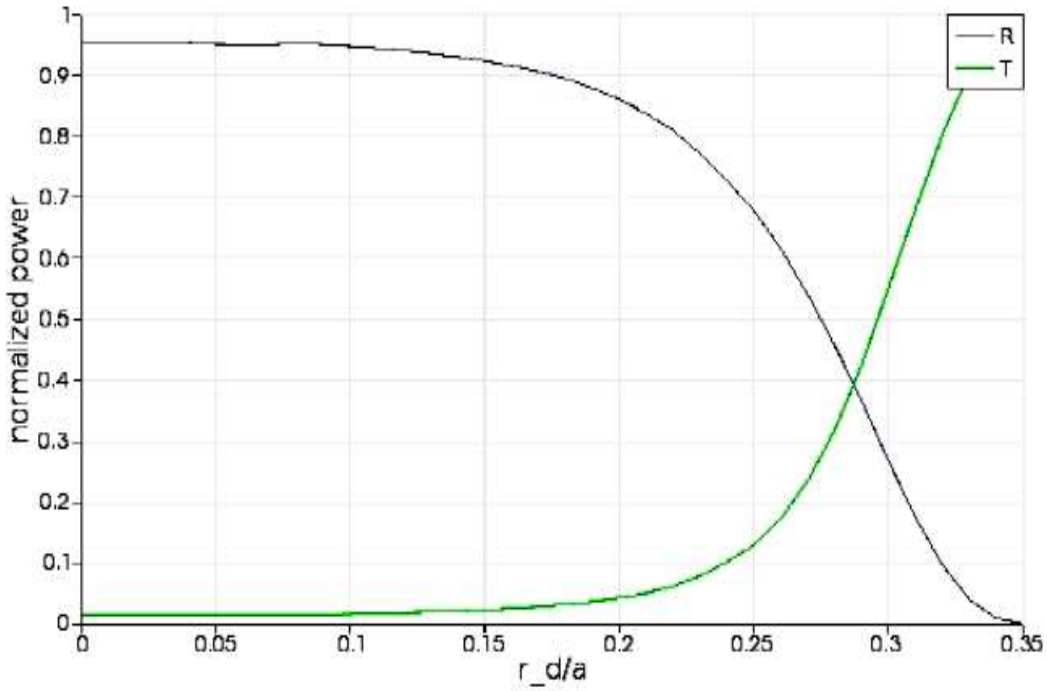

Figure 3-11(b): The transmission and reflection coefficients of optical divider versus radius changes.

Before applying the inputs for checking the switch function and logic functions, the phase difference between reflection and transmission beams must be determined. As compared to Feitelson (1988) [162], there is a phase difference between radiation and reflection beams. If the rod defection radius is smaller than the radius of the host rod, then while passing transmission and reflection beams through the divider, the delay of $\pi/2$ occurs between reflection and transmission waves. In contrast, if the rod defection radius larger than the radius of the host rods, then the delay of $-\pi/2$ is observed between reflection and transmission waves. Therefore, in this structure, in which the linear defect is created by reducing the rods' radius, the phase difference between reflection and transmission beams is $\pi/2$.

Given reference Feitelson (1988) [162], as applying two input beams to the structure, the optical divider outputs are as follows (**Equation 3-21 and 3-22)**:

$$I_{E_1} = \left|uE\right|^2.\left(1+\sin\left(\varphi_1-\varphi_2\right)\right) \qquad (3.21)$$

$$I_{E2} = \left|uE\right|^2.\left(1-\sin\left(\varphi_1-\varphi_2\right)\right) \qquad (3.22)$$

If $\varphi_1-\varphi_2 = 2k\pi+\frac{\pi}{2}$, then $I_{E_1} = 2\left|uE\right|^2$ and $I_{E_2} = 0$.

Figure 3-12 is for AND gate design. In this structure, two dividers of S_1 and S_2 and mirrors of M_1 and M_2 have been used. S_1 and S_2 are partial reflectors, and M_1 and M_2, general reflectors.

The structure has two input ports, A and B, and one output port I **Equation 3-23 and 3-24**. The optical path difference between two optical beams has been used to create a phase difference of $\pi/2$ with accordance to the relationship of $\Delta\varphi = K.\Delta L$. Suppose the divider outputs are S1, E1, E2, and then a coherent light beam of intensity I can be measured as follows:

$$I = E_1^2.T + E_2^2.R + 2E_1E\sqrt{RT}.\cos\varphi \qquad (3.23)$$

$$\varphi = 2\pi\frac{\Delta L}{\lambda} - \Delta\varphi \qquad (3.24)$$

R and T are the reflections and transmission coefficients of the reflector S_2. $\Delta\varphi$ is the phase difference between reflection and transmission beams, which is determined by the reflector radius, as well as ΔL is the optical path difference of two partial reflectors.

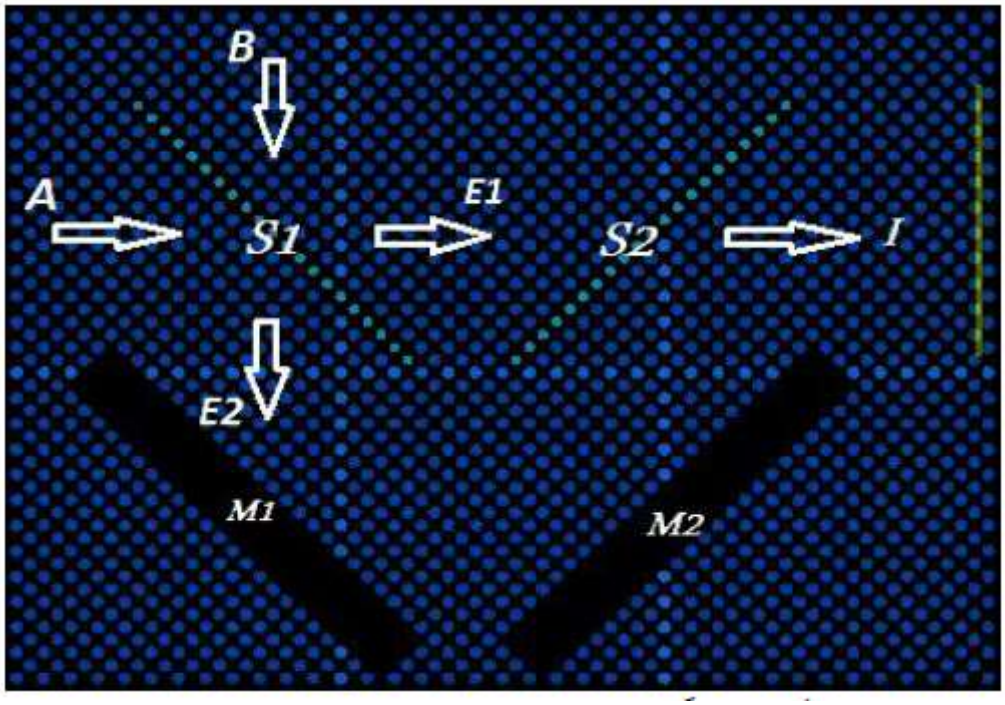

Figure 3.12: The proposed AND gate based on a self- *collimating* phenomenon.

Therefore, when the input beams A and B are applied to the structure, then we have $E_2 \cong 0$ and subsequently, the output will be $I = {E_1}^2.T$. When only one input is applied to the structure, the output must be zero to realize the AND gate. Concerning **Equation 3-23**, when $\cos\varphi = -1$, then the output I will have the smallest value. To get this value using **Equation 3-24**, the phase delay of $\pi/2$ will occur between the transmission and reflection waves. The deflection radius in the partial reflectors is smaller than the radius of the host rod. Therefore, the desired output can be achieved from the optical path differences of $18\sqrt{2a}$ between the two optical dividers.

The field distribution of the suggested AND gate for different input modes is obtained using a finite difference method in the time domain and is shown in **Figure 3-13**.

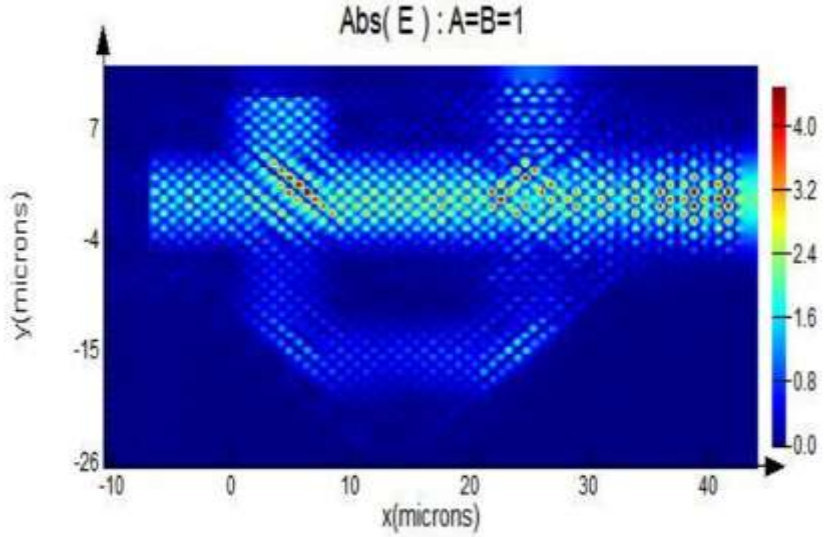
Abs(E) : A=B=1
y(microns)
7
-4
-15
-26
-10
0
10
20
30
40
x(microns)
4.0
3.2
2.4
1.6
0.8
0.0

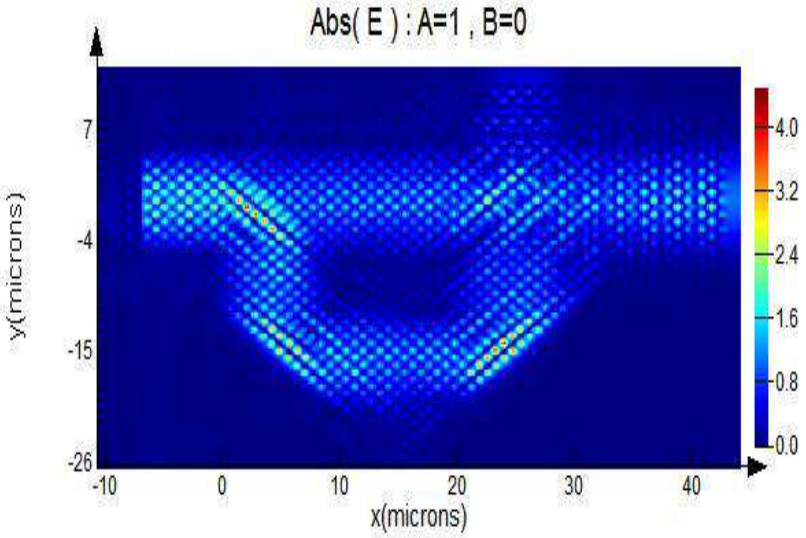
Abs(E) : A=1 , B=0
y(microns)
7
-4
-15
-26
-10
0
10
20
30
40
x(microns)
4.0
3.2
2.4
1.6
0.8
0.0

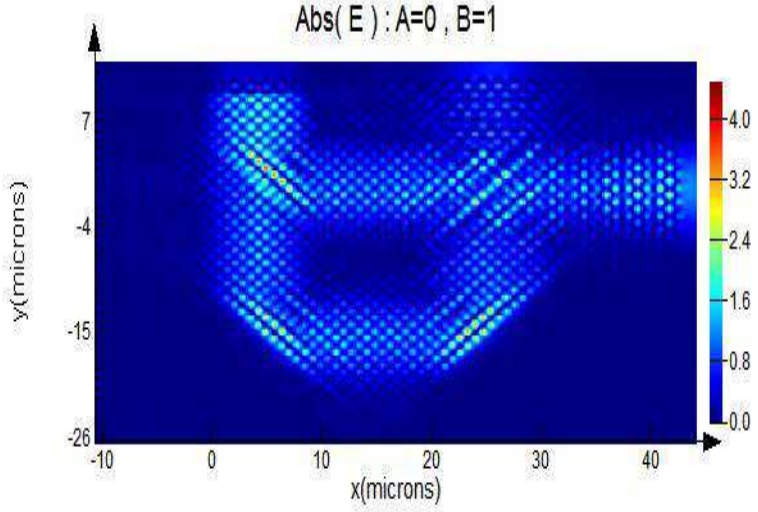
Abs(E) : A=0 , B=1
y(microns)
7
-4
-15
-26
-10
0
10
20
30
40
x(microns)
4.0
3.2
2.4
1.6
0.8
0.0

Figure 3-13: The field distribution of a proposed AND gate based on the self-collimating phenomenon for different input states (finite difference method in the time domains).

The structure acts as the OR gate. In this structure, point defects play an important role in transferring power to the output port and reducing reflection.

As a result, it requires specially designed components with smaller sizes while being efficient. Optical logic gates are one of the most paramount components for optical integrated circuits. The small size of these structures is an important advantage that allows their use in optical integrated circuits. Therefore, photonic crystal-based logic gates collected the most significant optical components due to their low loss, high performance, and small size. The contrast ratio between logic "0" and logic "1" for the self-collimating-based proposed AND gate in Section is 12.8db. The contrast ratio based on the self-collimating phenomenon for optical AND gates in Christina and Kabilan.(2012) [156] and Xavier et al (2014) [157] is 6dB and 10dB contrasts respectively. The gate presented in Christina and Kabilan.(2012) [156] has smaller dimensions than the self-collimating-based proposed AND gate, but the contrast ratio of the scheme presented in this research Section is higher. Additionally, these gates require an additional control signal to accomplish the AND logic gate operation, which increases the power consumption of the structures.

3-10- Numerical Methods

Most of the (PhCs) structures rely on the bandgap effect and consist of defects in an otherwise perfectly periodic PhC. Although a three-dimensional (3D) PhC has better light confinement capability, a PhC slab that has a two-dimensional (2D) periodic pattern in a layered medium is much easier to fabricate and widely used. A typical PhC slab consists of a triangular lattice of air holes in a high-index dielectric slab surrounded by lower-index media. In a PhC slab, a waveguide can be introduced by filling a row of air holes.

To design and optimize PhC slab waveguides, efficient numerical methods are needed for computing the waveguide modes. The 3D finite-difference time-domain method has been used to analyze PhC slab waveguides, but it requires a long computing time. This is especially true for structures with large index contrast, where a very small lattice size is needed to resolve the interfaces. In the frequency domain, the standard formulation leads to an eigenvalue problem in a 3D region S that covers one period along the waveguide axis and is unbounded in the two transverse directions. To find the dispersion relations of the waveguide modes, the eigenvalue problem must be solved for various values of the propagation constant (the Bloch wavenumber). Standard numerical methods, such as the plane-wave expansion method, and the finite element method, can be used to solve this eigenvalue problem. For the finite element method, it is necessary to truncate the unbounded directions of S and discretize the truncated domain. For the plane-wave expansion method, the unbounded directions of S may be truncated with periodic boundary conditions, and then the electromagnetic fields are expanded into the Fourier series. All these methods give rise to matrix eigenvalue problems involving very large

matrices. To find accurate solutions for the waveguide modes by these methods, prohibitive computer resources (including both CPU time and memory) are usually needed. In an alternative frequency-domain formulation, a PhC slab waveguide can be analyzed for given frequencies with eigenvalues related to the Bloch wavenumber. This can be achieved by using the scattering matrix for one period of the PhC slab waveguide.

The eigenvalue problem is linear even for dispersive media, and the involved matrices are smaller but nonsparse. Unfortunately, this approach is still quite expensive since it is not easy to calculate the scattering matrix and also the eigenvalue problem with dense matrices. Furthermore, an even smaller is not easy to solve, but a nonlinear eigenvalue problem was obtained using a lateral scattering matrix formalism, but these scattering matrices are calculated based on a lateral staircase approximation of the structure, which limits the accuracy.

3-11- Frequency-Domain vs. Time-Domain

There are two common computational electromagnetic approaches to study the dielectric structures: frequency-domain and time-domain. Each one has its own place in a researcher's toolbox and its unique advantages and disadvantages. The MIT Photonic Bands (MPB) package is frequency-domain**.** It does a direct computation of the eigenstates and eigenvalues of Maxwell's equations using a plane wave basis. Each field computed has a definite frequency. In contrast, time-domain techniques mention Maxwell's equations in time Taflove and Hagness(2005) [2]- Sadiku (2017) [158]-Kang Ning et al (2017) [159] .

3-11-1- The disadvantage of Frequency-Domain vs. Time-Domain

A traditional disadvantage of frequency-domain methods was that you had to compute all of the lowest eigenstates, up to the desired one, even if you didn't care about the lower ones. This was especially problematic in defect calculations, in which a large supercell was used because the lower bands were "folded" many times in the Brillouin zone. Thus, you often had to compute a large number of bands to get to the one you wanted, incurring high costs both in time and in storage Taflove and Hagness (2005)- Sadiku (2017) Kang Ning et al (2017) [25]-[158]-[159].

3-12- MPB Software Package

MPB is a software package to compute definite-frequency eigenstates of Maxwell's equations in periodic dielectric structures. It can compute optical dispersion relations and eigenstates for structures such as strip waveguides and optical fibers. MPB is well suited for studying **photonic crystals:** periodic dielectric structures are exhibiting a band gap in their optical modes and prohibiting propagation of light in that frequency range. High-performance 3D/2D (*FDTD*) Maxwell's solver for design, analysis, and optimization of nanophotonic devices and processes, which is used in this work, is *Version* S2019A-R1 (8.21.1781) Olyaee et al (2019) [101].

3-12-1- The disadvantage of the MPB Software Package

The disadvantages of frequency-domain versus time-domain disappear to some degree in MPB. However, the targeted eigen solver method used in MPB still has poor convergence, so time-domain methods such as Meep still have an advantage here Taflove and Hagness (2005)- Kang Ning et al (2017) [25]-[159]. FDTD can give almost arbitrarily accurate answers to the macroscopic Maxwell's equations for any geometry. This could be further improved by repeating many of the steps.

3-13- Demultiplexer design

Before presenting the optimal design method, first, the procedure of the quality factor calculation (Q factor) would be discussed. It is necessary to describe the performance of a multi-channel filter. There are two main methods for calculating the Q factor. In the first method, since the electric field amplitude decreases exponentially, the Q factor can be calculated by **Equation 3-25**.

$$Q = \frac{w_r(T_1 - T_2)\Delta t}{2\ln(\frac{E_1}{E_2})} \qquad (3.25)$$

Where E_1 and E_2 are electric fields in time steps T_1 and T_2, respectively.

In the second method, **Equation 3-26** is utilized.

$$Q = \frac{\omega}{\Delta\omega} = \frac{\lambda}{\Delta\lambda} \qquad (3.26)$$

Where ω is the angular resonant frequency, $\Delta\omega$ is the bandwidth mode, λ is the resonant wavelength, and Δλ is the half power bandwidth.

The shape of the proposed demultiplexer structure is shown in **Figure 3-14**, which consists of three main parts, (a) a horizontal input waveguide in the middle of the structure, (b) six output waveguides at the top and bottom parts, and (c) six circular resonance rings located between the input waveguide and each of the output waveguides. This structure consists of one input channel, and seven output channels called C', C, B', B, A', A, and D.

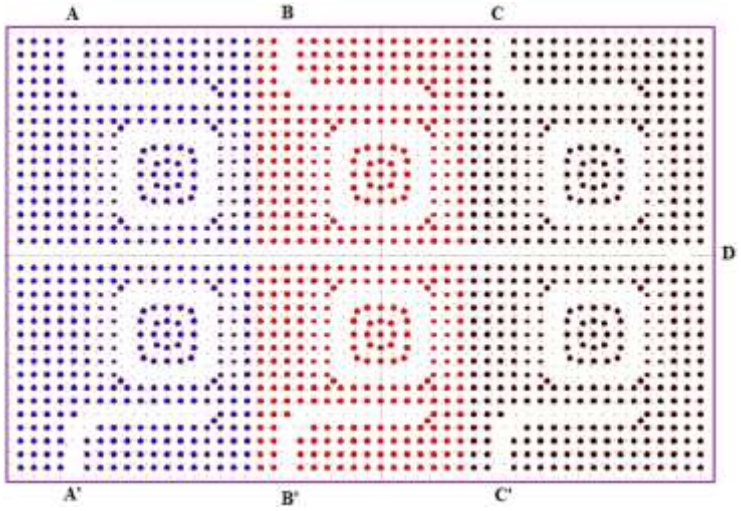

Figure 3-14: Proposed design structure.

The input waveguide enters light into the resonator. It is created using a linear defect. In the simulation environment, the main and output waveguides are created by selecting certain points and deleting them. The same method is used for resonant loops. The rod must be selected and located in the Z and X directions to place the dielectric rods.

Compared to cavities, photonic crystals with point or linear defects offer resonant rings which are scalable in size and flexible in fashion design due to their multifaceted nature. Resonant rings are a new type of cavity defect whose size is determined by the desired resonance wavelength. Resonant rings are obtained by removing a ring shape from dielectric cells in a square lattice. For different applications, the loop selection is determined by the desired resonance wavelength and the relationship between ring's Q factor and the specified ring volume. By placing the resonant ring and the waveguide close together, the waveguide's electromagnetic energy will be trapped in the resonant ring. This is due to the coupling between the waveguide and the resonant ring at the resonant frequency. The basis of this filter is the interaction between the waveguide and the hole.

In **Figure 3-15**, supercell dimensions are selected as 7a × 7a, and the optimal number of bands required for calculating the structure of the supercell in the band is 77 = 7× (7 + 4). To improve the spectral selectivity and increase the coupling efficiency, four scatter bars have been added with green colors in the structure, which have similar characteristics to other cells to perform better in the structure but have no effect on wavelength. These bars are displaced about half of the lattice constant from their original position. The effect of back reflection is minimized in the sharp corners of the resonant ring, which creates undesirable modes. The important point is that the values and the radius of scattering rods are obtained through trial and error by performing a few simulations. Coupling rods and adjacent rods are marked in red and yellow in **Figure 3-15**, respectively, and their difference with the dielectric rods of the lattice have a radius of 97% and 87% for better transmission.

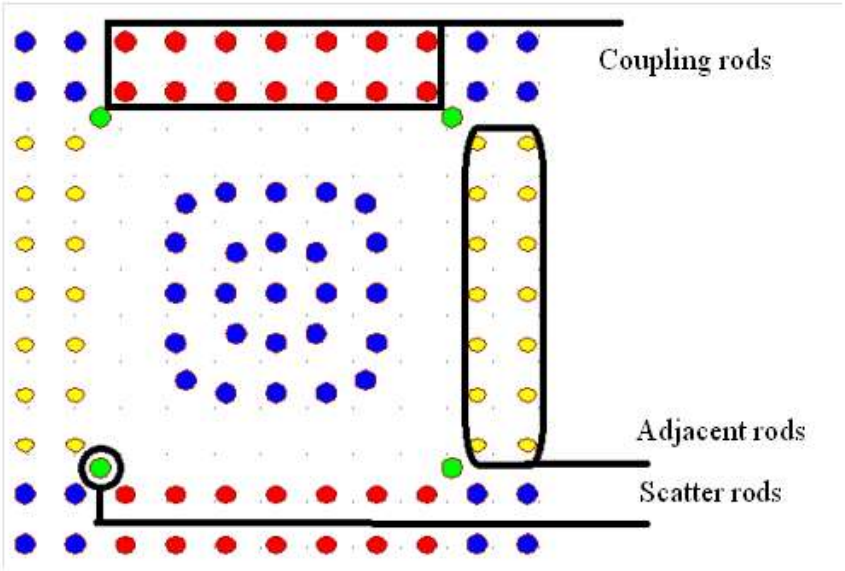

Figure 3-15: Structure of ring resonator with selected supercell for calculating resonant modes.

To improve the transmission power of ports C and C ', B', B, A ', A, and to obtain the maximum transmission efficiency, the radius of the adjacent rods is 0.87r, where r is the rods' radius. The upper resonators of the design have a coupling rod radius of 0.97r, and the lower resonators have a coupling rod radius of 0.93r. As shown in **Figure 3.15**, the ring's inner rods embedded in the corners are shifted to the center of the ring, which is a quarter of the lattice constant, allowing the ring to look like a circle.

The operation of multi-channel filters will be based on coupling the resonant rings' cavity modes and the guided waveguide modes. When a resonant ring is coupled to a waveguide with a linear defect, it traps photons at a specific wavelength and emits them in the waveguide. In return, this leads to the transmission of power from the bus waveguide (main waveguide) to a waveguide that the light falls in a specific wavelength, and the filter operates in a specific wavelength.

Given that each cavity of the photonic crystal structure only intensifies at a certain wavelength. Therefore, to perform such complex calculations, the numerical method of 2D Finite Difference Time Domain (2D FDTD) must be used. In the algorithm of finite time domain equations, the Cartesian lattice replaces the Maxwell equations to obtain boundary condition calculations in very small cell dimensions. Therefore, in the proposed design to calculate and obtain the desired wavelength spectra of the resonance cavity region of two-dimensional photonic crystal demultiplexer, Full-wave simulator software will be utilized.

Chapter 4

Proposed photonic crystal gates designs

4-1- Introduction

In this chapter, six structures would be proposed. Four of these structures implement functions of logical gates, one works as a 2DPC demultiplexer, and the last one is a gas sensor. This chapter introduces new designs with an appropriate contrast ratio, and the goal in their design has been to improve the reflection on the proposed designs' input ports. The operation of logical structures in the same wavelength is essential for ease of integration.

4-2- Optical crystal gates based on point and linear defects

Having a high contrast ratio and minimum losses in optical crystal gates is very important. The change of structure’s characteristics such as form and radius of rods, the shape of cavities, the lattice constant, and the dielectric constant of rods leads to better control in features of losses and improvement of contrast ratio.

First, the structure and operation process for the three base gates NOT, OR, AND would be discussed. And next, with coupling the gates, we will also propose structures to implement NOR and NAND gates.

4-2-1- Introduction and review of proposed NOT gate structure

As shown in **Figure 4-1**, in order to design the NOT gate, two linear waveguides and two-point defects are used in the structure. Linear waveguides are created by removing a series of rods (missing rows of defects in an otherwise periodic distribution are known as linear defects). The distance between the two dielectric rods is known as the structure constant.

This structure includes an input waveguide for the introduction of a Gaussian optical pulse at a wavelength of 1550 nm. Furthermore, the structure also contains an input path for a control signal with the continuous light flow that is applied permanently to the device. This control signal is of the same wavelength as the one of the input signal of the gate.

Point defects are placed around the center of the structure. Assume that the input light beam $E_1 = uEe^{i\varphi_1}$ is introduced into input "In" and the light beam of $E_2 = uEe^{i\varphi_2}$ into the control signal input path. E represents a plane wave in these expressions, u being the wave envelope, with the same spatial period as the PC structure.

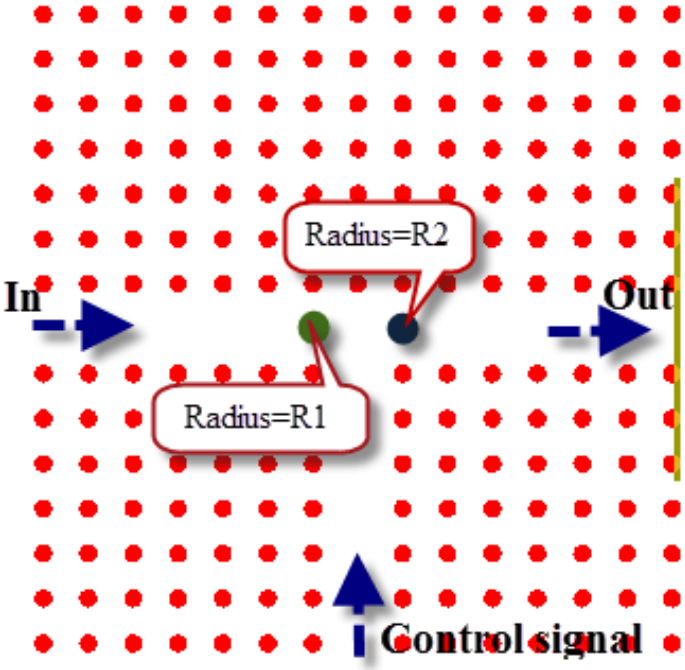

Figure 4-1: Schematic of the NOT gate based on point and linear defects.

The beam injected to E_1 traverses a direct path to the output, the beam injected to E_2 enters into the waveguide with a phase difference of $\pi/2$ Goudarzi et al (2016) [63].

the amplitude of the intensity of the output beam (its module) can be expressed as**:**

$$I = |out|^2 = |E_1 + E_2|^2 = 4|uE|^2 \cos^2(\frac{\varphi_1}{2} - \frac{\varphi_2}{2} - \frac{\pi}{4}) = 2uE(1 + \sin(\varphi_1 - \varphi_2)) \quad (4.1)$$

Concerning **Equation 4-1**, when the output of the I is zero, then $\sin(\varphi_1 - \varphi_2) = -1$ and the equality of $\varphi_1 - \varphi_2 = 3\pi/2$ can be obtained. To create this phase difference between the two input beams, a point defect with the radius of R_1 is used **Equation 4-2**. To obtain the radius of R_1 **Equation 4-2** can be used Goudarzi et al (2016) [63]:

$$\Delta\varphi = K\Delta L = \frac{2\pi}{\lambda} n.2\Delta R_1 \quad (4.2)$$

$\Delta\varphi = \frac{3\pi}{2}$, and the parameters of λ and n are wavelength and refractive index of the structure, respectively.

To control the power transmission at the out port, a point defect with the radius of R_2 is used. The radius of this rod is larger than the radius of the selected host rods. To obtain more power at the output. **Figures 4-2 and 4-3 are plots of** the power transfer and contrast ratio, respectively.

According to **Figure 4-2,** the power delivered to the output is maximum when the radiuses of the defects are 0.15 μm= 0.3a and 0.26 μm= 0.55a (It can be seen that the maximum output (P_{out} / P_{in}) happens when the radius of R_2 is 0.26 μm). On the other hand, in **Figure 4-3**, the smallest contrast ratio is obtained around a radius of 0.26 μm. Thus, to set the power transfer in the output port and to obtain the appropriate contrast ratio in designing this gate, the point defect radius of 0.15 μm is selected.

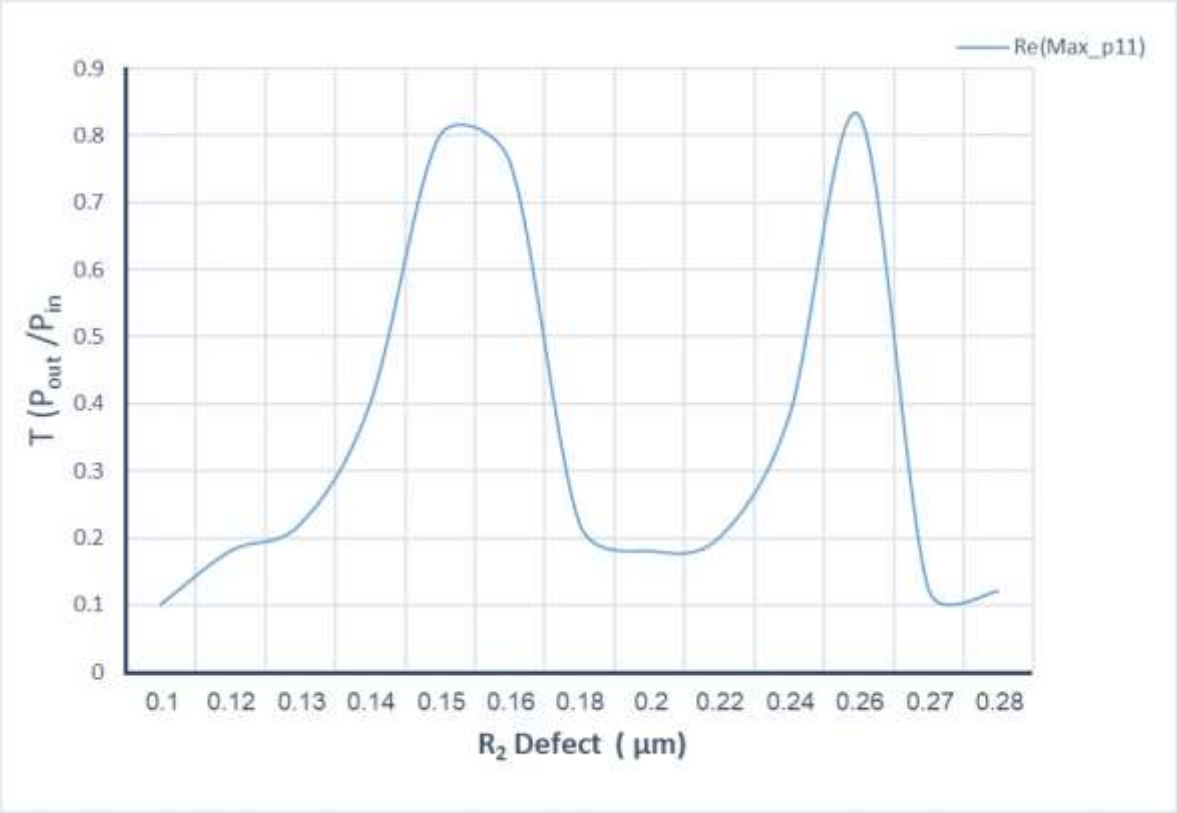

Figure 4-2: The ratio of the output to the input power of NOT gate versus R_2 defect radius (maximum transmission power at the output obtained from the radius of point defects).

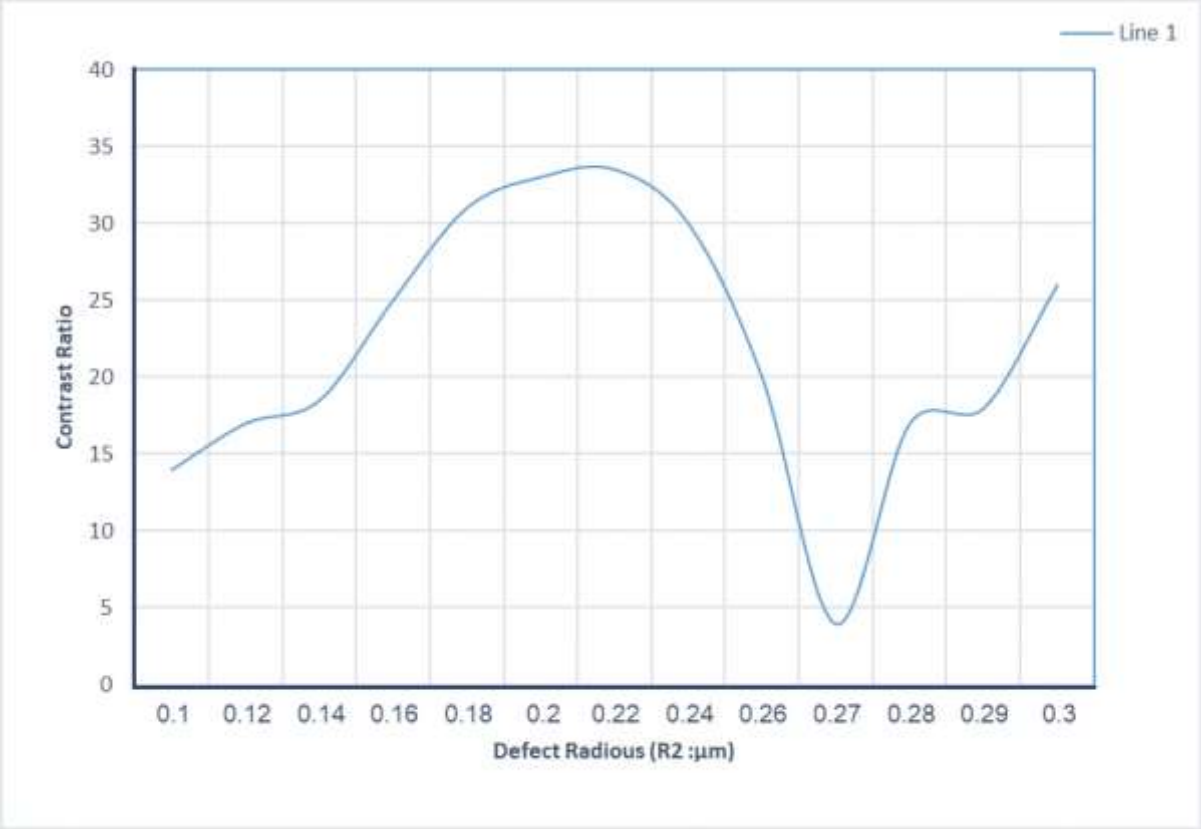

Figure 4-3: The contras ratio of the NOT gate versus R_2 defect.

In this structure, the phase and power of the inputs are the same. We can see the field distribution for the NOT gate outputs in **Figure 4-4 (a) and (b)**. In this case, we studied two states, state one (in=1) and state two (in = 0). The simulation results and **Table 4-1** show that the proposed structure's performance is as the NOT gate. In the state one (in = 1) shown in **Figure 4-4(a)**, the created phase difference by a point defect radius of R_1 in the input beams causes the power received at the output to be very low, which is equivalent to logical "0".as shown in **Figure 4-4 (b).** In contrast, in state two (in = 0) the control signal is transmitted to the output by an amplified point defect radius of R_2 .

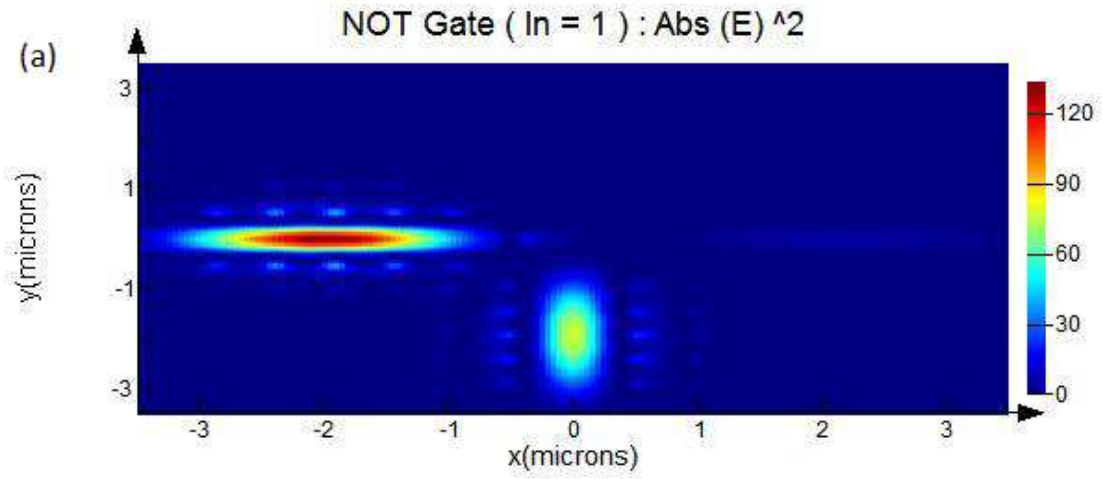

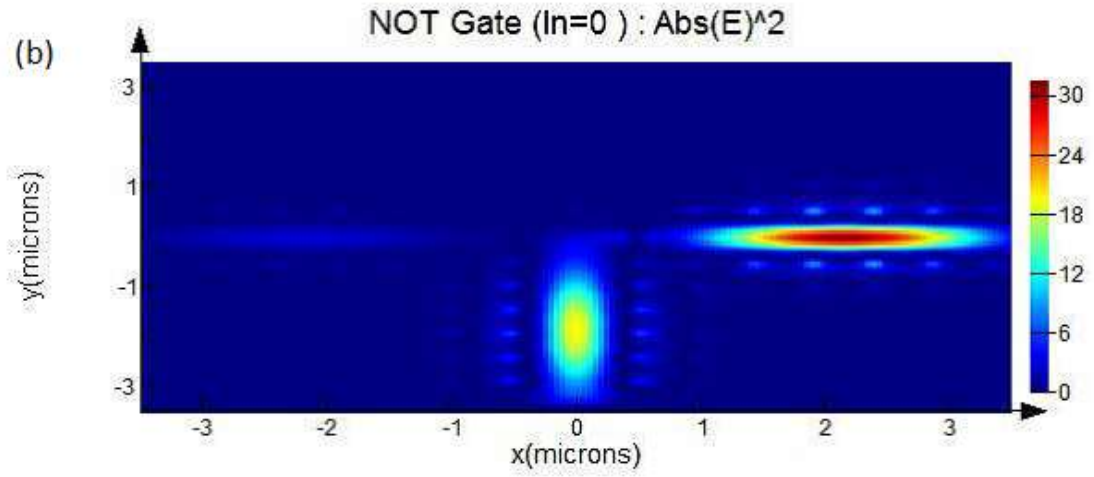

Figures 4-4(a) (in = 1), 4-4(b) (in = 0): NOT gate field distribution for different input states. (a point defect radius and an amplified point defect radius).

Table 4-1: Point and linear defects-based NOT gate.

Input (in)	Control signal	Logical value	Output (P_{out} / P_{in})
0	1	1	0.82
1	1	0	0.073

4-2-2- Introduction and review of the suggested OR gate structure

To design the OR gate, a structure related to the NOT gate described above is used. In it, the radius of the pillars and the lattice constant are the same. The schematics of the OR gate are shown in **Figure 4-5**. The structure also includes two input waveguides, A and B, for a Gaussian optical signal arrival with a 1550 nm wavelength and a point defect.

Point defect's radius has a considerable role in concentrating field energy and in reducing reflections to obtain the highest power possible transferred to the output. The point defect's radius is optimized to obtain the highest contrast ratio. In **Figure 4-6** it can be seen that the maximum power is obtained at the output port for radiuses of 0.15 μm= 0.3a and 0.25μm ≅ 0.52a (It can be seen that the maximum output (P_{out} / P_{in}) happens when the radius of R is 0.25 μm.). But considering that this structure is used in designing NOR gate and regarding to **Figure 4-3**, to obtain the proper contrast ratio between the logic "0" and logic "1" in the proposed NOR gate, the point defect radius of 0.15 μm is selected. This structure also includes two input waveguides, A and B, for the entrance of an instant signal with a wavelength of 1550 nm and

a point defect. The ratio of output power to input of OR gate is obtained in terms of point radius changes.

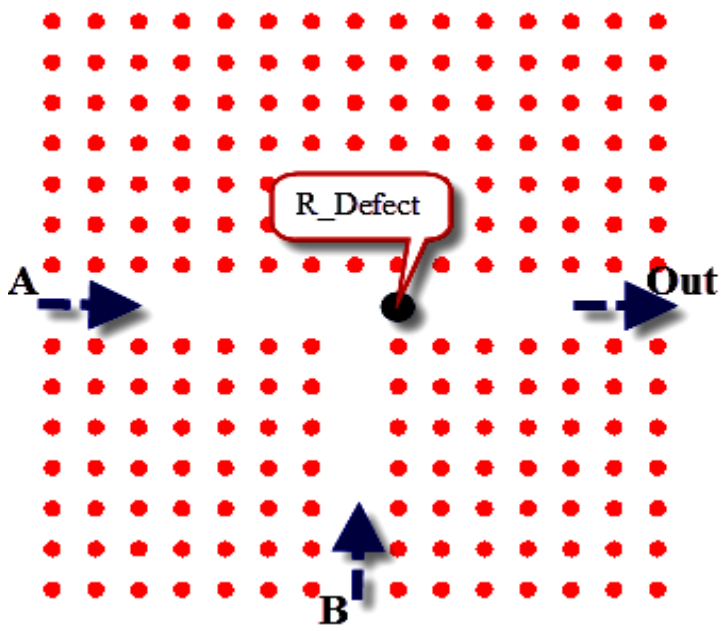

Figure 4-5: Schematic of point and linear defect based OR gate.

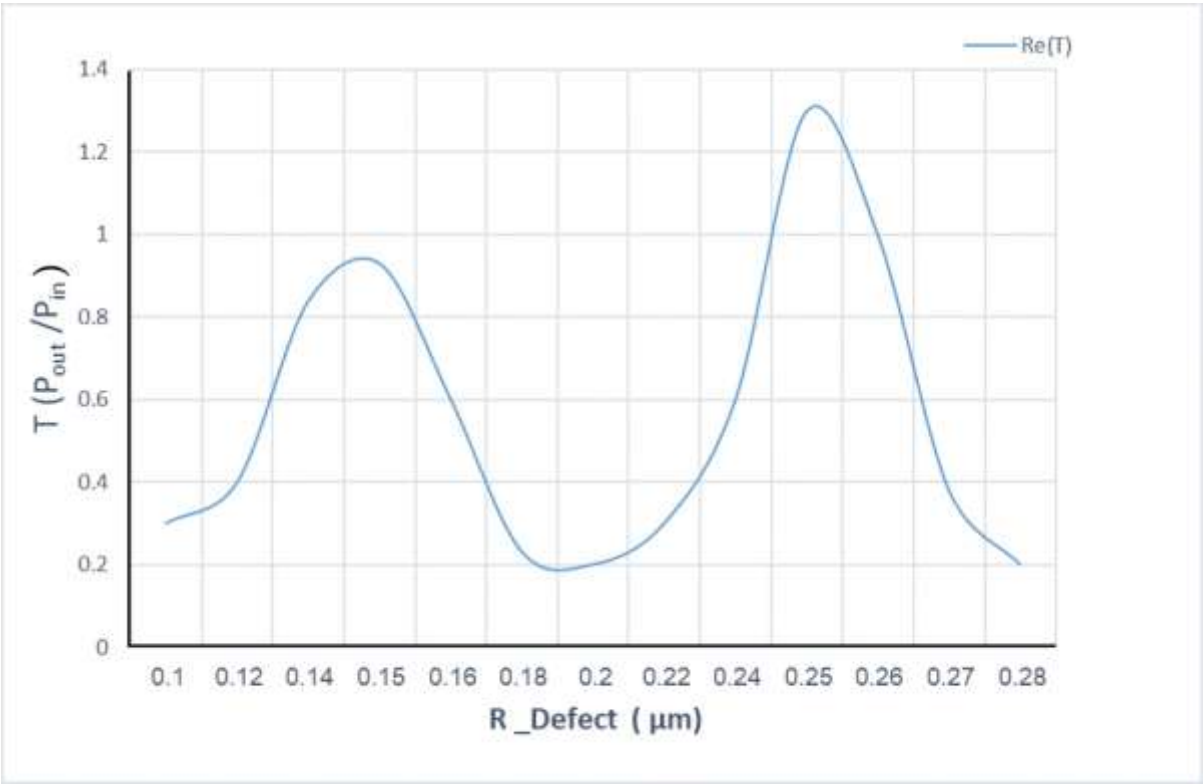

Figure 4-6: The ratio of the output power to the input power of the OR gate versus the variation of the point defect radius (maximum transmission power at the output obtained from the radius of point defects).

The field distribution of the proposed OR gate for different input modes is shown in **Figure 4-7**. Also, it is shown that four states are studied; in the first state, both inputs are logical "0"; therefore, there is no light propagation to the output. In the second state (A=0, B=1) shown in **Figure 4-7(a),** in the third state (A=1, B=0) shown in **Figure 4-7(b)** and in the fourth state (A=1, B=1) shown in **Figure 4-7 (c)**.

The results of the field distributions and the content of **Tables 4-2** show that the structure acts as an OR gate. According to **Table 4-2**, when A and B are both “1” (state 4), we have the most power in the output, and when A=”0” and B=”1” (state 2), we have the lowest output power in this structure, point defects play an important role in transmitting power to the output port and reducing the reflection.

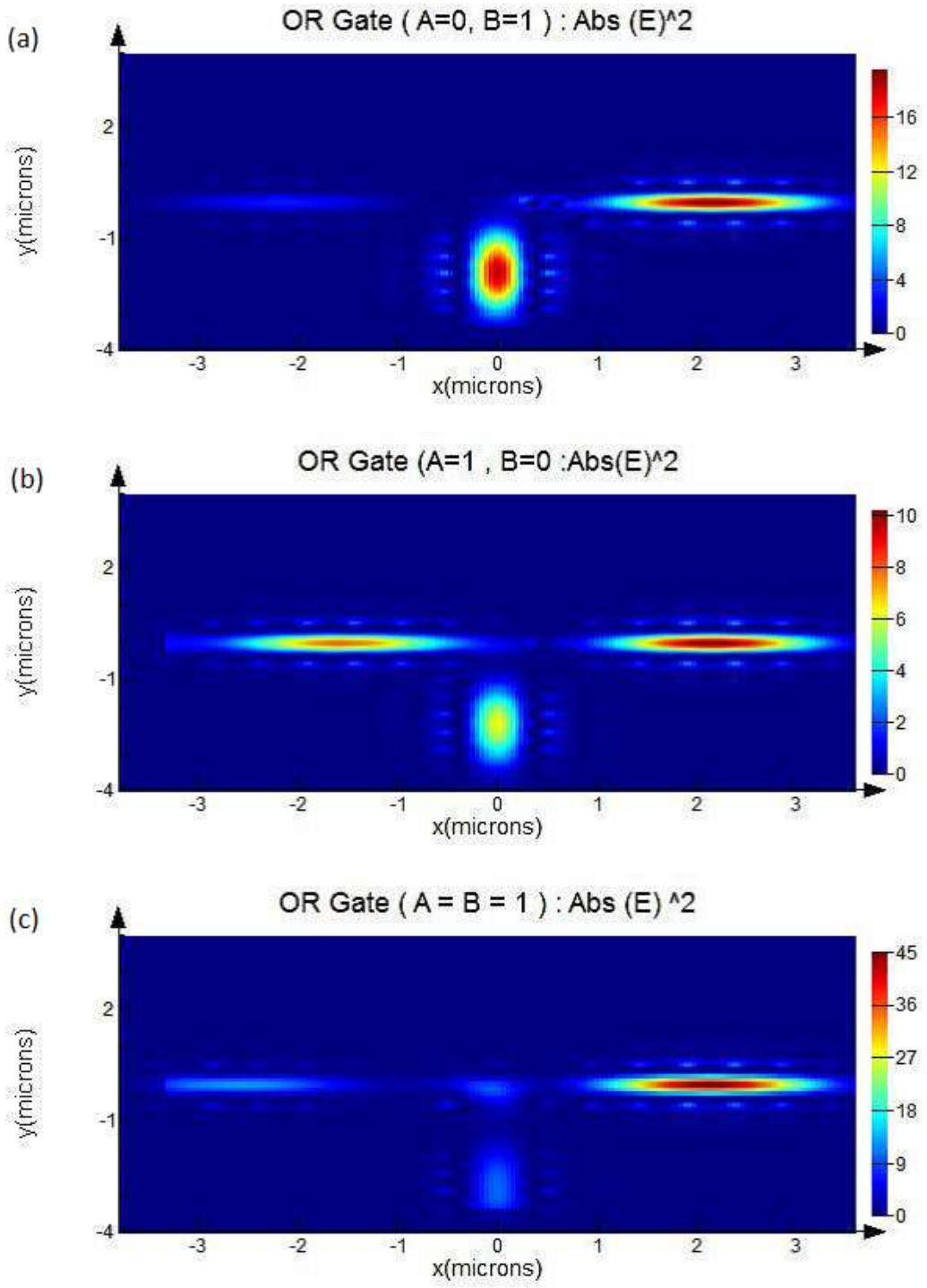

Figure 4-7(a) (A=0, B=1), (b) (A=1, B=0), and (c) (A= B=1): Field distribution of OR gate for different input modes (figures depicted differentiate the result of the various values of A and B).

Table 4-2: Truth Table of points and linear defect based OR gate.

Input A	Input B	Logical value	Output (P_{out} / P_{in})
0	0	0	0
0	1	1	0.62
1	0	1	0.73
1	1	1	0.93

4-2-3- Introducing and reviewing the suggested AND gate structure

For designing the AND gate, which is similar to the NOT gate, a square lattice of silicon rods in the air, with the same radius and lattice constant, is used. The proposed structure for the AND gate is shown in **Figure 4-8**.

We have two input ports in this structure, A and B, in which the input signals with the same wavelength (1550 nm) are applied to the structure . Also, the structure includes an input control port, in which a continuous signal with the same wavelength as the inputs (1550 nm) with zero phase is applied to the structure. To design the AND gate, the binary phase-shift keying (BPSK) is used. The applying phase modulation (BPSK) instead of intensity modulation On-off keying (OOK) reduces the noise ratio of the input signal. In this condition, the system performance's dependency to the input signals intensities would be reduced Tang et al (2016) [68]. In this case, the output value is measured based on light intensity.

In the phase modulation (BPSK), depending on the input state (0 or 1), the input signal phase switches between two modes of 0 and π. In a way that if the input is "1", then the input phase is considered "0", and if the input is "0", then the input signal domain will not change, but the input signal phase is π. The point defect radius is optimized to obtain the maximum power transfer in the output, which equals to 15 μm.

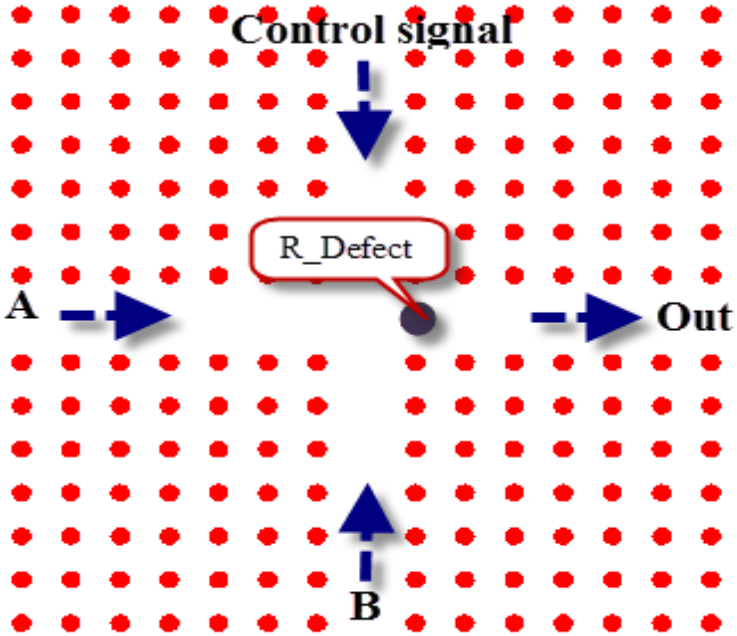

Figure 4-8: Schematic of the proposed point and linear defect Based AND gate.

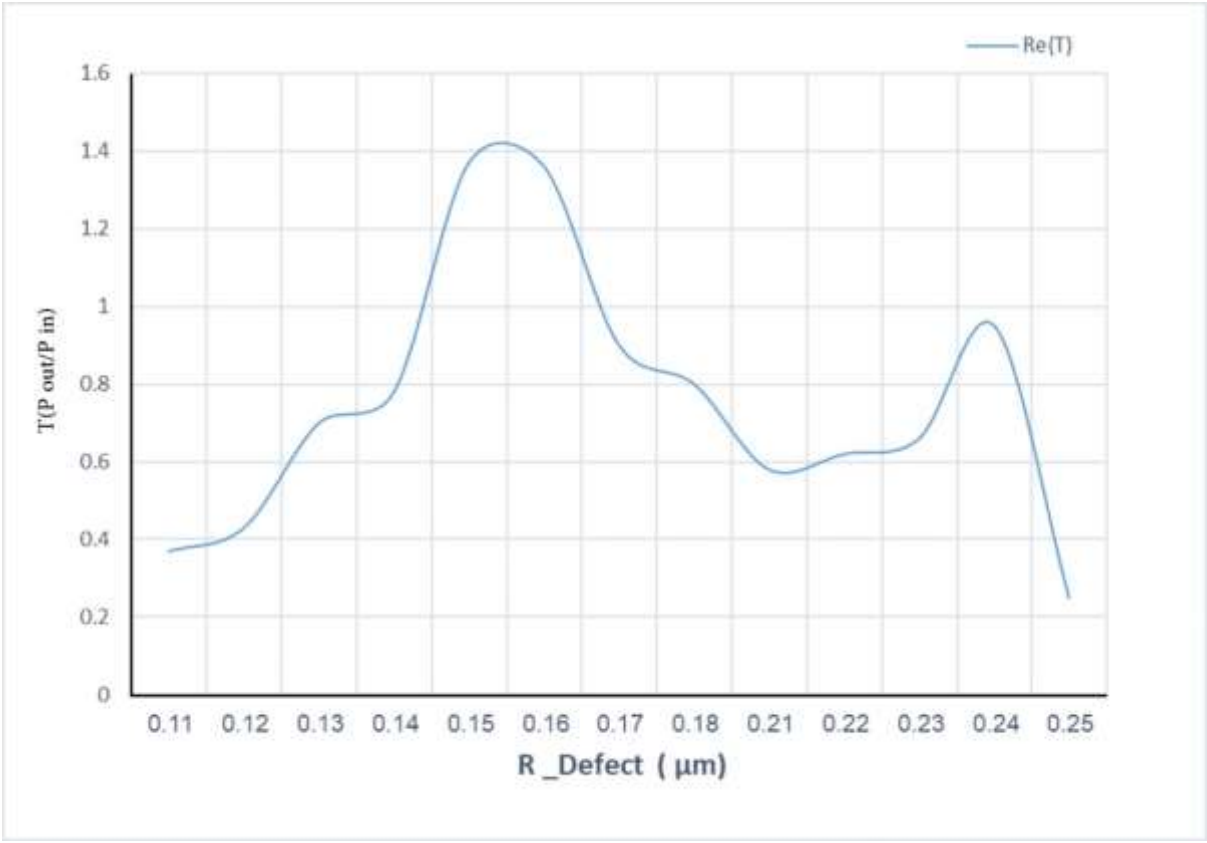

Figure 4-9: The ratio of the output power to the input power of the AND gate versus the variation of the point defect radius (maximum transmission power at the output obtained from the radius of point defects).

The power transfer as a function of the variation of the point defect radius is shown in **Figure 4-9**. The maximum power transfer at the output has been obtained by changing the radius of the point defect of **15µm**.

A point defect with a different radius causes better power transfer in both inputs. The field distribution for different input states. In **Figure 4-10,** four states are studied, in the first state (A=0, B=0) shown in **Figure 4-10(a),** in the second state (A=0, B=1) shown in **Figure 4-10(b)** and in the third state (A=1, B=0) shown in **Figure 4-10 (c),** and in the fourth state (A=1, B=1) shown in **Figure 4-10 (d)**. As can be seen in **Table 4-3,** the maximum power happens in state four (A=1, B=1) regarding to the AND gate.

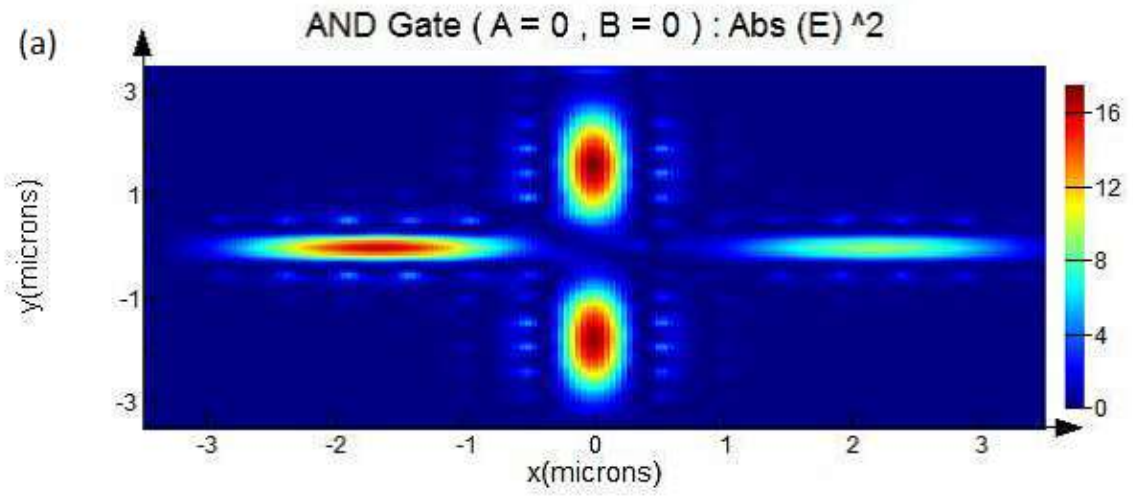

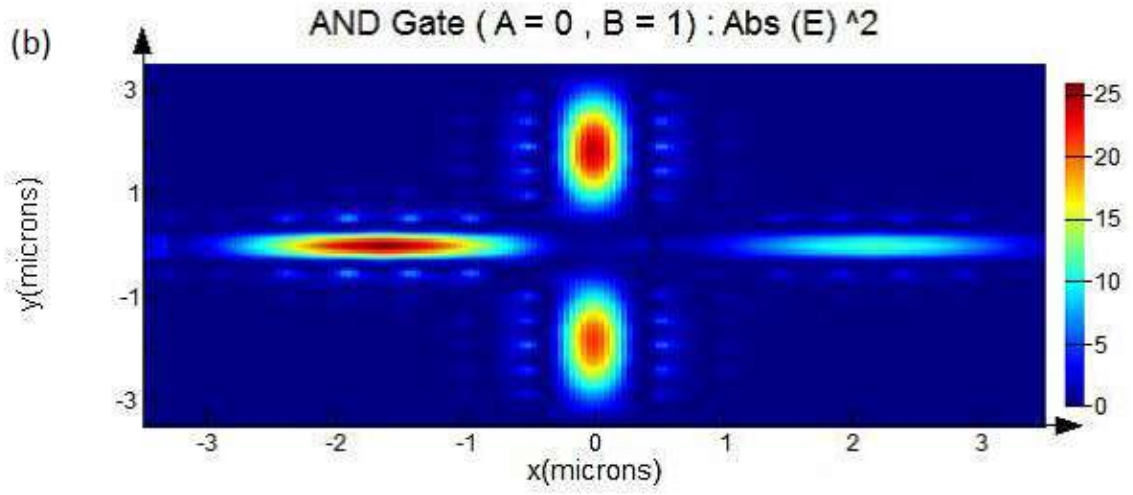

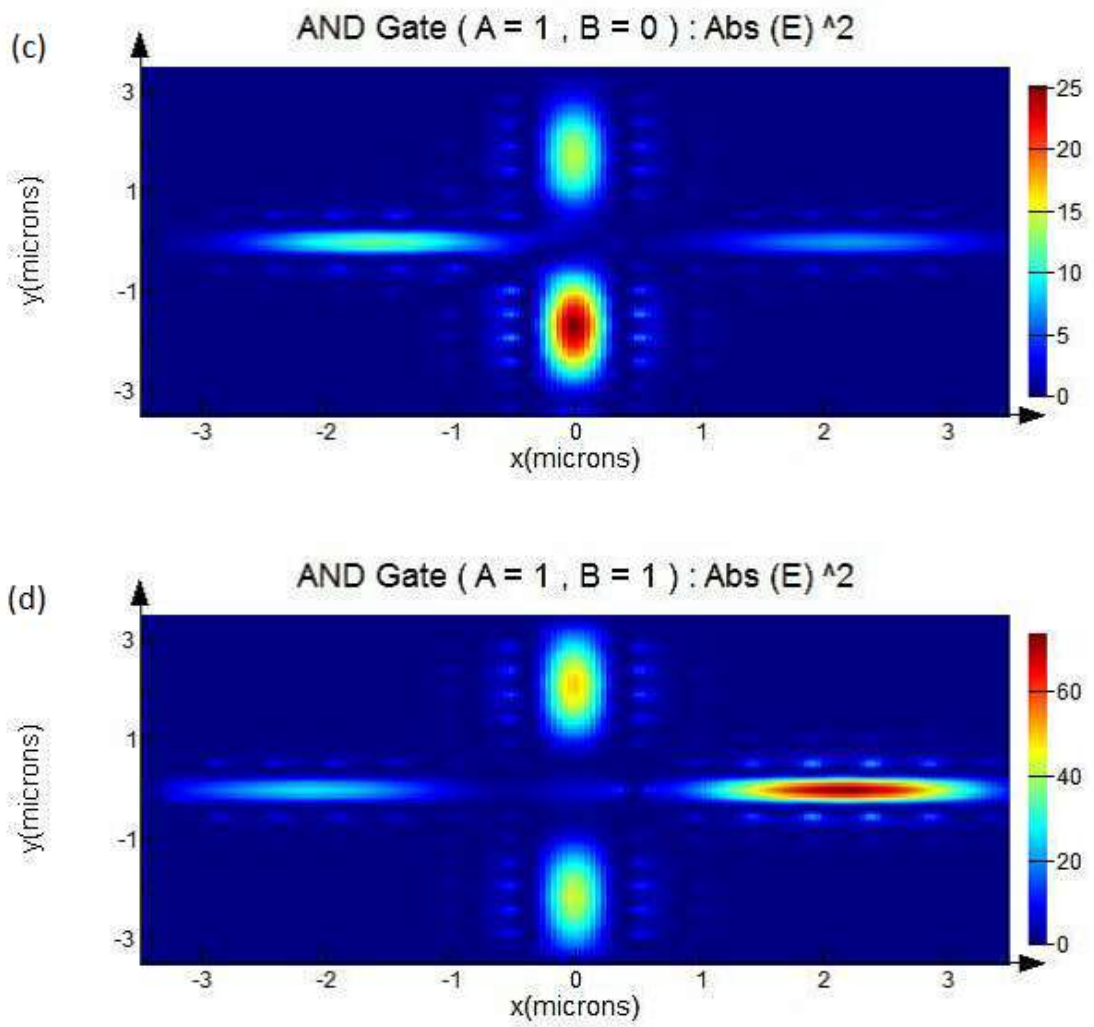

Figure 4-10(a) (A=0, B=0), (b) (A=0, B=1), (c) (A=1, B=0), and (d) (A=1, B=1): Field distribution for the proposed AND gate in different input modes.

Table 4-3. Input modes of the proposed AND gate (φ, input signal phase).

Input (A)		Input (B)		Control signals		Output(P_{out}/P_{in})	
Logical value	φ	Logical value	φ	Logical value	φ	Logical value	P_{out}/P_{in}
0	π	0	π	1	0	0	0.176
0	π	1	0	1	0	0	0.12
1	0	0	π	1	0	0	0.21

1	0	1	0	1	0	1	1.42

4-2-4- Design and simulation of NOR gates

The Logic function of the NOR gate completes the logic function of the OR gate. Here the NOR gate is created by combining the OR and NOT gates without adding any amplifier and coupler. This gate is also designed in a two-dimensional square lattice. And the other structural parameters such as radius, the lattice constant, position, and radius of reflection rods are similar to the OR and NOT gates. It can be seen in **Figure 4-11** that the logical NOR gate comprises three waveguides. The output of the OR gate acts as input of the NOT gate, and the output of the NOT gate acts as the output of the NOR gate. The point defect radius is optimized to obtain the maximum contrast ratio in the output, which equals to 15 μm shown in **Figure 4-12**.

The behavior of the gate in each of the four states can be seen in **Figure 4-13**, in the first state (A=1, B=0) shown in **Figure 4-13(a),** in the second state (A=0, B=0) shown in **Figure 4-13(b),** in the third state (A=0, B=1) shown in **Figure 4-13 (c),** and in the fourth state (A=1, B=1) shown in **Figure 4-13 (d)**.

It can be seen that the profiles of field distribution for the NOR gate. Given the field distribution and **Table 4-4**, the proposed structure acts like the NOR gate, and we can see the output power only in the second state (A=0, B=0).

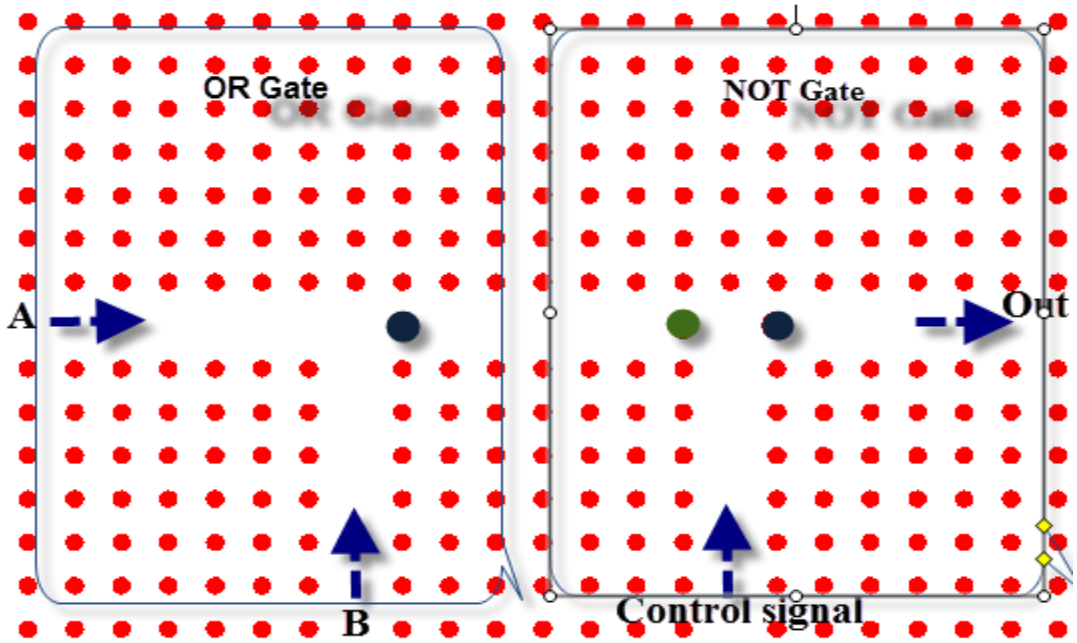

Figure 4-11: Schematic of the suggested NOR gate. The structure consists of two OR and NOT gates.

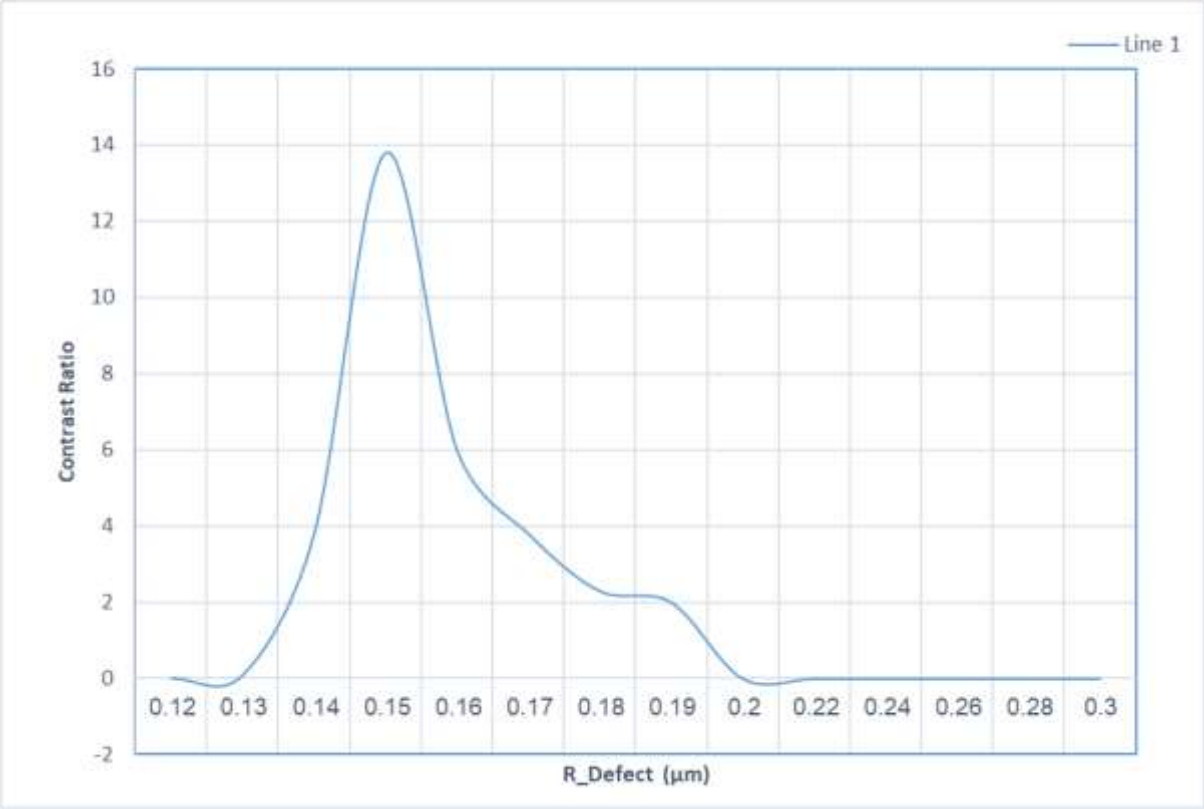

Figure 4-12: The contrast ratio of the proposed NOR gate versus point defect radius.

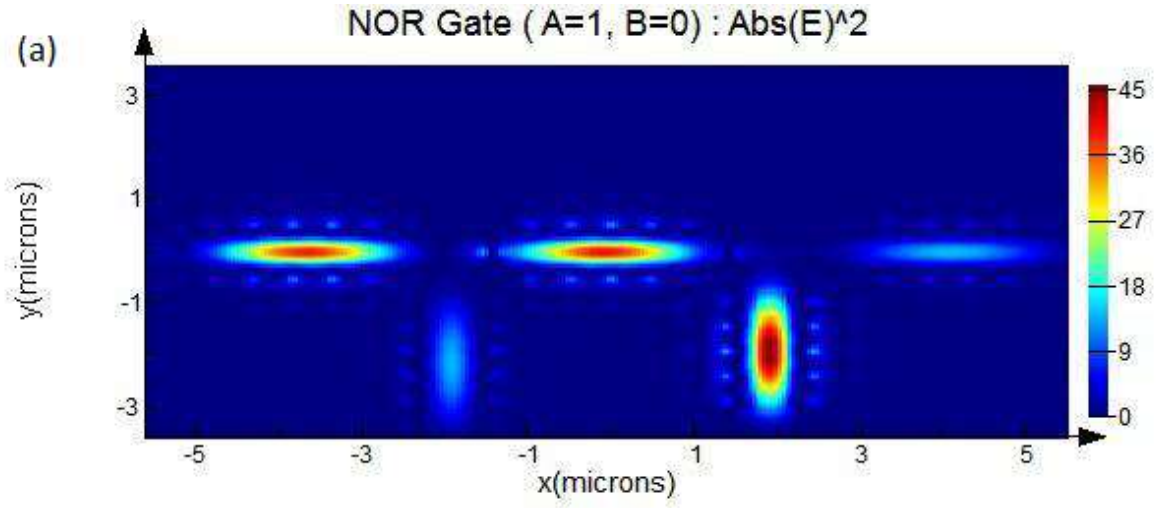

(b)

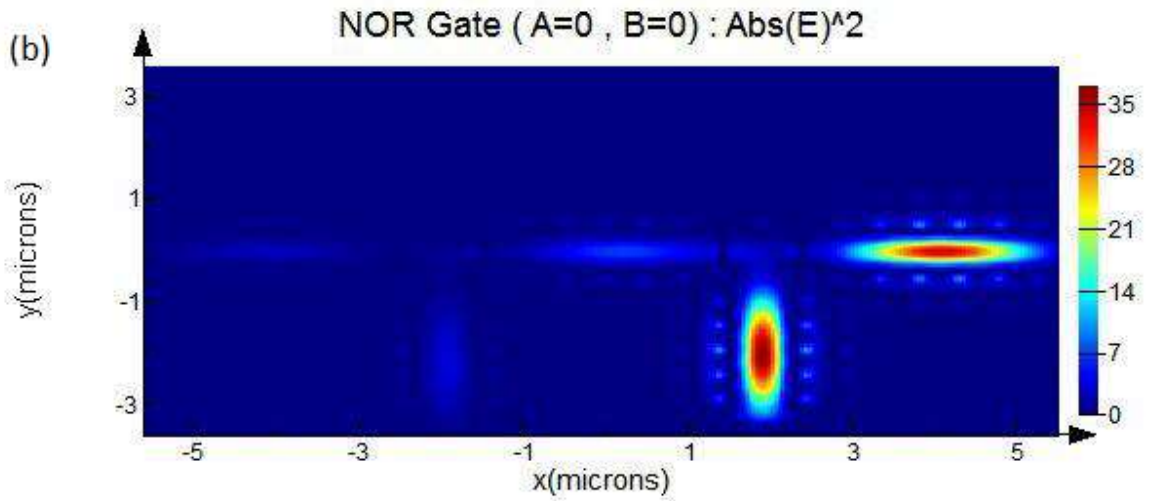
NOR Gate (A=0 , B=0) : Abs(E)^2
y(microns)
x(microns)
3
1
-1
-3
-5
-3
-1
1
3
5
35
28
21
14
7
0

(c)

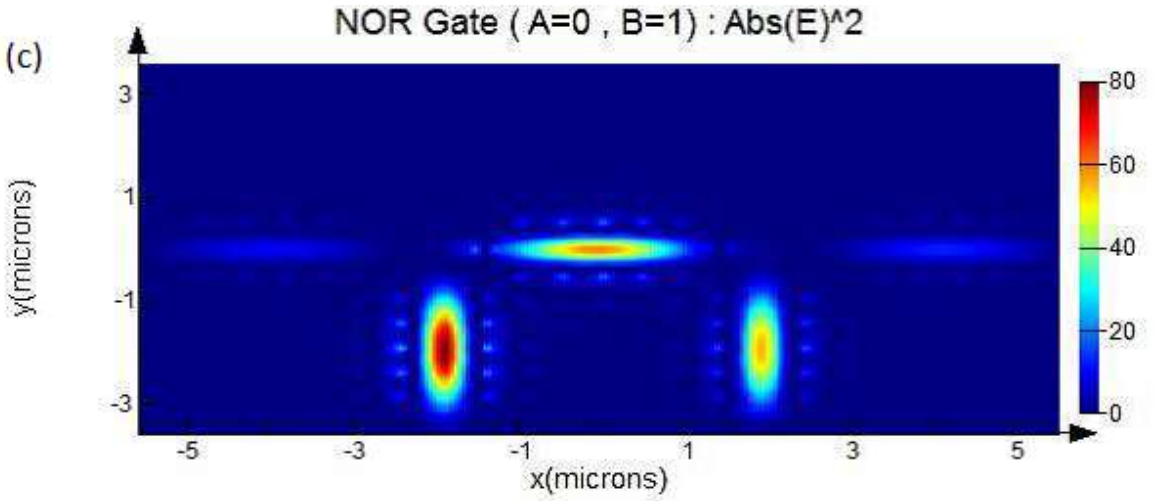
NOR Gate (A=0 , B=1) : Abs(E)^2
y(microns)
x(microns)
3
1
-1
-3
-5
-3
-1
1
3
5
80
60
40
20
0

(d)

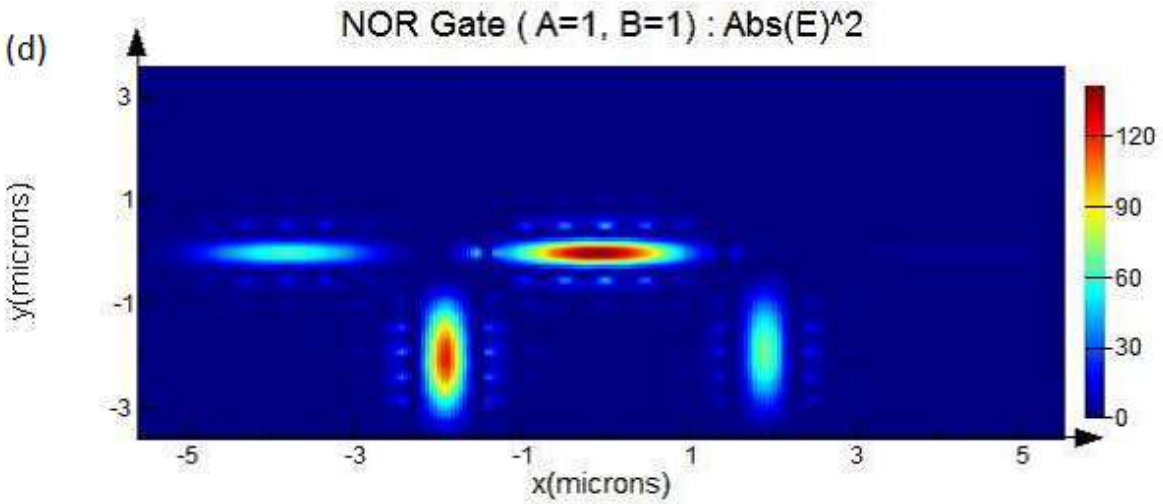
NOR Gate (A=1, B=1) : Abs(E)^2
y(microns)
x(microns)
3
1
-1
-3
-5
-3
-1
1
3
5
120
90
60
30
0

Figures 4-13 (a) (A=1, B=0), (b) (A=0, B=0), (c) (A=0, B=1) and (d) (A=1, B=1): Field distribution of the proposed NOR gate for different input states (figures depicted differentiate the result of the various values of A and B).

Table 4-4: Truth Table of NOR Gate.

Input A	Input B	Logical value	Output (P_{out}/P_{in})
0	0	1	1.37
0	1	0	0.193
1	0	0	0.173
1	1	0	0.01

4-2-5- Design and simulation of NAND gates

Since the NAND gate function is complementary to the AND gate function, the combination of two NOT and AND gates is used for designing the NAND gate. As the NOR gate, all parameters of this structure are identical to those of the other presented gates. Furthermore, the output of the AND gate, based on the output field intensity, is considered as the NOT gate input, and NOT gate output acts as NAND gate output. **Figure 4-14** show the NAND gate structure.

As can be seen in **Figure 4-15,** four states are studied, in the first state (A=0, B=0) shown in **Figure 4-15(a),** in the second state (A=0, B=1) shown in **Figure 4-15(b),** in the third state (A=1, B=0) shown in **Figure 4-15 (c),** and in the fourth state (A=1, B=1) shown in **Figure 4-15 (d)**. The point defect radius is optimized to obtain the maximum contrast ratio in the output, which equals to 15μm show in **Figure 4-16**.

The simulation results and the data in **Table 4-5** show that the structure acts as a NAND gate.

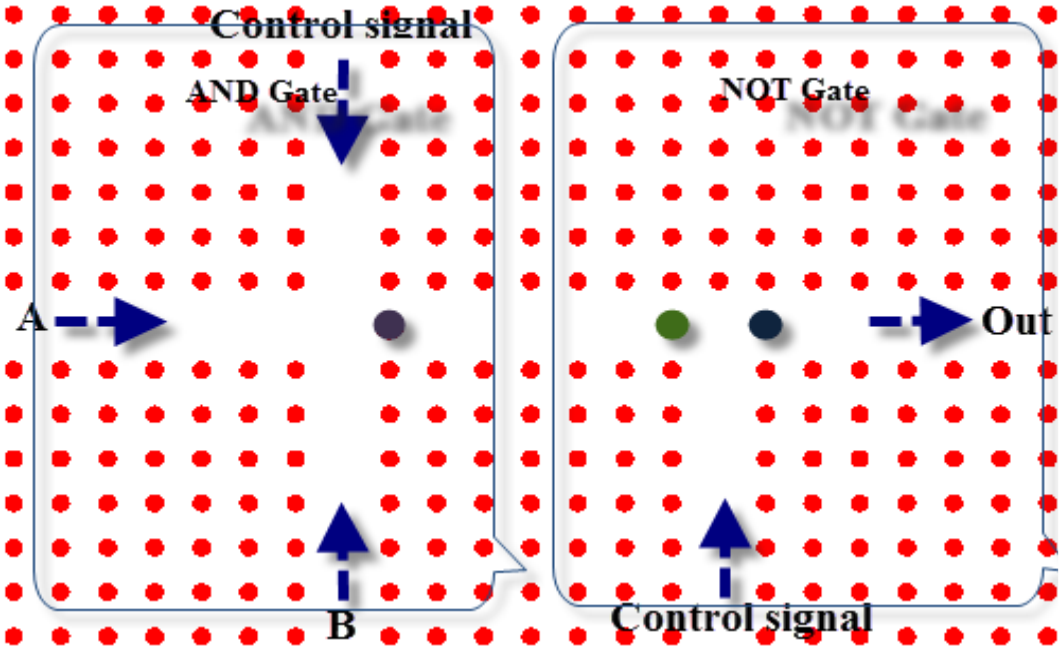

Figure 4-14: Schematic of the suggested NAND gate, with the structure composed of two AND and NOT gates.

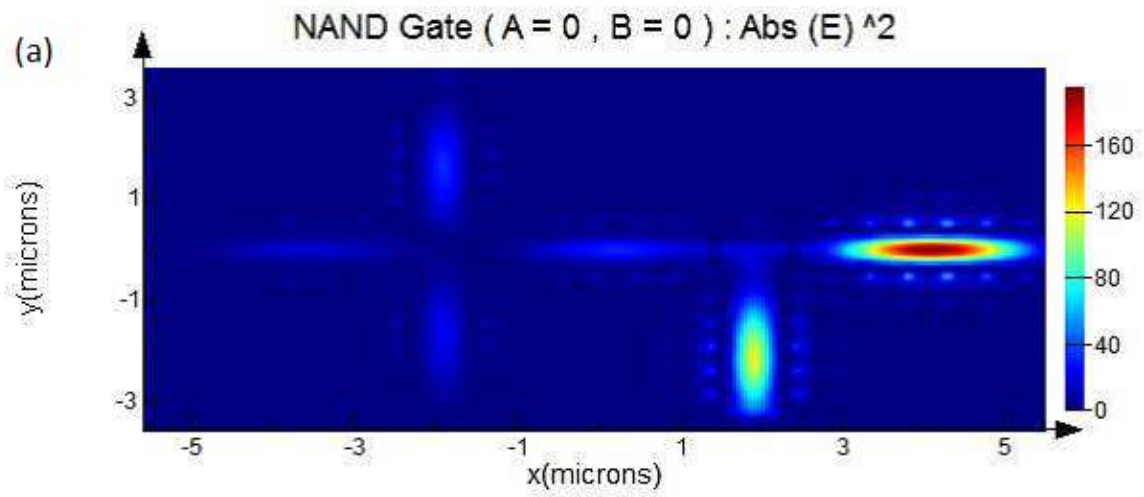

(b)

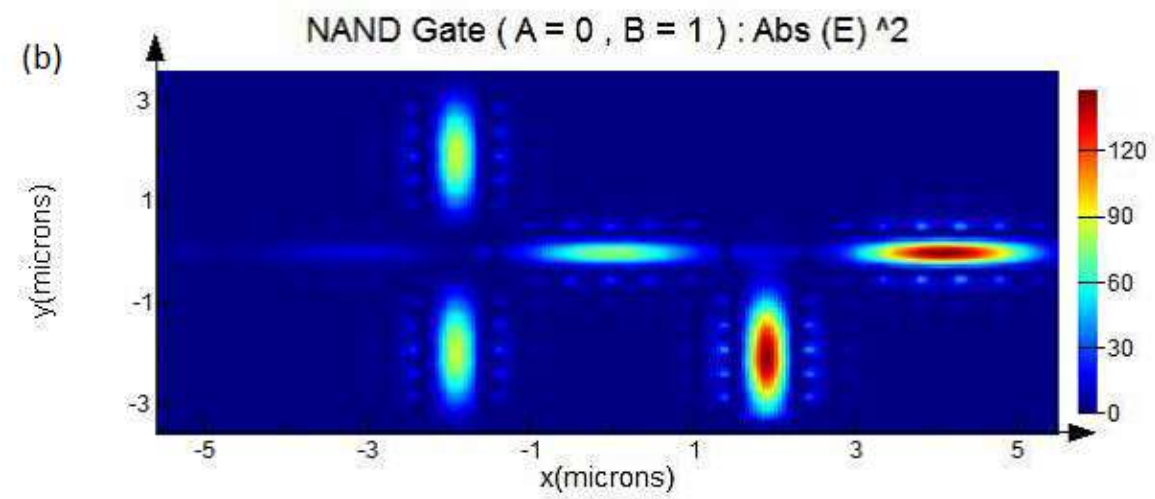
NAND Gate (A = 0 , B = 1) : Abs (E) ^2
y(microns)
x(microns)
3
1
-1
-3
-5
-3
-1
1
3
5
120
90
60
30
0

(c)

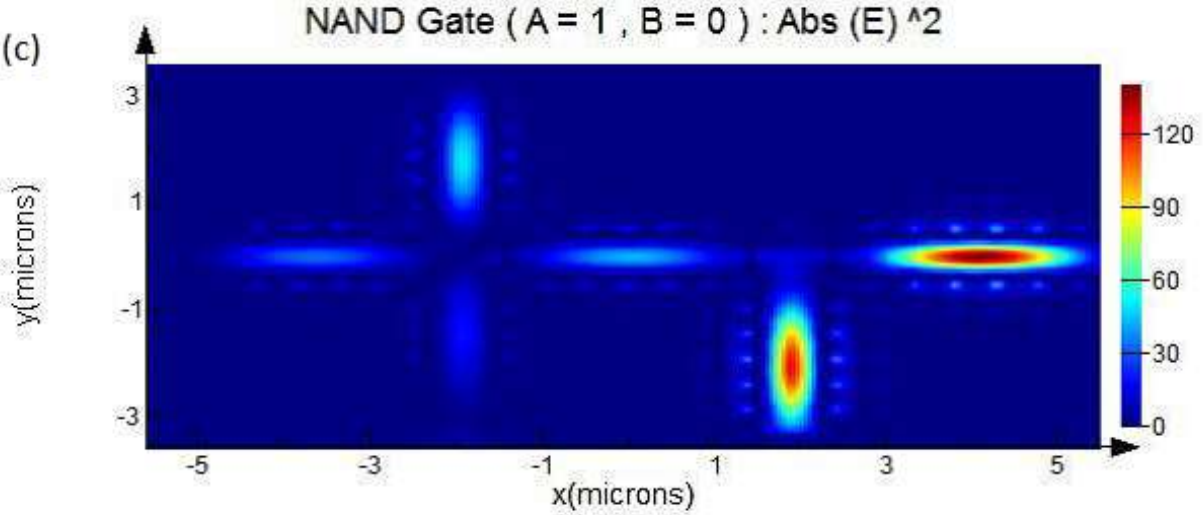
NAND Gate (A = 1 , B = 0) : Abs (E) ^2
y(microns)
x(microns)
3
1
-1
-3
-5
-3
-1
1
3
5
120
90
60
30
0

(d)

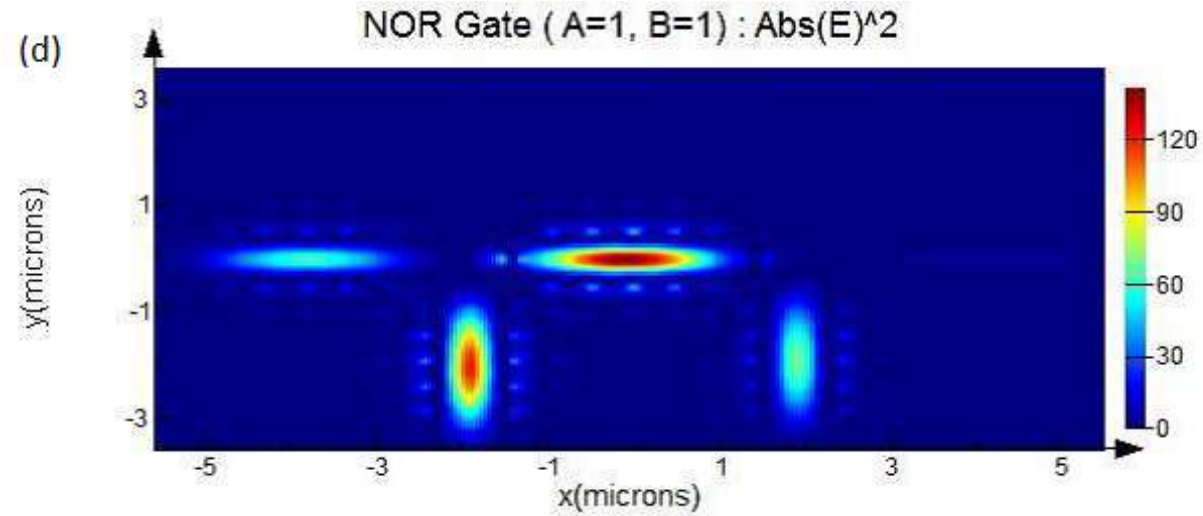
NOR Gate (A=1, B=1) : Abs(E)^2
y(microns)
x(microns)
3
1
-1
-3
-5
-3
-1
1
3
5
120
90
60
30
0

Figure 4-15(a) (A=0, B=0), (b) (A=0, B=1), (c) (A=1, B=0), and (d) (A=1, B=1): Field Distribution of the suggested NAND gate for different input modes (figures depicted differentiate the result of the various values of A and B).

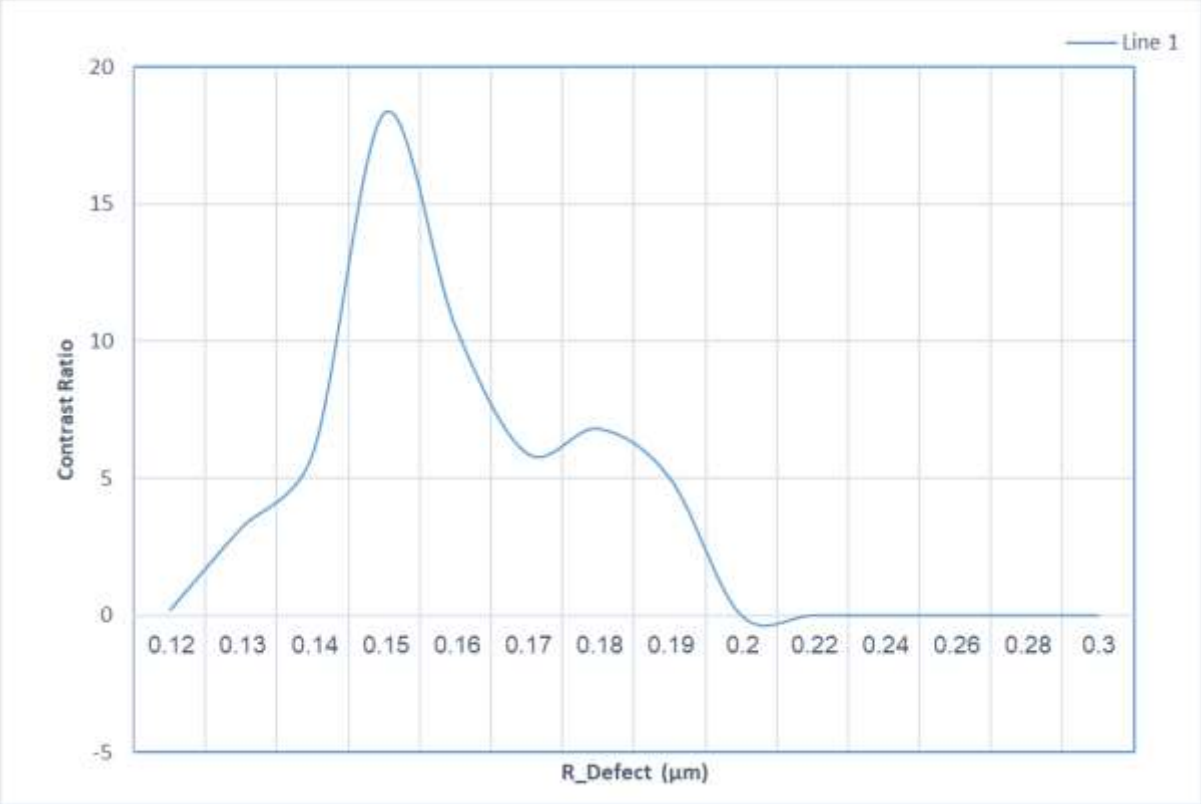

Figure 4-16: The contrast ratio of the proposed NAND gate versus point defect radius.

Table 4-5: Input modes of the suggested NAND Gate.

Input A		Input B		Control signals		Output (P_{out}/P_{in})	
φ	Logical value	φ	Logical value	φ	Logical value	Logical value	P_{out}/P_{in}
π	0	π	0	0	1	1	1.47
π	0	0	1	0	1	1	1.08
0	1	π	0	0	1	1	0.75
0	1	0	1	0	0	0	0.12

4-3- Design AND Gate based on the nonlinear Kerr effect

Using linear and nonlinear photonic crystal properties, a structure for designing a logical AND gate would be presented in this section. To achieve this, a triangular photonic crystal slab structure of rod in the air has been used, shown in **Figure 4-18**. The function of logical structures at the same wavelength is essential for facilitating *complex circuit* configuration. Therefore, in the design of these logical gates, the goal is to make the wavelength of inputs (1550 nm) equal at zero input phase. On the other hand, knowing that the power level is important in structures with a nonlinear Kerr effect, the power required for the circuit switching operation with P_0 has been shown. It should be mentioned that in this structure, the power in all inputs is the same and equal to P_0.

The selected optical crystal topology is checked in the next stage, and then we move on to the all-optical logic design. The important default is that the structure's wavelength is within the third communication window range (1550 nm). Furthermore, input signals to the structure are coupled to the crystal through a waveguide. This single-mode laser waveguide at 1550 nm wavelength should propagate in a linear waveguide in the photonic crystal. It should not be damped in the crystal, and the wavelength should be in the range of the optical band gap. After studying different photonic crystal structures, such as square and hexagonal structures, we decided to use the triangular photonic crystal structure in TM propagation mode. In the proposed structure, a photonic crystal slab with a triangular lattice is provided using silicon dielectric rods in the air. The lattice dimensions are 51 × 61 rectangle lattice. The lattice constant (a) and the radius in all rods are 0.54 μm and 0.22a, respectively. These numbers are obtained based on the optical band gap analysis of the structure. The method of analyzing and calculating the optical band gap is the plane wave expansion method.

As can be seen in **Figure 4-17**, the first band (base) is within the frequency range of 0.26538-0.41923(a/λ). Due to the dimensions of the lattice structure, the wavelength of 1550 nm is also within this band gap propagation wavelength.

As previously explained, all materials have the nonlinear Kerr effect. In these materials, the increase in the reflected intensity can change the material's refractive index.

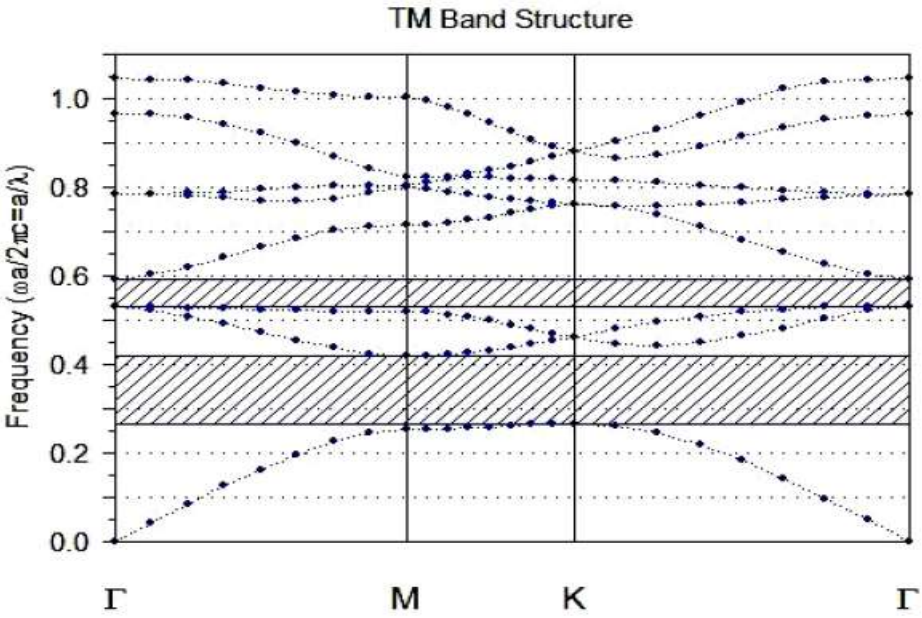

Figure 4-17: The structure of optical band gap obtained by plane wave expansion (PWE) method.

The nonlinear Kerr coefficient for silicon is approximately 10^{-18} m^2/W. As compared to other materials, this coefficient is not very large. Some materials have a ten times larger nonlinear Kerr coefficient than silicon. For nonlinear defects, the antimony-contaminated silicon, which has a nonlinear Kerr coefficient as twice that of silicon ($n_2=10^{-16}$ m^2/W), is used Xavier et al (2012) [72]. The reason for using crystalline antimony-contaminated silicon is its similar behavior with silicon and its constructability.

In the switch's structure based on the nonlinear Kerr effect, the input threshold power is important, by which the switching operation is performed. The structure presented is shown in **Figure 4-18**.

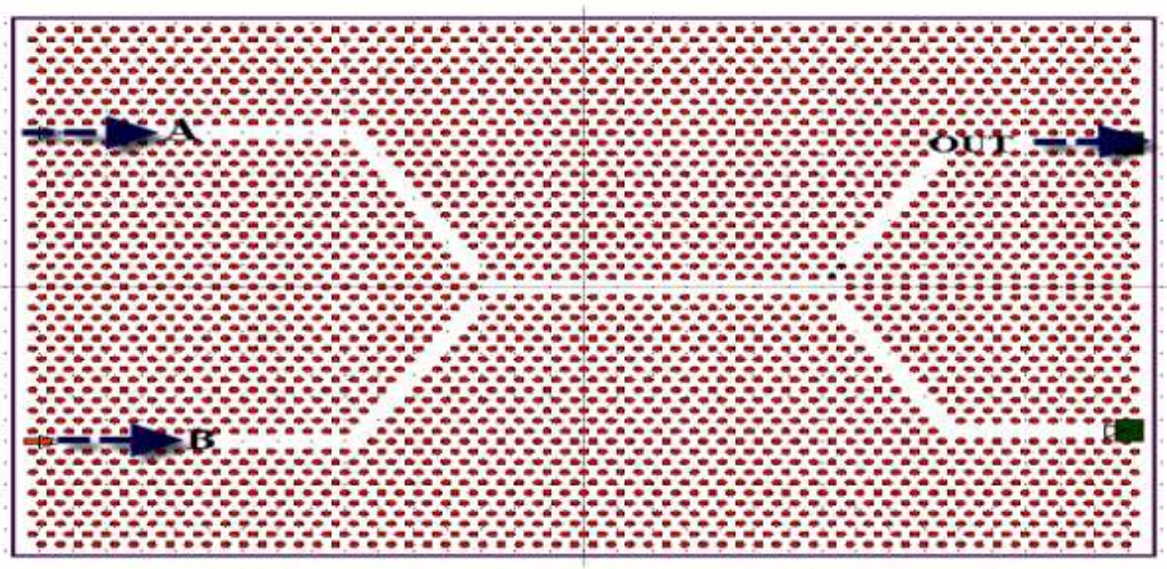

Figure 4-18: The proposed AND gate based on nonlinear Kerr effect.

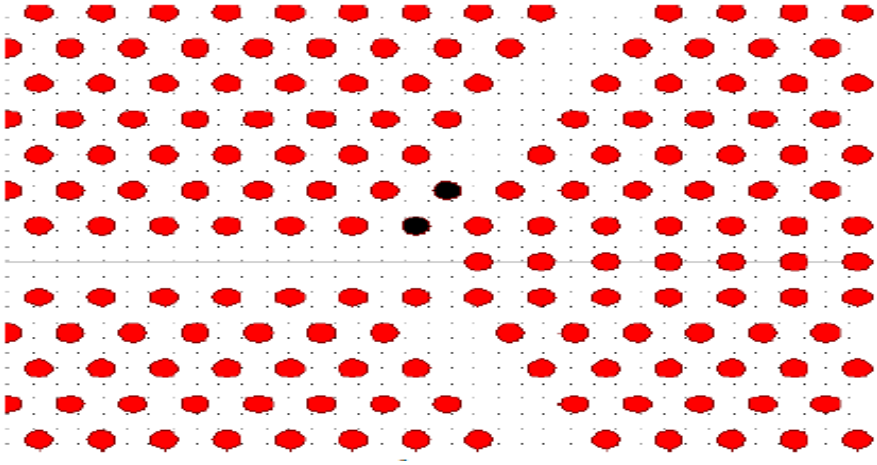

Figure 4-19: The location of rods for the proposed AND gate based on nonlinear Kerr effect.

In **Figure 4-19,** the inputs' structure is symmetrical so that there is no phase difference between the two signals before the optical signals reach each other. In the first output channel, two nonlinear rods are used. The nonlinear rods are shown in black color.

To prevent the occurrence of the phase shift in this design, an attempt has been made to avoid changing the rods' radius. In the first step, as shown in **Figure 4-20**, to obtain an input threshold (P_o) for nonlinear behavior analysis, an operator was created for scanning the behavior of outputs for inputs with different powers (from 1 to 18 watts) by a 0.5 lattice constant. The input of 18 W is equal to 246W/μm^2 at the input. Obviously, when two input channels produce the power of 246W/μm^2**,** some of the power would be damped along the way in the crystal, but the amount of power that reaches the nonlinear rods should lead to the switching. Let us define P_o as the required power is considered. The vertical axis is a normalized field. The normalized field is equal to the value of a monitored field in a time unit.

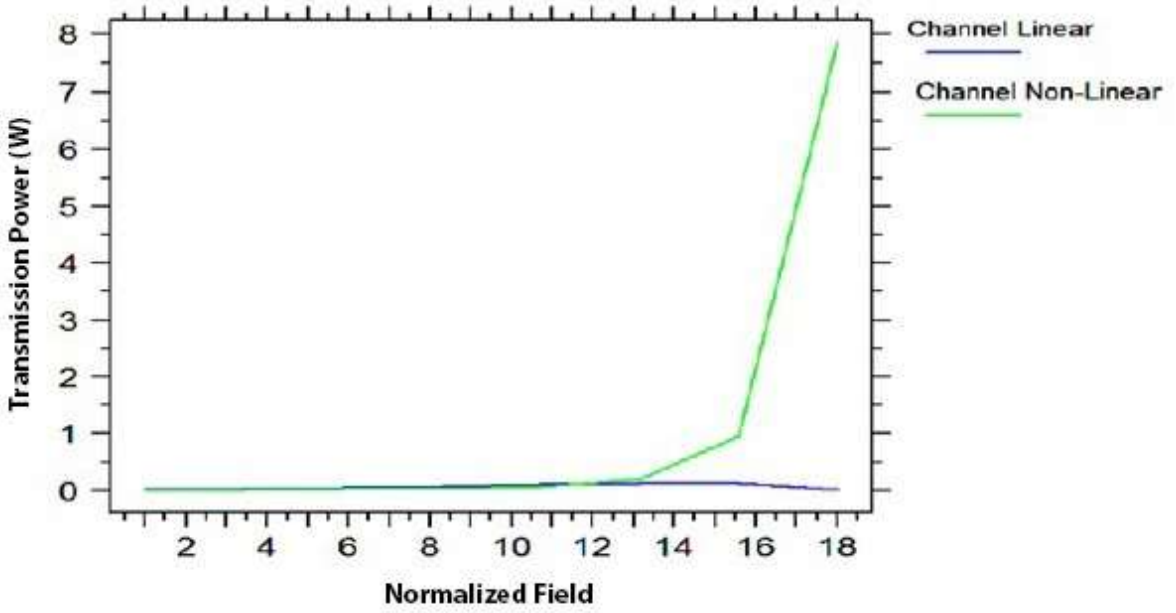

Figure 4-20: The switching behavior of AND gate at a nonlinear Kerr effect-based structure (the vertical axis represents transmission power and the horizontal axis represents normalized field).

To examine the function of the gate, different input states have been studied. By applying Gaussian light sources with a wavelength of 1550 nm and the power intensity of P_0on the inputs of the proposed structure, the logic function of the AND gate can be obtained. Simulations have been carried out for various inputs. In this study, we have four states described as follow: In state one, when both inputs are off (A=0, B= 0), regarding to the AND gate, the output is zero, and there is no light propagation in the output; therefore, we didn't present any simulation in this case. But when one of the inputs is "1" in state two (A=0, B=1), and three (A=1, B=0), the outputs are transmitted to the lower output channels, and the received power in the outputs (out) is very low. The simulation of these two states is depicted in **Figures 4-21 and 4-22,** respectively. It is evident from these figures that there is no power for states one and two in the output, which are considered as a logic "0".

Finally, in state four both inputs are one (A=1, B=1), the output regarding to the AND gate is logic "1", the simulation of this state is shown in **Figure 4-23**. In this state, the received power around the nonlinear rods is P_0, nonlinear effects cause the switching(as mentioned in **chapter 3, section 3-9**), so the power is transmitted to the output.

Table 4-6 shows the different input states and their output values. According to the simulation results, the maximum received power at the output in state four. The efficiency of optical logic gates is evaluated by several parameters. One important parameter in evaluating the performance of logic gates is the contrast ratio. This parameter distinguishes the logical level "1" and "0"; the larger the power difference between the two logic states "0" And "1", the larger

the ratio and the better the logic gate performance. This parameter is defined as follows Mohebzadeh-Bahabady and Olyaee (2018) [164]:

$CR = 10 \times \log P_{on} / P_{off}$

Where, P_{on} is the amount of optical power for logic "1" and P_{off} is the amount of optical power for logic "0". Since the "0" And "1" logic may have different values for different states, to calculate the contrast ratio, the minimum value for Pon mode and the maximum value for Poff are considered. So this ratio is calculated in the worst case scenario of each output.

According to the results obtained from the simulation, the contrast ratio for the proposed structure is $41/7\,dB$.

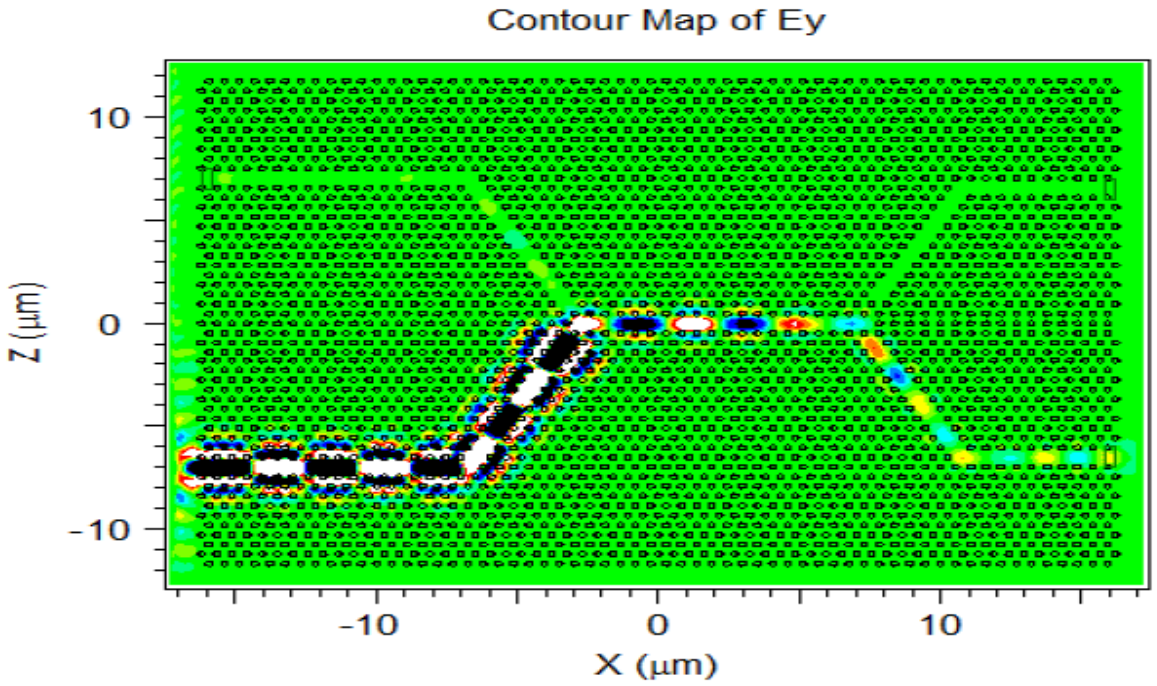

Figure 4-21: Field distribution of the gate based on nonlinear effects for state two (A=0, B=1).

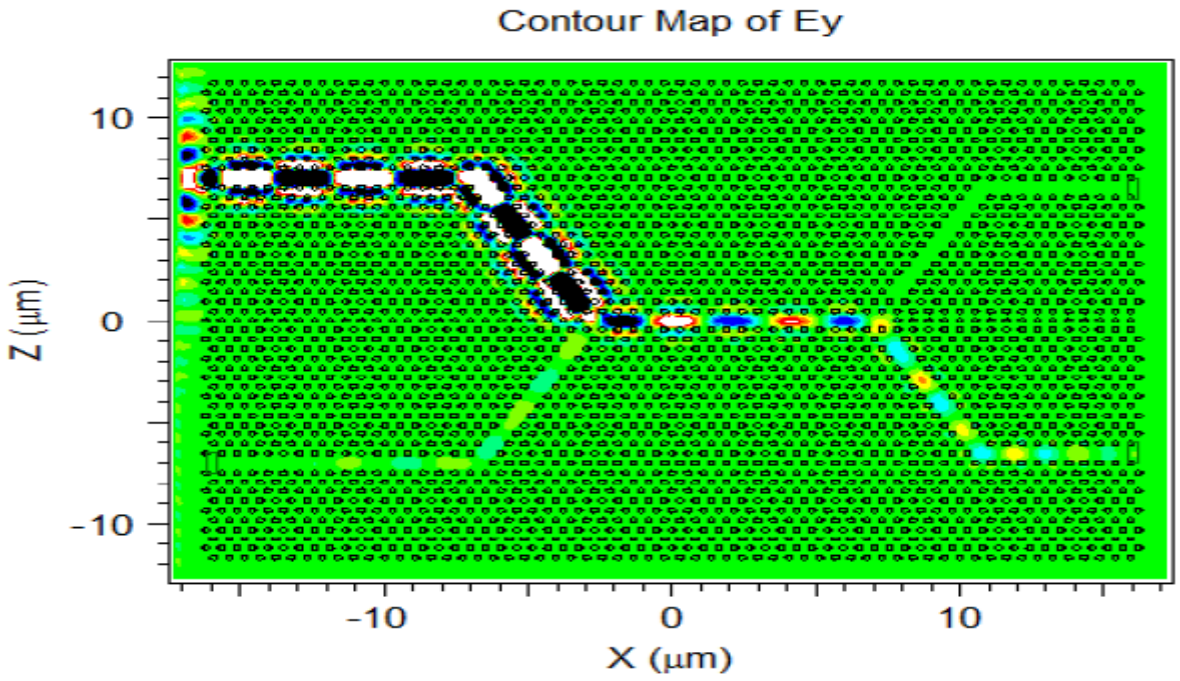

Figure 4-22: Field distribution of the nonlinear effects based gate for state three (A=1, B=0).

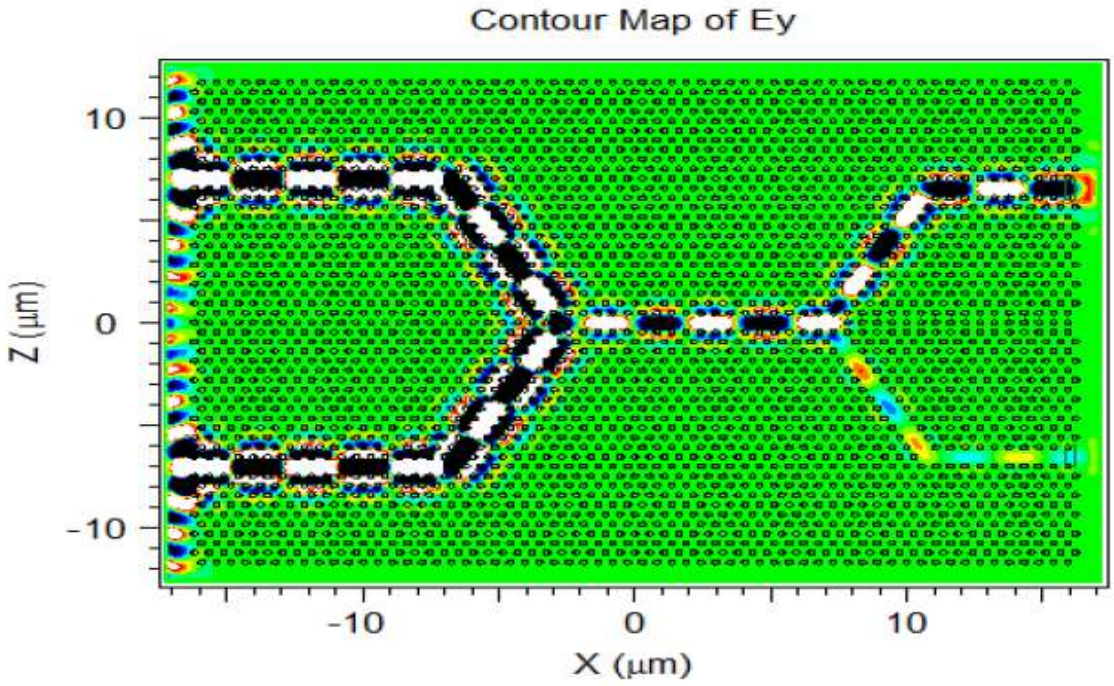

Figure 4-23: Field distribution of the nonlinear effects based gate for state four (A=1, B=1).

Table 4-6: Various input modes and output values of the AND gate based on the nonlinear Kerr effects.

Input A	Input B	logical value	Output
0	0	0	0
0	1	0	$0.03\ P_0$
1	0	0	$0.04\ P_0$
1	1	1	$2.32P_0$

4-4- Simulation results CNTFET-LIKE-MOSFET

In this section, all the proposed designs are performed with an HSPICE simulator at room temperature. They are based on 32-nanometer CNTFET-LIKE-MOSFET technology related to Stanford University [160]. Moreover, to compare the proposed designs in this research with the designs of other articles better, in addition to the use of different models based on the parameters of delay and power consumption, another parameter has also been used as a fair compromise between power and delay called power-delay product (PDP). In the field of digital electronics, achieving circuits with higher speeds and lower power consumption is important. Therefore, it is essential to improve the implementation of computational circuits such as multipliers, which are widely used in microprocessors, signal processing and many cryptographic algorithms. In addition, compressors are the most important implementation unit in the multiplier, which among different compressors, 4-2 compressor is one of the most widely used methods for implementation. On the other hand, the implementation of this compressor depends entirely on the XOR gates. Therefore, having a suitable design for XOR improves the 4-2 compressor's performance and can improve the efficiency of the entire multiplier system.

The XORs simulation environment presented in this research is based on **Figure 4-24**. A C-load capacitor is used at the circuit's output to approach the actual simulation conditions.

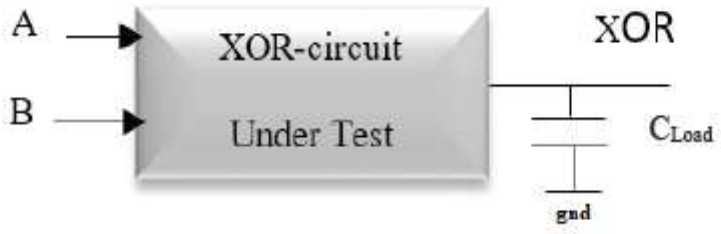

Figure 4-24: XOR simulation environment.

In **Figure 4-25,** the capacitance is studied in terms of PDP, which can be obtained by multiplying the power into the delay in 5 models, which are Model-1, Model-2, DPL-XOR, C-

CNTFET, and Inverter-based-XOR. The size of this capacitance is between 1 fF and 3 fF, and the maximum PDP was for 3fF capacitor shown in **Figure 4-25.** It shows that Model-1 functions with a less PDP value in different capacitances.

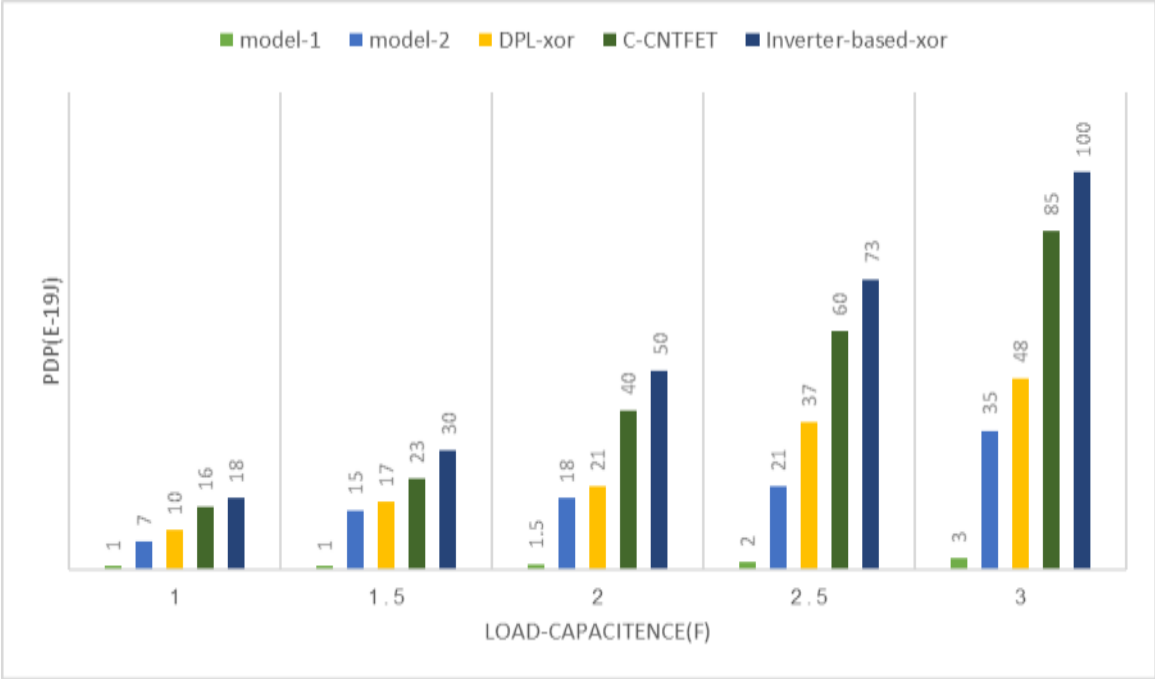

Figure 4-25. Comparison of PDPs in different models of capacitors 1-3 fF.

Also, the comparison between the delay, the power, and PDP of different XOR models, with the output capacitor of 2fF and at voltages of 0.8v, 0.9v, and 1v, is given in **Figures 4-26, 4-27, 4-28**, respectively. It should be noted that the capacitance is the same in these figures, and the only factor changing is the voltage.

As **Figure 4-26** shows, Model-1, compared to others, has a reasonable value for the delay in different voltages. According to **Figure 4-27**, Model-1 shows a power value with different voltages compared to other models. As can be seen in **Figure 4-28**, Model-1 is working with less PDP value, and it shows that this model is better in performance, so we used this model in our proposed structure.

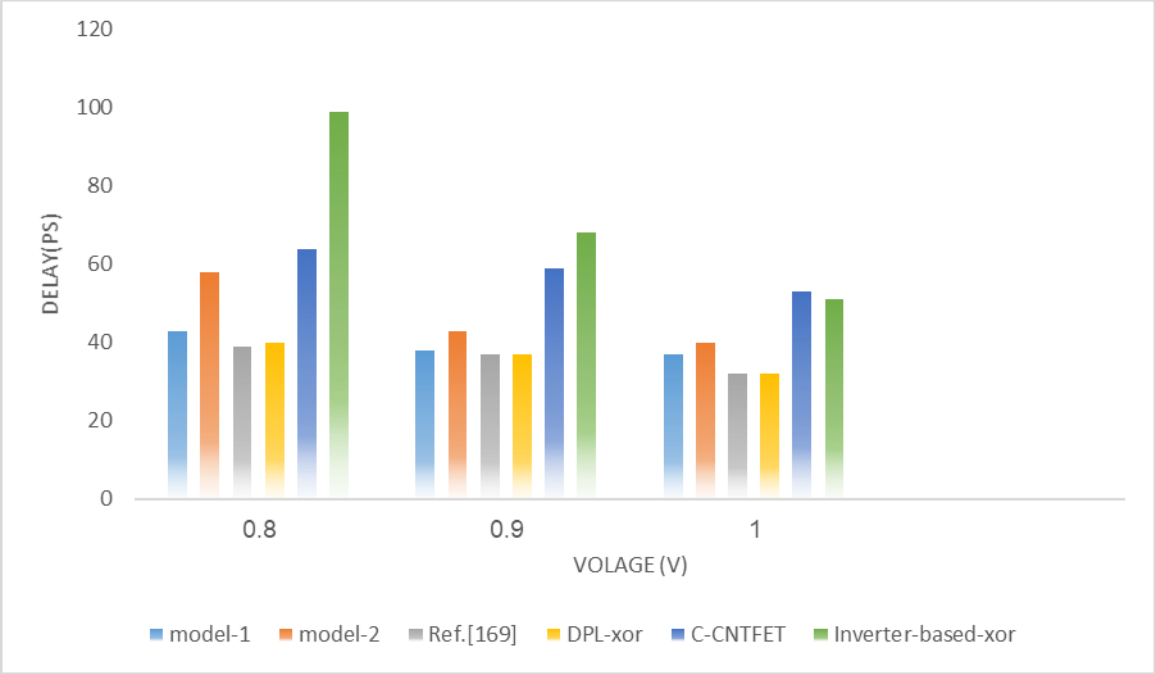

Figure 4-26: Delay changes at different voltages.

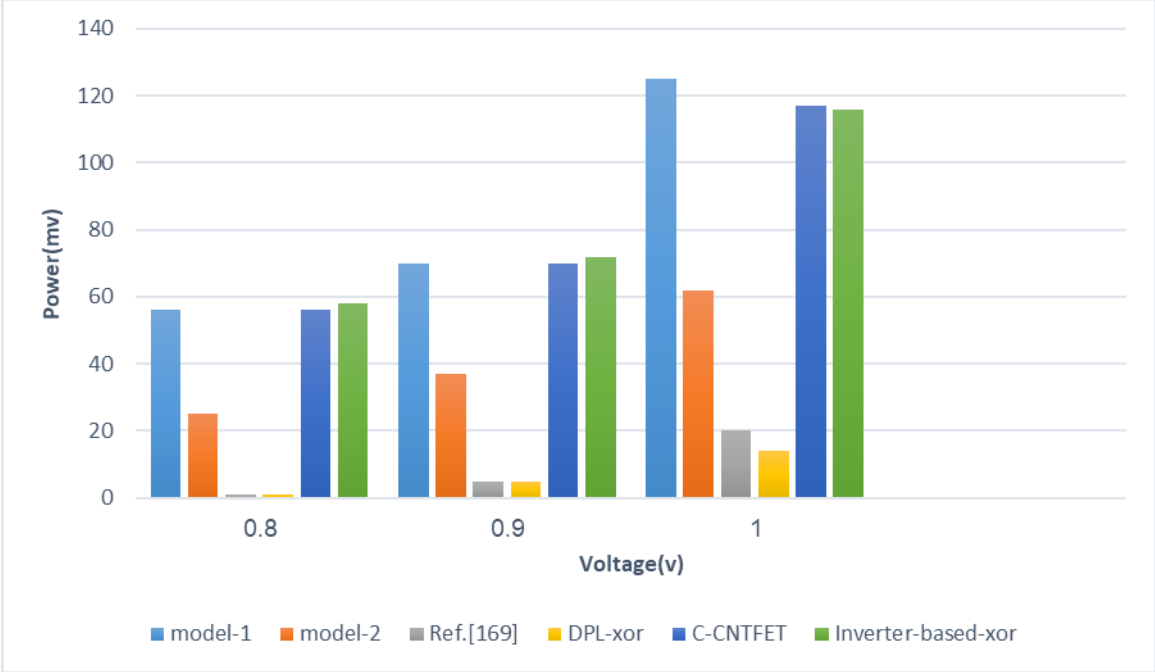

Figure 4-27: Power changes at different voltages.

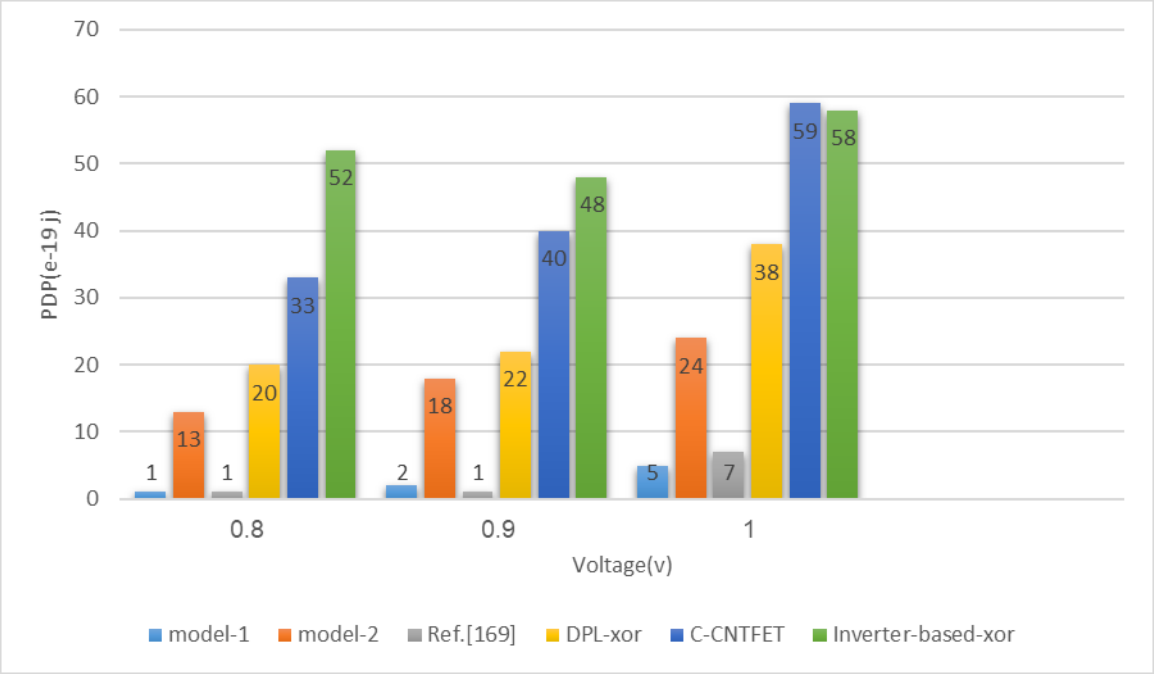

Figure 4-28: PDP changes at different voltages.

One of the most important parameters in CNTFET technology is the number of nanotubes in the discussed gate structure, which affects the circuit's speed and power consumption. Generally, the different numbers of nanotubes in the discussed transistor channel (chapter 3 section 3-9) lead to a change in the transistor's delay and power. The effect of the nanotube number on PDP (operating in voltage of 0.9 volts) is considered in **Figure 4-29**.

In this study, Stanford's 32-nanometer model is used, in which the default number of tubes for simulation is one, and relying on it, the comparison was based on the use of a nanotube [160]. On the other hand, to investigate the effect of increasing nanotubes on the circuit, XOR models with non-default numbers are used here (3-tube samples have been considered). With the same number, the simulation process has been done. Of course, this comparison can be considered for many other nanotubes, not necessarily limited to this number.

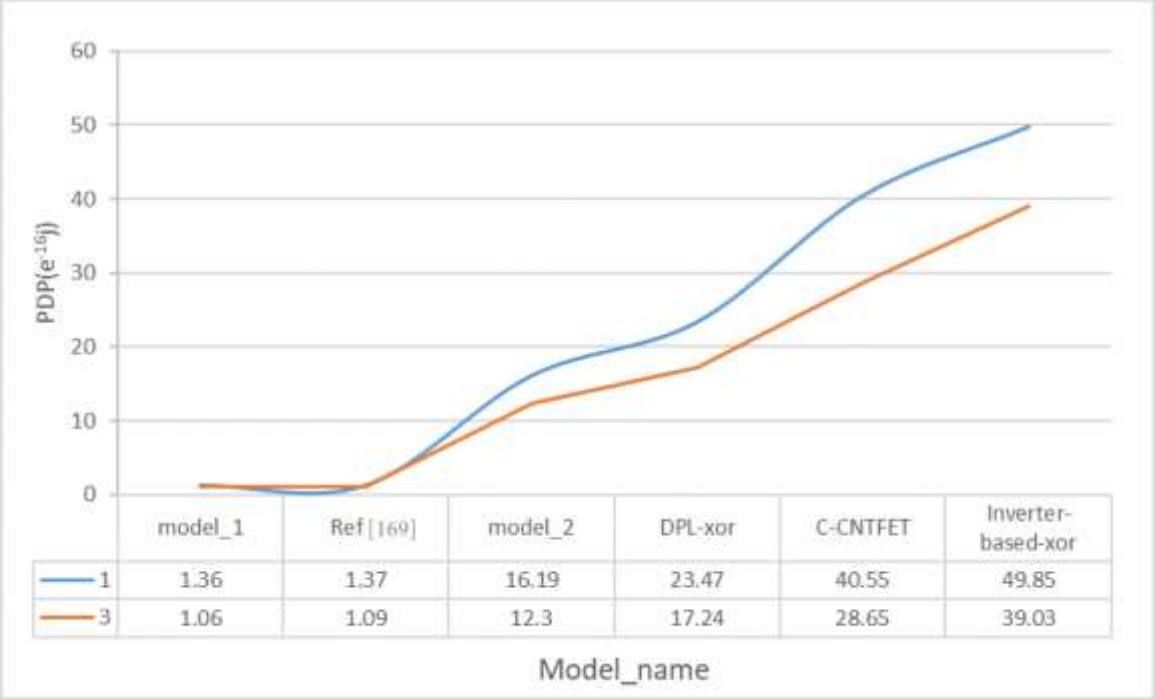

Figure 4-29: The effect of nanotube number on the PDP changes of different models.

According to the results obtained from the comparison of XORs, Model-1 is better than other models. In Model-1, compared to the latest model presented in 2018 Saraswat and Sharma [169] there is a 2.98% improvement in PDP. According to **Figure 4-29**, we studied the effects of nanotube number on the PDP changes with two capacitances with 1 fF (shown in the blue curve) and 3 fF (shown in the orange curve) in different models Saraswat and Sharma (2018) [169], there is a 2.98% improvement in PDP and a 13.77% improvement in power consumption.

Therefore, in the compressor design (4:2) shown in **Figure 3-5**, this model has been used, and the simulation results are given for voltages of 0.8 to 1.1 volts in **Table 4-6**. Of course, the compressor's compression environment (4:2) is such that all inputs and outputs pass through a standard buffer, and a 5fF capacitor is used at the output of the circuit. The waveform obtained from the proposed compressor for a 1v is shown in **Figure 4-30**.

Furthermore, according to **Equation (3-17)**, the Chiral Vector changes obtained by changing the integers (m, n) cause a change in the nanotube's diameter. Here, we used the values that have been used in the Stanford model and the articles investigated. The chirality of n-type and p-type nanotubes is considered (0.19).

Table 4-6: Proposed compressor simulation results.

Comparison parameters	Power supply voltage, v			
	0.8	0.9	1	1.1

Worst-case Delay(ps)	111.80	94.137	85.505	79.299
Power(µw)	0.25694	0.3751	0.77076	7.8339
PDP(aJ)	28.7258	34.8786	65.9033	620.672

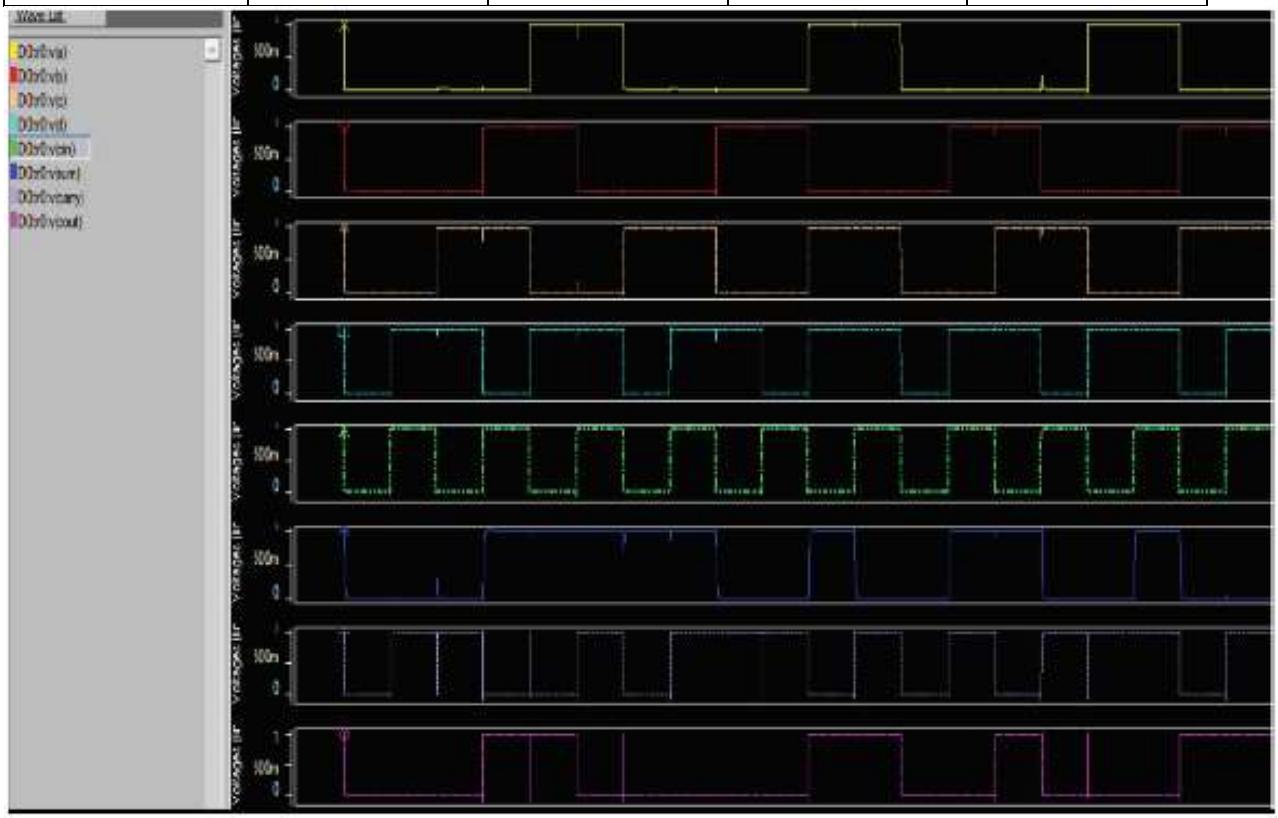

Figure 4-30: Input and output waveforms of the compressor (4:2).

The proposed compressor for 1 volt is shown in **Figure 4-30**. It should be noted that to achieve the real simulation environment conditions, the delay is based on the worst-case scenario. The lower the delay and the PDP, the more efficient the structure is.

Moreover, a comparison between the number of transistors used in different designs and the delay in the compressor circuit's critical path at the gate level has been noted in **Table 4-7**, which shows the proposed compressor design that uses the XOR of Model-1. In this method, compared to other designs, fewer transistors are used.

Table 4-7: A comparison between area and delay of the critical path in different models.

Number of transistors used in the compressor	The delay of the critical path based on the gate	Compressor models

52	$3\Delta XOR$	Ref. [151]
36	$\Delta XOR + 2\Delta MUX$	Ref. [149]
50	$\Delta XOR - 3IN + 2\Delta XOR + \Delta MUX$	Ref. [153]
74	$3\Delta AND + 3\Delta NOR$	Ref. [154]
58	$\Delta XOR + 2\Delta MUX$	Ref. [155]
32	$3\Delta XOR$	Proposed

In the following, the comparisons between the power, the delay, and PDP in different models of the compressor (4:2) have been exhibited in **Figures 4-31**, **4-32**, and **4-33**, respectively. As shown in the mentioned figures, the PDP value for the proposed model is the lowest. It should be noted that to achieve the real simulation environment conditions, the delay is based on the worst-case scenario. By studying these figures and **table 4-7**, it can be seen that the proposed structure functions with less power consumption, delay value, and PDP value, so this structure has an advantage in fields of power, delay, and PDP compared to other models.

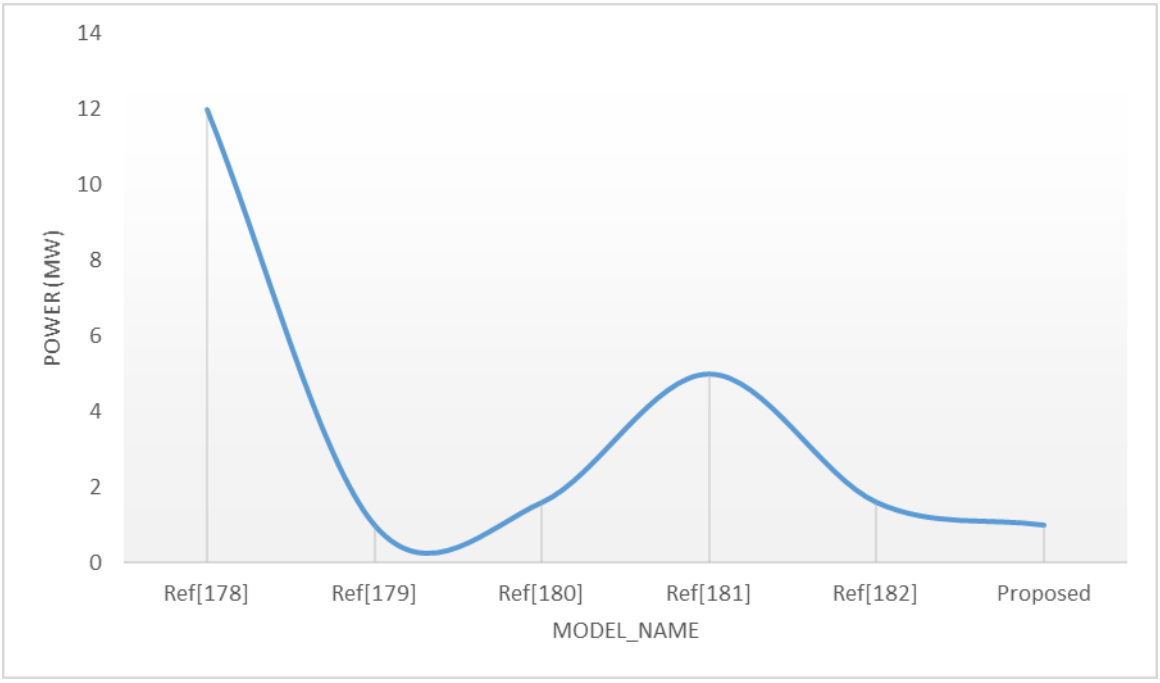

Figure 4-31: Comparison of power in different (4:2) compressors.

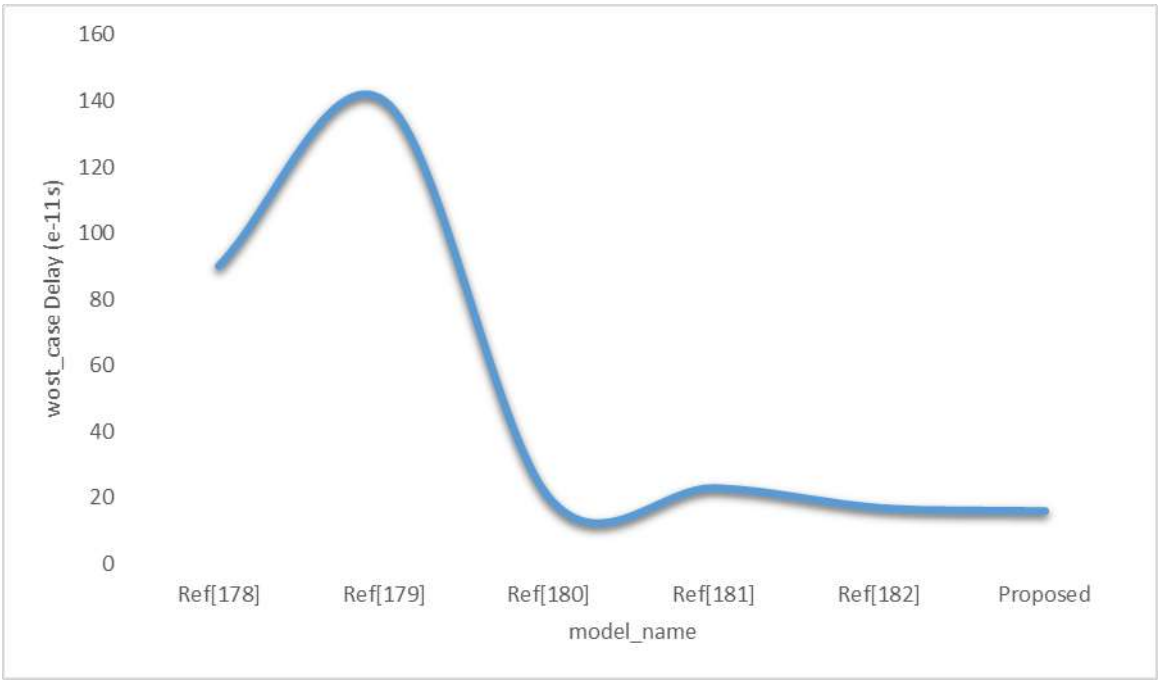

Figure 4-32: Comparison of delay in different (4:2) compressors.

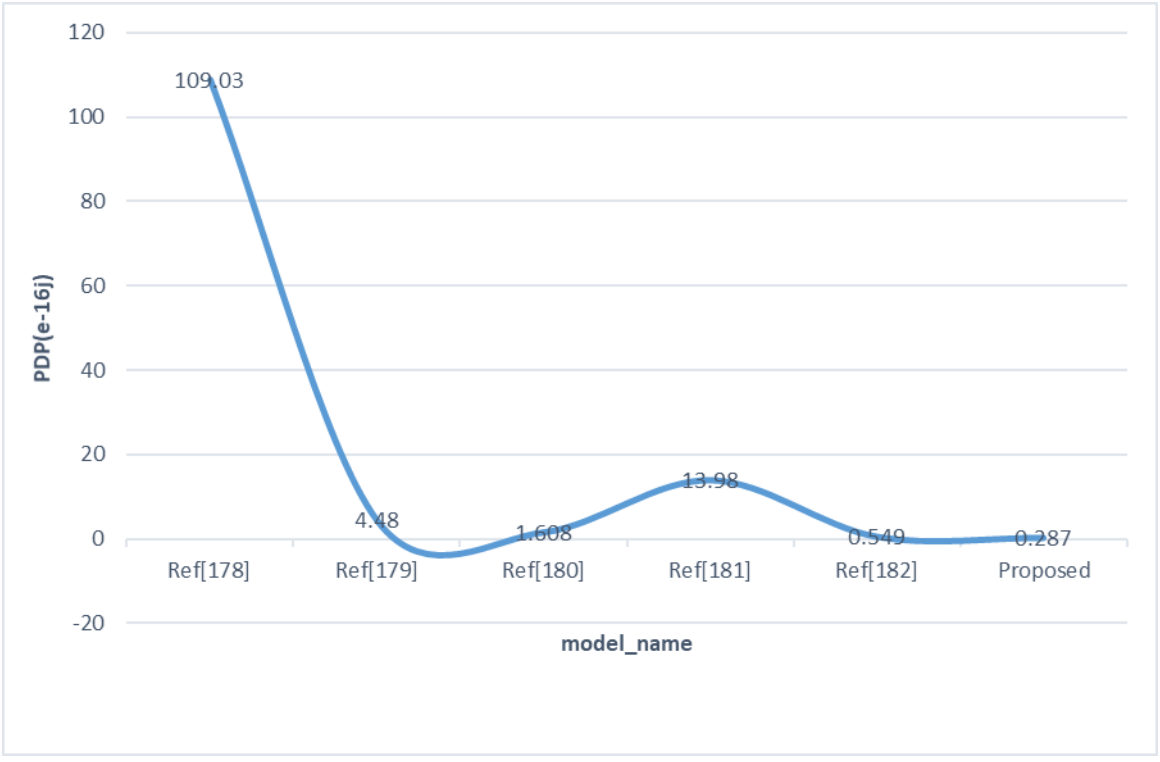

Figure 4-33: Comparison of PDP in different (4:2) compressors.

One of the design parameters is the study of temperature changes on the circuit to measure its performance in different temperature ranges. Therefore, the proposed compressor circuit has been tested in temperature ranges of 10 to 90 ^{0}C to check its resistance to temperature noise.

The simulation results in **Figure 4-34** show that the almost constant PDP for this circuit results from thermal stability of the CNT circuits, which has acceptable performance at different temperature ranges Mehrabi et al (2013) [161].

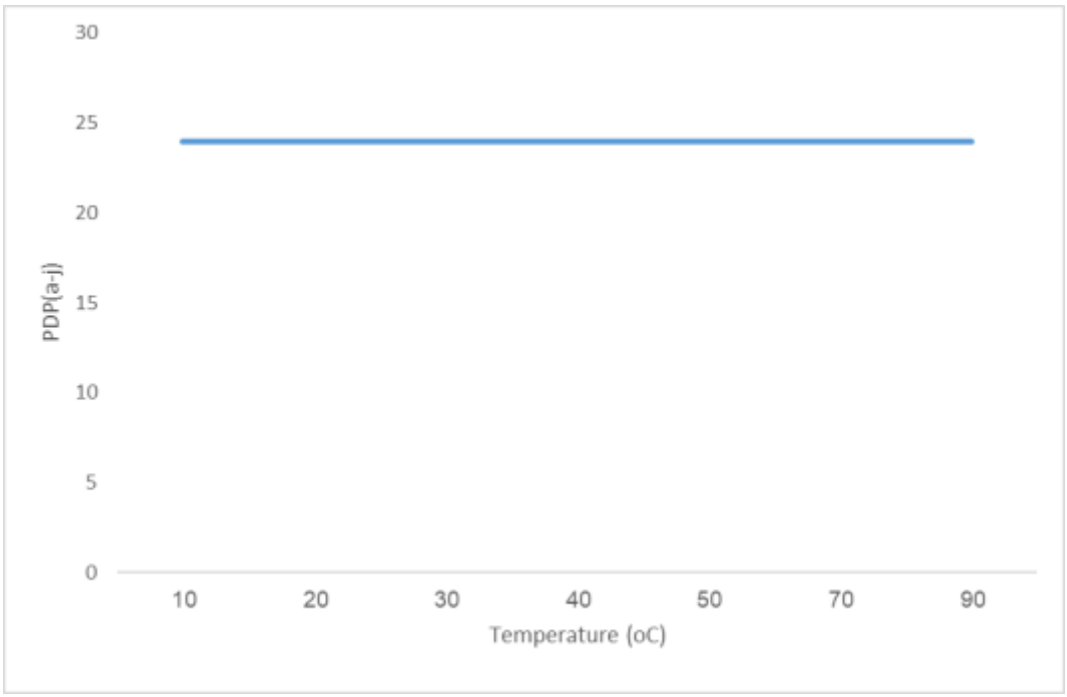

Figure 4-34: Temperature effect on the proposed compressor delay.

4-5- Simulation and results for half-Subtractor

4-5-1- Numerical Analysis Methods:

Analysis of the components with structure-based photonic crystals is done in two ways:

1. To specify the logic gateway frequency range performed by the PWM waveform expansion method.

2. Determination of the transmission range and reflection of optical power in the photonic network structure of all-optical logic gates, which is done by the Finite-Difference Time-Domain (FDTD) method.

The simulation process of the proposed optical photonic crystal logic gate is performed with Rsoft software. The calculation method of the listed tools is PWE. The Transmission diagram

and reflection of optical power in the logical gate output are simulated using the Rsoft FULLWAVE tool. The calculation method of the tool mentioned above is FDTD.

4-5-2- Layout description:

The proposed design has 15 x 15 square lattice of 2-D PhC silica dielectric rods embedded in air substrate of refractive index (n=1) in the hexagonal lattice, which analogous to a fused coupler with waveguides. In this structure, the defects are created by removing the corresponding PhC dielectric rods in the structure that forms the waveguide. The refractive index of chosen Silica rods is about 1.46, and the dielectric constant, ε_r, is about 11.56. The radius, r, of the rods in this work is considered to be 0.18a, where "a" is known as the lattice constant (618 nm for this structure), which is the distance between two dielectric rods. In this design, several junction rods and reflection rods are used. The radius for the central junction/reflection rod (shown in blue color in **Figure 4-35**) is chosen as 0.05a, and the rod shown in green color, in the same figure, has a radius of 0.12a. So that the half subtractor can produce the anticipated output. It is noticed that the maximum power is transmitted at the output ports (Difference and Borrow output Port). **Figure 4-35** shows the all-optical half Subtractor design layout, and it is simulated using the finite difference time domain (FDTD) method.

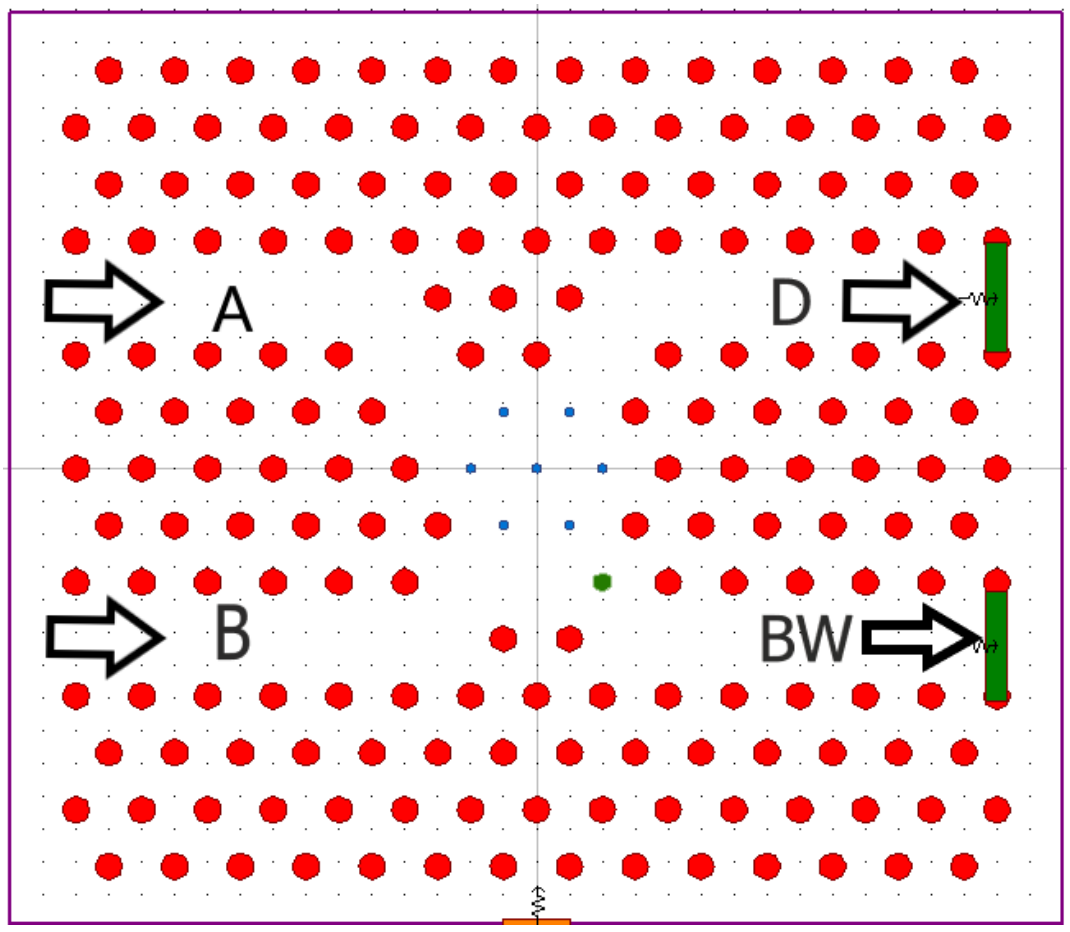

Figure 4-35: Design for half-Subtractor.

4-5-3- Bandgap configuration of for half-Subtractor

The Plane Wave Expansion (PWE) method for obtaining the band structure **Figure 4-36** shows the normalized band structure for the proposed structure. The band structure is obtained for the TE mode. The calculated band structure depicts that the main Photonic Band Gap (PBG) half-Subtractor is situated in the range of $a/\lambda = 0.31$ to 0.479. Then the selected wavelength sources should be in this PBG range, and therefore $\lambda = 1550$ nm is used for this simulation.

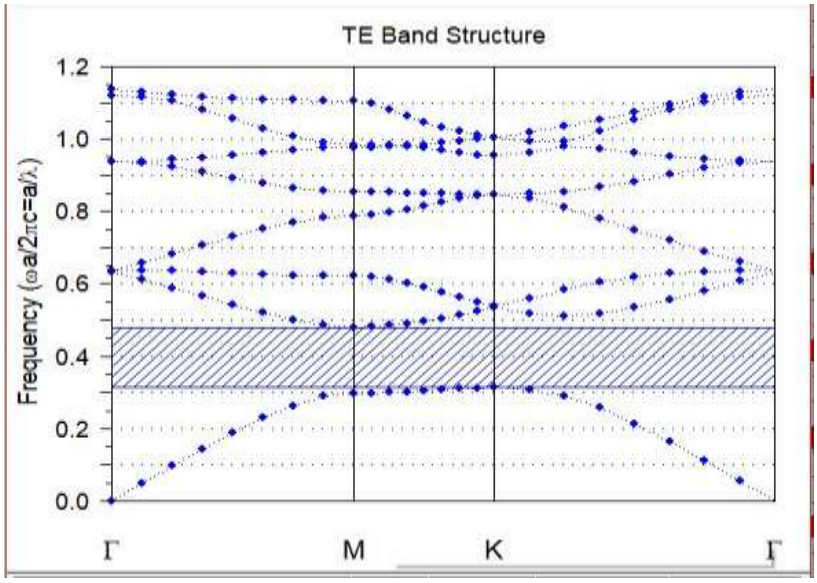

Figure 4-36: Calculated bandgap for proposed Structure.

The refractive index diagram of the proposed crystal photonic structure is depicted in **Figure 4-36**.

The proposed Optical Half-Subtractor has two inputs (A and B) and two outputs (D and BW), where D is the difference of two inputs and BW is the Borrow output bit. Two optical sources with a 1550 nm wavelength are used as inputs. The defect lines of the proposed half-Subtractor's inputs and outputs are shown in the layout **Figure 4-37**. The defect lines are selected to intercross each other. These rods act as scatterers which will control and conduct electric field in their output ports.

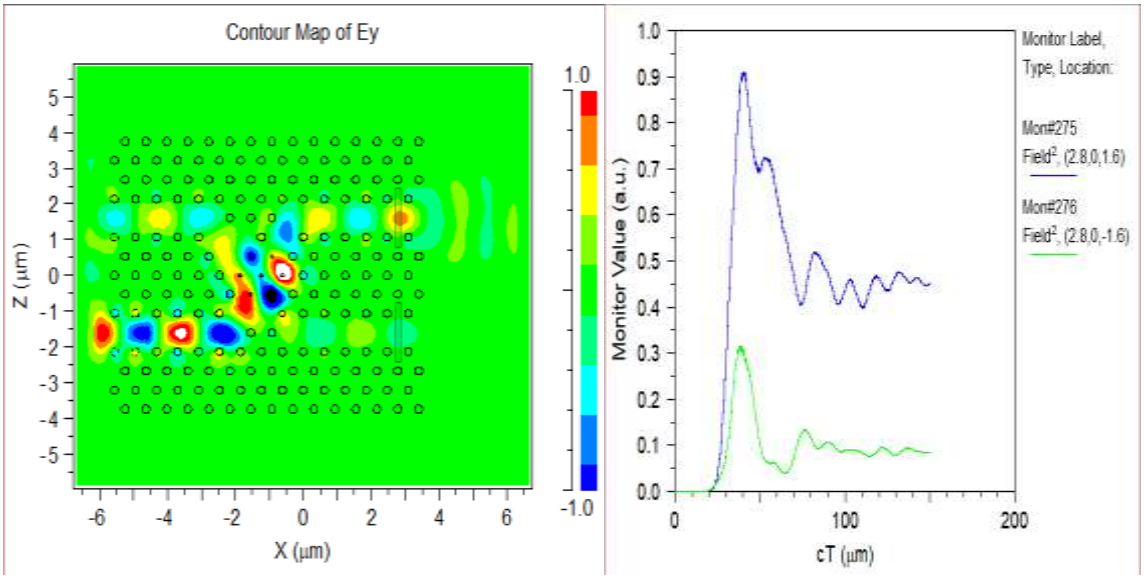
Contour Map of Ey
Z (μm)
X (μm)
1.0
-1.0
Monitor Value (a.u.)
cT (μm)
Monitor Label,
Type, Location:
Mon#275
Field², (2.8,0,1.6)
Mon#276
Field², (2.8,0,-1.6)

(a)

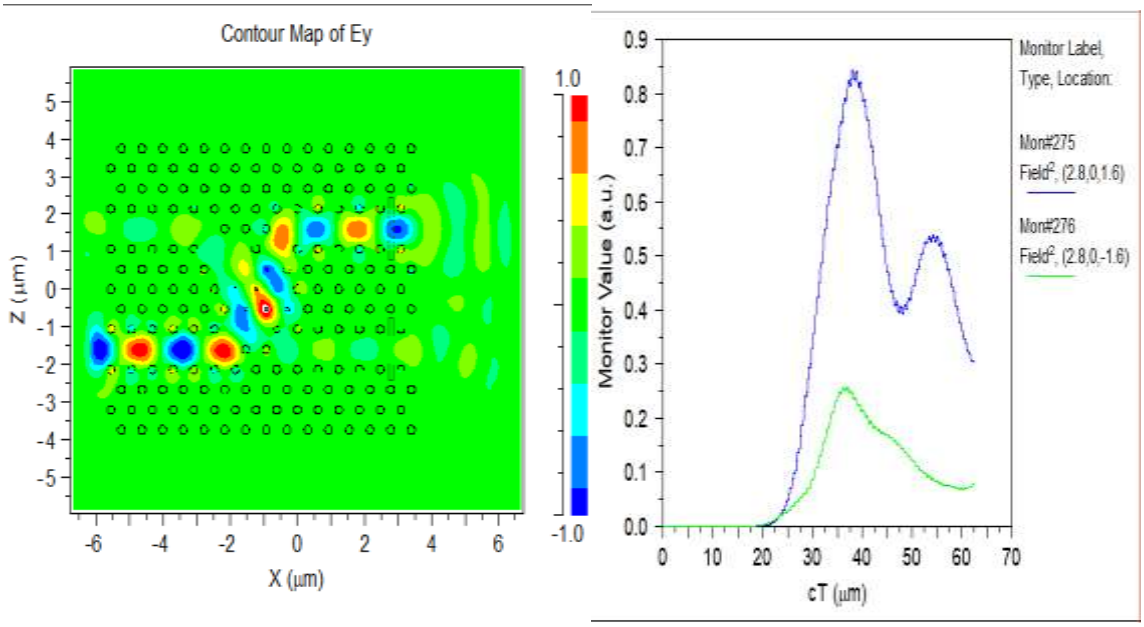
Contour Map of Ey
Z (μm)
X (μm)
1.0
-1.0
Monitor Value (a.u.)
cT (μm)
Monitor Label,
Type, Location:
Mon#275
Field², (2.8,0,1.6)
Mon#276
Field², (2.8,0,-1.6)

(b)

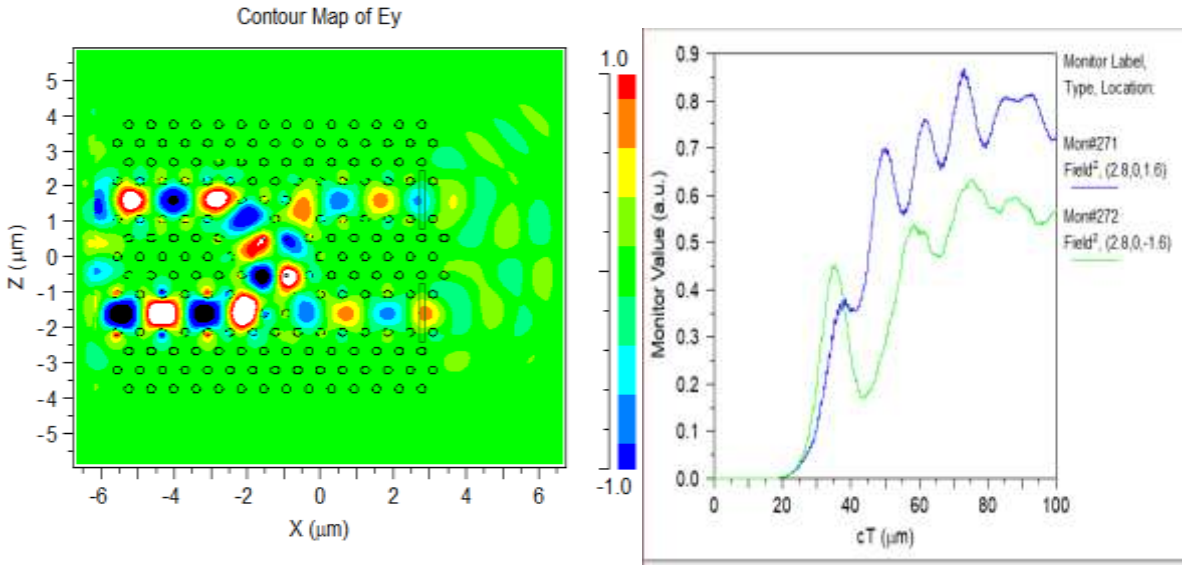

(c)

Figure 4-37 a) (A = 0, B = 1), b) (A = 1, B = 0), and c) (A = B = 1): Electric field distribution of inputs (cT shows time in horizontal axis).

In this study, we have four states described as follows. When the two input sources are off A = B = "0" (state one), there is no light at the output, so D and BW will be zero. For a special case of A = "0" and B = "1"(state two), the output value is HIGH at both outputs (D=0.85 µW, BW=0.58 µW). When the inputs A = "1", B ="0", the output at D is significant than compared to the BW output (D=0.82 µW, BW=0.1 µW) and in case of A = B = "1" (state four), then both of the outputs are LOW (D=0.22 µW, BW=0.1 µW). All those states are clearly shown in **Figures 4-37 (a), (b), and (c). Table 4-8** presents the results of the proposed structure to verify half-subtractor operations.

Table 4-8: Input and output values for 1550 nm half-subtractor Input power = 1.0 Mw.

INPUT				OUTPUT			
A		B		D		BW	
VALUE	LOGIC	VALUE	LOGIC	VALUE	LOGIC	VALUE	LOGIC
0	0	0	0	0	0	0	0
0	0	1	1	0.85	1	0.58	1
1	1	0	0	0.82	1	0.1	0
1	1	1	1	0.22	0	0.1	0

In this simulation, electric field variations in the bandwidth range (1530-1610 nm) are shown in **Figures 4-38, 4-39, and 4-40**. Here, in these three figures.

Considering that the designed subtractor cannot be ideal and any equipment has an ideal error value, it must be measured. In photonic crystal structures, due to lack of an ideal refractive index, and problems such as errors in the lattice's fixed distance and the intervals between the holes, there is always some leakage from the input wave into the structure or the presence of electromagnetic power in undesirable outputs. This amount of leakage power should not exceed the threshold limit defined for the subtractor's proper functioning. In this section, the amount of power in desirable outputs and the amount of leakage power to unwanted outputs are shown in **Figures 4-38, 4-39 and 4-40.**

The difference between these powers in the design's wavelengths should be less than the threshold limit defined for the proper functioning of the equipment.
If A = "1", B = "0", the desirable and ideal value of D output is 1 μm to indicate the logic "1" value in this output. However, this power value is ideal, and in practical operation, this power value is less than 1. Also, the leakage power value to the BW output should be 0 μm, whose value in the normal operation of the equipment is not 0. Its value for the wavelengths of the design is shown in the **Figure4-39**.

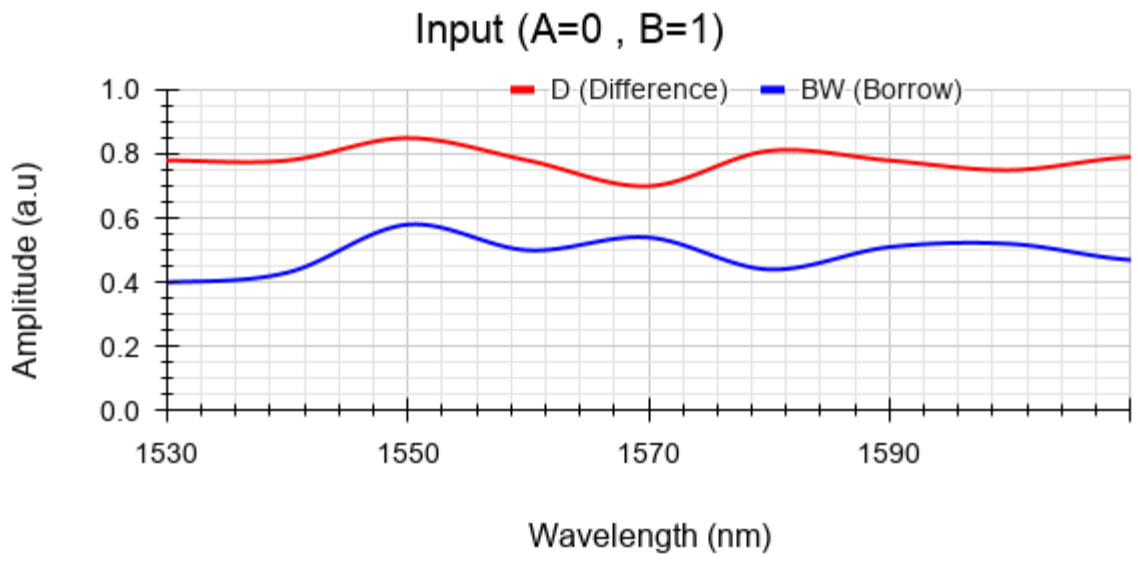

Figure 4-38: Output graph for various wavelengths with inputs A = “0” and B = “1”.

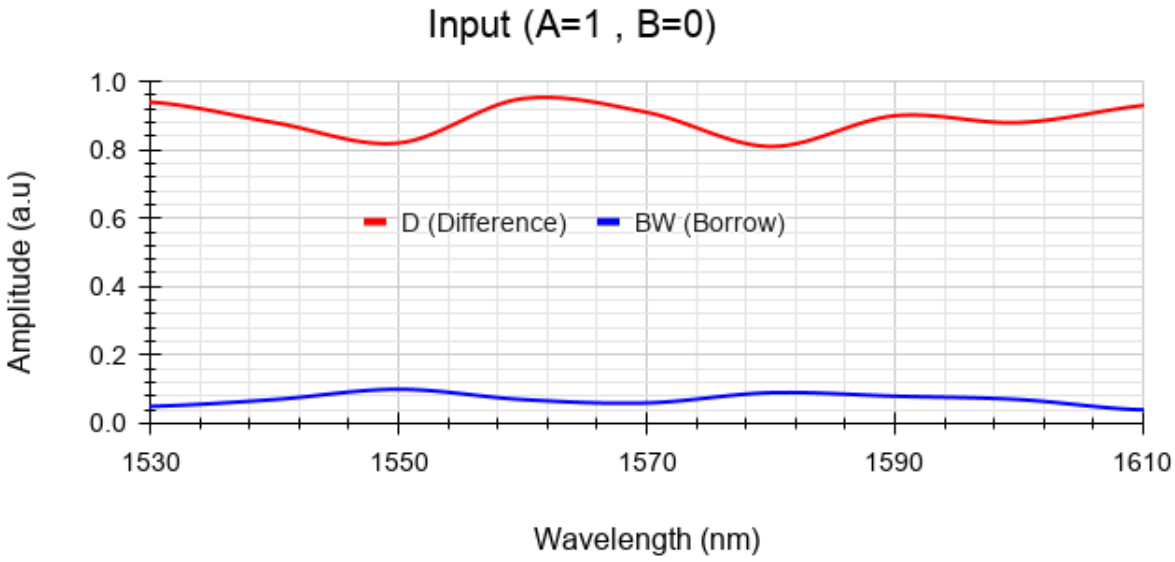

Figure 4-39: Output graph for various wavelengths with inputs A = 1 and B = 0.

In Figure 4-38, both the output values are HIGH (state three), and in the wavelength of 1550 nm, it can be seen that D=0.85 µW and BW=0.58 µW. As shown in **Figure 4-39**, When A = "1", B = "0"(state three), the output at D is HIGH, whereas, in BW port, the output is LOW. As we can see in the C-band (1530-1565 nm) the power value in D is lower than 1 µW and is higher than 0.8 µW, and the power leakage to the BW output at the most of wavelengths is less than 0.18 µW. The difference between these two values is high enough to consider a suitable threshold limit for logic values of "0" and "1".

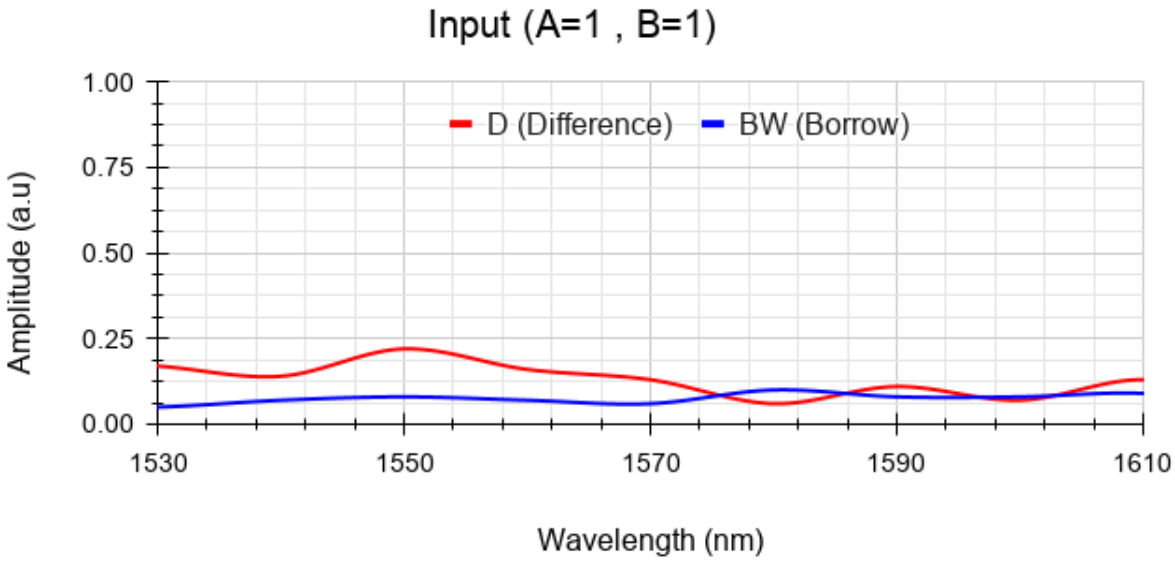

Figure 4-40: Output graph for various wavelengths with the inputs A=B=1.

In **Figure 4-40**, both inputs are stimulated to the unit power. In this case, A = B = "1" (state four), and the difference and the residual subtraction in the correct function require the logic value of "0" on both D and BW outputs. As shown in **Figure 4-40**, the output power of wavelengths (D and BW) is less than 0.22 μW, which indicates the proper functioning of the designed gate.

The contrast ratio is defined as the ON power ratio to OFF power in single ports and calculated using **Equation 4-3** Mohebzadeh-Bahabady and Olyaee (2018) [164]:

$$CR = 10 \times \log P_{ON} / P_{OFF} \quad (4.3)$$

Where P_{ON} and P_{OFF} are the levels of logic powers "1" and "0", the contrast ratio is 17.24 dB and 25.88 dB in D and WB outputs, respectively. This improved contrast ratio plays an important role in photonic integrated circuits.

4-6- Discussion and results of the 4-input OR logic gate

The structure and dimensions of a 4-input OR logic gate are illustrated in **Figure 4-41**. We assume that the threshold of the optical electric field amplitude in the waveguides is equal to 0.4. If the field amplitude is greater than 0.4, it will be assumed as a logical "1", and if the field amplitude is less than 0.4, it will be assumed as a logical "0".

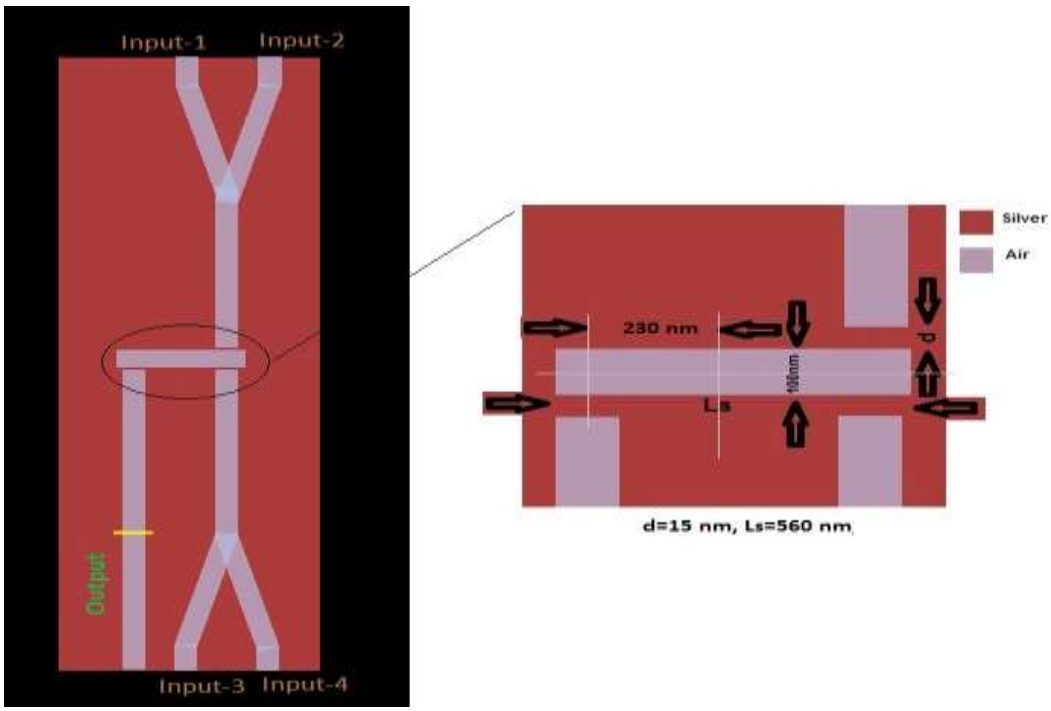

Figure 4-41. The structure and dimensions of a 4-input OR logic gate.

First, resonance wavelengths for the proposed photonic crystal structure are obtained. The following graph, **Figure 4-42**, is obtained for the transmission coefficient of the structure.

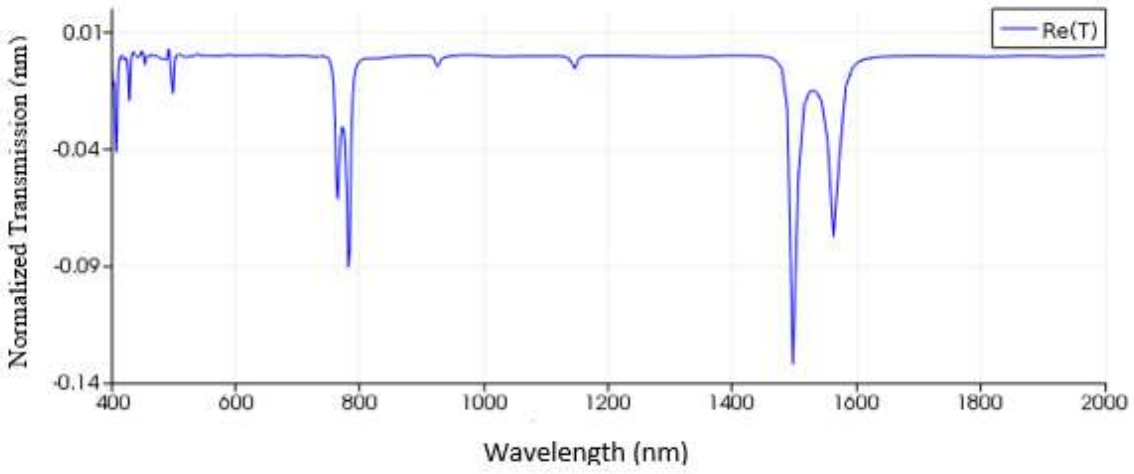

Figure 4-42: The resonance wavelengths for the structure (various telecommunication windows).

Considering **Figure 4-42**, a wavelength of 1490 nm will be suitable for the gate's operation. Of course, we have resonance in a wavelength of 780 nm, but since the telecommunication windows are within 1470-1550 nm, we consider the main wavelength at 1490 nm.

The resonance wavelength is obtained from **Equation 4-4**, which λ depends on the length of the rectangle lattice (l) (photonic crystal structure) in the cavity shown in **Figure 4-43**.

$$\lambda = \frac{(k)\Pi}{l}, \text{ k = 1, 2,} \qquad (4.4)$$

Where 780 nm is synonymous with the first resonance and 1490 nm is synonymous with the second resonance.

In state one, shown in **Figure 4-43** (wavelength of 1490 nm), we assume that all four inputs are active and equal to logical "1" (we assume the electric field amplitude of the input electromagnetic wave at each of the four inputs as being equal to the normalized one). In this state, the amplitude of the optical electric field at the output is about 1.3 units, as shown in **Figure 4-43(b**). Since it is greater than 1.3 units, it will be considered equal to a logical "1" as expected. The electric fields in the OR gate structure are illustrated in **Figure 4-43(c**), and it can be seen that the circuit has operated correctly.

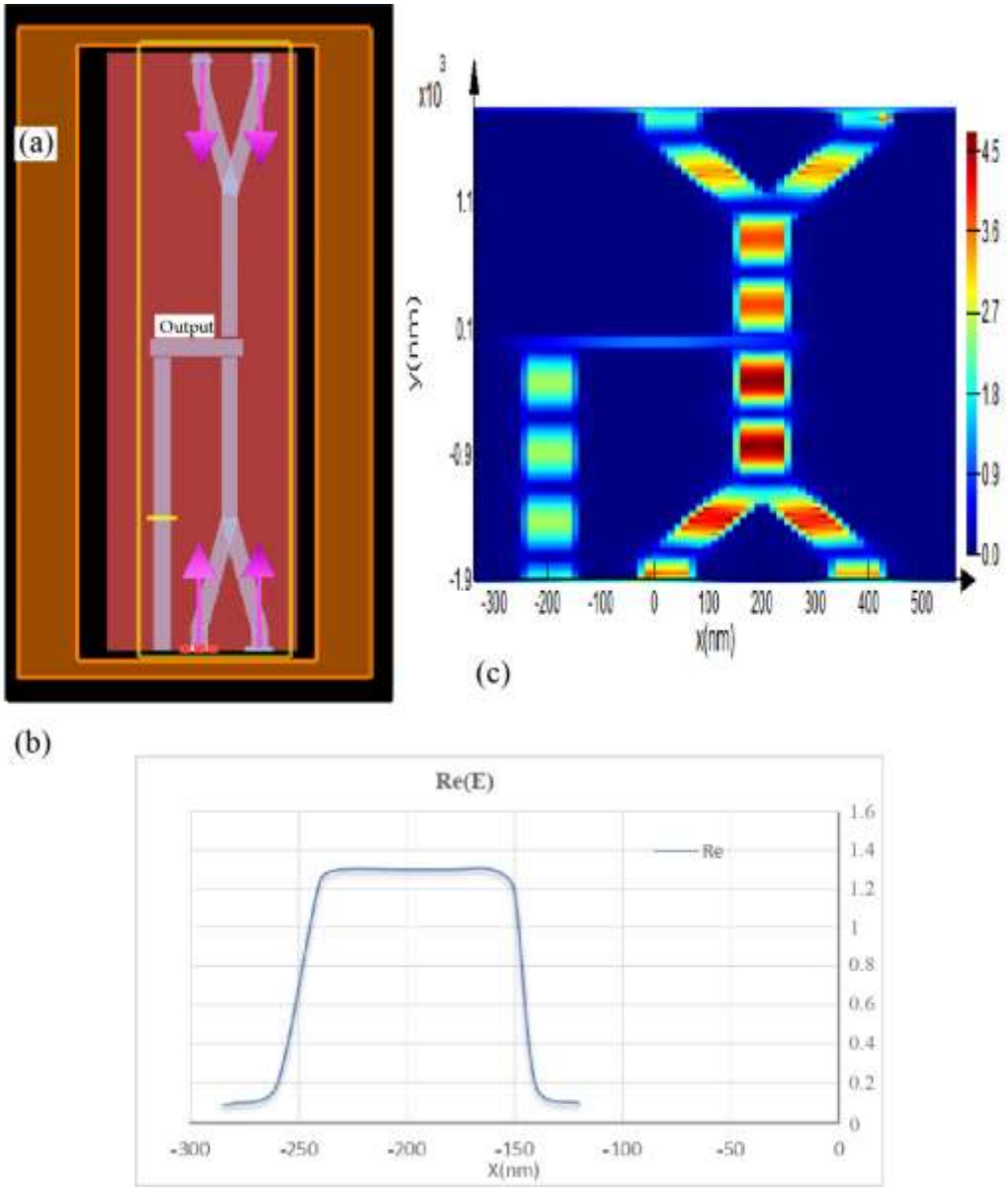

Figure 4-43: The structure of the designed 4-input OR gate: (a) The state where all four input ports are active and stimulated;(b) The electric field amplitude at a wavelength of 1490 nm at the output port; (c) Shows the fields in the gate structure at a wavelength of 1490 nm.

Due to the symmetry of the shape in state two shown in **Figure 4-44** where Input-1 = "0", Input-2 = "1", Input-3 = "0", and Input-4 = "1", (wavelength of 1490 nm). **Figure 4-44(a)** shows the shape of the inputs and outputs, and **Figure 4-44(b**) shows the amplitude of the electric field at the output, which is about 0.65 units, which represents a logic "1" because it is larger than the threshold. The electric fields in the OR gate structure are illustrated in **Figure 4-44(c)**, and it can be seen that the circuit has operated correctly. In this state, due to the resonance of the field caused by the rectangular resonator, the waveguide side has inclined towards orange, which represents a field resonating into the waveguide.

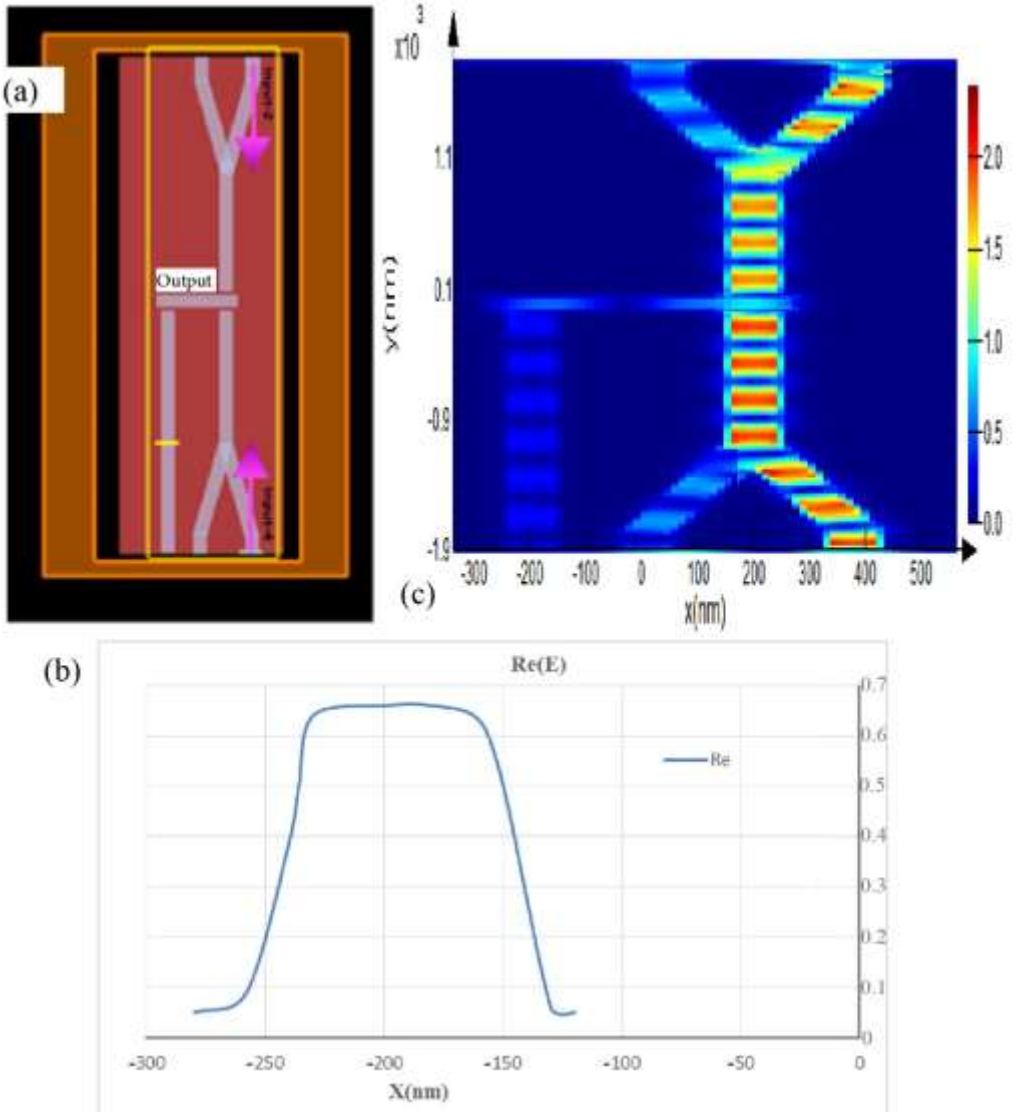

Figure 4-44: The structure of the designed 4-input OR gate: (a) The stimulation state where Input-1 = 0, Input-2 = 1, Input-3 = 0, and Input-4 = 1; (b) The electric field amplitude at a wavelength of 1490 nm at the output port; (c) Shows the fields in the gate structure at a wavelength of 1490 nm.

In state three, where the two opposite inputs are stimulated, and the two other ones are off in wavelength of 1490 nm (Input-1 = "1", Input-2 = "1", Input-3 = "0", and Input-0 = "0"), the conditions are like those in the previous state. Hence, to avoid repetition, describing these states is avoided.

We assume that two of the neighboring inputs are stimulated with a normalization power of 1, and the two others are inactive, shown in **Figure 4-45**. As for this state, **Figure 4-45(a)** shows the shape of the inputs and outputs, and **Figure 4-45(b)** shows the amplitude of the electric field at the output, which is about 2.3 units, and represents a logic "1" because it is larger than the threshold. The electric fields in the OR gate structure are illustrated in **Figure 4-45(c),** and it can be seen that the circuit has operated correctly. In this state, due to the resonance of the

field caused by the rectangular resonator, the side of the Input-1 and Input-2 waveguides has inclined towards red, which represents a field resonating into these two waveguides.

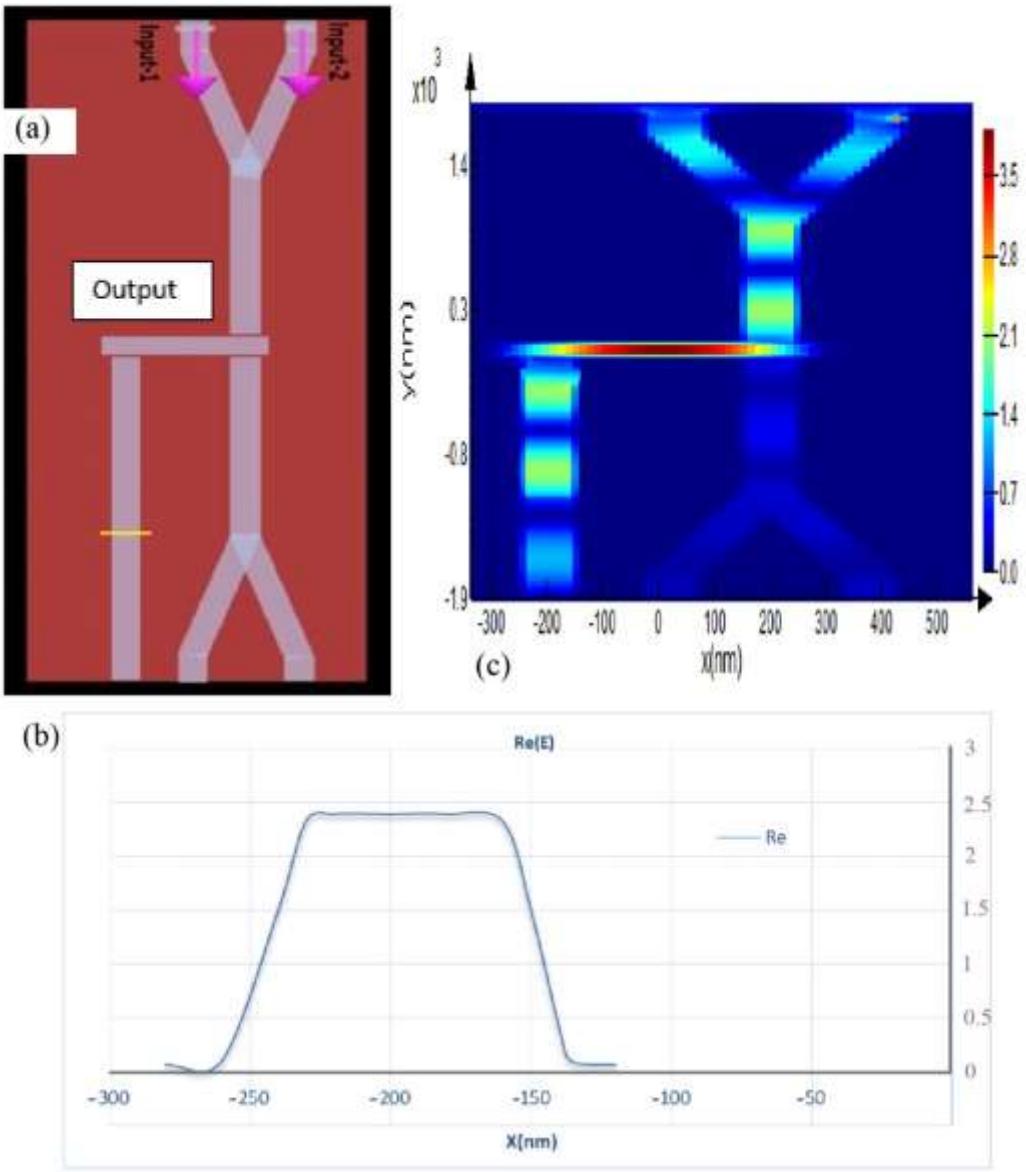

Figure 4-45: The structure of the designed 4-input OR gate: (a) The stimulation state where Input-1 = "1", Input-2 = "1", Input-3 = "0", and Input-0 = "0"; (b) The electric field amplitude at a wavelength of 1490 nm at the output port; (c) Shows the fields in the gate structure at a wavelength of 1490 nm.

In state four, where Input-1 = "1", Input-2 = "0", Input-3 = "0", and Input-0 = "0" (wavelength of 1490 nm), we assume that only one of the inputs is active, and the rest are inactive. Since the structure is symmetric, there is no difference in the input you choose as the active input, as shown in **Figure 4-46**. In this state, the logic gate structure is considered as shown in **Figure 4-46(a)**. The electric field at the output is about 1.4 units and illustrated in **Figure 4-46(b), and Figure 4-46(c)** shows the size of the fields in the gate structure using colored markers.

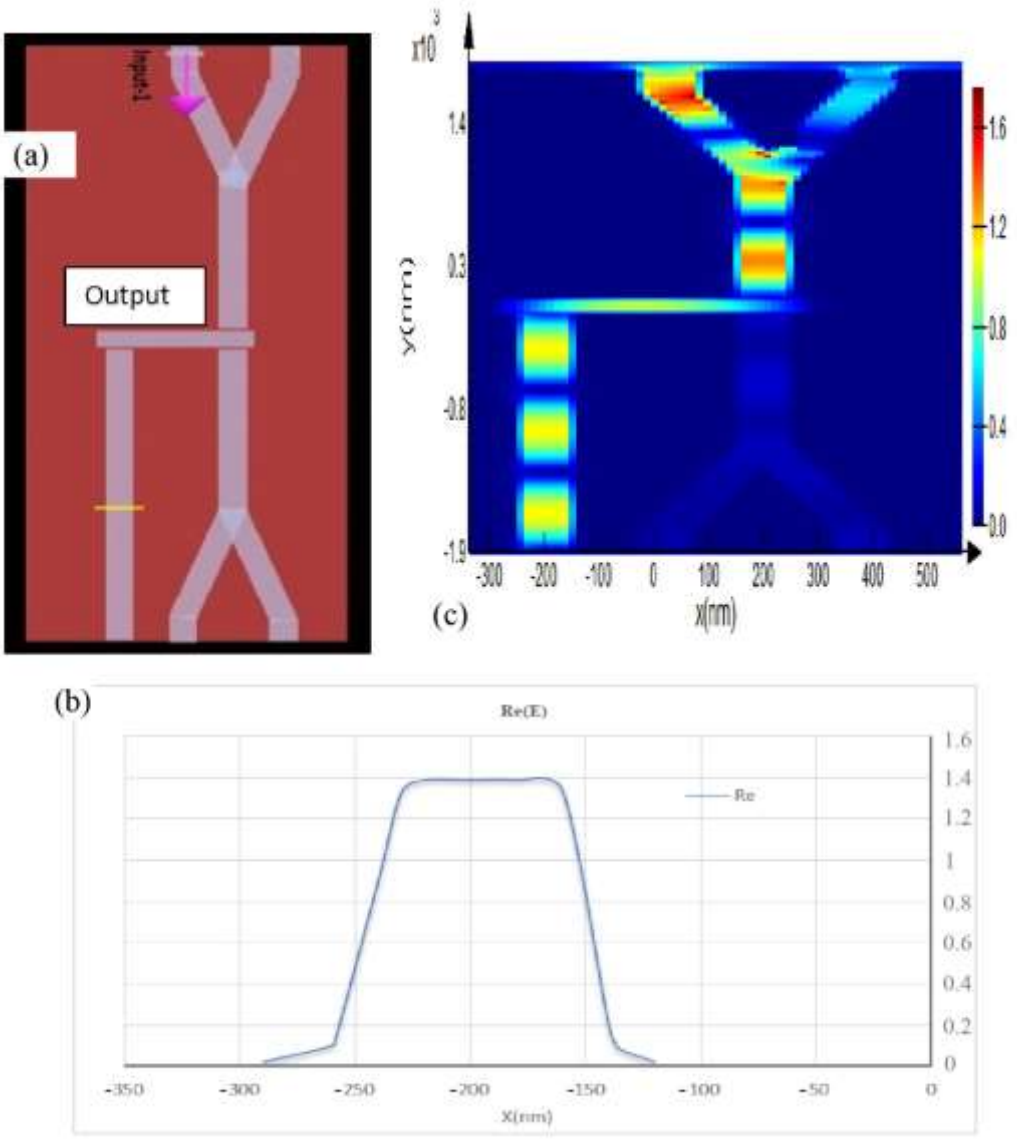

Figure 4-46: The structure of the designed 4-input OR gate: (a) The stimulation state where Input-1 = “1”, Input-2 = “0”, Input-3 = “0”, and Input-0 = “0”; (b) The electric field amplitude at a wavelength of 1490 nm at the output port; (c) Shows the fields in the gate structure at a wavelength of 1490 nm.

In the final state where Input-1 = "0", Input-2 ="0", Input-3 = "0", and Input-0 = "0"(wavelength of 1490 nm), where all four input ports are "0", logically, none of the fields get into the output port. Therefore, the amplitude of the electric field at the output port is zero, which represents the correct function of the proposed 4-input OR logic gate. **Table 4-9** shows the electric field amplitudes at the inputs and outputs of the proposed logic gate as well as the correct functioning states of the logic gate. The remaining combinations of the four inputs are not shown in **Table 4-9** due to their structural symmetry.

Table 4-9: Electric field amplitudes at the inputs and outputs of the proposed logic gate.

No.	Elec Amplitude	Elec Amplitude	Elec Amplitude	Elec Amplitude	Elec Amplitude
Input-1	1	0	1	1	0
Input-2	1	1	1	0	0
Input-3	1	0	0	0	0
Input-4	1	1	0	0	0
Output Elec Amplitude	1.3	0.65	2.3	1.4	0
Output	1	1	1	1	0

4-7- Simulation and analysis of results 2DPC based eight channels demultiplexer

The normalized output transmission response of the proposed eight-channel demultiplexer is estimated using FDTD numerical method. A light source of Gaussian pulse with TE polarization is passed through the eight-channel demultiplexer bus waveguide for power spectral density (PSD) measurement. The PSD gives the normalized output spectrum directly, measured by keeping the power monitor for each dropping waveguide. The normalized transmission spectra is calculated using the equation given below:

$$T(f) = \frac{\int real\,(p(f)^{monitor})dS}{source\ power} \qquad (4.5)$$

In this equation, T (f) is the normalized transmission, a function of frequency, p (f) is the pointing vector, and dS is the surface differential. Normalization on the output side does not affect the results because the input source power is normalized. Finally, T (f) will be a function of wavelength, where T (f) denotes normalized transmission about the frequency, T (f) is the pointing vector, and ds denotes surface normal preserving the right time step. The time step shows the band separation of light during the propagation in the waveguide. The time step equation is stated in **Equation (4-5)**.

Figure 4-47 shows the input field and output channels.

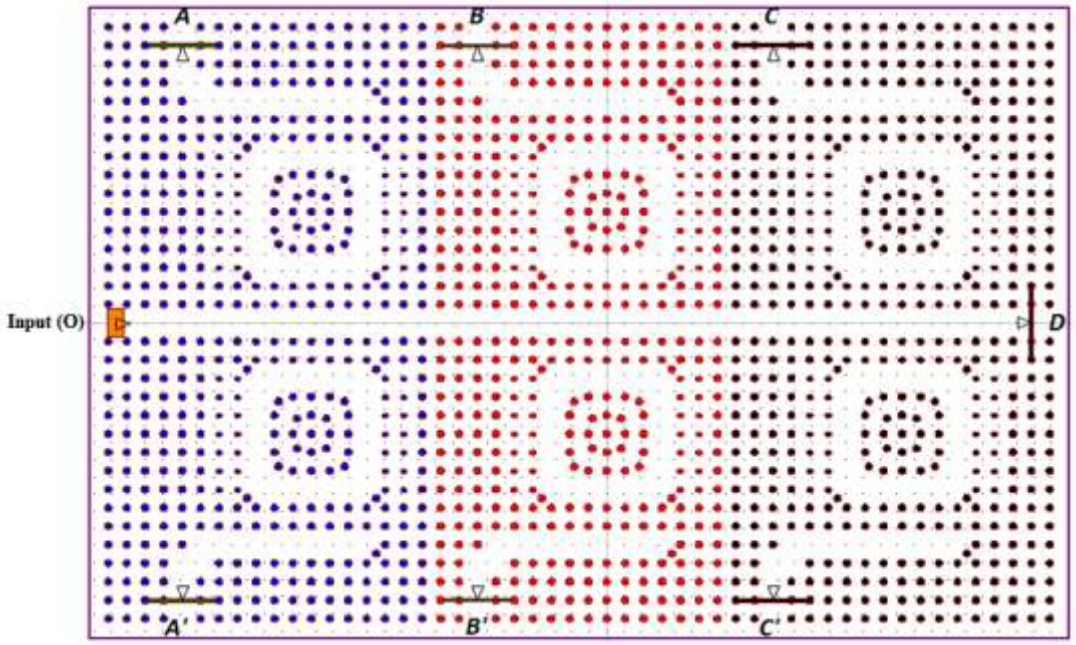

Figure 4-47: Proposed design including the input field and the power monitors of the output channels.

To avoid spurious reflections from the boundaries, a sponge-like perfectly matched layer (PML) is implemented. A perfectly matched layer (PML) is an artificial absorbing layer for wave equations, commonly used to truncate computational regions in numerical methods to simulate problems with open boundaries, especially in the FDTD methods. The following parameters are considered for simulation: a perfectly matched layer (PML) is used as the boundary condition for simulating the structure. The width of the PML is 500 nm, which is placed around the proposed demultiplexer. In the FDTD method, two important parameters, which need to be carefully adjusted, are the spatial lattice sizes and time step values. The lattice sizes determine the amount of meshing of the structure and are determined by:

$$\Delta x=\Delta z=\frac{a}{16} \qquad (4.6)$$

Where "a" is the lattice constant. The time step is important to simulate stability.

Boundary conditions are also defined by considering the PML layer with a thickness of 500 nm around the structure. The computational steps for Δz and Δx are considered to be a/16 = 33/75 nm. For more stability of the time steps, the $\Delta t \leq \frac{1}{c\sqrt{\frac{1}{\Delta x^2}+\frac{1}{\Delta x^2}}}$ is used in which c is the light speed in the open space. Therefore, from the above equation t ≤0.0239 is obtained to perform this simulation. To obtain analyzable results, the settings are adjusted so that each channel's output spectra are normalized according to the input signal.

The designed structure will be very important in terms of size. Therefore, since the designed channels are symmetrically facing each other, the design foreground's size is optimized here, which is one of the important advantages of optical demultiplexer design. The design's main

point is to change the radius determined for each scattering and coupling rod, which has a different value from the reviewed articles. These values are obtained experimentally and after repeated simulations.

According to **Figure 4-48,** the results of the output spectrum obtained for the new design are shown after the time specified by the software.

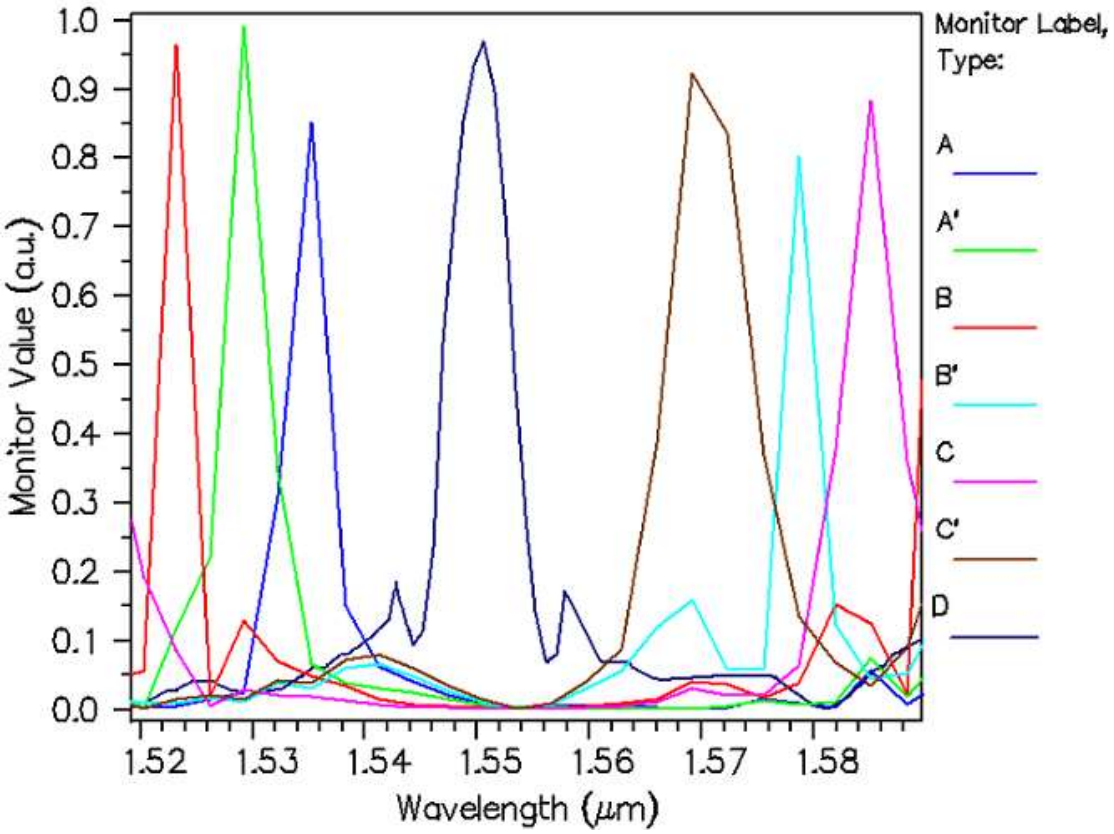

Figure 4-48: Normalized output spectrum of the final design.

The results obtained from the output spectrum of the proposed demultiplexer are presented in **Table 4-10**. This table provides the Q factor, transmission efficiency, and other important specifications related to each of the output channels. As can be seen, the highest efficiency and the lowest efficiency are related to channels A' and B'. Channel B has the best conditions among the output channels because its Q factor is the highest, and transmission efficiency is reasonable compared to the other channels.

Table 4-10: Table of simulation results.

Channel	Central wavelength (nm)	Half power bandwidth (nm)	Q factor	Transmission efficiency (%)
A	1535.4	4.2	365.5	84.8
A'	1529	4	382.25	98.5
B	1523.2	3	507.7	95.8
B′	1578.7	3.5	451	79.5
C	1585	5	317	87.5
C′	1596.3	7	224.1	91.6
D	1550	5.5	281.8	96.2

Considering the value of the refractive index in the three regions and the results of **Table 4-13**, it can be inferred that the larger wavelengths are related to the higher refractive index and conversely. **Figure 4-49** shows the electric field pattern along the y-axis for a continuous Gaussian wave at the input.

In **Figure 4-49(a),** the only open port is A. The light propagates through the structure with 1550 nm from input O and passes through the output A with a central wavelength of 1535.4 nm; in this mode, the transfer efficiency is 84.8%.

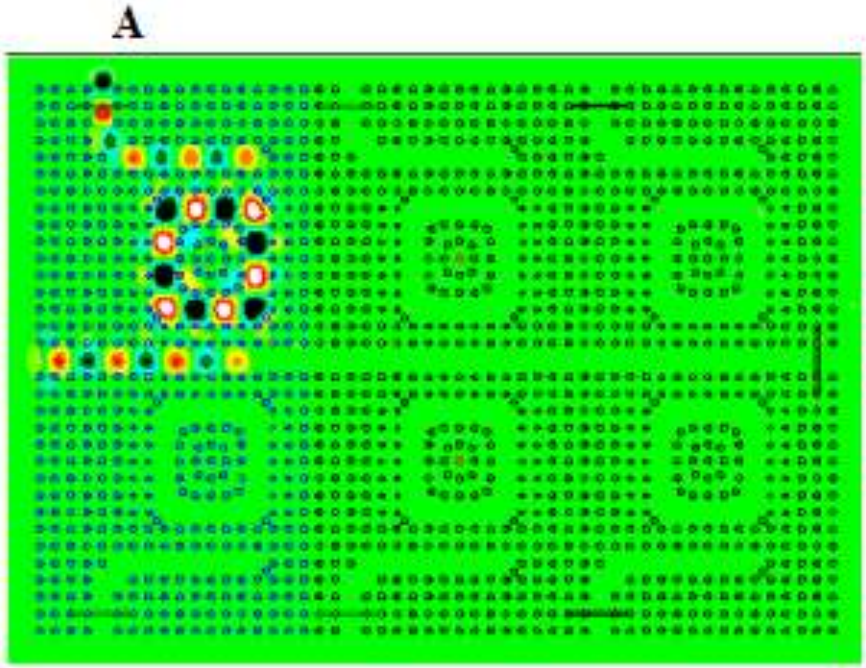

(a) Channel (1535.4nm)

In **Figure 4-49(b),** the only open port is A’. The light propagates through the structure with 1550 nm from input O and passes through the output A’ with a central wavelength of 1529 nm; in this mode, the transfer efficiency is 98.5%.

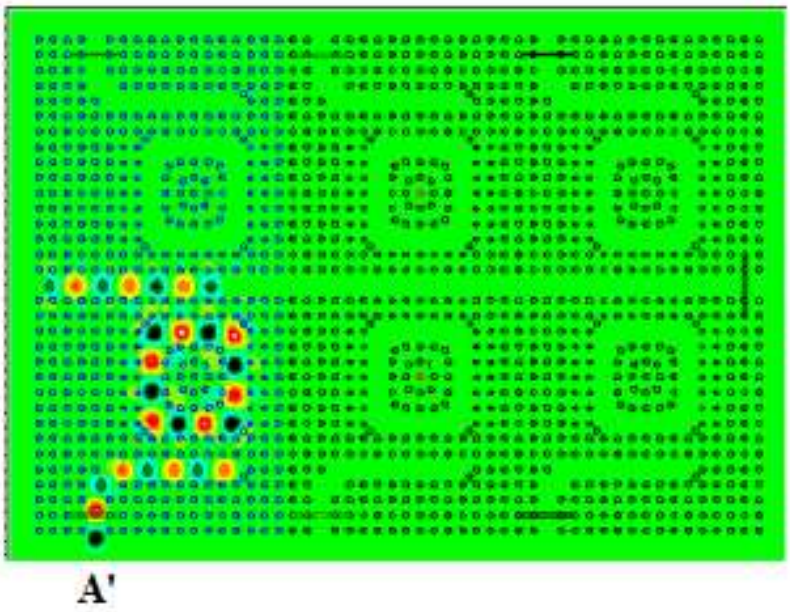

(b) Channel A'(1529 nm)

In **Figure 4-49(c)**, the only open port is B. The light propagates through the structure with 1550 nm from input O and passes through the output A with a central wavelength of 1523.2 nm; in this mode, the transfer efficiency is 95.8%.

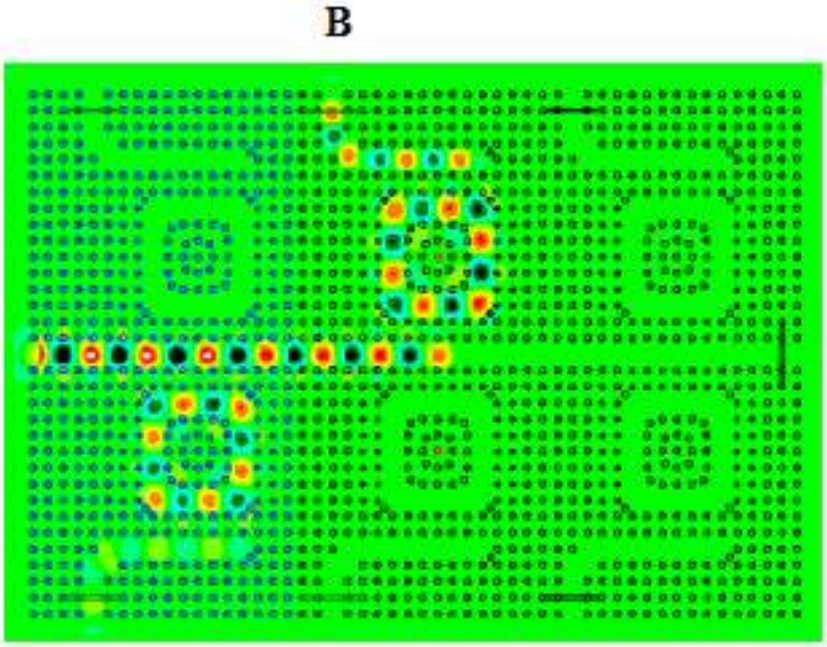

(c) Channel B (1523. 2nm)

In **Figure 4-49(d),** the only open port is B’. The light propagates through the structure with 1550 nm from input O and passes through the output B’ with a central wavelength of 1578.7 nm; in this mode, the transfer efficiency is 79.5%.

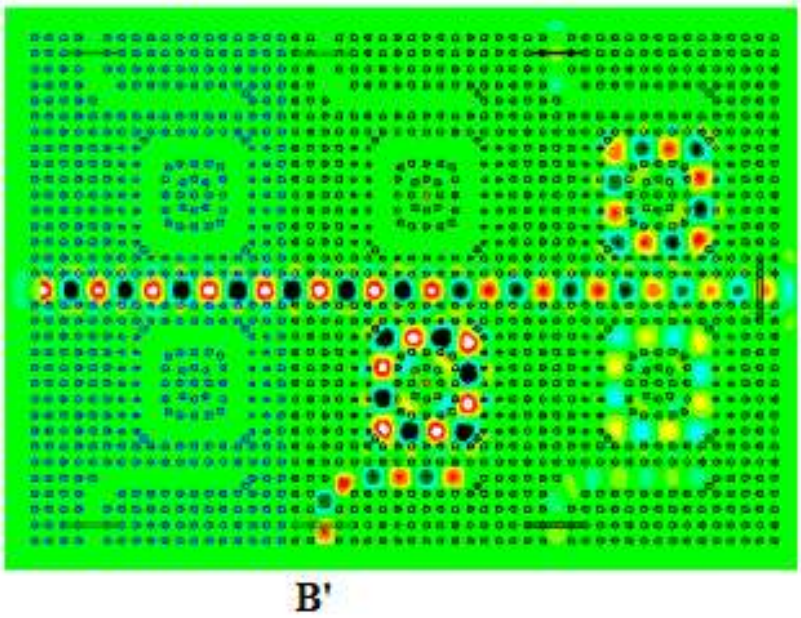

(d) Channel B'(1578. 7nm)

In **Figure 4-49(e)** the only open port is C. The light propagates through the structure with 1550 nm from input O, and passes through the output A with a central wavelength of 1596.3 nm; in this mode, the transfer efficiency is 91.6%.

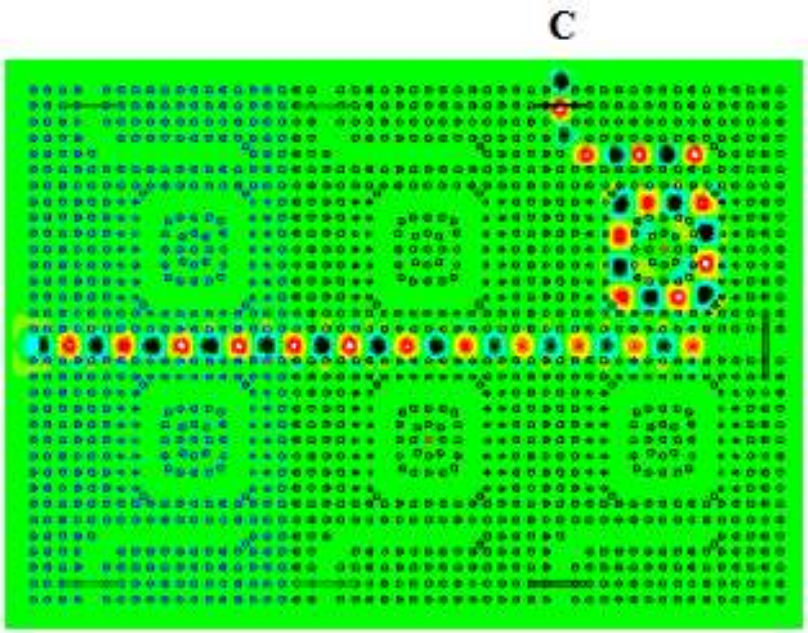

(e) Channel C (1585nm)

In **Figure 4-49(f)** the only open port is C'. The light propagates through the structure with 1550 nm from input O and passes through the output B' with a central wavelength of 1550 nm; in this mode, the transfer efficiency is 91.2%.

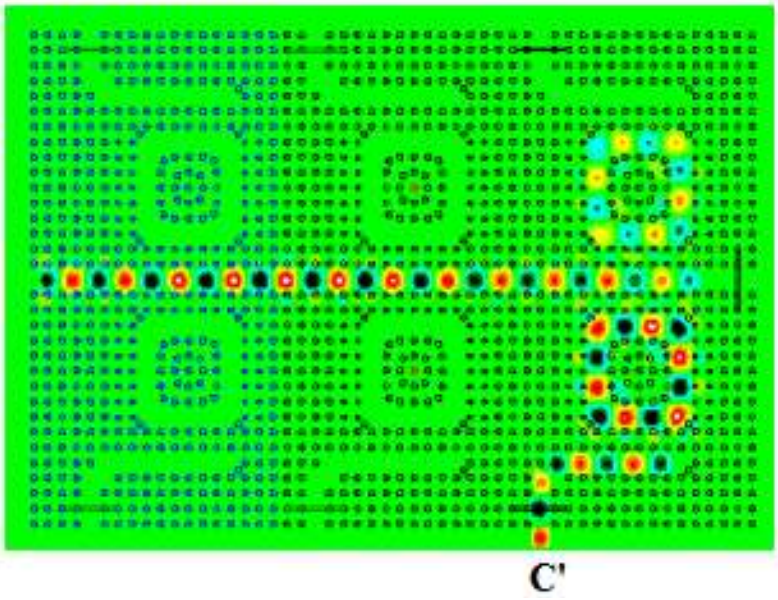

(f) Channel C'(1569. 3nm)

In **Figure 4-49(g),** the only open port is D'. The light propagates through the structure with 1550 nm from input O and passes through the output D' with a central wavelength of 1550 nm; in this mode, the transfer efficiency is 96.2%.

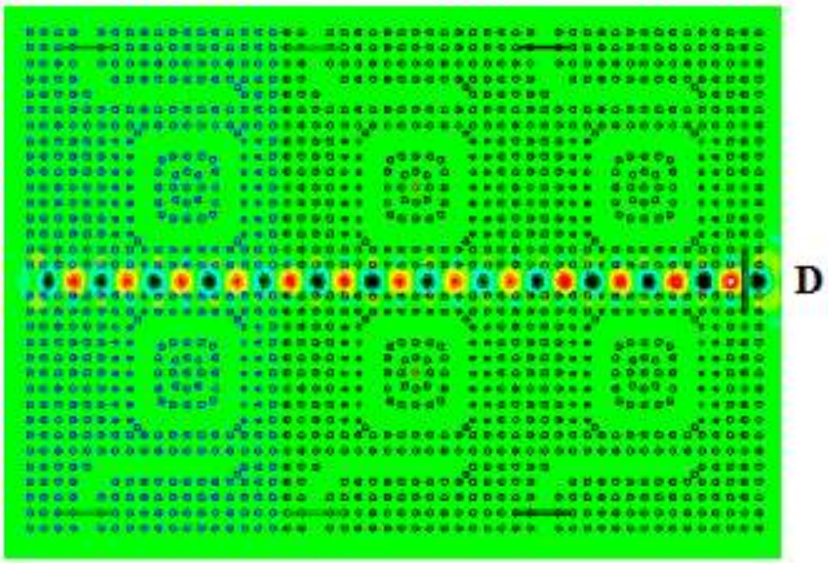

(g) Channel D (1550nm

Figure 4-49: Electric field pattern of output channels.

4-7-1- Investigation of effective factors in the simulation of eight-channel multiplexer

In this section, the results of changing effective parameters in the performance of resonator rings are studied. We consider the effect of change of refractive index, rod radius, and lactic constant. Because channel D also has output in the non-resonant state, we study the output wavelengths of the resonant channels, C, B ', B, A', A, and C '.

4-7-1-1- Change in the radius of the cells

One of the most important parameters of filters is that they can be adjusted for different wavelengths. One of the issues that can adjust the filter is the radius of dielectric rods. The initial radius was 20% of the lattice constant. The secondary radius of rods is used to check the output diagrams of each simulation. Now by varying the radius, the effect of radius change is displayed for different switching wavelengths, shown **in Figure 4-50 (a), (b) and (c).**

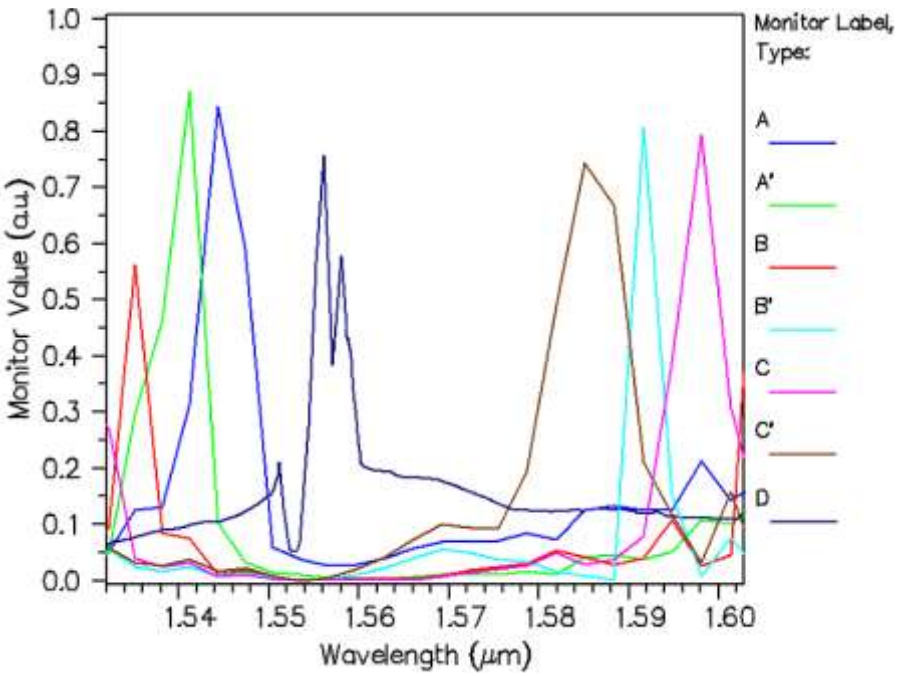

(a) r′=110nm

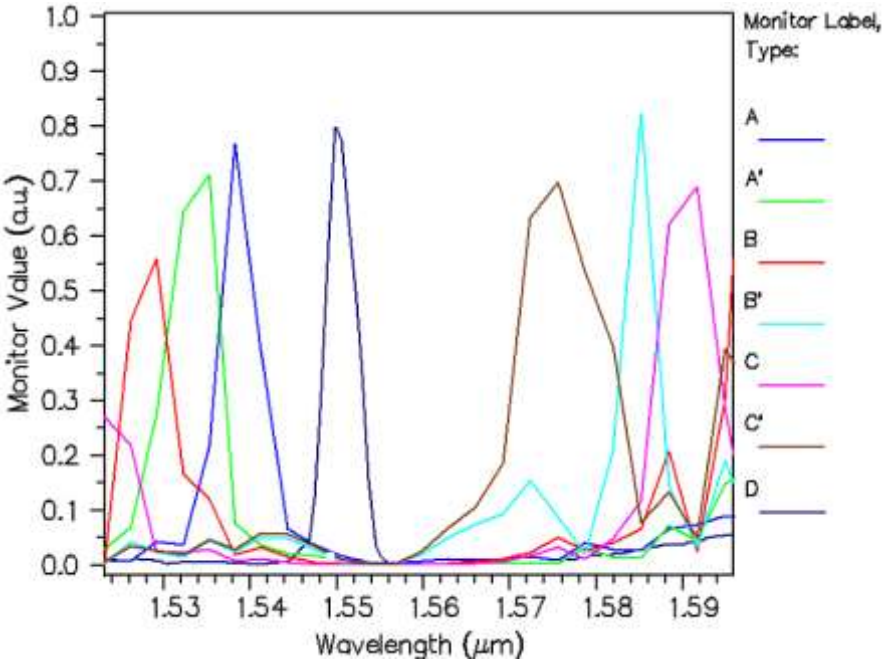

(b) r′=111.5nm

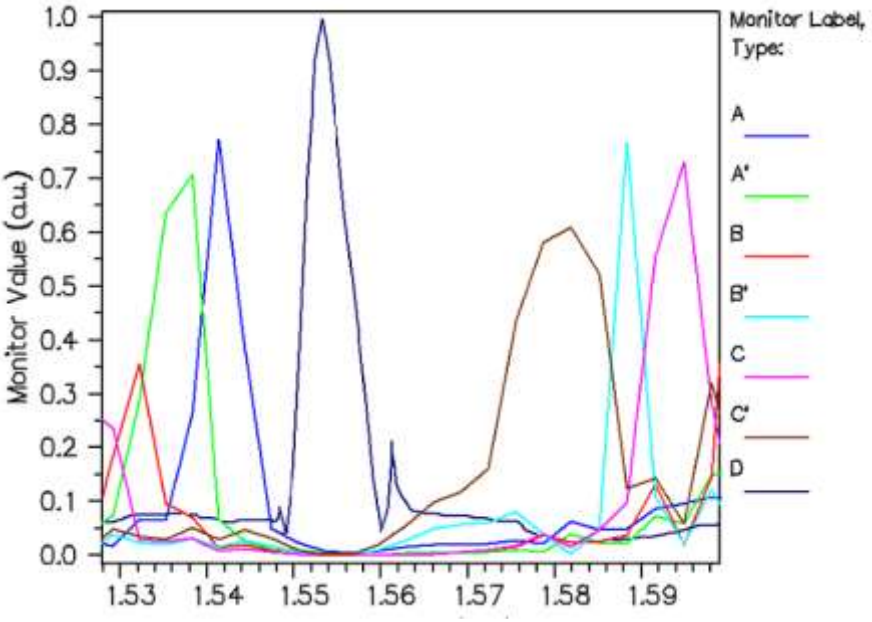

(c) r′=113nm

Figure 4-50: The diagram of output ports while increasing radius of dielectric rods.

In **Figure 4-50(a),** the radius is 110 nm (the lowest) and therefore wavelength is the lowest; in **Figure 4-50(b),** the radius is 111.5 nm, and the wavelength has increased, and in **Figure 4-50(c)** the radius is 113 nm, and the wavelength is the most. Therefore, we can see that an increase in radius can result in increasing wavelengths.

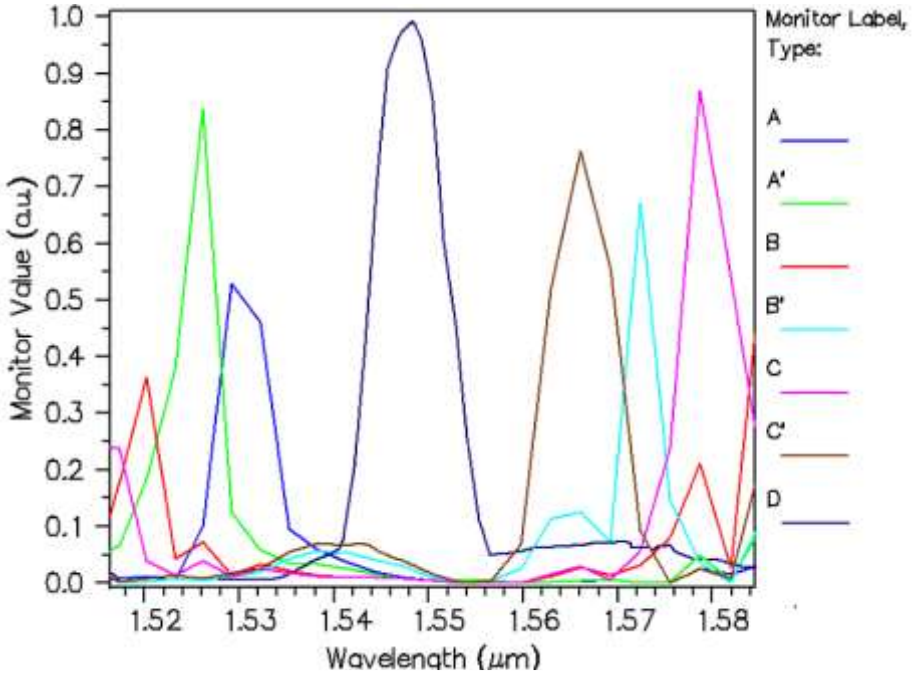

(a) r′=106nm

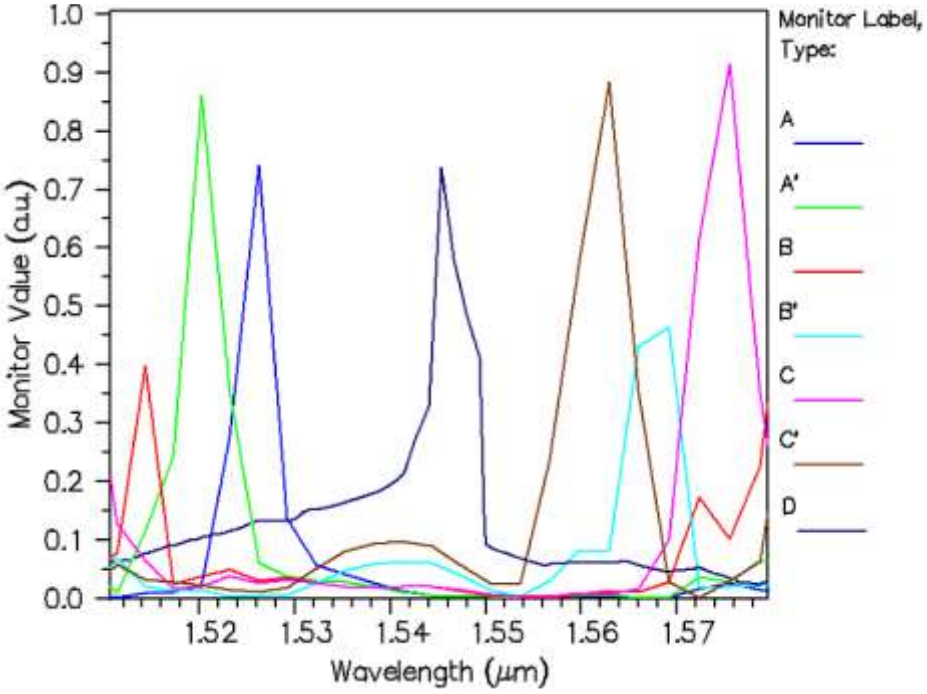

(b) r′=104nm

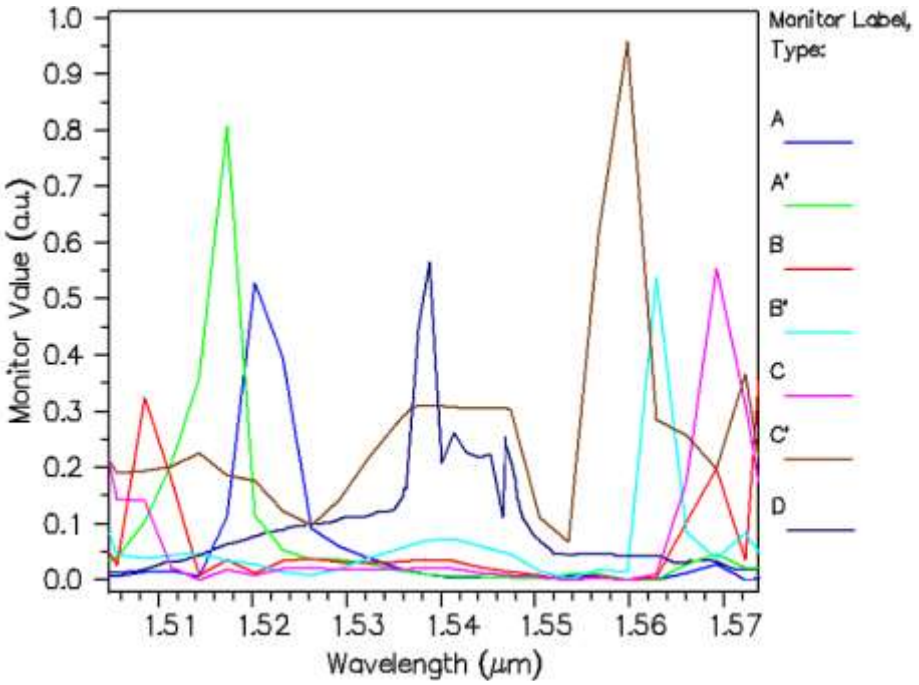

(c) r′=102nm

Figure 4-51: The diagram of output ports while decreasing radius of dielectric rods.

In **Figure 4-51(a),** the radius is 106 nm (the highest), and therefore wavelength is the highest; in **Figure 4-51(b)**, the radius is 104 nm, and the wavelength has decreased, and in **Figure 4-51(c)** the radius is 102 nm, and the wavelength is the lowest. As a result, the radius reduction leads to the decrease of each wavelength.

4-7-1-2- Change of the refractive index

Only the refractive index would be increased and decreased under the initial conditions, and wavelengths would be checked at each stage. The effect of these changes is depicted in **Figures 4-52 and 4-53**.

The parameter n_i corresponding to the refractive index of the rods of primary photonic crystals and n_i' corresponding to the refractive index of photonic crystals after increasing or decreasing are considered to examine the output wavelengths.

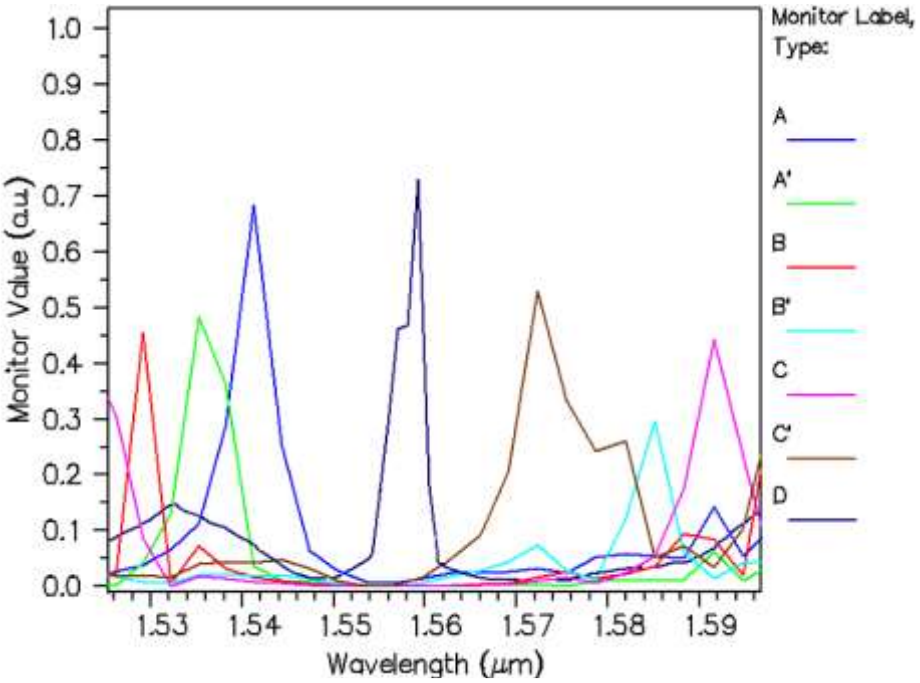

(a) $n_i' = n_i + 0.01$

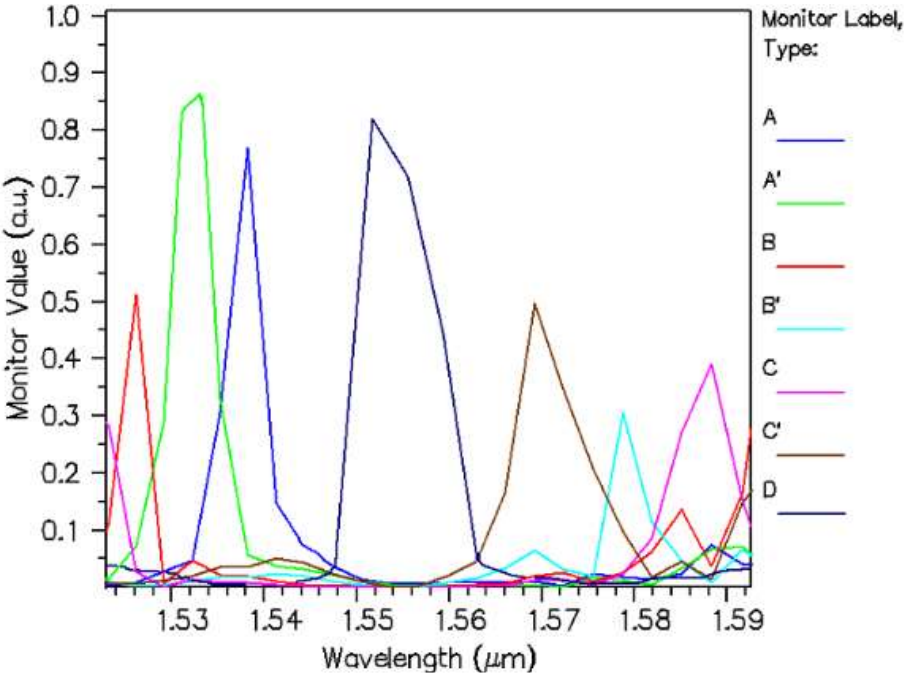

(b) $n_i' = n_i + 0.0\ 2$

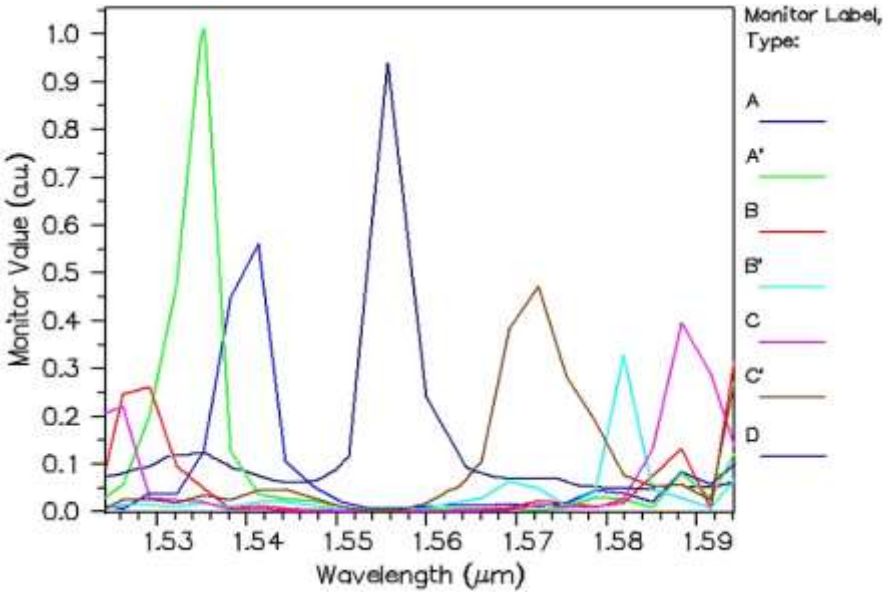

(c) $n_i{}' = n_i + 0.03$

Figure 4-52: The diagram of output ports while increasing the refractive index of the dielectric.

In **Figure 4-52(a),** the refractive index is $n_i + 0.01$ (the lowest) and therefore wavelength is also the lowest; in **Figure 4-52(b),** the refractive index is $n_i + 0.0\,2$, and the wavelength has increased, and in **Figure 4-52(c)**, the refractive index is $n_i + 0.03$, and the wavelength is the highest. It is observed that while increasing the refractive index, the wavelengths also increase.

By modifying the radius and refractive index of the rods, it is possible to change the output wavelength. Results of simulation showed that by increasing the refractive index of the crystal background, the central wavelength of the filter changes to longer wavelengths, and conversely. Also, by increasing the dielectric rods' radius, the central wavelength of the filters increases towards longer wavelengths. These options can be used to adjust the center wavelength of each channel. This multiplexer is suitable for WDM applications and can also be used in integrated optical circuits.

The proposed structure in this section works by small dimensions to find high quality wavelengths in optical telecommunication systems. The microcavity used in this structure acts as a reflector in a certain range of frequencies and makes the structure useful as a device to separate the main telecommunication wavelength. One of the prominent features of the structure presented in this study is the simplicity of the frequency selection mechanism of this structure and the appropriate interest of the channels.

4-8- Development of gas sensor

Gas sensors have found a broad spectrum of applications highly demanded in chemistry, biology, medicine, etc. The main types of gas sensors include catalytic, electrochemical, thermal, ultrasonic, semiconductor and infrared sensors.
In the literature, one can find papers demonstrating sensors working in IR, based in the evanescent field absorption in the presence of a gas. However, the most common optical sensor type uses an optical spectrum analyzer. Infrared light is shone into a gas cell where interacts with a mixture of gases. Each gas in the mixture will absorb certain wavelengths proportionally to its concentration. Measuring this absorption allows determining which gases are present and their concentrations. Manufacturing the glass cell is expensive and requires precise fabrication technology.
The purpose of this paper is to propose a cheap and simpler alternative to conventional optical spectrum analyzers. This sensor consists of three main parts: a light source, an appropriate photonic crystal structure, and a photodiode.

4-8-1- Simulation of gas sensor

The devices studied here are photonic crystal slabs with embedded coupled rings resonators, as shown in **Figure 4-54**. The complete structure includes waveguides for insertion and extraction of light. The resonating rings are placed at the waveguide intersection, as depicted in **Figure 4-54** region (1) and (2). The variation of the refractive index in the interaction volume will change the resonant characteristics of the rings. Optimization of the coupling between the two cavities is done by tailoring the radius of the rings surrounding cavities.

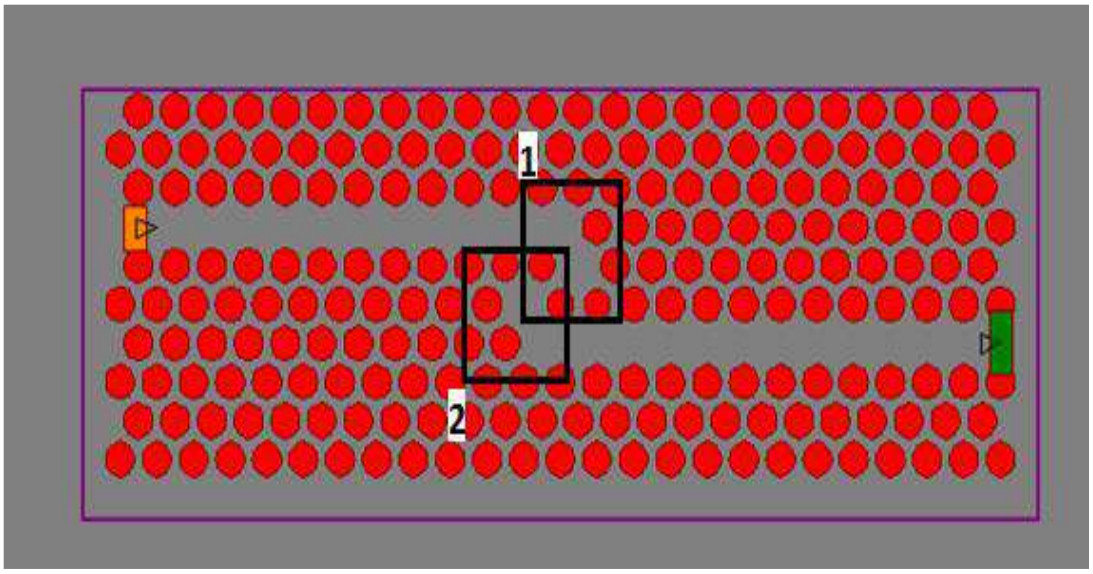

Figure 4-54: Schematics of the studied photonic crystal slab structure. The input waveguide is at the left (orange), and the output one is on the right (green). The two resonators are marked in the Figure as (1) and (2).

Pore placement and dimensions were precisely tuned during the design stage. The structures were optimized for the detection of CO. In particular, the diameters of the pores that define the ring resonators are slightly smaller than the rest of the slab. The precise dimensions have been determined through an iterative optimization process.
Simulation of the response of the devices has been performed using the commercial software RSOFT. The effect of the gas has been considered by setting the dielectric material of the pore voids to that of the considered gas mixture in each step.
For the first step, the structure's simulation, the pores were filled with air, with refractive index of one. Simulations were run for 5000 time steps what ensured appropriate convergence of the results. The second step models the presence of CO in the volume of the pores by setting the reflective index proportional to the value corresponding to the CO concentration and considering that pure CO in standard conditions has a refractive index of 1.000438.

4-8-2- Results

Figure 4-55 shows the spectra corresponding to the cases with pure air filling the pores and to the case in which they are filled with pure CO. By comparing the intensity of the transfer function of the outputs corresponding to both cases, it can be seen how the transmission spectrum changes. This is because the presence of CO is modifying the resonance characteristics of the rings. As optical communication is a well-established technology, we are most interested to work in the 1.55 μm to 1.62 μm range to take advantage of the technology already available. In this region it can be seen a promising variation with the change of gas.

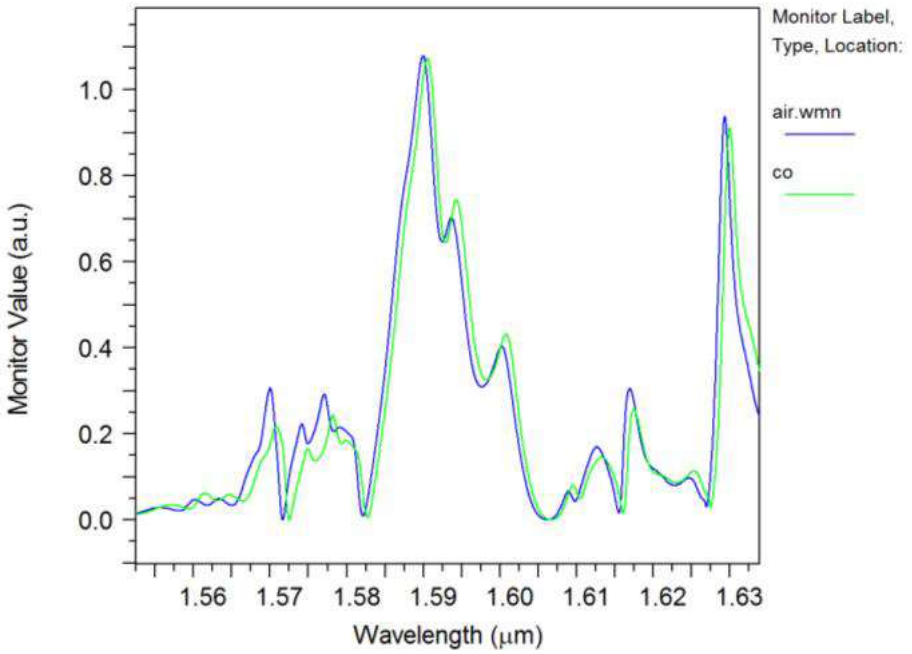

Figure 4-55: Comparison of the output intensity with and without presence of gas. The blue line is air with reflective index of 1, and the green line is carbon monoxide with a reflective index of 1.000438.

After analyzing the whole spectrum, we can see variations between the cases corresponding to pure air and to CO: on the one hand, the amplitude of the intensity at the output, corresponding to a given frequency changes. On the other hand, the position of the peaks of the frequency response has also shifted.
In the studied margin of frequencies, the largest variation of intensity between both cases is found at a wavelength of 1.57 microns. In **Figure 4-56,** both functions are represented with more detail around this wavelength.
In regard to the frequency range, we can see from **Figure 4-56** that the most useful range comprises from λ=1,565 μm to 1,575 μm. The spectral variations are remarkable, and different strategies of detection are possible:

- Measure amplitude at any particular wavelength
- Measure the displacement of the maximum position.
- Monitor the movement of the minimum of the transfer function.
- Measure the variation of the power transmitted integrated in a given margin of frequencies.

For a practical application, probably the strategy of simplest implementation is the last one, as it requires of the circuitry of lower complexity, and therefore it allows the implementation of low cost portable systems. However, in this study, we are measuring the amplitude variation at the frequency of the peak (λ=1,57 μm). A 17% variation in amplitude is observed when pure CO is inserted into the device, as shown in **Figure 4-56.**

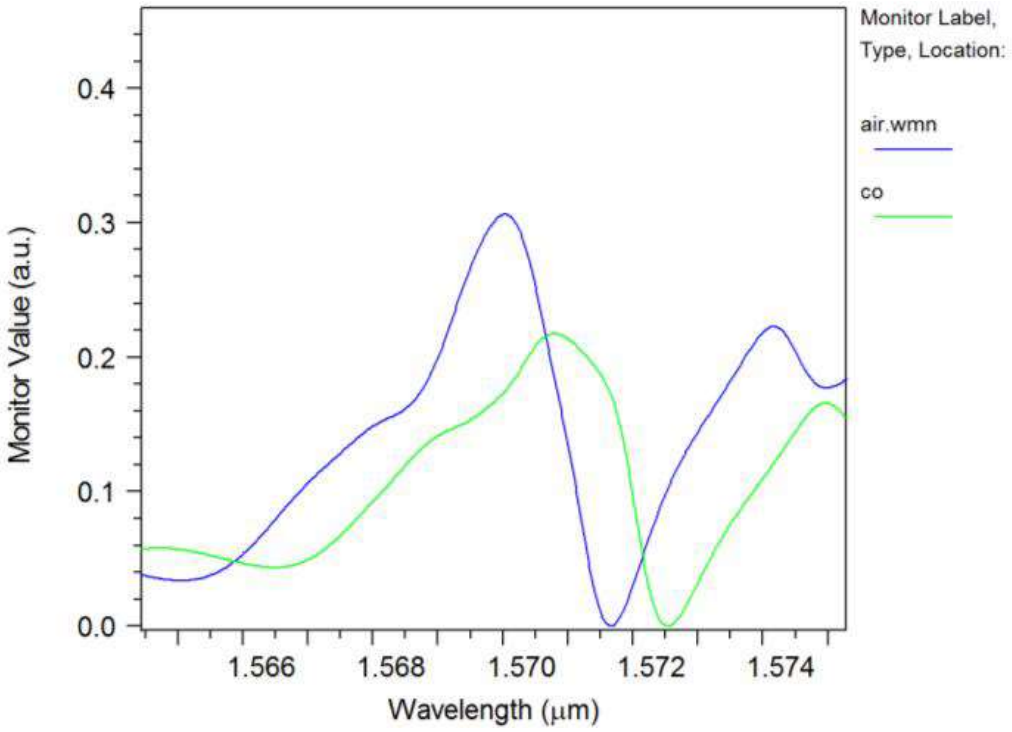

Figure 4-56: Comparison of two different outputs corresponding to pure air (blue), and pure CO (green). As it can be seen, a 17% of transmission change is achieved.

Chapter 5

Conclusion and Future Work

5-1- Introduction

In recent decades, research on optical electronics has developed considerably. With the advancement of technology, the size of components decreases, and consequently, the integrated circuits will be more complex and larger. As a result, it requires specially designed components that become small in size while being efficient. Optical logic gates are one of the most paramount components for integrating optical circuits. The small size of these structures is an important advantage that allows using them in optical integrated circuits. Therefore, photonic crystal-based logic gates are among the most significant optical components due to their low loss, high performance, and small size.

5-2- Discussion and conclusion

In **Chapter 1**, Before employing the wavelength-division multiplexing (WDM) method, the notion of the electromagnetic wave in free space and in conductors with a description of equations was defined (**Section 1-2**). Wave equations for the electric field and Wave equations for the magnetic field were defined. Next, the Relations between electric and magnetic fields in a plane wave in free space were studied. **Section 1-2** was finished by introducing the complex notation for free waves.

After discussing the electromagnetic wave in free space in **Section 1-2**, we studied the electromagnetic waves in conductors in **Section 1-2-2**, and phase velocity and group velocity were studied in **Section 1-2-3**.

In **Section 1-3**, The WDM method, which is used as the main method for transmitting information in optical telecommunication systems since 1980, was explained. The concepts related to WDM and methods of sending information were clarified, and in the next step, the reasons for choosing DWDM were explained. Multiplexing and the reason for applying transmission of multiple signals with different wavelengths in special cases was explained. Next, Dense WDM and the advantages of using this method were discussed, and finally, the standards defined for DWDM were studied.

In **Chapter 2**, we started by studying the history of photonic crystals in **Section 2-2**, and we moved on to Introduction and review of the properties of photonic crystals. Next, we explained the Photonic band gap in **Section 2-4**. In the same section, gates are designed without using nonlinear materials and optical amplifiers. In these designs, point and linear defects are applied. Since a single structure is used to design different gates, such designs have suitable conditions to integrate in full-optical circuits. Additionally, the designs presented in this section are very small.

Next, in **Section 2-5**, Defects in photonic crystals and their applications were explained. Next, the history of photonic Crystal based Logic Gates was explained. In the following subsections, Interference-based, Resonance-based, and Self-collimation-based photonic crystal logic gates are explained in **Subsections 2-7-1, 2-7-2**, and **2-7-3**, respectively.

In **Subsection 2-7-4**, the physical phenomenon of the "nonlinear Kerr effect" was described as it was used in the thesis to design some of the structures. For explaining the "nonlinear Kerr effect", the third-order nonlinear processes, the tensor nature of the third-order susceptibility, electro-optical Kerr effect, and Optical Kerr effect were explained in **subsections 2-7-4-1 to 2-7-4-4.**

In the next stage, all-optical logic gates were studied in **Section 2-8**. Gates such as "AND" Gate, "OR" Gate, "NOT" Gate, "XOR" Gate, "NAND" Gate, "NOR" Gate, and "XNOR" gate. In the following, photonic crystal fiber-based gas sensors and photonic crystal waveguide-based gas sensor were discussed in **Sections 2-9** and **2-10**, respectively. And finally, we reviewed the method of making photonic crystal gas-based sensor and the method of manufacturing photonic crystal fiber-based gas sensor.

In the third chapter, schemes were proposed based on point and linear defects and the self-collimation phenomenon, which work on the TM polarization. In all designs, the material used is silicon as the optical properties and the technology of manufacturing optical integrated devices based on silicon are well known.

In **chapter 3**, **Section 3-1**, theoretical equations of plasmonic structures were described as we used metal-insulator-metal (MIM) waves to implement logic gates in this study. After studying plasmonic basics, numerical analysis in PBG and normalized output spectra of the periodic and non-periodic PC structure were studied. After that, CNT transistors and two input XORs were reviewed.

In **chapter 3, Section 3-8**, Optical crystal gates based on point and linear defects were studied, and the structures that have high contrast ratio and low losses were described. The proposed designs are based on the interference of waves.

Next, we studied Self-collimation (SC), which allows self-guiding propagation in photonic crystals. As previously mentioned, a series of optical gates are designed using the self-collimating phenomenon. The self-collimating phenomenon is an interesting light guidance mechanism that allows divergent input beams to propagate parallel without using nonlinear effects. By this phenomenon, an electromagnetic wave with a certain frequency moves in the direction of propagation.

One way to parallelize the diffusion beams in photonic crystal (PhC) structures and create a self-collimating phenomenon is to reduce the rod's radius instead of eliminating them to create a linear defect. This way leads to the overall reflection and leaves the partial reflection of the tunneling wave. Then, it is expected to see a phase difference between the reflecting beam and tunneling beam (transmission beam). Therefore, if another self-collimating beam is introduced with a suitable initial phase, the transmission or reflection beams may create a destructive or constructive interference and set logic and switching functions.

Here, we proposed a structure that performs based on linear defects. In designing this structure, the TM polarized wave at a frequency of 0.194 is used for a presented logical gate. The provided logic gate in this structure also requires direct power divider devices. An optical power divider is a row of rods, which is arranged with a radius of rd in the direction of ΓM.

Finally, we studied frequency-Domain vs. Time-Domain, the disadvantage of Frequency-Domain vs. Time-Domain, MPB Software Package were discussed, and the methodology was explained. In the last part of **Chapter 3**, the demultiplexer design was explained.

In **chapter 4, Section 4-2**, for designing the NOT gate, two linear waveguides and two point defects are used in the structure. Linear waveguides are created by removing a series of rods that are known as linear defects. The distance between the two dielectric rods is known as the structure constant. This structure has an input waveguide for applying a Gaussian optical pulse at a wavelength of 1550 nm. Furthermore, a control signal with the continuous light flow is applied permanently to the structure with the same wavelength.

We could obtain different (P_{out}/ P_{in}) value with the changing the radius of R_2 defect from 1 μm to 28 μm. By changing this radius, we obtained two high transmission peaks which were in 15 μm and 26 μm. Although the 26 μm radius has a higher power transmission, But regarding to figure 4-3 the smallest contrast ratio is obtained in the radius of 26 μm so we used the radius of 15 μm for making a defect in the center rod.

In this case, we studied two states, state one (in=1) and state two (in = 0). The simulation results show that the proposed structure's performance is as the NOT gate.

In the OR gate, we obtained two high transmission peaks by changing the R_1 defect radius in 15 μm and 25 μm. Because the higher contrast ratio is obtained in the radius of 15 μm, we chose this radius for making a defect in the center rod.

In chapter **4, Section 4-2-2**, for AND gate, we obtained a high transmission peak in a radius of 15 μm, by changing the R defect radius. We have studied four states, regarding to AND gate, we have only one output in state A=”1” and B=”1”.

In **chapter 4, Section 4-2-3**, the NOR gate is created by combining the OR and NOT gates without adding any amplifier and coupler. This gate is also designed in a two-dimensional lattice square. And the rest of the structural parameters, such as radius, the lattice constant, position, and radius of reflection rods, are similar to the OR and NOT gates. The logical NOR gate comprises three waveguides, and OR gate output acts as NOT gate input, and NOT gate output acts as NOR gate output. The point defect radius is optimized to get the maximum power transfer in the output, which is equal to 15 μm.

The NOR gate was studied in four states. Regarding to NOR gate we have only one output in state A=”0” and B=”0”**.**

In **chapter 4**, **Section 4-2-4**, Since the NAND gate function is complementary to the AND gate function, the combination of two NOT and AND gates is used for designing the NAND gate. As the NOR gate, all parameters of this structure are identical to those of the other presented gates. Furthermore, the output of the AND gate, which is based on the output field intensity, is considered as the NOT gate input and NOT gate output acts as NAND gate output. The NAND gate structure and the field distribution for various input states, respectively.

The NAND gate was studied in four states. Regarding to NAND gate we have only one output in state A=”0” and B=”0”**.**

Designed AND gate based on the nonlinear Kerr effect is studied in **chapter 4, Section 4-3**. In this section using linear and nonlinear photonic crystal properties, a structure for designing a logical AND gate is presented. To achieve this, a triangular photonic crystal blade structure of the rod in the air is used. The function of logical structures at the same wavelength is important for facilitating complex circuit configuration. Therefore, in the design of these logical gates, the goal is to make the wavelength of inputs (equal to 1550 nm) equal to the input phase zero. On the other hand, knowing that the power size is important in structures with the nonlinear

Kerr effect, the power required for the circuit switching operation has been shown with P_0, and in this structure, the power in all inputs is the same (equal to P_0).

The selected optical crystal topology is checked in the next stage, and then we move on to the all-optical logic design. The important default is that the structure's wavelength is within the third communication window range (1550 nm). Furthermore, input signals to the structure are coupled through a waveguide to the crystal. This single-mode laser waveguide at 1550 nm wavelength should propagate in a linear waveguide in the photonic crystal. It should not be damped in the crystal, and the wavelength should be in the optical band gap. The triangular photonic crystal structure in TM propagation mode would be used by studying different photonic crystal structures such as square and hexagonal structures. In the proposed structure, a photonic crystal blade with a triangular lattice is provided using silicon dielectric rods in the air. The lattice dimensions are 51 × 61 arrays. The lattice constant (a) and the radius in all rods are 0.54a and 0.22a, respectively. These numbers are obtained based on the optical band gap analysis of the structure. The method of analyzing and calculating optical band gap is the same plane wave expansion method.

In this section, four states were studied for the AND gate. In state four, When both inputs are one (A="1", B="1"), the output regarding to the AND gate is logic "1". In this state, the received power around the nonlinear rods is P_0, nonlinear effects cause the switching, and the power is transmitted to the output.

In **chapter 4, Section 4-4**, a compressor (4:2) based on the proposed XOR gate and using CNTFET technology is presented. Given the results obtained in the simulation section, the proposed XOR gate has a 2.98% improvement in PDP and 13.57% in power consumption compared to the model available in reference Saraswat and Sharma (2018) [169]. Additionally, in contrast to other models the, compressor presented in this study has better results in terms of delay by 4.31%, power consumption by 45.99%, and the power-delay product by 47.72%. The new compressor, which is used in computing systems, especially in multiplier circuits, could improve the entire system's efficiency while reducing the number of transistors used.

In **chapter 4**, **Section 4-5**, simulation and results for half-Subtractor are studied. The proposed design has 15 x 15 arrays of 2-D PhC silica dielectric rods embedded in air substrate of refractive index (n=1) in the hexagonal lattice which analogous to a fused coupler with waveguides. In this structure, the defects are created by removing the corresponding PhC dielectric rods in the structure that forms the waveguide. The refractive index of chosen Silica rods is about 1.46, and the dielectric constant, εr, is about 11.56. The rods' radius, r, is considered to be 0.18a in this work, where “a” is known as the lattice constant (618 nm for this structure), which is the distance between two dielectric rods. In this design, several junction rods and reflection rods are used. The radius for the central junction/reflection rod is chosen as 0.05a, and the one rod below the central one has a radius of 0.12a. So that the half subtractor can produce the anticipated output. It is noticed that the maximum power is transmitted at the output ports (Difference and Borrow output Port).

In this study, we have four states describe as follows. When the two input sources are off, A = B = "0" (state one), there is no light at the output, so D and BW will be zero. For a special case of A = "0" and B = "1"(state two), the output value is HIGH at both outputs (D=0.85 μW, BW=0.58 μW). When the inputs A = "1", B =" 0, the output at D is significant than compared to the BW output (D=0.82 μW, BW=0.1 μW) and in case of A = B = "1" (state four), then both of the outputs are LOW (D=0.22 μW, BW=0.1 μW). We have two outputs, in state 2, whose transmission power values are more than the threshold value, so they are equal to logic "1". In state three, only one output has an output transmission power value more than the threshold.

In state four, the outputs transmission value is zero, so they are equal to logic "0" in this state., from simulation results, we obtained that the contrast ratio is 17.24 dB and 25.88 dB in D and WB outputs, it is obvious that the proposed design has a better contrast ratio than the previously presented works, and our proposed subtractor provides a specific space in the output power between the logic "0" and "1" modes.

We designed a half adder circuit with a simple structure by propagating plasmonic waves at an optical frequency and window of 1550 nm with the aid of the designed logic gates. In **chapter 4, section 4-6**, we used a 4-input OR gate to design and simulate a full adder circuit, which used plasmonic waves to transmit signals. A 4-input gate was presented in this study with a simple structure and is manufactured at a low cost. By optimizing the structure's dimensions, we managed to reduce the losses and achieve a transmission coefficient of about 0.62, presented in **chapter 4, Section 4-6**; thus, we reduced the losses down to 25% less than the design in reference Wang et al (2016) [93]**.** The structure and dimensions of a 4-input OR logic gate are illustrated in this section. We assumed that the threshold of the optical electric field amplitude in the waveguides is equal to 0.4. If the field amplitude is greater than 0.4, it would be assumed as a logical "1", and if the field amplitude is less than 0.4, it will be assumed as a logical "0".

Considering the resonance wavelengths for the structure (various telecommunication windows), we have resonances in a wavelength of 780 nm and 1490 nm, , but since the telecommunication windows are within 1470-1550 nm, we consider the main wavelength at 1490 nm. This structure studied in 5 states, and all of the amplitude of the electric field at the output was greater than the threshold shows us the propagation of the optical field at the output.

Furthermore, in the proposed structure, given that the number of input ports varies in different states, amplitude's transmission coefficient cannot, in practice, show the changes in the output. In this condition, a wave radiates to one of the inputs. The transmission coefficient at the output equals to the ratio of the output wave amplitude to the input wave amplitude. In other words, when light is radiated to both input ports, the transmission coefficient at the output is equaled to the ratio of the output wave amplitude to the sum of the amplitudes of both waves at the two inputs.

In **chapter 4, Section 4-7**, a 2DPC based eight channels demultiplexer is proposed and designed using an octagonal ring resonator for WDM applications. The functional parameters

are resonant wavelength, *Q* factor, channel spacing, spectral width, output efficiency, and crosstalk, are investigated. In this attempt, the channel selection is carried out by altering the size of the octagonal ring resonator. The average transmission efficiency, *Q* factor, spectral width, and channel spacing of the proposed demultiplexer are 98.65%, 2212, 0.76 nm, and 1.75 nm, respectively. The proposed demultiplexer's crosstalk is very low and amounts to 30 dB as the even number of channels and the odd number of channels are dropped separately. The demultiplexer's size is about 752.64 μm^2, and the functional characteristics of the proposed demultiplexer are meeting the requirements of WDM systems. Hence this demultiplexer can be incorporated for integrated optics.

By analyzing the articles closer to the design presented in **chapter 4, Section 4-7**, in terms of the number of output channels, it can be seen that their main advantage is the small design size. Still, they are at a lower level in terms of transmission efficiency. The advantage of this design is the main feature of annular amplifiers, which is its high ability to adjust the wavelength, transmission efficiency, and overall better flexibility. The final work has seven output channels with an area of 473 μm^2**,** which has a very suitable and small size for construction due to the high number of channels. The average total power transfer is 90%, and The Q factor of each channel is also suitable for WDM systems.

In **chapter 4, Section 4-7-1,** the results of changing effective parameters in the performance of resonator rings would be studied, which are the results of a change of refractive index, rod radius and lactic constant. Because channel D also has output in the non-resonant state, we study the output wavelengths of the resonant channels, C, B ', B, A', A and C '.

By increasing the inner radius of the resonator ring, the filtered wavelength tends to larger wavelengths. Of course, it should be noted that this power will decrease slowly. The power loss in one of the rings is due to coupling in the other ring. When one ring is in the resonant state and absorbs the light, it is as if the other ring is reflective. Since the size is an important parameter in integration, it should be noted that the rings, when facing each other pairwise, have less distance than when they are together. As the radius of the scattering rods increases, the transfer efficiency also increases. It should be noted that increasing the radius of these rods reduces the size of the rings.

Afterward, we explained that under the initial conditions, only the refractive index would be increased, and wavelengths would be checked at each stage.

The parameter ni corresponding to the refractive index of the rods of primary photonic crystals and ni' corresponding to the refractive index of photonic crystals after increasing or decreasing are considered to examine the output wavelengths.

This research's proposed structure can be used with small dimensions to find high quality wavelengths in optical telecommunication systems. The microcavity used in this structure acts as a reflector in a certain frequency range and causes the structure to be used as a device to separate the main telecommunication wavelength. One of the prominent features of the

structure presented in this study is the simplicity of the frequency selection mechanism of this structure and the appropriate interest of the channels.

In **Section 4-8**, we propose a new photonic crystal slab for its use in gas sensing applications. Theoretical studies have been done to determine the response of the proposed structure to carbon dioxide. For the simulation of this device, a simple laser with around 1 nm spectral width can be used. Measurements can be done in two steps, which can be done simultaneously by using a reference device: step one with synthetic air and then adding known concentrations of CO. The output is referenced to the measurement with synthetic air. Our theoretical results show that variations of 17% in the transmission intensity and a clear variation on the central wavelength of the transmission peaks. These results are already very promising for the development of gas sensors. The proposed structure has small dimensions as well as a wide functional interval.

5-3- Recommendations

Due to the high capabilities of optical crystals, nowadays, researchers continue their research in various fields for better and more efficient use of this group of gates. The process of making optical crystals is easier than a rod type. Due to the fact that light is used in calculations, the processing speed is high enough, but power consumption can be reduced. Graphene has become a unique material due to its potential and excellent properties, having high electrical and thermal conductivity, the excitability of optical charge carriers, and excellent mechanical properties. Graphene can be used to design logic devices in the terahertz field that have many applications in the field of telecommunications.

Reference

[1] Bouamami, S. and Naoum, R., 2013. Compact WDM demultiplexer for seven channels in photonic crystal. *Optik*, 124(16), pp.2373-2375.

[2] Taflove, A. and Hagness, S., 1998. Computational Electrodynamics: The Finite Difference Time Domain Method. 3rd ed. Boston: Artech House

[3] Brillouin, L. and Massey, H., 2013. Wave Propagation and Group Velocity. Burlington: Elsevier Science.

[4] Ballart, R. and Ching, Y.C., 1989. SONET: Now it's the standard optical network. *IEEE Communications Magazine*, *27*(3), pp.8-15.

[5] Ahmed, R., Khan, M.M., Ahmmed, R. and Ahad, A., 2013. Design, simulation & optimization of 2D photonic crystal power splitter.

[6] Cameron, R.I. and Yu, M., 2007. Design of manifold-coupled multiplexers. *IEEE microwave magazine*, *8*(5), pp.46-59.

[7] Carbonneau, T.H. and Wisely, D.R., 1998, January. Opportunities and challenges for optical wireless: the competitive advantage of free space telecommunications links in today's crowded marketplace. In *Wireless Technologies and Systems: Millimeter-Wave and Optical* . 3232, pp. 119-128

[8] Ahmed, J., Hussain, A., Siyal, M.Y., Manzoor, H. and Masood, A., 2014. Parametric analysis of four wave mixing in DWDM systems. *Optik*, *125*(7), pp.1853-1859.

[9] Rostami, A., Nazari, F., Banaei, H.A. and Bahrami, A., 2010. A novel proposal for DWDM demultiplexer design using modified-T photonic crystal structure. *Photonics and Nanostructures-Fundamentals and Applications*, *8*(1), pp.14-22.

[10] Sun, J., Chan, C.C., 2007. Photonic bandgap fiber for refractive index measurement, *Sensors and Actuators*, B, 128 , pp.46–50.

[11] Rayleigh, L., 1887. XVII. On the maintenance of vibrations by forces of double frequency, and on the propagation of waves through a medium endowed with a periodic structure. *The London, Edinburgh, and Dublin Philosophical Magazine and Journal of Science*, 24(147), pp.145-159.

[12] Johnson, S. and joannopoulos, J.D., 2003. Introduction to Photonic Crystals: Bloch's Theorem, Band Diagrams, and Gaps (But No Defects) . *MIT Tutorial*

[13] Bykov, V., 1975. Spontaneous emission from a medium with a band spectrum. *Soviet Journal of Quantum Electronics*, 4(7), pp.861-871.

[14] Ohtaka, K., 1979. Energy band of photons and low-energy photon diffraction. *Physical Review B*, 19(10), pp.5057-5067.

[15] Yablonovitch, E., 1987. Inhibited Spontaneous Emission in Solid-State Physics and

Electronics. *Physical Review Letters*, 58(20), pp.2059-2062.

[16] John, S., 1987. Strong localization of photons in certain disordered dielectric superlattices. *Physical Review Letters*, 58(23), pp.2486-2489.

[17] Ho, K., Chan, C. and Soukoulis, C., 1990. Existence of a photonic gap in periodic dielectric structures. *Physical Review Letters*, 65(25), pp.3152-3155.

[18] Gruning. U., Lehman. V., Englehardt. C. M., 1995 .Larg scale 2D photonic crystals in visible, *Applied Physics Letters*,Vol .66 .

[19] Gruning. U., Lehman. V., Englehardt. C. M., 1998 .Small scale photonic crystals in near visible large scale inverted Opals, *Applied Physics Letters* , 82.

[20] Ohtaka. K., 1979. Energy band of photons and low-energy photon diffraction, *Physical Review B*, 56(20) , pp. 5057-5067,.

[21] Joannopoulos. J. D., Johnson. S. G., Winn. J. N.,and Meade. R. D.,2008 . Photonic crystals: Modeling the flow of light, *Second Ed Princeton university Press*.

[22] Oleg, L. Berman, Vladimir S. Boyko, Roman Ya. Kezerashvili and Yurii E. Lozovik, 2014. Electromagnetic Wave Propagation in Two-Dimensional Photonic Crystals, *InTech*.

[23] Foteinopoulou, S., 2003. Electromagnetic wave propagation in two-dimensional photonic crystals. *Retrospective Theses and Dissertations*.

[24] Agio, M., Lidorikis,E., and Soukoulis,C.M, 2000 . Impurity modes in a two-dimensional photonic crystal: coupling efficiency and Q factor, *Journal of the Optical Society of America B*, 17(12) ,pp. 2037-2042

[25] Kosaka, H., Kawashima, T., Tomita, A., Notomi, M., Tamamura, T., Sato, T. and Kawakami, S., 1999. Self-collimating phenomena in photonic crystals. *Applied Physics Letters*, 74(9), pp.1212-1214.

[26] Shi, L., Yin, H., Zhu, X., Liu, X. and Zi, J., 2010. Direct observation of iso-frequency contour of surface modes in defective photonic crystals in real space. *Applied Physics Letters*, 97(25), p.251111.

[27] Xin, Q., Duhm, S., Bussolotti, F., Akaike, K., Kubozono, Y., Aoki, H., Kosugi, T., Kera, S. and Ueno, N., 2012. Accessing surface brillouin zone and band structure of picene single crystals. *Physical review letters*, *108*(22), p.226401.

[28] Johnson, S. and joannopoulos, J.D., 2003. Introduction to Photonic Crystals: Bloch's Theorem, Band Diagrams, and Gaps (But No Defects) . *MIT Tutorial.*

[29] Scholz, S., Hess, O. and Rühle, R., 1998. Dynamic cross-waveguide optical switching with a nonlinear photonic band-gap structure. *Optics Express*, 3(1), pp.28-34.

[30] Centeno, E. and Felbacq, D., 2000. Optical bistability in finite-size nonlinear bidimensional photonic crystals doped by a microcavity. *Physical Review B*, 62(12), pp.R7683-R7686.

[31] Soljačić, M., Ibanescu, M., Johnson, S., Fink, Y. and Joannopoulos, J., 2002. Optimal bistable switching in nonlinear photonic crystals. *Physical Review E*, 66(5).

[32] Fan, S., 2002. Sharp asymmetric line shapes in side-coupled waveguide-cavity systems. *Applied Physics Letters*, 80(6), pp.908-910.

[33] Mingaleev, S. and Kivshar, Y., 2002. Nonlinear transmission and light localization in photonic-crystal waveguides. *Journal of the Optical Society of America B*, 19(9), p.2241.

[34] Locatelli, A., Modotto, D., Paloschi, D. and De Angelis, C., 2004. All optical switching in ultrashort photonic crystal couplers. *Optics Communications*, 237(1-3), pp.97-102.

[35] Cuesta-Soto, F., Martínez, A., García, J., Ramos, F., Sanchis, P., Blasco, J. and Martí, J., 2004. All-optical switching structure based on a photonic crystal directional coupler. *Optics Express*, 12(1), p.161.

[36] Zhu, Z., Ye, W., Ji, J., Yuan, X. and Zen, C., 2006. High-contrast light-by-light switching and AND gate based on nonlinear photonic crystals. *Optics Express*, 14(5), pp.1783-1788.

[37] Zhang, Y. and Li, B., 2007. Optical switches and logic gates based on self-collimated beams in two-dimensional photonic crystals. *Optics Express*, 15(15), p.9287-9289.

[38] Shinya, A., Matsuo, S., Yosia, Y., Tanabe, T., Kuramochi, E., Sato, T., Kakitsuka, T. and Notomi, M., 2008. All-optical on-chip bit memory based on ultra high Q InGaAsP photonic crystal. *Optics Express*, 16(23), p.19382-19887.

[39] Liu, Q., Ouyang, Z., Wu, C., Liu, C. and Wang, J., 2008. All-optical half adder based on cross structures in two-dimensional photonic crystals. *Optics Express*, 16(23), p.18992.

[40] Lee, K., Lin, J., Yang, Y., Yang, Y., Wu, J., Lin, Y. and Lee, W., 2008. The designs of XOR logic gates based on photonic crystals. *Optoelectronic Materials and Devices III*,.

[41] Andalib, P. and Granpayeh, N., 2009. All-optical ultracompact photonic crystal AND gate based on nonlinear ring resonators. *Journal of the Optical Society of America B*, 26(1), p.10.

[42] Jung. Y.J., 2009. Reconfigurable all-optical logic AND, NAND, OR, NOR, XOR and XNOR gates implemented by photonic crystal nonlinear cavities, *2009 Conference on Lasers & Electro Optics & The Pacific Rim Conference on Lasers and Electro-Optics*, Shanghai, China, pp. 1-2

[43] Lee, K., Yang, Y., Lin, Y., Lee, W., Lee .C., and Wong, S. 2009. The designs of 4×2 encoder based on photonic crystals, *2009 Asia Communications and Photonics conference and Exhibition (ACP)*, Shanghai, China, 2009, pp. 1-2

[44] Ishizaka, Y., Kawaguchi, Y., Saitoh K., and Koshiba, M., 2010, Design of all-optical XOR and AND logic gates based on multi-mode interference devices, *2010 10th International Conference on Laser and Fiber-Optical Networks Modeling*, Sevastopol, Ukraine, pp. 53-55,

[45] Salmanpour, A., Mohammadnejad, S. and Bahrami, A., 2014. Photonic crystal logic gates: an overview. *Optical and Quantum Electronics*, 47(7), pp.2249-2275.

[46] Ishizaka, Y., Kawaguchi, Y., Saitoh, K. and Koshiba, M., 2011. Design of ultra compact all-optical XOR and AND logic gates with low power consumption. *Optics Communications*, *284*(14), pp.3528-3533.

[47] Notomi, M., Shinya, A., Mitsugi, S., Kuramochi, E. and Ryu, H., 2004. Waveguides, resonators and their coupled elements in photonic crystal slabs. *Optics Express*, 12(8), p.1551.

[48] Shinya, A.,Mitsugi, S., Kuramochi, E., Takasumi, T., Kim, G., Kira, G., Kondo, S., Yamada, K., Watanbe, T., Tsuchizawa, T,. and Natomi, M., 2005. Ultrasmall resonant tunneling/dropping devices in 2D photonic crystal slabs, *Optoelectronics Integrated Devices VII (International Society for Optics and Photonics)*

[49] Passaro, V., 2009. *Modeling of photonic devices*. New York: Nova Science Publishers.

[50] Youcef Mahmoud, M., Bassou, G., Taalbi, A. and Chekroun, Z., 2012. Optical channel drop filters based on photonic crystal ring resonators. *Optics Communications*, 285(3), pp.368-372.

[51] Djavid, M., Monifi, F., Ghaffari, A. and Abrishamian, M., 2008. Heterostructure wavelength division demultiplexers using photonic crystal ring resonators. *Optics Communications*, 281(15-16), pp.4028-4032.

[52] Ahmadi Tameh, T., Isfahani, B., Granpayeh, N. and Javan, A., 2011. Improving the performance of all-optical switching based on nonlinear photonic Crystal microring resonators. *AEU - International Journal of Electronics and Communications*, 65(4), pp.281-287.

[53] Mehdizadeh, F., Alipour-Banaei, H. and Serajmohammadi, S., 2013. Channel-drop filter based on a photonic crystal ring resonator. *Journal of Optics*, 15(7), p.075401

[54] Witzens, J., Loncar, M. and Scherer, A., 2002. Self-collimation in planar photonic crystals. *IEEE Journal of Selected Topics in Quantum Electronics*, 8(6), pp.1246-1257.

[55] Moreno, M, 2018. Kerr Effect, Instituto de Física de São Carlos, Universidade de São Paulo

[56] New, G., 2011.Introduction to Nonlinear Optics. 1st ed. *New York: Cambridge University Press;*

[57] Mills. D., 1999. Nonlinear Optics Basic Concepts. Nonlinear op-tics. 3rd ed. *Germany: Springer;*

[58] Alipour-Banaei, H., Rabati, M., Abdollahzadeh-Badelbou, P. and Mehdizadeh, F., 2016. Application of self-collimated beams to realization of all optical photonic crystal encoder. *Physica E: Low-dimensional Systems and Nanostructures*, 75, pp.77-85.

[59] Danaie, M. and Kaatuzian, H., 2011. Design and simulation of an all-optical photonic crystal AND gate using nonlinear Kerr effect. *Optical and Quantum Electronics*, 44(1-2), pp.27-34.

[60] Yang, Y., Lin, K., Yang, I., Lee, K., Lin, Y., Lee, W. and Tsai, Y., 2013. All-optical photonic

crystal AND gate with multiple operating wavelengths. *Optics Communications*, 297, pp.165-168.

[61] Fu, Y., Hu, X. and Gong, Q., 2013. Silicon photonic crystal all-optical logic gates. *Physics Letters A*, 377(3-4), pp.329-333.

[62] Zhang, Y., Zhang, Y. and Li, B., 2007. Optical switches and logic gates based on self-collimated beams in two-dimensional photonic crystals. *Optics Express*, 15(15), p.9287.

[63] Goudarzi, K., Mir, A., Chaharmahali, I. and Goudarzi, D., 2016. All-optical XOR and OR logic gates based on line and point defects in 2-D photonic crystal. *Optics & Laser Technology*, *78*, pp.139-142.

[64] Younis, R.M., Areed, N.F. and Obayya, S.S., 2014. Fully integrated AND and OR optical logic gates. *IEEE Photonics Technology Letters*, *26*(19), pp.1900-1903.

[65]] Jiang, J., Qiang, Z., Xu, X. and Chen, X., 2011. Analysis of photonic logic gates based on single hexagonal-lattice photonic crystal ring resonator. *Journal of Nanophotonics*, *5*(1), p.053519.

[66] Noshad, M., Abbasi, A., Ranjbar, R. and Kheradmand, R., 2012. Novel All-Optical Logic Gates Based on Photonic Crystal Structure. *Journal of Physics: Conference Series*, 350, p.012007.

[67] Lee, K.Y., Lin, J.M., Yang, Y.C., Yang, Y.B., Wu, J.S., Lin, Y.J. and Lee, W.Y., 2008, November. The designs of XOR logic gates based on photonic crystals. In *Optoelectronic Materials and Devices III* (Vol. 7135, p. 71353Y). International Society for Optics and Photonics .

[68] Tang, C., Dou, X., Lin, Y., Yin, H., Wu, B. and Zhao, Q., 2014. Design of all-optical logic gates avoiding external phase shifters in a two-dimensional photonic crystal based on multi-mode interference for BPSK signals. *Optics Communications*, 316, pp.49-55.

[69] Kabilan. A, Christina. X, Caroline. P, 2009. Realization of optical logic gates using photonic crystal, *International Conference on Optic Photonics*, pp. 3–6.

[70] Bao, J., Xiao, J., Fan, L., Li, X., Hai, Y., Zhang, T. and Yang, C., 2014. All-optical NOR and NAND gates based on photonic crystal ring resonator. *Optics Communications*, 329, pp.109-112.

[71] Alipour-Banaei, H., Serajmohammadi, S. and Mehdizadeh, F., 2014. All optical NOR and NAND gate based on nonlinear photonic crystal ring resonators. *Optik*, 125(19), pp.5701-5704.

[72] Christina Xavier, S. and Arunachalam, K., 2012. Compact design of all-optical logic gates based on self-collimation phenomenon in two-dimensional photonic crystal. *Optical Engineering*, 51(4), p.045201.

[73] Xavier, S., Arunachalam, K., Caroline, E. and Johnson, W., 2013. Design of two-

dimensional photonic crystal-based all-optical binary adder. *Optical Engineering*, 52(2), p.025201.

[74] Ramamoorthy, R., Dutta, P. K. and Akbar, S.A., 2003. Oxygen sensors: Materials, methods, designs and applications. *Journal of material science*, 38, pp. 4271 - 4282 .

[75] Bridge, C., Bicudo, J. and Lykkeboe, G., 1979. Oxygen content measurement in blood containing haemocyanin. *Comparative Biochemistry and Physiology Part A: Physiology*, 62(2), pp.457-461.

[76] Healey, B. G., Li, L., and Walt, D.R., 1997. Multianalyte biosensors on optical imaging bundles, *Biosensors and Bioelectronics*, 12, pp. 521-529 .

[77] Hoo, Y.L., Jin, W., Shi, C., Ho, H.L., Wang, D.N. and Ruan, S.C., 2003. Design and modeling of a photonic crystal fiber gas sensor. *Applied Optics*, *42*(18), pp.3509-3515.

[78] Haxha, S. and Ademgil, H., 2008. Novel design of photonic crystal fibres with low confinement losses, nearly zero ultra-flatted chromatic dispersion, negative chromatic dispersion and improved effective mode area. *Optics communications*, *281*(2), pp.278-286.

[79] Wu, T., Shao, Y., Wang, Y., Cao, S., Cao, W., Zhang, F., Liao, C., He, J., Huang, Y., Hou, M. and Wang, Y., 2017. Surface plasmon resonance biosensor based on gold-coated side-polished hexagonal structure photonic crystal fiber. *Optics express*, *25*(17), pp.20313-20322.

[80] Wolfbeis, O. and Posch, H., 1986. Fibre-optic fluorescing sensor for ammonia. *Analytica Chimica Acta*, 185, pp.321-327.

[81] Knight, J., 2003. Photonic crystal fibres. *Nature*, 424(6950), pp.847-851.

[82] Zhi-guo, Z., Fang-di, Z., Min, Z. and Pei-da, Y., 2008. Gas sensing properties of index-guided PCF with air-core. *Optics & Laser Technology*, *40*(1), pp.167-174.

[83] Olyaee, S. and Naraghi, A., 2013. Design and optimization of index-guiding photonic crystal fiber gas sensor. *Photonic Sensors*, *3*(2), pp.131-136.

[84]Olyaee, S., Naraghi, A. and Ahmadi, V., 2014. High sensitivity evanescent-field gas sensor based on modified photonic crystal fiber for gas condensate and air pollution monitoring. *Optik*, *125*(1), pp.596-600.

[85] Park, J., Lee, S., Kim, S. and Oh, K., 2011. Enhancement of chemical sensing capability in a photonic crystal fiber with a hollow high index ring defect at the center. *Optics express*, *19*(3), pp.1921-1929.

[86] Ranka, J., Windeler, R. and Stentz, A., 2000. Optical properties of high-delta air–silica microstructure optical fibers. *Optics Letters*, 25(11), p.796.

[87] Birks, T., Knight, J. and Russell, P., 1997. Endlessly single-mode photonic crystal fiber. *Optics Letters*, 22(13), p.961.

[88] Peyrilloux, A., Chartier, T., Hideur, A., Berthelot, L., Melin, G., Lempereur, S., Pagnoux, D. and Roy, P., 2003. Theoretical and experimental study of the birefringence of a photonic

crystal fiber. *Journal of Lightwave Technology*, 21(2), pp.536-539.

[89] Quimby, R., 2006. *Photonics and lasers*. Hoboken, N.J.: Wiley-Interscience.

[90] Fang, X., MacDonald, K. and Zheludev, N., 2015. Controlling light with light using coherent metadevices: all-optical transistor, summator and invertor. *Light: Science & Applications*, 4(5), pp.e292-e292.

[91] Zhang, J., MacDonald, K. and Zheludev, N., 2012. Controlling light-with-light without nonlinearity. *Light: Science & Applications*, 1(7), pp.e18-e18.

[92] Dixit, N., and Singh, V., 2013. The Evolution of Optical Computing- Past, Present & Future. *International Journal of Scientific & Engineering Research*, 4(6), p 2572.

[93] Wang, C., Zhang, W., Zhao, Z., Wang, Y., Gao, P., Luo, Y. and Luo, X., 2016. Plasmonic Structures, Materials and Lenses for Optical Lithography beyond the Diffraction Limit: A Review. *Micromachines*, 7(7), p.118.

[94] Gramotnev, D. and Bozhevolnyi, S., 2010. Plasmonics beyond the diffraction limit. *Nature Photonics*, 4(2), pp.83-91.

[95] Song, M., Wang, D., Peana, S., Choudhury, S., Nyga, P., Kudyshev, Z., Yu, H., Boltasseva, A., Shalaev, V. and Kildishev, A., 2019. Colors with plasmonic nanostructures: A full-spectrum review. *Applied Physics Reviews*, 6(4), p.041308.

[96] Yan, M., 2019. Complex-k modes of plasmonic chain waveguides. *Journal of Physics Communications*, 3(11), p.115015.

[97] Yu, X., Sugeta, M., Yamagami, Y., Fujita, M. and Nagatsuma, T., 2019. Corrigendum: "Simultaneous low-loss and low-dispersion in a photonic-crystal waveguide for terahertz communications" *Applied Physics Express*, 12(11), p.119301.

[98] Kour, R., Arya, S., Young, S., Gupta, V., Bandhoria, P. and Khosla, A., 2020. Review—Recent Advances in Carbon Nanomaterials as Electrochemical Biosensors. *Journal of The Electrochemical Society*, 167(3), p.037555.

[99] Madsen, S., Christiansen, J., Christiansen, R., Vester-Petersen, J., Møller, S., Lakhotiya, H., Nazir, A., Eriksen, E., Roesgaard, S., Sigmund, O., Lissau, J., Destouesse, E., Madsen, M., Julsgaard, B. and Balling, P., 2019. Improving the efficiency of upconversion by light concentration using nanoparticle design. *Journal of Physics D: Applied Physics*, 53(7), p.073001.

[100] Sung, M., Ma, Y., Chau, Y. and Huang, D., 2010. Surface plasmon resonance in a hexagonal nanostructure formed by seven core shell nanocylinders. *Applied Optics*, 49(5), p.920.

[101] Olyaee, M., Tavakoli, M.,and Mokhtari, A., 2019. Propose, Analysis and Simulation of an All Optical Full Adder Based on Plasmonic Waves using Metal-Insulator-Metal Waveguide Structure. *Journal of Optoelectronical Nanostructures*, 4(3), 95-116.

[102] Lu, C., Hu, X., Yang, H. and Gong, Q., 2014. Chip-integrated ultrawide-band all-optical

logic comparator in plasmonic circuits. *Scientific reports*, *4*(1), pp.1-8.

[103] Bozhevolnyi, S. I.,2008 . Plasmonic Nano-Guides and Circuits, *Pan Stanford Publishing Pte. Ltd.*

[104] Kaboli, M. and Akhlaghi, M., 2016. Investigating the optical AND gate using plasmonic nano-spheres. *Journal of Computational Electronics*, *15*(1), pp.295-300.

[105] Fu, Y., Hu, X., Lu, C., Yue, S., Yang, H. and Gong, Q., 2012. All-Optical Logic Gates Based on Nanoscale Plasmonic Slot Waveguides. *Nano Letters*, 12(11), pp.5784-5790.

[106] Rouholamini, M., Kavehie, O., Mirbaha, A., Jasbi S. J., and Navi, K., 2007. A New Design for 7:2 Compressors, *2007 IEEE/ACS International Conference on Computer Systems and Applications*, Amman, Jordan, pp. 474-478.

[107] Aliparast, P., Koozehkanani, Z. and Nazari, F., 2013. An Ultra High Speed Digital 4-2 Compressor in 65-nm CMOS. *International Journal of Computer Theory and Engineering*, pp.593-597.

[108] Theis, T. and Wong, H., 2017. The End of Moore's Law: A New Beginning for Information Technology. *Computing in Science & Engineering*, 19(2), pp.41-50.

[109] Cho, G., Kim, Y., Lombardi, F., and Choi, M., 2009 . Performance evaluation of CNFET-based logic gates, *2009 IEEE Instrumentation and Measurement Technology Conference*, Singapore, pp. 909-912.

[110] Ghasemzadeh, H., 2016. Robustness Analysis of Controllable-Polarity Silicon Nanowire Devices and Circuits, Phd thesis, EPFL University.

[111] Raychowdhury, A., Keshavarzi, A., Kurtin, J., De, V. and Roy, K., 2006. Carbon Nanotube Field-Effect Transistors for High-Performance Digital Circuits—DC Analysis and Modeling Toward Optimum Transistor Structure. *IEEE Transactions on Electron Devices*, 53(11), pp.2711-2717.

[112] Hoanca, B., 2002. DWDM Fundamentals, Components, and Applications. *Journal of Optical Networking*, 1(5), pp. 184-185.

[113] Wu, Z., Xie, K. and Yang, H., 2012. Band gap properties of two-dimensional photonic crystals with rhombic lattice. *Optik*, 123(6), pp.534-536.

[114] Sakoda, K., 2004. *Optical Properties of Photonic Crystals*. Berlin, Heidelberg: Springer Berlin / Heidelberg.

[115] Joannopoulos. J. D., Johnson. S. G., Winn. J. N.,and Meade. R. D.,1995 . Photonic crystals: Modeling the flow of light, *Princeton University Press, Princeton.*

[116] Savarimuthu, R. and Rangaswamy, N., 2011. Bandstop filter for photonic integrated circuits using photonic crystal with circular ring resonator. *Journal of Nanophotonics*, 5(1), p.053521.

[117] Djavid, M., Monifi, F., Ghaffari, A. and Abrishamian, M., 2008. Heterostructure

wavelength division demultiplexers using photonic crystal ring resonators. *Optics Communications*, 281(15-16), pp.4028-4032.

[118] Youcef Mahmoud, M., Bassou, G., Taalbi, A. and Chekroun, Z., 2012. Optical channel drop filters based on photonic crystal ring resonators. *Optics Communications*, 285(3), pp.368-372.

[119] Rao, W., Song, Y., Liu, M. and Jin, C., 2010. All-optical switch based on photonic crystal microcavity with multi-resonant modes. *Optik*, 121(21), pp.1934-1936.

[120] Liu, Y. and Salemink, H., 2012. Photonic crystal-based all-optical on-chip sensor. *Optics Express*, 20(18), p.19912.

[121] Cui, Y., Wu, Q., Schonbrun, E., Tinker, M., Lee, J. and Park, W., 2008. Silicon-Based 2-D Slab Photonic Crystal TM Polarizer at Telecommunication Wavelength. *IEEE Photonics Technology Letters*, 20(8), pp.641-643.

[122] Yang, D., Tian, H. and Ji, Y., 2012. High-bandwidth and low-loss photonic crystal power-splitter with parallel output based on the integration of Y-junction and waveguide bends. *Optics Communications*, 285(18), pp.3752-3757.

[123] Park, I., Lee, H., Kim, H., Moon, K., Lee, S., O, B., Park, S. and Lee, E., 2004. Photonic crystal power-splitter based on directional coupling. *Optics Express*, 12(15), p.3599.

[124] Manzacca, G., Paciotti, D., Marchese, A., Moreolo, M. and Cincotti, G., 2007. 2D photonic crystal cavity-based WDM multiplexer. *Photonics and Nanostructures - Fundamentals and Applications*, 5(4), pp.164-170.

[125] Rawal, S. and Sinha, R., 2009. Design, analysis and optimization of silicon-on-insulator photonic crystal dual band wavelength demultiplexer. *Optics Communications*, 282(19), pp.3889-3894.

[126] Zhang, X., Liao, Q., Yu, T., Liu, N. and Huang, Y., 2012. Novel ultracompact wavelength division demultiplexer based on photonic band gap. *Optics Communications*, 285(3), pp.274-276.

[127] Alipour-Banaei, H., Mehdizadeh, F. and Serajmohammadi, S., 2013. A novel 4-channel demultiplexer based on photonic crystal ring resonators. *Optik*, 124(23), pp.5964-5967.

[128] Sakoda, K., 2004. *Optical Properties of Photonic Crystals*. Berlin, Heidelberg: Springer Berlin / Heidelberg.

[129] Alipour-Banaei, H., Serajmohammadi, S. and Mehdizadeh, F., 2014. Optical wavelength demultiplexer based on photonic crystal ring resonators. *Photonic Network Communications*, 29(2), pp.146-150.

[130] Scholz, S., Hess, O. and Rühle, R., 1998. Dynamic cross-waveguide optical switching with a nonlinear photonic band-gap structure. *Optics Express*, 3(1), pp.28-34.

[131] Hussein, H., Ali, T. and Rafat, N., 2018. New designs of a complete set of Photonic Crystals logic gates. *Optics Communications*, 411, pp.175-181.

[132] Alipour-Banaei, H., Serajmohammadi, S., Mehdizadeh, F.2017. All optical nand gate based on nonlinear photonic crystal ring resonators. Optik Int. J. Light Electron Opt. 130, 1214–1221

[133] Ahmadi Tameh, T., Isfahani, B., Granpayeh, N. and Javan, A., 2011. Improving the performance of all-optical switching based on nonlinear photonic Crystal microring resonators. *AEU - International Journal of Electronics and Communications*, 65(4), pp.281-287.

[134] Pashamehr, A., Zavvari, M. and Alipour-Banaei, H., 2016. All-optical AND/OR/NOT logic gates based on photonic crystal ring resonators. *Frontiers of Optoelectronics*, 9(4), pp.578-584.

[135] Johnson, S. and Joannopoulos, J., 2001. Block-iterative frequency-domain methods for Maxwell's equations in a planewave basis. *Optics Express*, 8(3), p.173.

[136] Pendry, J. and MacKinnon, A., 1992. Calculation of photon dispersion relations. *Physical Review Letters*, 69(19), pp.2772-2775.

[137] Pelosi, G., Coccioli, R., Selleri, S., 1997. *Quick Finite Elements for Electromagnetic Waves*, Artech House, Boston, London.

[138] Kane Yee, 1966 . Numerical solution of initial boundary value problems involving maxwell's equations in isotropic media," in *IEEE Transactions on Antennas and Propagation*, vol. 14, no. 3, pp. 302-307.

[139] Bachtold, A., Hadley, P., Nakanishi, T. and Dekker, C., 2001. Logic Circuits with Carbon Nanotube Transistors. *Science*, 294(5545), pp.1317-1320.

[140]Rodriguez, S., Rusu A., and de la Rosa, J. M., 2015. Overview of carbon-based circuits and systems, *2015 IEEE International Symposium on Circuits and Systems (ISCAS)*, Lisbon, Portugal, pp. 2912-2915,

[141] Ali Usmani, F. and Hasan, M., 2010. Carbon nanotube field effect transistors for high performance analog applications: An optimum design approach. *Microelectronics Journal*, 41(7), pp.395-402.

[142] Park, S., Vosguerichian, M. and Bao, Z., 2013. A review of fabrication and applications of carbon nanotube film-based flexible electronics. *Nanoscale*, 5(5), pp.1727-1752.

[143]M. Moaiyeri, R. Faghih, K. Navi, and et al, 2010 .Novel direct designs for 3-input XOR function for low-power and high-speed applications, ”International J. of Electronics, 97(6), pp. 647-662.

[144] Shankar, S., Kumar, A., and Nagaria, R.K., 2010 . A comparative performance analysis of various CMOS design techniques for XOR and XNOR circuits, *International Journal on Emerging Technologies*.

[145] Lee, H., and G. E. Sobelman, 1997. New low-voltage circuits for XOR and XNOR, *Proceedings IEEE SOUTHEASTCON '97. 'Engineering the New Century'*, Blacksburg,

VA, USA.

[146] Sharma, T., Sharma, K.G., Singh, B.P., and Arora, N., 2010 . New efficient design for XOR function on the transistor level*, 2010 International Conference on Methods and Models in Science and Technology*, India, pp.346-348.

[147] Singh, S., Sharma, T., Sharma, K.G., and Singh B.P., 2012 . New design of low power 3T XOR cell, *International Journal of Computer Engineering & Technology*, 3, pp. 76-80.

[148] Hatefinasab, S., 2016. CNTFET-Based Design of a High-Efficient Full Adder Using XOR Logic. *Journal of Nano- and Electronic Physics*, 8(4(2), pp.04061-1-04061-6.

[149] Kumar, M., and Nath, J., 2017 . Design of an Energy efficient 4-2 compressor, *IOP Conference Series: Materials Science and Engineering*, *225*,2017 *International Conference on Materials, Alloys and Experimental Mechanics,* Narsimha Reddy Engineering College, India

[150] Koren, I., 2002. *Computer arithmetic algorithms*. Natick: A K Peters/CRC Press.

[151] Chang, C., Gu, J. and Zhang, M., 2004. Ultra Low-Voltage Low-Power CMOS 4-2 and 5-2 Compressors for Fast Arithmetic Circuits. *IEEE Transactions on Circuits and Systems I: Regular Papers*, 51(10), pp.1985-1997.

[152] Nehru, K., Nagarjuna, T. and Vijay, G., 2017. Comparative Analysis of CNTFET and CMOS Logic based Arithmetic Logic Unit. *Journal of Nano- and Electronic Physics*, 9(4), pp.04018-1-04018-4.

[153] Dadashi, M., Manochehri, K., and Pourmozafari, S., 2016 . Low power CNTFET based 42 and 5-2 compressor, *International Conference on Computer Engineering and Signal Processing*

[154] Pishvaie, A., Jaberipur G., and Jahanian, A., 2013 . Redesigned CMOS (4; 2) compressor for fast binary multipliers, *Canadian Journal of Electrical and Computer Engineering*, 36(3), pp. 111-115.

[155] Rahnamaei, A., Zare Fatin, G., and. Eskandarian, A., 2019. Design of a low power high speed 4-2 compressor using CNTFET 32nm technology for parallel multipliers. *International Journal of Nano Dimension*, 10(1), pp. 114-124.

[156] Christina. X, Kabilan. A, 2012 . Design of optical logic gates using self-collimated beams in 2D photonic crystal, Photonic Sensors, 2(2) , pp. 173-179.

[157] Xavier. S, Arunachalam. K, Caroline. E, Johnson. W, 2014 .Design of two-dimensional photonic crystal-based all-optical binary adder, *Optical Engineering*, 52.

[158] Sadiku, M., 2009. Monte Carlo methods for electromagnetics. *Boca Raton: CRC PRESS*.

[159] Ning, K., Yufeng, H., Hongsen W., and Guilan, L., 2017 . The comparison of frequency domain method and time domain method in absorber reflectivity measurement, *2017 IEEE 5th International Symposium on Electromagnetic Compatibility (EMC-Beijing)*, Beijing, China, pp. 1-5.

[160] http://nano.stanford.edu/models.php.

[161] Mehrabi, S., Mirzaee, R., Moaiyeri, M., Navi, K. and Hashemipour, O., 2013. CNFET-Based Design of Energy-Efficient Symmetric Three-Input XOR and Full Adder Circuits. *Arabian Journal for Science and Engineering*, 38(12), pp.3367-3382.

[162] Feitelson, D., 1988. *Optical computing*. Cambridge, Mass.: *MIT Press*

[163] Alwayn, V., 2004. *Optical network design and implementation*. Cisco Press.

[164] Mohebzadeh-Bahabady, A. and Olyaee, S., 2018. All-optical NOT and XOR logic gates using photonic crystal nano-resonator and based on an interference effect. *IET Optoelectronics, 12*(4), pp.191-195.

[169]Saraswat, K., and Sharma, A., 2018 . An optimized XOR circuit using CNTFET technology, *International Journal of Advanced Research in Computer and Communication Engineering, IJARCCE,* 7, pp. 216-220.